Spring 2011

Evaluating mode of loading effect and laboratory fatigue performance of asphalt concrete using viscoelastic continuum damage mechanics

Aravind Krishna Swamy
University of New Hampshire, Durham

Follow this and additional works at: https://scholars.unh.edu/dissertation

EVALUATING MODE OF LOADING EFFECT AND LABORATORY FATIGUE

PERFORMANCE OF ASPHALT CONCRETE USING VISCOELASTIC CONTINUUM

DAMAGE MECHANICS

BY

ARAVIND KRISHNA SWAMY

Bachelor of Engineering, Visvesvaraya Technological University, India, 2003
Master of Technology, Indian institute of Technology Kanpur, India, 2006

DISSERTATION

Submitted to the University of New Hampshire
in Partial Fulfillment of
the Requirements for the Degree of

Doctor of Philosophy

in

Civil Engineering

May, 2011

UMI Number: 3467365
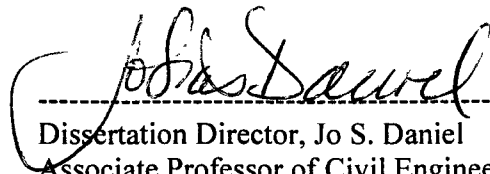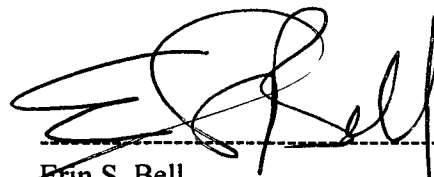
This dissertation has been examined and approved.
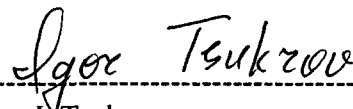
Dissertation Director, Jo S. Daniel
Associate Professor of Civil Engineering
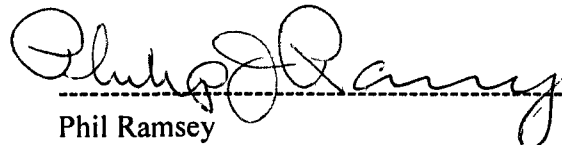
David L. Gress
Professor of Civil Engineering

Erin S. Bell
Associate Professor of Civil Engineering

Igor I. Tsukrov
Professor of Mechanical Engineering

Phil Ramsey
Adjunct and Visiting Faculty of Statistics

May 4, 2011
Date

DEDICATION

My grandfather Subbaiah, who inspired to work hard.

My parents, for their sacrifices that made this dissertation possible.

ACKNOWLEDGEMENTS

TABLE OF CONTENTS

LIST OF TABLES

LIST OF FIGURES

ABSTRACT

EVALUATING MODE OF LOADING EFFECT AND LABORATORY FATIGUE

PERFORMANCE OF ASPHALT CONCRETE USING VISCOELASTIC

CONTINUUM DAMAGE MECHANICS

by

Aravind Krishna Swamy

University of New Hampshire, May, 2011

In this research, an existing uniaxial constitutive model has been extended to flexural loading mode and a new approach to predict fatigue behavior is proposed. The proposed methodology involves dynamic modulus testing to obtain viscoelastic properties and subsequent fatigue testing. Several asphalt concrete beams were tested according to the proposed methodology. The analysis of data indicates that there exists a unique relationship between the flexural pseudostiffness and amount of damage in the specimen. To verify the accuracy of the fatigue prediction model, fatigue tests were conducted on specimens that were not part of preliminary analysis. The fatigue life predictions made were comparable to actual measurements. The proposed methodology offers advantages like considerable savings in testing time and materials when compared to the existing AASHTO protocol.

An alternative approach for the determination of the fatigue endurance limit of asphalt concrete using the elastic-viscoelastic correspondence principle is proposed. The proposed testing procedure consists of applying stress or strain blocks of loading starting from low to high amplitude. The development of loops and changes in stress-pseudostrain loops is used to detect damage in the specimen. To verify the proposed methodology, tests were conducted under different modes (stress and strain controlled, uniaxial and flexure). When compared to strain controlled mode, the stress controlled mode required shorter testing time, had less noise and offered better control during testing.

The third part of this research is to study the effect of mode of loading on viscoelastic properties and damage characteristics. Several specimens were tested under uniaxial, biaxial and flexure mode to obtain fingerprints of viscoelastic and damage properties. It was found that viscoelastic and damage properties are dependent on loading mode and testing frequency. A systematic variation of viscoelastic properties was found between different loading modes. Several frequency dependent modular ratios are proposed which, in principle, can be used as modal correction factors. It was observed that the specimen undergoes damage at a faster rate under uniaxial mode when compared to flexure loading mode. At a given value of normalized pseudostiffness, the damage parameter ratio remained approximately same and is a function of material properties.

CHAPTER 1

INTRODUCTION

1.1 Importance of asphalt concrete characterization

Asphalt concrete is a composite material composed of aggregates and asphalt binder where randomly oriented aggregates are held together by asphalt cement. The internal arrangement/orientation of aggregates, particle size distribution, thickness and nature of asphalt coating on aggregates affect the load transfer mechanism, which in turn affects overall behavior of asphalt concrete. At low temperature and/or fast loading rate asphalt concrete behaves elastically whereas at high temperature and/or slow loading rate asphalt concrete exhibits viscoelastic and/or viscoplastic behavior. Thus asphalt concrete behavior is a function of testing temperature, loading rate, loading frequency, relative proportions and properties of individual components. Such a range of behavior makes asphalt concrete modeling challenging.

Asphalt concrete undergoes fatigue when subjected to cyclic loads. Under damage inducing stress (or strains), the internal structure of the asphalt concrete changes at places of high stress (or strain) concentrations and microcracks originate from these zones. If a sufficient time lag (rest period) is provided between successive loads, these microcracks close; otherwise, these microcracks coalesce to form macrocracks (Kim and Little 1990, Kim et al. 1995). In the absence of a crack arresting mechanism, these macrocracks further propagate leading to failure of the material. This damage

development is usually accompanied with a decrease in elastic modulus, yield stress, hardness, and density as well as increase in creep strain rate (Lemaitre and Desmorat 2005). To improve the performance of asphalt concrete, complete understanding of its behavior is required.

In general, there are two different approaches for studying the fatigue behavior. These can be broadly classified into phenomenological (empirical) approaches and mechanistic approaches. The phenomenological approaches are completely based on experimental data and are popular among engineering communities due to their simplistic nature. On the other hand, mechanistic approaches are based on fundamental energy; mechanics based principles and are complex but applicable to wide range of loading and environmental conditions.

The phenomenological models relate the fatigue performance to the properties of asphalt concrete in an undamaged state. However, damage evolution in asphalt concrete is complicated due to interaction among viscoelastic effects, relaxation, healing and the heterogeneous nature of the mix. As such, the fatigue life obtained by the laboratory calibrated phenomenological model is usually lower than that observed in field. Some reasons for such discrepancy are densification under traffic, temperature fluctuations, lateral wander of traffic, healing and differences in geometry and test conditions in pavement when compared to laboratory setup (Molenaar 2007, Prowell et al. 2008). To account for these differences, a shift factor is often applied to the lab calibrated fatigue model. The shift factor suggested by some researchers is between 13-20 (Finn et al. 1977, Prowell et al. 2008) whereas others have used shift factor in the range of 100-750 (Brown 1974, Brunton et al. 1987). Molenaar (2007) has noted that type of fatigue

testing and mode of loading affects the magnitude of the shift factor. When compared to an empirical approach, use of a mechanistic approach to characterize asphalt concrete increases the reliability of the prediction model. Hence it can be expected that the shift factor for a mechanistic model will be small when compared to shift factor in empirical model. Also, the asphalt concrete behavior is dependent on the mode of loading and applied boundary conditions. Thus, one has to conduct a factorial experiment to account for above-mentioned factors in a phenomenological model. Development of a phenomenological model requires large amount of materials and time. Any phenomenological model will be of limited use if the response of a material needs to be predicted in a new condition. Under such circumstances, the mechanistic approach offers an efficient alternative.

As mentioned earlier, mechanistic approaches are more fundamental. Some examples of mechanistic approaches are micromechanics, fracture mechanics, and continuum damage approach. In the micromechanical approach, the behavior of material is modeled using the microcrack orientation and the crack density in an idealized representative volume. However, such an approach is difficult to use for routine work due to the complex microstructure of asphalt concrete, interaction among defects within the sample and computational requirements. The fracture mechanics approach assumes that the material has preexisting microcracks (Jacobs et al. 1995) and the damage process is localized. Thus it fails to explain the behavior in an undamaged state and the process of crack initiation. Fracture mechanics approach requires extensive experimental data for validating the damage model. Researchers have found that some parameters used in fracture mechanics approach are not material constants (Park 1994,

C333 1999). In continuum damage models, a damaged body is represented by a homogeneous continuum where the scale of the test specimen is much larger than the defect size. Any change in microstructure affects overall behavior of the material. The continuum damage models use these macroscale observations to capture the net effect of microstructure changes. Thus a continuum damage model is convenient for modeling overall behavior of the material. Present day continuum damage models can handle performance based tests with sufficient accuracy.

1.2 Objectives of this research

Due to limitations of equipment, personnel, or specimen fabrication, different test geometries have been used by various agencies and researchers for developing constitutive models and studying fatigue behavior. Some of the testing geometrics presently used are shown in Figure 1-1 (Daniel 2001, AASHTO 2003, Rowe 1993, Kim et al. 2004, Molenaar 2002, Kim et al. 2002). Each test geometry induces a different stress and/or strain distribution in the specimen, resulting in different values for measured properties. This in turn affects the development of the model itself. Thus a model developed under a specific geometry may not be directly related to another geometry. Very little work has been done to relate fundamental viscoelastic properties under different geometries. Establishing these relationships will provide a link between modeling efforts on viscoelastic materials based on different testing methods.

4
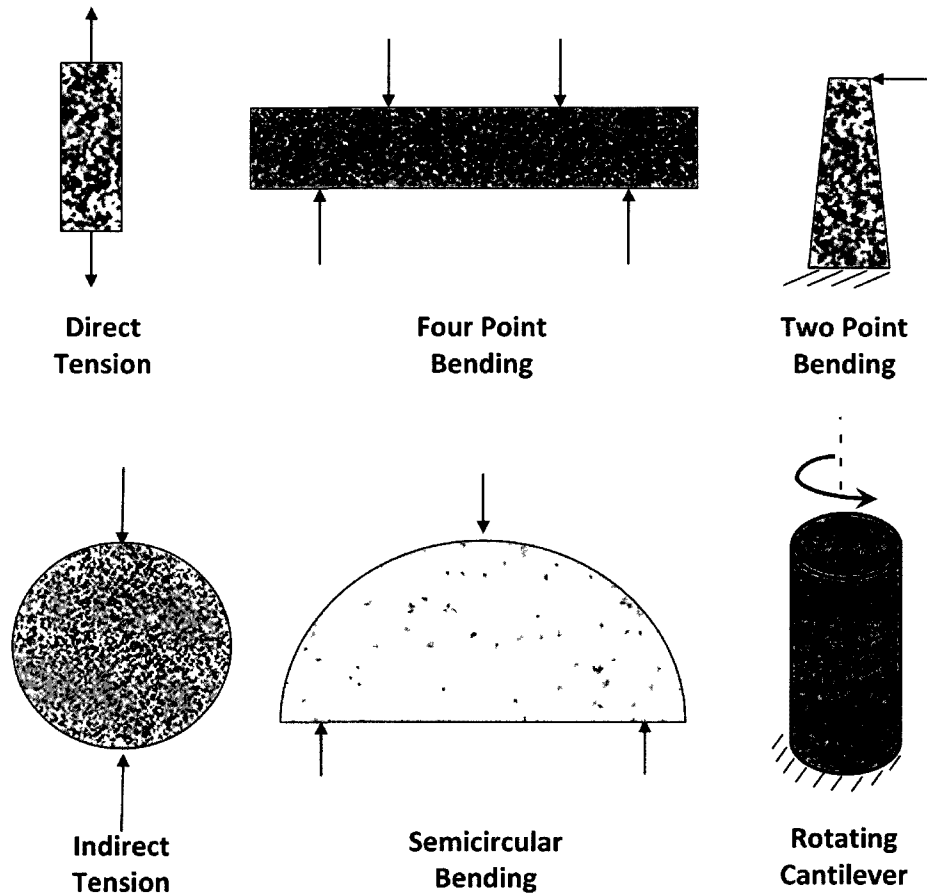
Figure 1-1: Commonly used testing configurations in asphalt concrete research

Previous research indicated that the fatigue life (number of load repetitions before failure) is dependent on mode of loading and testing configuration. Tayebali et al. (1994) found that fatigue life under controlled strain mode is approximately 2.4 times greater than under controlled stress mode of loading. Molenaar (2007) reported that fatigue life under two point flexure is less when compared to four point flexure which was attributed to differences in volume of material subjected to fatigue. However the slope of the fatigue curves remained same. Using Weibull's theory, Pronk (1998) showed that fatigue life under four point flexure is approximately 2.8 times fatigue life

under two point flexure. Adhikari and You (2010) found a strong linear correlation between the flexural stiffness and compression modulus of asphalt concrete, with the flexural stiffness about 30% lower than the compression modulus.

The present research studies the effect of mode of loading on viscoelastic properties and fatigue behavior. These viscoelastic and damage properties between different modes of loading are related through experimental results. The damage evolution mechanism among different testing configurations and modes of loading are related using principles of continuum damage mechanics. The specific objectives of this study are as follows:

- Extension of uniaxial constitutive model to flexure mode of loading,
- Development of the testing protocol to find the fatigue endurance limit of asphalt concrete,
- Comparison of viscoelastic properties under the different modes of loading (uniaxial, biaxial and flexural),
- Comparison of the damage evolution mechanism between uniaxial and flexure mode of loading.

1.3 Organization of the dissertation

This dissertation contains eight chapters of which this is the first one. This chapter is followed by literature review, where a review of topics related to this research is presented. Chapter three discusses materials, specimen fabrication, testing setup and experimental testing details used in this research. Details regarding tests conducted and

analytical methods to obtain viscoelastic properties from measured test data are presented in chapter four. The chapter five is on extension of uniaxial constitutive model to flexure mode of loading. Chapter six presents a new approach to determine the fatigue endurance limit of asphalt concrete. Chapter seven compares viscoelastic and damage model parameters obtained under different modes of loading. The conclusions and further scope have been given in chapter eight.

CHAPTER 2

THEORETICAL BACKGROUND AND LITERATURE REVIEW

This chapter briefly discusses the background related to different aspects of modeling, characterization of asphalt concrete behavior and testing. The topics that are discussed in this chapter are theory of viscoelasticity, viscoelastic continuum damage (VECD) mechanics, and experimental characterization of fatigue and fatigue endurance limit. These topics are discussed as individual sections below.

2.1 Phenomenological models for fatigue characterization

Phenomenological models have been widely used in fatigue behavior modeling. Traditionally third point loaded rectangular beams have been used to evaluate fatigue characteristics. The phenomenological model development involves testing several beams at different stress or strain levels (usually strain) until failure of the specimen. The sample is typically considered to have failed when its stiffness is reduced by 50% of its initial stiffness (Van Dijk and Vesser 1977, Tayebali et al. 1993). Using regression analysis, a relationship between number of repetitions and initial stress (or strain) (and associated variables) to failure is developed. Thus these models are empirical in nature. Strain based fatigue models widely used in asphalt concrete characterization are given in Equations 2-1 and 2-2 (Monismith et al. 1985, Tayebali et al. 1993).

$$N_f = a_1 \left[\frac{1}{\varepsilon_0}\right]^{a_2}$$

<div align="right">2-1</div>

$$N_f = a_3 \left[\frac{1}{\varepsilon_0}\right]^{a_4} \left[\frac{1}{S_0}\right]^{a_5}$$

<div align="right">2-2</div>

where N_f = number of cycles to failure;

      ε_0 = initial tensile strain;

      S_0 = initial stiffness; and

      a_i = regression coefficients.

It has been observed that the plot of number of cycles to failure against initial strain (both on log scale) generally follows a straight line relationship. An example for relationship between number of cycles to failure and initial tensile strain is given in Figure 2-1 (Tayebali et al. 1996). Approximately 10 beam specimens to be tested for fatigue performance at different strain levels to obtain the fatigue curve. Monismith and McLean (1972) observed that relationship between the applied strain and number of cycles to failure (both on log scale) converged below 70 microstrain at approximately 5 million cycles.
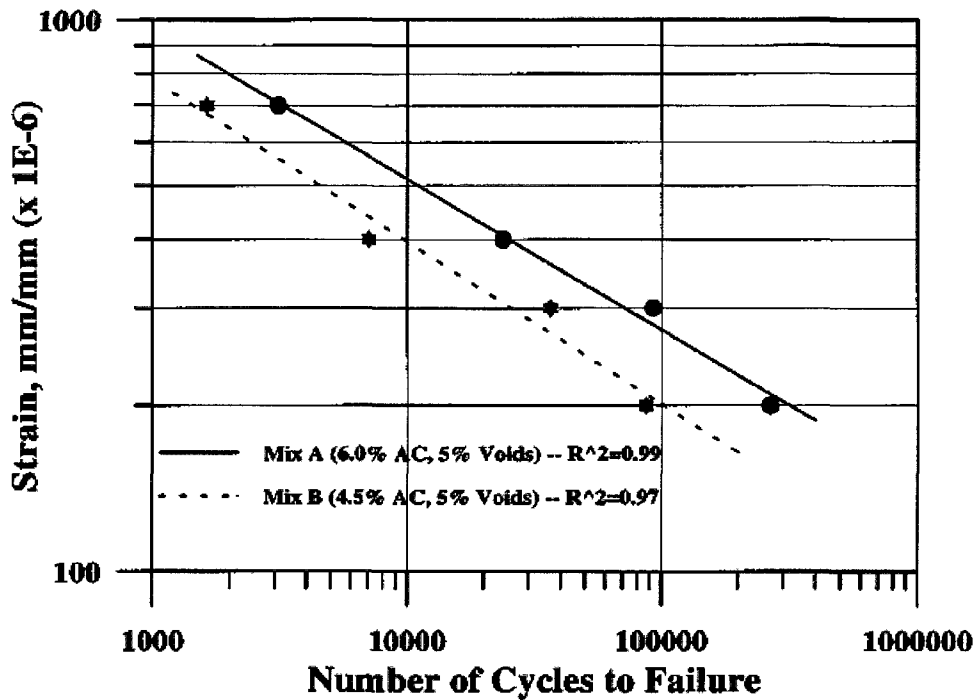
Figure 2-1: Relationship between strain and number of cycles to failure by phenomenological approach

If the stress or strain level is very low, damage induced in the specimen during each loading cycle is very small. Thus, the sample can sustain a large number of load repetitions before failure. For all practical purposes, significantly large number of cycles to failure (around 50 million cycles) can be considered to be infinite (Prowell et al. 2008). This stress or stain level at which the specimen can sustain infinite number of cycles before failure is defined as the fatigue endurance limit.

Birgisson et al. (2007) used a fracture mechanics approach to find a crack growth threshold. Their study found that fracture energy density is a threshold for crack growth in viscoelastic materials. During their study it was found that if the strain energy threshold is not exceeded, any microdamage developed in specimen is fully healable.

Due to the lengthy testing time, limited studies have been conducted for the determination of fatigue endurance limit. To reduce the required testing time, the specimens are tested to limited number of cycles, fit with analytical functions, and extrapolated to determine the fatigue endurance limit. In recent studies, logarithmic and Weibull function have been used to extrapolate the test data at lower cycles to predict the fatigue endurance limit (Prowell et al. 2008).

Based on limited test results, Monismith and McLean (1972) concluded that the fatigue endurance limit of asphalt concrete is 70 microstrain. Using the beam fatigue test data, Carpenter et al. (2003) concluded that fatigue endurance limit of asphalt concrete is in range of 70-90 microstrain at 20 ^{0}C. However this threshold of 70 microstrain has been questioned by Molenaar (2007).

2.2 Theory of viscoelasticity

Viscoelastic materials exhibit time and rate dependent behavior. These materials store energy like an elastic material and dissipate energy like a viscous material. If such a material satisfies conditions of homogeneity and superposition, then it is referred to as a linear viscoelastic (LVE) material. The conditions of homogeneity and superposition are given in Equations 2-3 and 2-4, respectively. Schematic diagrams for homogeneity and superposition conditions are presented in Figures 2-2 and 2-3, respectively.

$$R\{a\,I_1\} = a\,R\{I_1\} \qquad\qquad 2\text{-}3$$

$$R\{I_2 + I_3\} = R\{I_2\} + R\{I_3\} \qquad\qquad 2\text{-}4$$

where I_1, I_2, I_3 = input histories;

      R = response; and

      a = arbitrary constant.
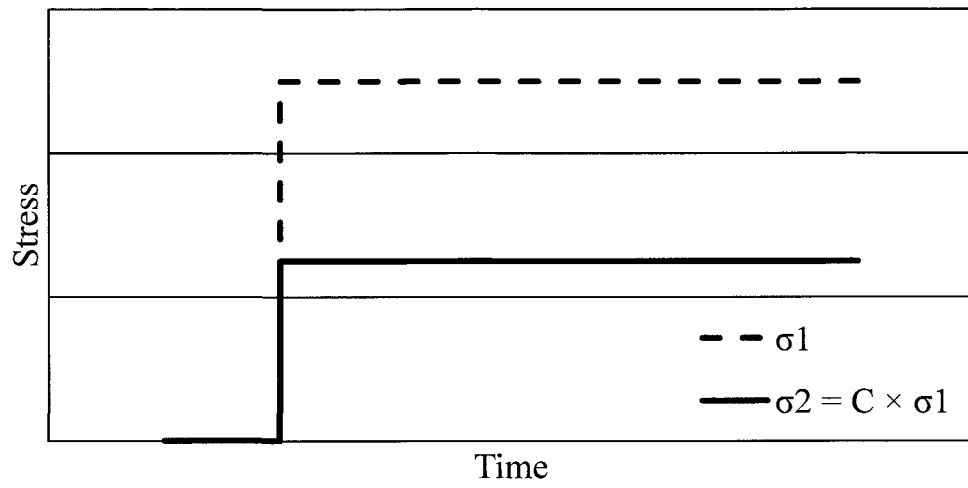
(a)
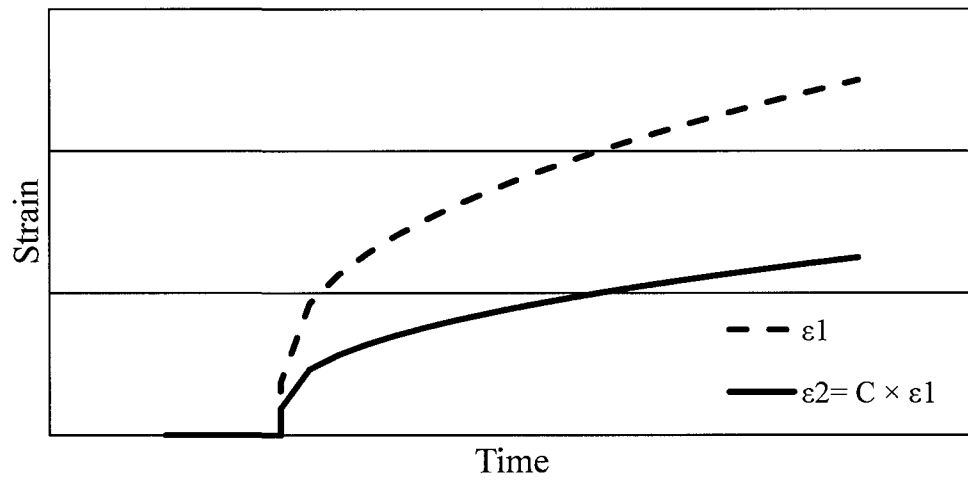
(b)

Figure 2-2: Illustration for principle of homogeneity
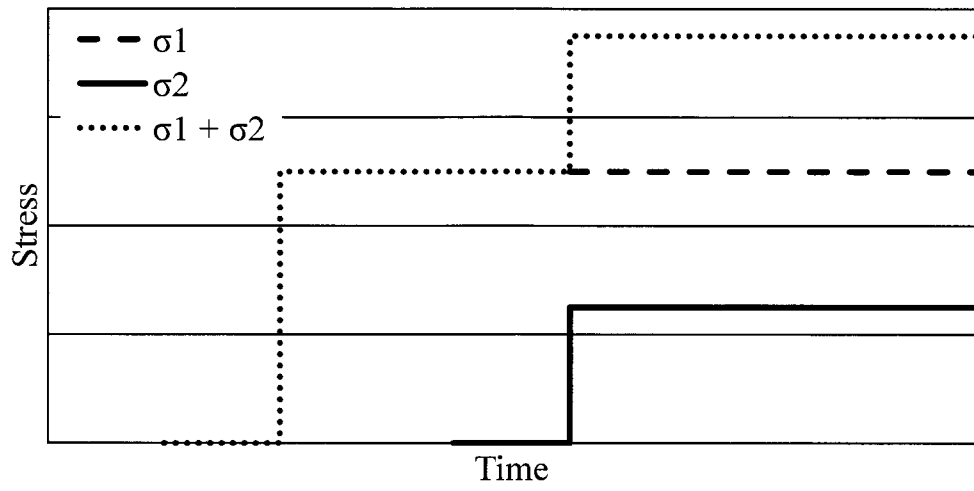
(a)
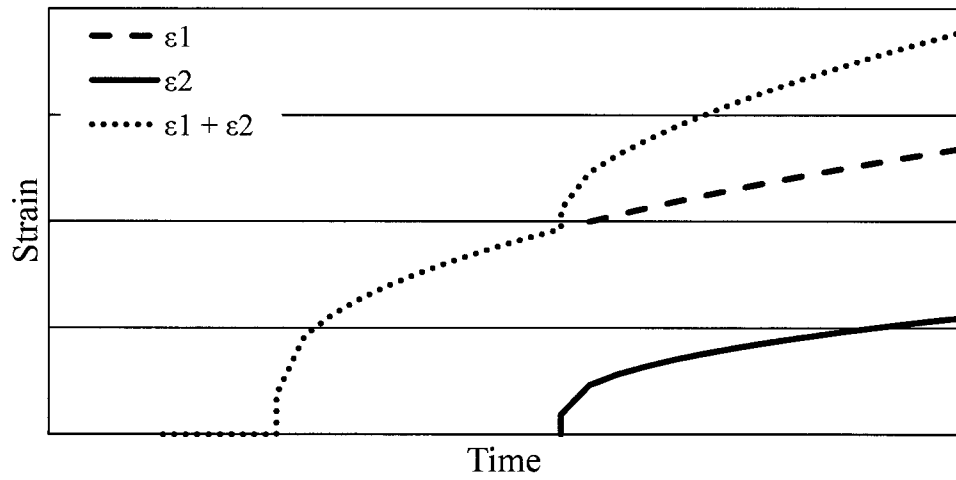
(b)

Figure 2-3: Illustration for principle of superposition

If the physical and/or chemical properties of a material's constituents remain the same with time, it is referred to as nonaging material. In the present study, the asphalt concrete is assumed to be a nonaging, linear viscoelastic material. However, asphalt concrete exposed to the environment will experience significant changes in physical and/or chemical properties over time.

Any viscoelastic material is considered as thermorheologically simple within linear viscoelastic limits if the time-temperature superposition principle can be applied. In other words, isothermal curves of any viscoelastic property obtained at different temperatures should yield a single continuous mastercurve by horizontally shifting the individual isothermal curves along frequency (or time) axis. The same temperature shift factors (calculated during horizontal shifting of isotherms) can be used for obtaining other mastercurves at a different temperature.

For a nonaging, anisotropic, linear viscoelastic material, stress-strain relations are given by Equations 2-5 and 2-6.

$$\sigma_{ij}(t) = \int_{-\infty}^{t} C_{ijkl}(t - \tau)\frac{d\varepsilon_{kl}}{d\tau}\, d\tau \qquad\qquad 2\text{-}5$$

$$\varepsilon_{ij}(t) = \int_{-\infty}^{t} S_{ijkl}(t - \tau)\frac{d\sigma_{kl}}{d\tau}\, d\tau \qquad\qquad 2\text{-}6$$

where ε = strain tensor of second order;

   σ = stress tensor of second order;

   C = relaxation function tensor of fourth order;

   S = creep function tensor of fourth order; and

t, τ = time variables.

If the input starts at $t = 0$, both the input and output are equal to zero before t < 0. Thus for $t < 0, \frac{d\varepsilon}{d\tau} = \frac{d\sigma}{d\tau} = 0$. When input is equal to zero, unit response functions (i.e. relaxation and creep function) will also be zero. For the uniaxial loading case, Equations 2-5 and 2-6 reduce to the following:

$$\sigma(t) = \int_0^t E\,(t - \tau)\frac{d\varepsilon}{d\tau}\,d\tau \qquad\qquad 2\text{-}7$$

$$\varepsilon\,(t) = \int_0^t D\,(t - \tau)\frac{d\sigma}{d\tau}\,d\tau \qquad\qquad 2\text{-}8$$

where ε = strain;

σ = stress;

$E\,(t)$ = uniaxial relaxation modulus function;

$D\,(t)$ = uniaxial creep compliance function; and

t, τ = time variables.

Using Boltzman's superposition integrals, Schapery proposed the elastic-viscoelastic correspondence principle for analyzing the fracture behavior of solid propellant (Schapery 1984). By using such an integral form, hereditary effects in the viscoelastic material are taken into account while predicting response of the material. The elastic-viscoelastic correspondence principle uses the concept of a pseudo variable through which a viscoelastic problem is reduced to an equivalent elastic problem. According to this theory, constitutive equations for a viscoelastic material

16

are similar to that of an elastic material, with the actual stress and/or the strain being replaced by pseudostress and/or pseudostrain, respectively. In other words, if linear elastic solution for a problem is known, it is possible to determine corresponding linear viscoelastic solution through the convolution integral. Under uniaxial loading conditions, expressions for the pseudostress and pseudostrain are given in Equations 2-9 and 2-10, respectively. The pseudo variables are made dimensionless by using reference modulus (E_R).

$$\sigma^R(t) = E_R \int_0^t D\,(t-\tau)\frac{d\sigma}{d\tau}\,d\tau \qquad\qquad 2\text{-}9$$

$$\varepsilon^R(t) = \frac{1}{E_R}\int_0^t E\,(t-\tau)\frac{d\varepsilon}{d\tau}\,d\tau \qquad\qquad 2\text{-}10$$

where ε^R = pseudostrain;

σ^R = pseudostress;

ε = strain;

σ = stress;

$E\,(t)$ = uniaxial relaxation modulus function;

$D\,(t)$ = uniaxial creep compliance function; and

t, τ = time variables.

When applied stress or strain is sufficiently small, any loops observed in stress vs. strain cross plots are completely due to viscoelastic response of asphalt concrete. In other words, at small stresses or strains applied, the damage is negligible. Hence the

pseudostrain is equal to the measured stress and the stress-pseudostrain relationship is linear. The slope of the stress vs. pseudostrain plot is equal to the reference modulus. A typical plot of stress vs. strain and stress vs. pseudostrain at levels well below damage inducing loads is shown in Figure 2-4. Since the specimen is subjected to non-damaging loads, development of loops in stress vs. strain cross plot is due to viscoelasticity only. However for same data, cross plot of stress vs. pseudostrain, all the loops collapses to a straight line.
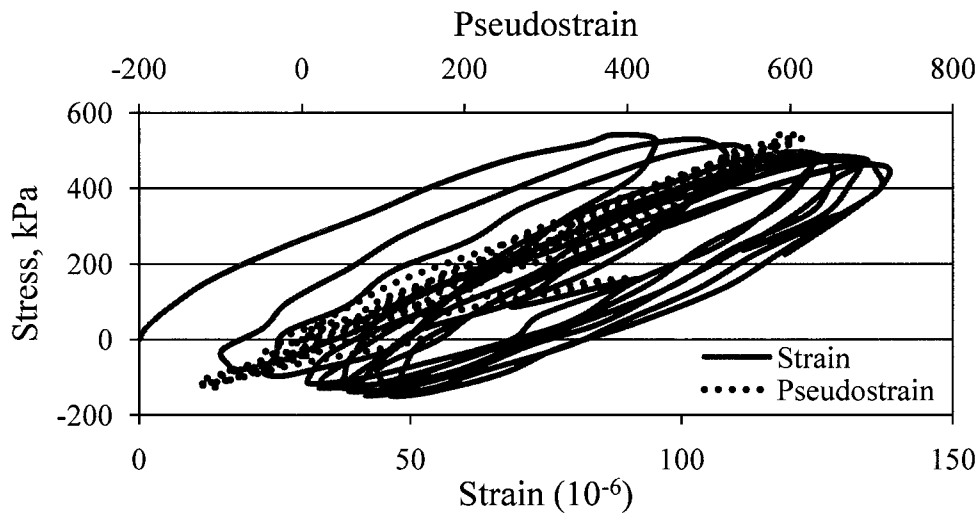
Figure 2-4: Linear viscoelastic behavior in undamaged viscoelastic material

2.3 Continuum damage mechanics

A continuum damage model is a convenient tool to predict the overall response of a material. This approach is based on the principles of thermodynamics where the stress-strain relationship is modeled using damage variables. This approach was initiated by the works of Kachanov (1958) and Rabotnov (1963) and is often referred to as Continuum Damage Mechanics (CDM).

Generally, a continuum damage model consists of (i) damage variable, (ii) strain energy density function and (iii) damage evolution law. While the damage variable quantifies the damage in the specimen, the strain energy density function relates the different parameters (like stress, strain) involved in the constitutive framework. Any damage variable can be represented by a scalar to a fourth order tensor (Lemaitre and Desmorat 2005). However, selection of the damage variable order is governed by the complexity of the problem, the mechanisms of damage evolution and the arrangement of particles in matrix (Park 1994, Lemaitre and Desmorat 2005). Sometimes these damage variables are referred to as Internal State Variables (ISV's).

Schapery (1990) developed a constitutive theory for the elastic medium with growing damage. This theory is based on the thermodynamics of irreversible process and is generally referred to as Schapery's Work Potential Theory (WPT). According to WPT, for an anisotropic elastic material without damage, expressions for the stress-strain relation and the strain energy density function are given in Equations 2-11 and 2-12, respectively. For an elastic material, the strain energy density function reduces to Equation 2-13.

$$\sigma_{ij} = \frac{\partial W}{\partial \varepsilon_{ij}}$$ 2-11

$$W = W(\varepsilon_{ij})$$ 2-12

$$W = \frac{1}{2} C_{ijkl} \varepsilon_{ij} \varepsilon_{kl}$$ 2-13

where W = strain energy density function;

19

ε = strain tensor of second order;

σ = stress tensor of second order; and

C = stiffness tensor of fourth order.

For an elastic material with growing damage, the above equations are suitably modified using thermodynamic principles. For such a problem, the strain energy density function and the damage evolution law are given in Equations 2-14 and 2-15, respectively.

$$W = W(\varepsilon_{ij}, S_m) \qquad \text{2-14}$$

$$-\frac{\partial W}{\partial S_m} = \frac{\partial W_S}{\partial S_m} \qquad \text{2-15}$$

where W = strain energy density function;

S_m = internal state variables;

ε = strain tensor of second order; and

W_S = dissipated strain energy.

Schapery (1990) proposed a method to extend the work potential theory to viscoelastic media with growing damage. According to this method, the basic equations developed in the work potential theory can be used for viscoelastic problems, provided the physical strain is replaced by the corresponding pseudostrain. Also, the rate type damage evolution law is employed to account for the rate dependent damage in viscoelastic materials. The strain energy density function and the damage evolution law for viscoelastic material with growing damage are given in Equations 2-16 and 2-17, respectively.

$$W^R = W^R\left(\varepsilon_{ij}^R, S_m\right) \qquad\qquad \text{2-16}$$

$$-\frac{\partial S_m}{\partial t} = \left(\frac{\partial W^R}{\partial S_m}\right)^\alpha \qquad\qquad \text{2-17}$$

where W^R = pseudostrain energy density function;

ε^R = pseudostrain;

S_m = internal state variables;

t = time variables; and

α = material constant.

2.4 Viscoelastic continuum damage mechanics

The modeling of damage evolution in asphalt concrete using the elastic-viscoelastic correspondence principle and damage mechanics principles was initiated by Kim (1988) and Kim and Little (1990). He successfully applied the elastic-viscoelastic correspondence principle for modeling sand-asphalt mixture behavior under multi level cyclic loading.

Schapery's WPT has been used in modeling asphalt concrete under monotonic and cyclic loading conditions (Lee 1996, Park et al. 1996, Lee and Kim 1998a). Lee and Kim (1998) incorporated the healing mechanism into the damage evolution process. The same research found that the secant pseudostiffness (stress corresponding to maximum pseudostrain divided by maximum pseudostrain in each cycle) value decreases with increasing damage. Also, the sample to sample variability was

eliminated through the normalization of the pseudostiffness values (dividing pseudostiffness values by initial pseudostiffness value). The general form of the uniaxial constitutive model used in above mentioned research is presented in Equation 2-18. Physically $C(S_m)$ denotes variation in the material stiffness with changing microstructure. This research assumes that any damage in specimen is reflected in changing material stiffness i.e. overall response.

$$\sigma = C(S_m)\, \varepsilon^R \qquad\qquad 2\text{-}18$$

where $C(S_m)$ = normalized pseudostiffness as function of damage parameters;

S_m = damage parameter (number of damage parameters depends on ISV's).

Daniel (Daniel 2001, Daniel and Kim 2002) found that the relationship between the normalized pseudostiffness ($C1$) and the damage parameter ($S1$) is unique for a given asphalt concrete mix (hereafter referred to as damage characteristic function) under uniaxial mode of loading. The damage parameter ($S1$) under monotonic and cyclic test conditions are calculated using Equations 2-19 and 2-20, respectively. Using the damage characteristic function, Daniel proposed that the monotonic test results can be used solely for the constitutive modeling of asphalt concrete. Also it was found that by using temperature shift factors, the effect of temperature can be eliminated. By such a process, a constitutive model developed using the monotonic test can be used to predict the behavior of asphalt concrete under varying testing conditions. These findings lead to decrease in the testing time and resources required.

$$S1(t) \cong \sum_{i=1}^{N} \left[\frac{I}{2}(\varepsilon_i^R)^2(C1_{i-1} - C1_i)\right]^{\frac{\alpha}{1+\alpha}} (t_i - t_{i-1})^{\frac{1}{1+\alpha}}$$ 2-19

$$S1(t) \cong \sum_{i=1}^{N} \left[\frac{I}{2}(\varepsilon_i^R)^2(C1_{i-1} - C1_i)\right]^{\frac{\alpha}{1+\alpha}} \left(\frac{t_i - t_{i-1}}{2}\right)^{\frac{1}{1+\alpha}}$$ 2-20

where ε_i^R = pseudostrain;

$S1(t)$ = damage parameter as a function of time (t);

I = initial pseudostiffness;

$C1$ = normalized pseudostiffness;

α = material constant; and

t = time variable.

Kim et al. (2002) verified the application of the elastic-viscoelastic correspondence principle under the shear mode of loading. This research used Dynamic Mechanical Analysis (DMA) to evaluate fatigue and healing mechanisms in sand asphalt mixtures. However, adoption of this protocol for asphalt concrete mixtures involves certain issues like larger specimen size requirements and higher capacity testing equipment.

It should be noted that in all the above-mentioned works, it was assumed that only elastic and viscoelastic components are acting during the process of damage evolution. It was the work of Chehab (Chehab 2002, Chehab et al. 2002) that recognized the importance of viscoplasticity in the damage evolution process in asphalt concrete. Chehab incorporated viscoplasticity into the continuum damage model using the strain hardening model (Uzan et al. 1985, Schapery 1999). It was found that the time-

temperature superposition principle is valid even when the material is in damaged state (Chehab 2002, Chehab et al. 2002).

Kutay et al. (2008) developed a simplified form of continuum damage model using dynamic modulus values instead of secant pseudostiffness. The maximum pseudostrain in each cycle was calculated using the product of linear viscoelastic dynamic modulus and peak strain in each cycle. This is based on the assumption that the material is at steady state with zero mean stress (Underwood et al. 2010). Since the damaged dynamic modulus accounts for cyclic stress and strain amplitudes only, this approach ignores the effect of permanent strain in the sample. Underwood et al. (2009, 2010) found that the steady state assumption introduces a minor error in calculation of the pseudostrain and used a correction factor to account for duration during which the specimen is under tensile stress. Another assumption in the simplified of continuum damage model was that pseudostrain is constant within the cycle which, in actuality is not so. Thus Hou et al. (2010) used a loading history dependent adjustment factor while calculating the damage parameter. Hou et al. (2010) defined a normalization parameter (I) based on dynamic modulus of the undamaged specimen and dynamic modulus value obtained from the master curve to account for specimen to specimen variability. This is a significant deviation from previous researches (Lee and Kim 1998, Daniel and Kim 2002) where initial slope of stress-pseudostrain in the first cycle was used as a normalization parameter.

2.5 Energy based methods for fatigue characterization

Other researchers have used the dissipated energy approach for modeling the fatigue behavior (Van Dijk and Vesser 1977, Rowe 1993, Ghuzlan 2001) in asphalt concrete. The dissipated energy is the amount of energy lost by the material during each loading-unloading cycle. This loss of energy is related to stress amplitude, strain amplitude and phase angle between stress and strain. This lost energy can be measured by calculating the area within the stress vs. strain loop (hysteresis loop). Any changes in location, area and slope of the hysteresis loop during a fatigue test reflect that microstructural change has occurred in the specimen. The expression to calculate the dissipated energy is given in Equation 2-21. Hysteresis behavior during a fatigue test is presented in Figure 2-5.

$$DE = \pi\, \sigma_{amp} \varepsilon_{amp} \sin \Phi$$

2-21

where DE = dissipated energy;

σ_{amp} = stress amplitude;

ε_{amp} = strain amplitude; and

Φ = phase angle.
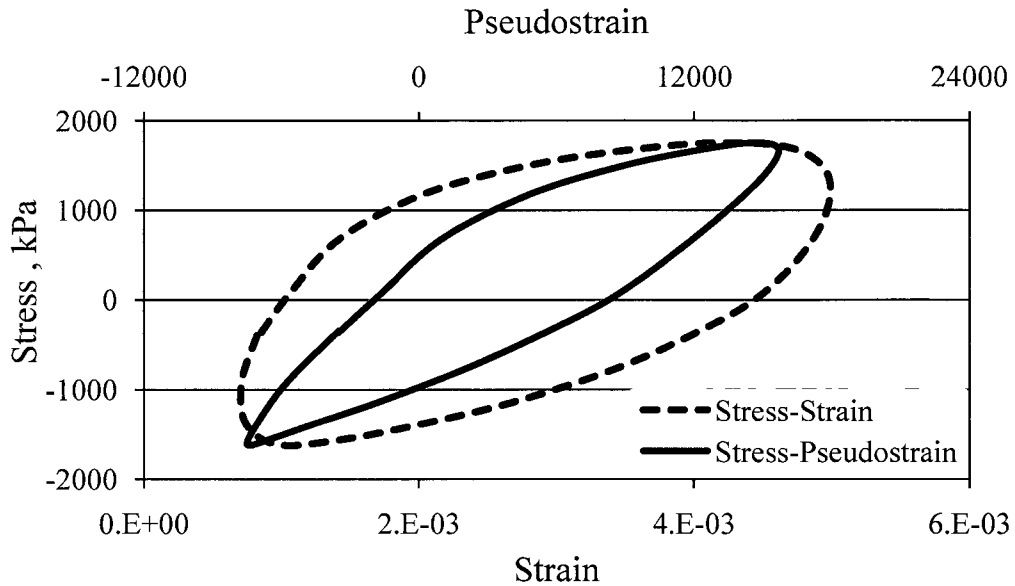
Figure 2-5: Typical hysteresis and pseudohysteresis loops in viscoelastic material

Rowe (1993) and Ghuzlan (2001) found that initial dissipated energy is a significant factor that affects HMA fatigue behavior. However, relationship between initial dissipated energy and fatigue life at low strain levels has been questioned by Carpenter and Shen (2006).

To account for the damage evolution during testing, the cumulative dissipated energy has been used (Chomton and Valayer 1972, Van Dijk and Vesser 1977). Van Dijk and Vesser (1977) found a strong correlation between cumulative dissipated strain energy and the number of loading cycles to failure. The empirical relationship between cumulative dissipated strain energy and the number of loading cycles to failure is given in Equation 2-22. Based on fatigue tests conducted at different frequencies and temperatures, and different strain and stress amplitudes, Van Dijk and Vesser (1977) reported a value of b to be between 0.6 and 0.7.

$$W_{tot} = A \, N_f{}^b \qquad\qquad \text{2-22}$$

where W_{tot} = total dissipated energy;

N_f = number of cycles to failure; and

A, b = experimentally derived mix coefficients.

In order to identify damage during fatigue testing, Guzlan and Carpenter (2000) used the Dissipated Energy Ratio (DER) to quantify relative change in dissipated strain energy. The expression for the DER is given in Equation 2-23. Guzlan and Carpenter (2000) found a strong relationship between DER and number of cycles to failure.

$$DER = \frac{DE_a - DE_b}{DE_a} \qquad\qquad \text{2-23}$$

where DER = dissipated energy ratio;

DE_a = dissipated energy in cycle a; and

DE_b = dissipated energy in cycle b.
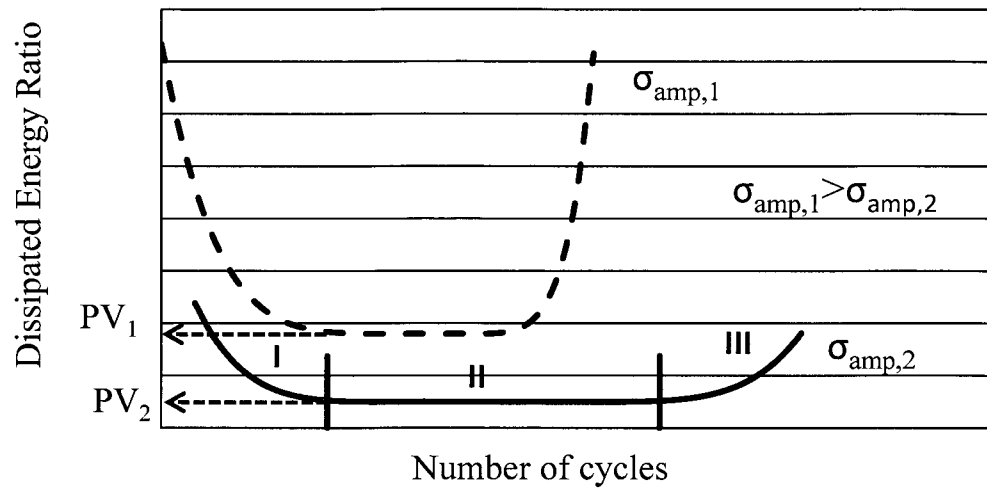
Figure 2-6: Variation of dissipated energy ratio and plateau value in fatigue test

Three distinct regions can be identified in a plot of the DER vs. number of loading cycles (Figure 2-6). Region-I represents the initial 'settling' of the sample where the rate of change of dissipated energy decreases. In this region, reorientation of material takes place due to application of load. In the next region, the rate of change of dissipated energy reaches a plateau, representing a period where the amount of damage occurring in the sample is constant. Physically, this plateau region indicates that the steady state of fatigue crack growth. The average value of DER in Region-II is identified as Plateau Value (PV). Finally, in Region-III, sample instability begins as the rate of change of dissipated energy increases rapidly, indicating failure of the specimen. A lower PV implies that less damage is occurring in the sample per cycle. This concept was used by Shen and Carpenter (2005) for finding the fatigue endurance limit of asphalt concrete. Their research indicated a linear relationship between the plateau value and number of cycles to 50 percent initial stiffness (both on log scale) for both

normal and low strain levels. A tentative plateau value of 8.57e-9 was identified as an indicator of the fatigue endurance limit.

The area enclosed by the stress vs. strain plot for a viscoelastic material is due to viscoelasticity and damage effects. Above a certain temperature, time and rate dependent effects predominantly govern response to the applied load and, in turn, affect the damage growth. As mentioned previously, by replacing physical strain by pseudostrain, viscoelastic effects can be separated from damage effects (Schapery 1990). Therefore, the area enclosed by the stress-pseudostrain plot corresponds to damage only. This concept has been researchers to model fatigue, healing behavior and moisture susceptibility (Si et al. 2002, Arambula et al. 2007, Little and Bhasin 2008, Masad et al. 2008).

CHAPTER 3

MATERIALS, MIX DESIGN AND SPECIMEN PREPARATION

In this research, eight asphalt concrete mixtures containing a variety of aggregates and binders were evaluated. The binders ranged from straight run asphalt to polymer modified asphalt binders. All binders were Performance Graded (PG) according to Superpave specifications. Also Reclaimed Asphalt Pavement (RAP) was used in some of the mixtures. Some of the mixtures were designed and mixed in the lab (here after referred to as Lab Mix, Lab Compacted (LMLC) mixtures), while others were bulk produced mixtures obtained from a plant (here after referred to as Plant Mix, Lab Compacted (PMLC) mixtures). 12.5 mm and 19.0 mm Nominal Maximum Aggregate Size (NMAS) gradations were used. The details about materials and mix designs used in this research are presented in the following sections. A summary of mixtures is given in Table 3-1.

Table 3-1: Summary of mixtures used in present research

General Designation	Binder	Contains RAP?	NMAS (mm)	Fabrication Method	Mixture ID
Mix 0	PG 64-28, Straight run	Yes		LMLC	M0
Mix 1	PG 70-28, PPA modified	No	12.5	LMLC	M1
Elvaloy Mix	PG 76-22, Elvaloy modified	Yes		PMLC	E1
SBS Mix	PG 76-22, SBS modified	Yes		PMLC	S1
CalTrans Mixtures	PG 64-28, Straight run	No	19.0	LMLC	6428
	PG 64-10, Straight run				6410
	PG 64-16, Straight run				6416
	PG 70-16, Straight run				7016

Mix 0 and Mix 1 were designed in the asphalt lab at the University of New Hampshire (UNH) whereas the Elvaloy and SBS mixtures were obtained from Trap Rock Industries through Rutgers, The State University of New Jersey, NJ. Uniaxial and biaxial test specimens from M0, M1, E1 and S1 mixtures were fabricated and tested at UNH while flexural test specimens from M0, M1, E1 and S1 mixtures were fabricated and tested at Rutgers. All test specimens from CalTrans mixtures were fabricated and tested at the Pavement Research Center, University of California, Davis, CA and data were analyzed at the University of New Hampshire.

3.1 Asphalt binder

In this research, eight different Performance Graded (PG) asphalt binders were used. The binders included straight run asphalt (PG 64-28, PG 64-10, PG 64-16, PG 70-16), Polyphosphoric Acid (PPA) modified asphalt (PG 70-28), Elvaloy modified asphalt (PG 76-22) and SBS modified asphalt (PG 76-22). Table 3-1 presents the details about binders in specific mixtures.

The straight run asphalt and PPA modified asphalt were donated by Pike Industries, Inc. Portsmouth, NH. Initially, the binders were brought to the asphalt lab at UNH in 5 gallon buckets and heated to 120 ^{0}C and then transferred to one gallon cans. The binders in these 1 gallon cans were heated to a temperature of 165 ^{0}C and then mixed with the aggregates before compaction. Elvaloy modified asphalt and SBS modified asphalt were directly used in production of asphalt concrete at the Trap Rock Industries batch mixing plant in Kingston, NJ. The binders for CalTrans mixtures were obtained from Valero and Paramount, asphalt producers located in the state of California.

Since the contractors (Pike Industries, Trap Rock Industries) and asphalt producers (Paramount and Valero) have had extensive experience with these liquid binders, these asphalt binders were considered to satisfy the Superpave criterion.   .

3.2 <u>Aggregates</u>

The coarse aggregates (12.5 mm and 9.5 mm) for M0 and M1 mixtures came from two stockpiles at the Tilcon plant, in Newington, Connecticut. The fine aggregates used in this project were also from two different stockpiles, a crushed stone sand from the Tilcon quarry in Wallingford, Connecticut and natural sand from Tilcon in Manchester, Connecticut. All aggregates were transported and stored in sealable plastic 55-gallon barrels at UNH. These aggregates were oven dried, cooled, sieved and stored in separate 5 gallon buckets according to particle size in the lab.

The aggregates used for the Elvaloy mix and SBS mix came from Trap Rock Industries plant in Kingston, NJ. These aggregates were stored in stockpiles and heated to remove moisture before mixing in the plant.

The aggregates used for the CalTrans mixtures were obtained from Syar Industries, Inc and the origin of aggregates was Syar's Lake Herman quarry near Vallejo, CA. The aggregate were stored in stockpiles and blend was obtained from four bins with size ranges namely 19 mm-12.5 mm, 12.5 mm-9.5 mm, 9.5 mm-dust, and 4.75 mm-dust.

3.3 Mix design and specimen preparation

The Mix 0 and Mix 1 were designed in the asphalt lab at UNH according to Superpave criterion. More details about the mixture M0 can be found elsewhere (Daniel and Mogawer 2010). The mixture M1 was same as mixture M0 except for the change in asphalt binder grade. The summary of these mix designs are presented in Table 3-2. The aggregate gradations for these two mixtures are presented in Table 3-3 and Figure 3-1. The aggregates stored in 5 gallon buckets were batched and heated to mixing temperature of 165 ^{0}C for at least 8 hours. The binder was kept in a preheated oven approximately two hours before mixing and was regularly stirred at 30 minute intervals. Two hours of binder heating was adopted so that mixing temperature is reached without aging the binder. Two hours of heating time was adopted for loose RAP (if used). The hot mixing bucket was placed on the scale and the dry aggregate (and RAP, if any) was added. Then the predetermined amount of asphalt was added to the dry mix. The hot mixing bucket was placed on the mixing machine and the aggregate and asphalt was mixed together. The loose mix was transferred to an aluminum pan and left to cool to room temperature. Once room temperature was reached, the loose mix was transferred to plastic bags. The sealed plastic bags were stored in air tight enclosures to avoid any further aging.

Table 3-2: Mix design summary

Parameter	Superpave Requirement		Mixture		
	19.0 NMAS	12.5 NMAS	Mix 0, Mix 1	Elvaloy Mix, SBS Mix	CalTrans Mixtures
Asphalt Content (%)	--	--	4	4.4	5
VMA	13.0	14.0	17.4	13.4	NA
VFA	65-75	65-75	77	72.9	NA
Air Voids (%)	4.0	4.0	4	3.6	6
Dust Proportion	0.6-1.2	0.6-1.2	0.55	1	NA

Table 3-3: Summary of mixture gradations

Sieve Size (mm)	Percent Passing		
	Mix 0, Mix 1	Elvaloy Mix, SBS mix	CalTrans Mixtures
25	100	100	100
19	100	100	95
12.5	94.1	94.0	80.0
9.5	73.2	82.9	--
4.75	49.4	48.8	50.0
2.36	37.0	35.9	36.0
1.18	24.6	29.4	--
0.6	16.3	23.4	15.5
0.3	10.3	12.5	--
0.15	6.7	7.1	--
0.075	3.0	5.1	4.5
Pan	0	0	0
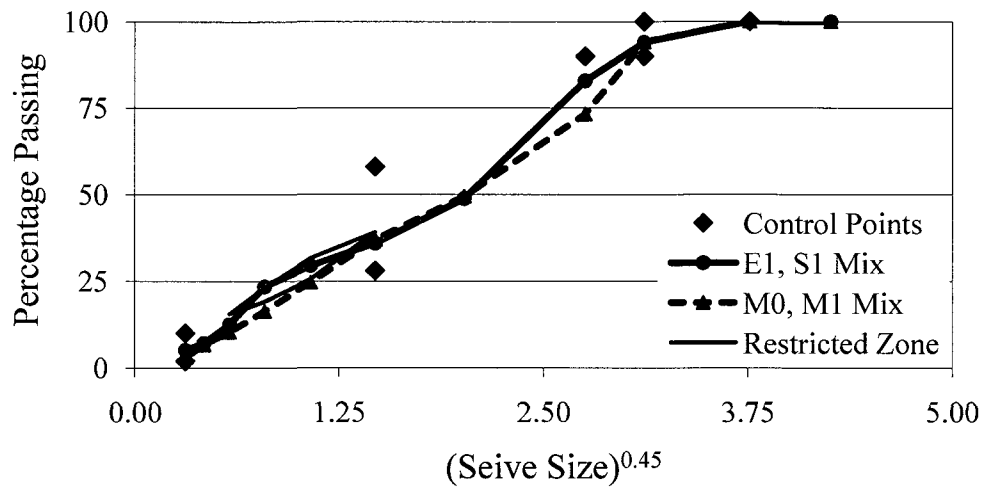
Figure 3-1: Gradation curves of 12.5 mm NMAS mixtures

The Elvaloy and SBS mixtures were designed by Trap Rock Industries. Details about these mixtures can be found elsewhere (Bennert 2010). A summary of these mix designs and gradations are presented in Tables 3-2 and 3-3, respectively. The aggregate gradations for these two mixtures are presented in Figure 3-1. These mixtures were collected from batch mix plant in 5 gallon metal buckets, sealed and stored in lab until they were ready to be compacted. To obtain the exact amount of loose mix for compaction, the entire stock was separated evenly. The material in 5 gallon buckets were heated to 120 ^{0}C for about 45 minutes and systematically quartered down to required amount using a hot aggregate splitter. After splitting the material, the loose mix was left to cool in separate aluminum pans. The air cooled loose mix was transferred to air tight bags and stored until further compaction.

The CalTrans mixtures were designed by Syar Industries, Inc the contractor for constructing the HVS Test Track. A summary of these mix designs and gradations are

presented in Tables 3-2 and 3-3, respectively. The aggregate gradations for these two

mixtures are presented in Figure 3-2. In the batching and mixing processes, 7000 grams

of aggregates was batched and heated to the mixing temperature (163^0C) for at least two

hours before mixing. The asphalt binder was heated to the same temperature for

approximately one hour, and then mixed with the aggregate until the aggregates were

fully coated (approximately about five minutes). Then the loose mix was short term

aged at 145^0C for about 4 hours with occasional mixing. The loose mix was compacted

immediately after short term aging.
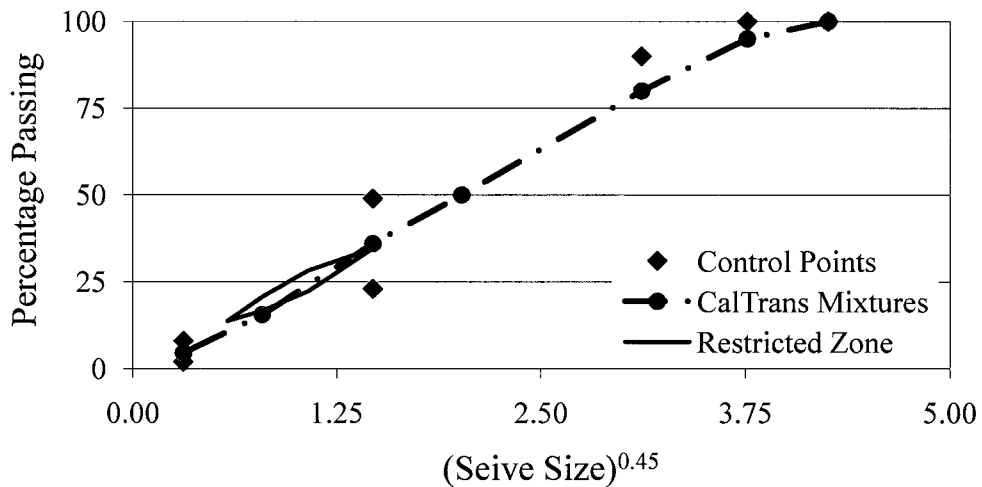
Figure 3-2: Gradation curves of 19.0 mm NMAS mixtures

The loose mix from plastic bags was transferred to aluminum pans. These pans were

then heated in a preheated oven at 160 ^{0}C for at least two hours. The loose mix was

turned and mixed at 30 minute intervals so that the mixture was uniformly heated. The

loose mix was then put into Superpave Gyratory Compactor (SGC) molds that had been

preheated to 170 ^{0}C and compacted using the SGC. The uniaxial and biaxial test

samples were compacted using the SGC to a set height. Similarly, flexure beams were compacted using beam compactors to a preset height. The height of the sample was adjusted so that specimens have the target air voids. The compacted specimens were extracted from mold and allowed to cool overnight. The pictures of the SGC and beam compactors used in this study are shown in Figures 3-3 and 3-4, respectively.

Figure 3-3: Superpave gyratory compactor at asphalt lab, UNH
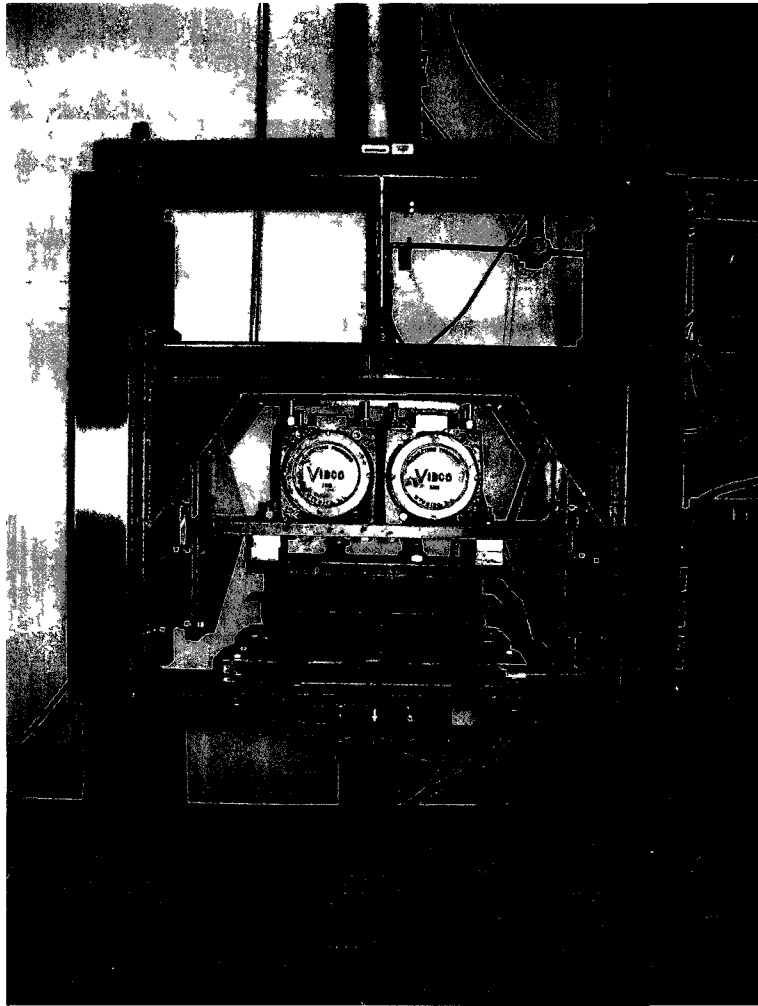
Figure 3-4: Beam compactor at Rutgers university

During the compaction process, a region of higher air void content occurs near the surface of the specimen (at top and bottom, and near mold walls) (Chehab et al. 2000). Thus compacted specimens were trimmed using a coring device and wet saw. The coring device used in this research was assembled at UNH. The wet saw was manufactured by MK Diamond Products, Inc. (MK-5005T BLK SAW) and was fitted with a 20" asphalt specific cutting blade. Pictures of coring machine and wet saw are shown in Figures 3-5 and 3-6, respectively.

Figure 3-5: Coring machine at asphalt lab, UNH

Figure 3-6: Wet saw at asphalt lab, UNH

The trimmed samples were left to air dry overnight in front of a fan. This ensured that water filled in pores (if any) is removed completely. Air voids of these trimmed samples were measured using a Corelok vacuum system is shown in Figure 3-7. The air voids were measured in accordance to AASHTO TP 69-04 specifications.
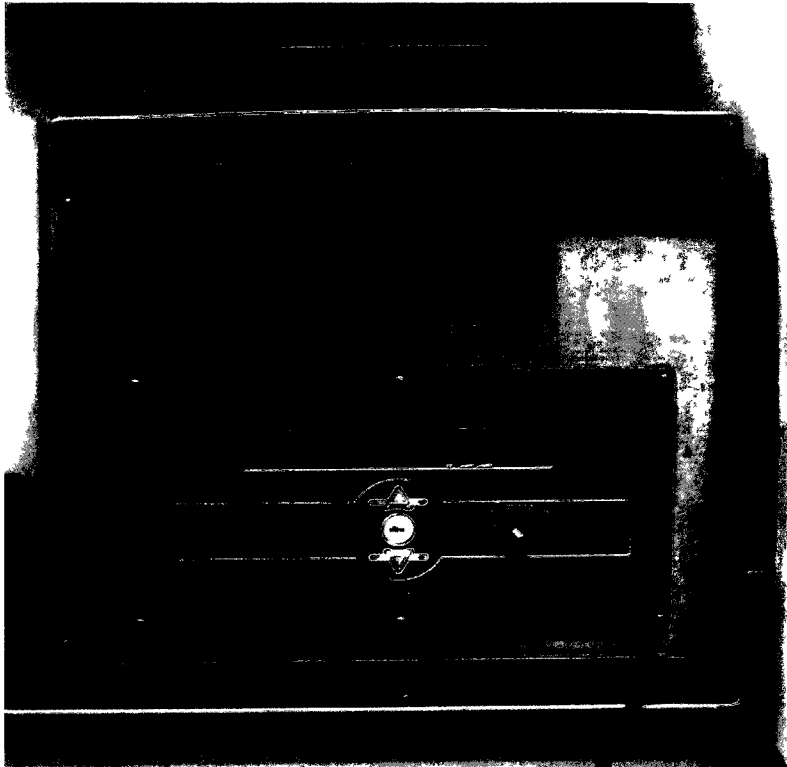
Figure 3-7: Corelok vacuum system at asphalt lab, UNH

Steel end plates were glued to uniaxial specimens using plastic epoxy glue in a gluing jig. Use of the gluing jig ensured that the axis of the end plates coincided with that of the trimmed specimen. A specimen during the process of gluing is shown in Figure 3-8.
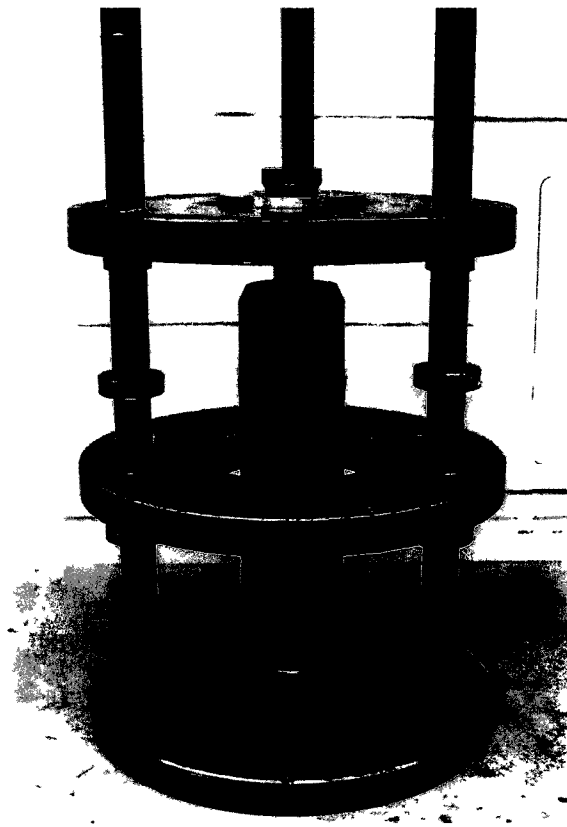
Figure 3-8: Gluing jig at asphalt lab, UNH

The determination of dynamic modulus and subsequent fatigue testing requires measurement of loads acting on the specimen and deformation in the specimen. During uniaxial and biaxial mode testing, the loads applied on the specimen were measured using the load cell attached to a closed-loop servo-hydraulic system, manufactured by Instron®. A picture of the closed-loop servo-hydraulic system is shown in Figure 3-9.

Figure 3-9: Closed-loop servo-hydraulic system at asphalt lab, UNH

The deformations in the test specimen were measured using Linearly Variable Differential Transducers (LVDT) mounted on the specimen. For uniaxial test specimens, LVDTs were spaced 90^0 apart around the circumference of the specimen using a 100 mm gage length. For biaxial test specimens, LVDTs were mounted on the horizontal and vertical axes on both faces of the specimen with a gage length of 50 mm. Flexure mode of loading did not require any special instrumentation as the load applied and central deflection were measured using a load cell and transducer that were a part of the beam fatigue testing apparatus. The flexure mode testing was performed using a beam fatigue apparatus manufactured by Industrial Process Controls (IPC) in Melbourne, Australia. Figures 3-10, 3-11 and 3-12 show an instrumented specimen ready for testing in the environmental chamber under uniaxial, biaxial and flexure mode of loading, respectively.
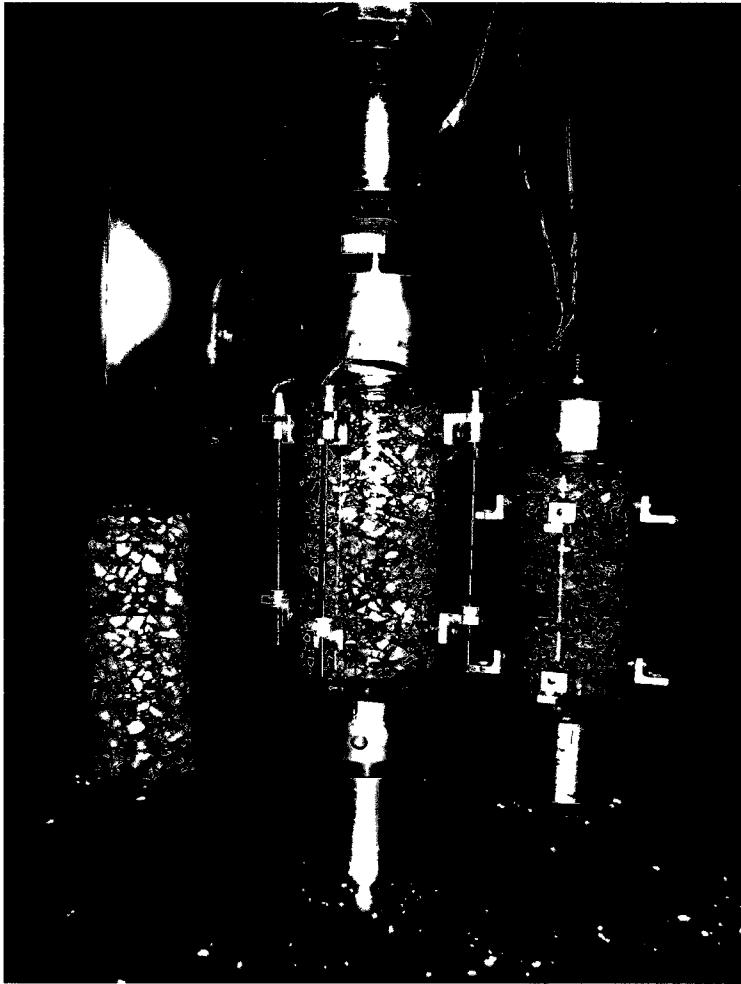
Figure 3-10: Uniaxial test specimen ready for testing in environmental chamber
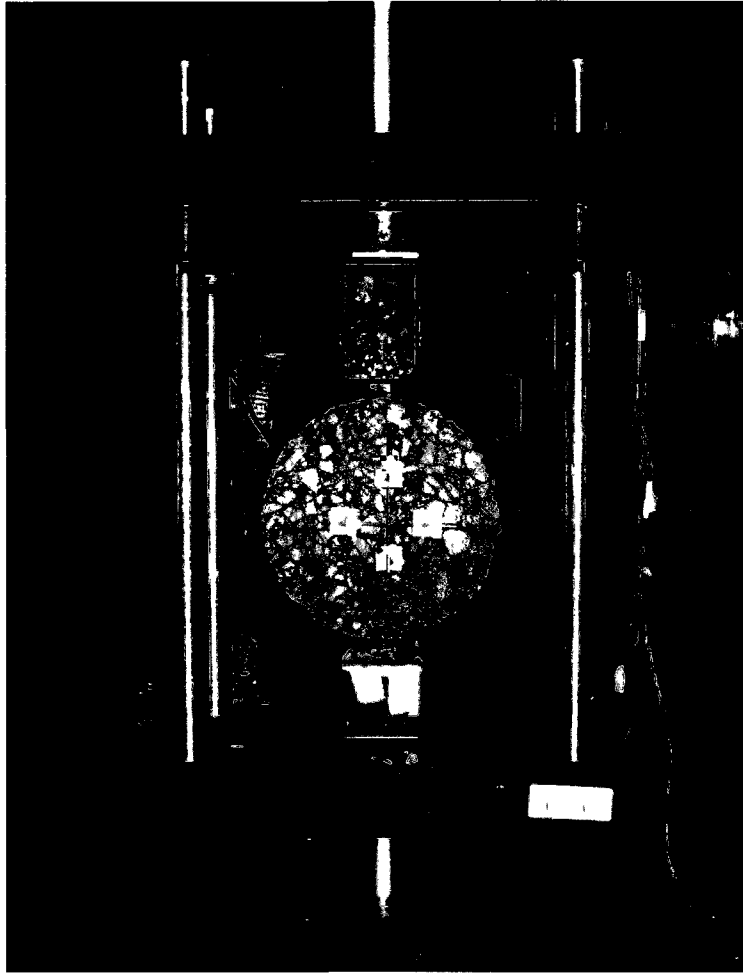
Figure 3-11: Biaxial test specimen ready for testing in environmental chamber
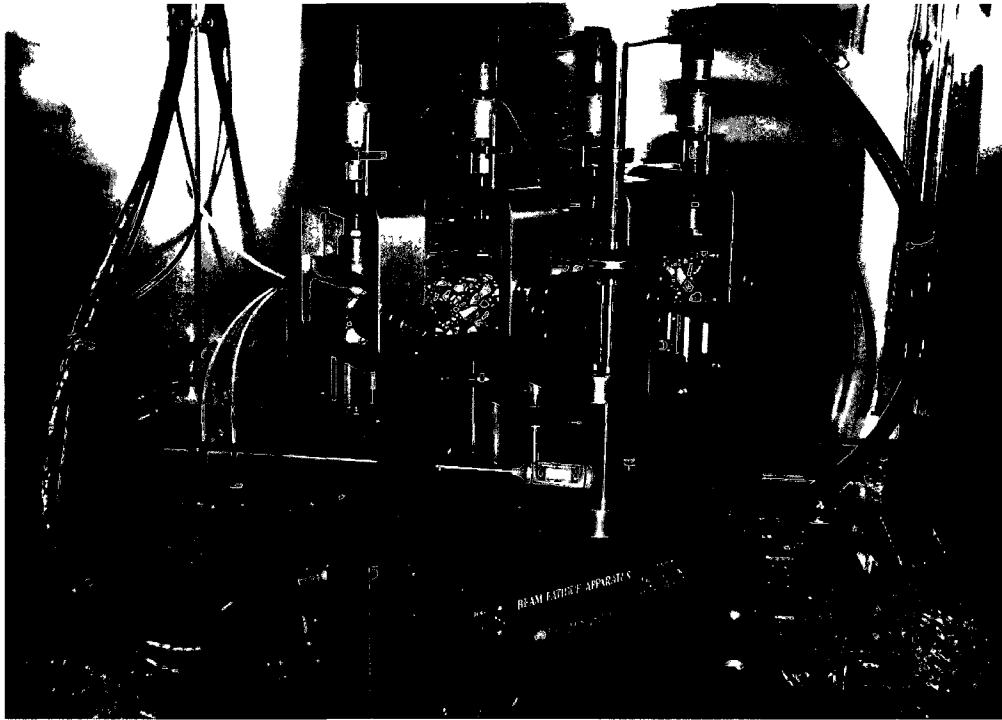
Figure 3-12: Flexural beam test specimen ready for testing in environmental chamber

3.4 Experimental plan and specimen identification

Each specimen prepared in this study at UNH and Rutgers carried an identification tag that was a combination of characters and numbers. The first two characters identify the asphalt concrete mixtures which was a combination of two characters. The third character indicates the mode of loading. The letters U, B and F are used for uniaxial, biaxial and flexure mode of loading, respectively. The fourth and fifth characters are numbers identifying the specimen number within a particular mix and loading mode. A summary of the specimen identification protocol used in this research is given in Table 3-4.

Specimen identification protocol for the CalTrans mixtures has two parts. The first part identifies asphalt binder grade used in mix while the second part corresponds to replicate number.

Table 3-4: Specimen identification guidelines

Mixture ID	Loading Mode		
	Uniaxial	Biaxial	Flexure
M0	M0U##	M0B##	--
M1	M1U##	--	M1F##
E1	E1U##	--	E1F##
S1	S1U##	--	S1F##
PG6428	--	--	6428$##
PG6410	--	--	6410$##
PG6416	--	--	6416$##
PG7016	--	--	7016$##

- indicates no specimens were tested

46

CHAPTER 4

TEST METHODS

The tests conducted in this research involved non-damage inducing tests to determine linear viscoelastic parameters and damage inducing tests to determine fatigue properties of the asphalt concrete. While conducting non-damage inducing tests, on-specimen strain was limited to 70 microstrain to limit damage to the specimen. The details about tests conducted, test mode and its purpose is summarized in Table 4-1.

Table 4-1: Summary of tests conducted

Test Type	Test Mode	Purpose
Cyclic test	Constant stress amplitude	LVE properties characterization
Monotonic test	Constant strain rate	Damage evolution characterization
Cyclic test	Constant stress amplitude	
	Constant strain amplitude	
	Increasing stress amplitude	Damage evolution characterization, Endurance limit determination.
	Increasing strain amplitude	

4.1 Complex modulus tests

The frequency sweep test was performed in this research to obtain the dynamic modulus and phase angle measurements at different temperatures and frequency. The frequency sweep test is a stress controlled test where the applied cyclic stress (input) is adjusted such that strain (response) in the sample is within the linear viscoelastic limit. The cyclic loading is continued until a steady state response is obtained. The data from the steady state response region is used to calculate dynamic modulus and phase angle.

The stress and strain data are fit with a generalized sinusoidal curve given in Equation 4-1 and 4-2, respectively. The value of dynamic modulus is obtained by dividing stress amplitude $(a_{3,\sigma})$ by strain amplitude $(a_{3,\varepsilon})$, as given in Equation 4-3. The phase angle (φ) is obtained using testing frequency (f) and time lag between stress and strain function ($\Delta t = a_{5,\sigma} - a_{5,\varepsilon}$), as presented in Equation 4-4. A typical stress and strain history and fitted curves in a stress controlled test are presented in Figure 4-1.

$$\sigma_{pre} = a_{1,\sigma} + \left(a_{2,\sigma} \times t\right) + a_{3,\sigma}\, sin\left(a_{4,\sigma} \times t + a_{5,\sigma}\right) \qquad \text{4-1}$$

$$\varepsilon_{pre} = a_{1,\varepsilon} + \left(a_{2,\varepsilon} \times t\right) + a_{3,\varepsilon}\, sin\left(a_{4,\varepsilon\times}t + a_{5,\varepsilon}\right) \qquad \text{4-2}$$

$$|E^*| = \frac{a_{3,\sigma}}{a_{3,\varepsilon}} \qquad \text{4-3}$$

$$\Phi = 2\,\pi\,f\,\Delta t \qquad \text{4-4}$$

where σ_{pre} = predicted stress;

ε_{pre} = predicted strain;

f = testing frequency;

Φ = phase angle;

$|E^*|$ = dynamic modulus; and

$a_{i,\sigma}, a_{i,\varepsilon}$ = regression coefficients.
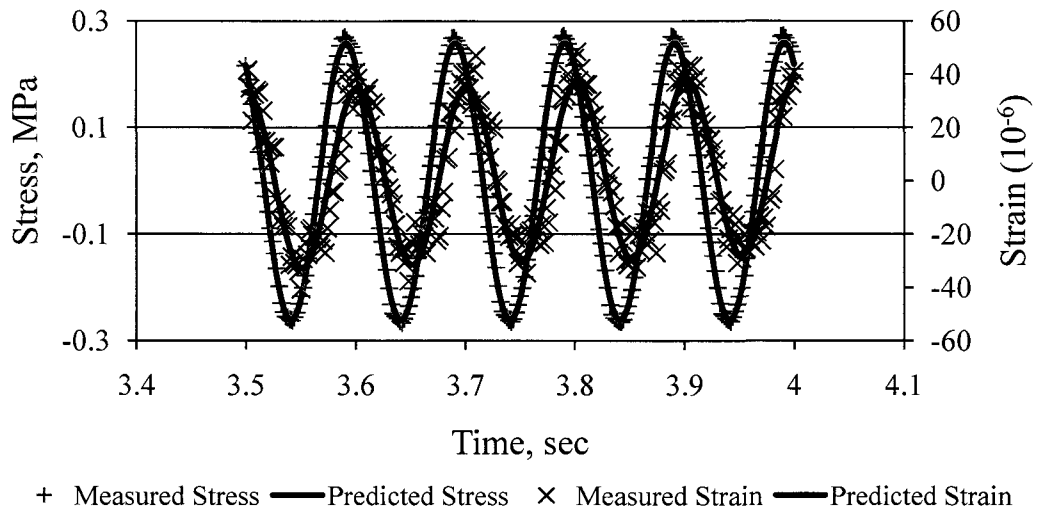
Figure 4-1: Typical stress and strain history in a temperature-frequency sweep test

The above mentioned procedure is repeated at several frequencies and temperatures. Under uniaxial and biaxial mode of loading, frequencies of 0.1 Hz, 0.2 Hz, 0.5 Hz, 1.0 Hz, 2.0 Hz, 5.0 Hz, 10.0 Hz, and 20.0 Hz and temperatures of -10^0C, 0^0C, 10^0C, 20^0C, and 30^0C, were used in this study. Due to limitations in the fatigue testing equipment, frequencies of 0.1 Hz, 0.5 Hz, 1.0 Hz, 5.0 Hz, 10.0 Hz, and 15.0 Hz and temperatures of 10^0C, 20^0C, 30^0C, and 40^0C, were used under flexural mode of loading. The testing was started at the lowest temperature and terminated at the highest temperature. Within each testing temperature, the testing was started at the fastest frequency and terminated at the slowest frequency. This procedure was adopted to minimize damage to the specimen.

Using the time-temperature superposition principle, the dynamic modulus mastercurve was constructed. The isotherm curves obtained using computed dynamic moduli at specific temperatures were shifted horizontally along the frequency axis to form a smooth curve at a reference temperature of 20^oC. Horizontal shift of individual

49

isotherm curves is quantified by temperature shift factors. The variation of temperature shift factors with temperature in specimen M1U22 is shown in Figure 4-2. The smooth curve was fit with a symmetrical sigmoid function given in Equation 4-5. The temperature shift factors determined during construction of dynamic modulus mastercurve were then used to construct the phase angle mastercurve for each specimen at the same reference temperature. The dynamic modulus values at different temperature and frequencies (before and after applying temperature shift factors) and the mastercurve obtained for a specific specimen (M1U22) are shown in Figure 4-3.

$$log(|E^*|) = c_1 + \frac{c_2}{1 + \frac{1}{e^{(c_3 + c_4 log(\gamma))}}}$$ 4-5

$$\gamma = f\, a_t$$ 4-6

where $|E^*|$ = dynamic modulus;

γ = reduced frequency;

f = testing frequency;

a_t = time-temperature shift factor; and

c_i = regression coefficients.
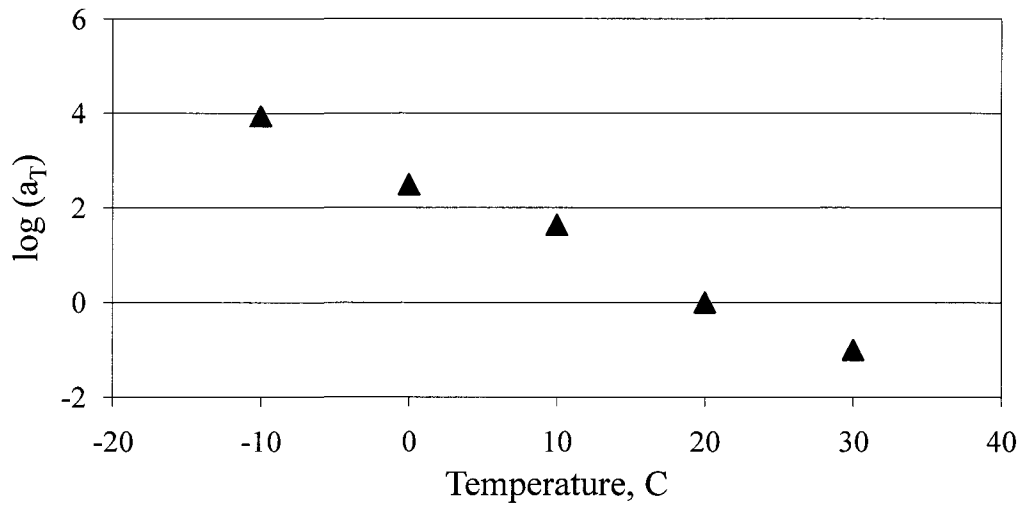
Figure 4-2: Variation of shift factors with temperature
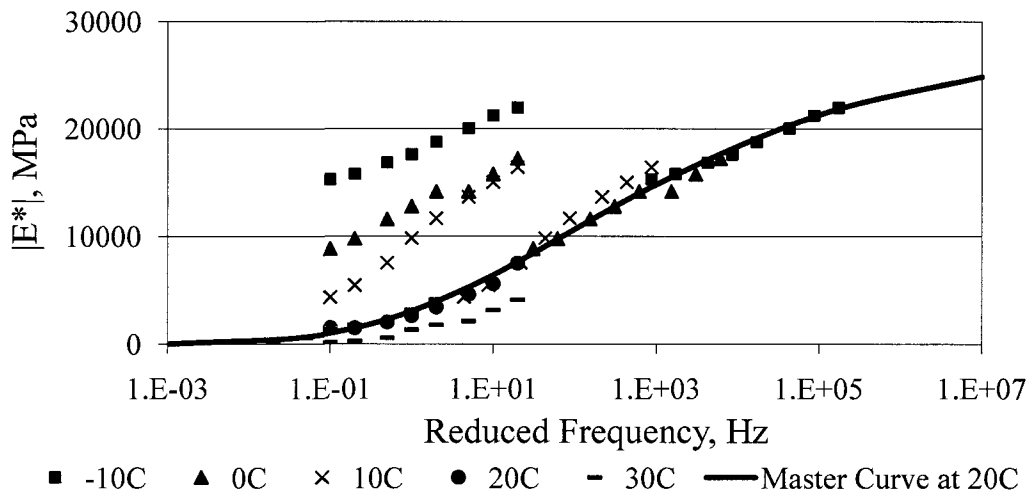
Figure 4-3: Illustration for construction of dynamic modulus mastercurve from temperature-frequency sweep test results

The stress input and strain response in uniaxial specimens were calculated from load and deformation measurements using Equations 4-7 and 4-8, respectively. Once the stress and strain histories were computed and fitted with the generalized sinusoidal curve, the dynamic modulus was calculated using Equation 4-3.

51

$$\sigma = \frac{load}{area} = \frac{4P}{\pi D^2} \qquad\qquad 4\text{-}7$$

$$\varepsilon = \frac{\Delta d}{GL} \qquad\qquad 4\text{-}8$$

where P = load;

D = diameter of specimen;

Δd = change in length; and

GL = gage length.

The maximum stress and maximum strain in the beam specimen was calculated using Equations 4-9 and 4-10, respectively (AASHTO 2003). Once the stress and strain histories were computed and fitted with the generalized sinusoidal curve, the dynamic modulus was calculated using Equation 4-3.

$$\sigma = \frac{P\,L}{b\,h^2} \qquad\qquad 4\text{-}9$$

$$\varepsilon = \frac{12\,h\,\delta}{3L^2 - 4a^2} \qquad\qquad 4\text{-}10$$

where P = load applied by actuator;

b = average specimen width;

h = average specimen height;

δ = deflection at center of beam;

a = distance between inside clamps; and

L = distance between outside clamps.

Due to loading direction and orientation of the test specimen in biaxial mode, tensile stresses develop in the direction perpendicular to the loading axis while compressive stresses develop along the direction of loading. Since tensile stress is induced in the specimen indirectly, this test is known as Indirect Tension (IDT) test. The elastic solution for such a case can be found if the point load acting at ends, diameter and thickness of specimen are known (Hondros 1959). The expressions to calculate the compressive and tensile stresses at the center of disk (assuming the material to be elastic) are given in Equations 4-11 and 4-12, respectively. The compressive stress and tensile stress contours generated when subjected to point load are presented in Figures 4-4 and 4-5, respectively. These contours were generated using the finite element analysis software Marc Mentat using quadrilateral mesh elements under the assumption of a plane stress condition.

$$\sigma_C = \frac{2\,P}{\pi\,D\,t} \qquad\qquad\text{4-11}$$

$$\sigma_T = \frac{6\,P}{\pi\,D\,t} \qquad\qquad\text{4-12}$$

where σ_C = compressive stress at center of disk;

        σ_T = tensile stress at center of disk;

        P = point load;

        D = diameter of test specimen; and

        t = thickness of test specimen.
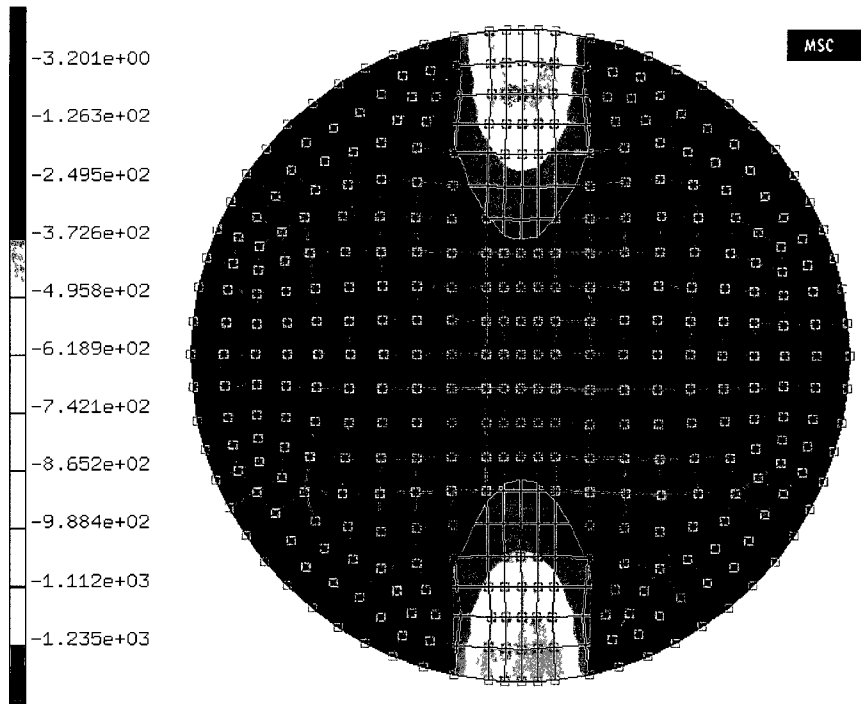
Figure 4-4: Compressive stress contours in an biaxial test specimen
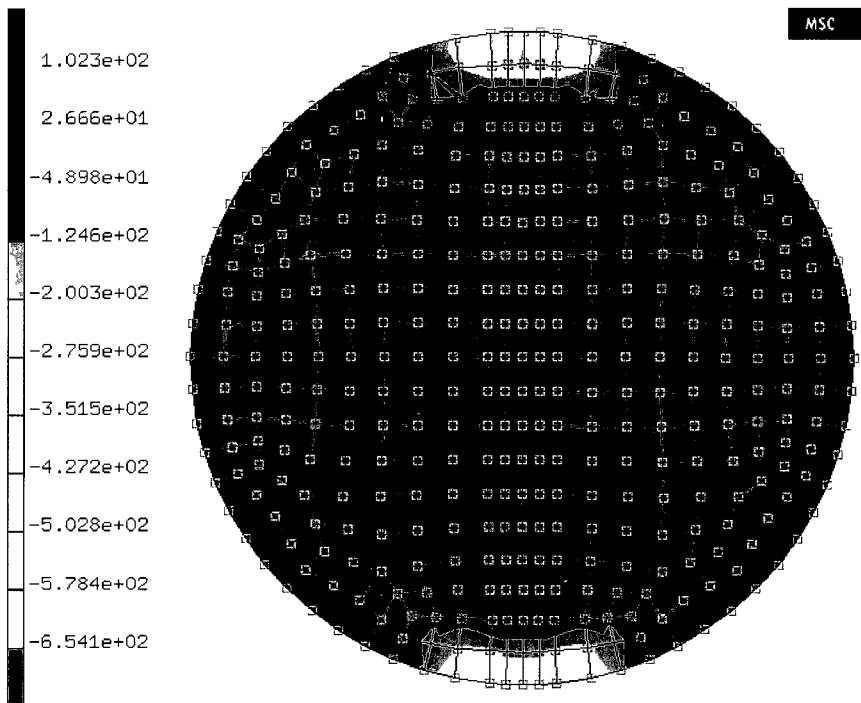
Figure 4-5: Tensile stress contours in an biaxial test specimen

For calculating dynamic modulus value under biaxial mode of loading, averaged horizontal displacement amplitude from both faces, averaged vertical displacement amplitude from both faces and applied load amplitude were used. The relationship developed by North Carolina State University (Kim et al. 2004, Kim et al. 2005) was used to calculate the dynamic modulus, as shown in Equation 4-13.

$$|E^*| = \left| \frac{2\,P}{\pi\,a\,t} \frac{-0.00014}{0.0116V_0 + 0.0042U_0} \right|$$ 4-13

where P = point load;

a = loading strip width;

t = thickness of specimen;

U_0 = horizontal displacement amplitude; and

V_0 = vertical displacement amplitude.

4.2 Interconversion of viscoelastic materials properties

For any viscoelastic material, complex modulus, creep compliance and relaxation modulus are fundamental properties. Due to equipment and time limitations, conducting the complex modulus test, creep tests and relaxation tests are difficult (in increasing order of difficulty). All of these material properties can be predicted from a measured property using the theory of linear viscoelasticity. In this research, creep compliance and relaxation modulus values are predicted from measured complex modulus data. The following paragraphs describe approach used in the prediction of relaxation modulus and creep compliance.

4.2.1 Relaxation modulus from complex modulus test data

Calculation of pseudostrain (Equation 2-10) requires relaxation modulus values over a range of time. In this research, an approximate analytical method proposed by Schapery and Park (1999) was adopted to obtain relaxation modulus from dynamic modulus and phase angle master curves.

In the first step, storage modulus (E') is calculated at regular intervals of frequency using dynamic modulus and phase angle mastercurve data as given in Equation 4-14. The relaxation modulus values are obtained from the storage modulus master curve by using Equation 4-15. A typical relaxation modulus mastercurve constructed through a storage modulus mastercurve is shown in Figure 4-6.

$$E'(\omega_r) = |E^*| \ cos\big(\Phi(\omega_r)\big) \qquad\qquad 4\text{-}14$$

$$E(t_r) = \frac{1}{\lambda'} E'(\omega_r)$$

$$\omega_r = \Gamma(1-n) \cos\left(\frac{n\pi}{2}\right) \qquad\qquad 4\text{-}15$$

$$n = \frac{d \ log \ E'(\omega_r)}{d \ log \ \omega_r}$$

where $E(t)$ = relaxation modulus as a function of time;

$E'(\omega_r)$ = storage modulus as a function of angular frequency;

Φ = phase angle;

$|E^*|$ = dynamic modulus;

ω_r = angular frequency;

t_r = reduced time;

Γ = gamma function; and

n = local slope of storage modulus mastercurve.

Using the predicted relaxation modulus values, the Prony series is fit over a range of time. The Prony series for relaxation modulus is given in Equation 4-16.

$$E(t) = E_\infty + \sum_{i=1}^{N} E_i\, e^{-\frac{1}{\rho_i}} \qquad \text{4-16}$$

where $E(t)$ = relaxation modulus as a function of time;

E_∞, E_i = material constants;

t = time variable; and

ρ_i = relaxation times.

.
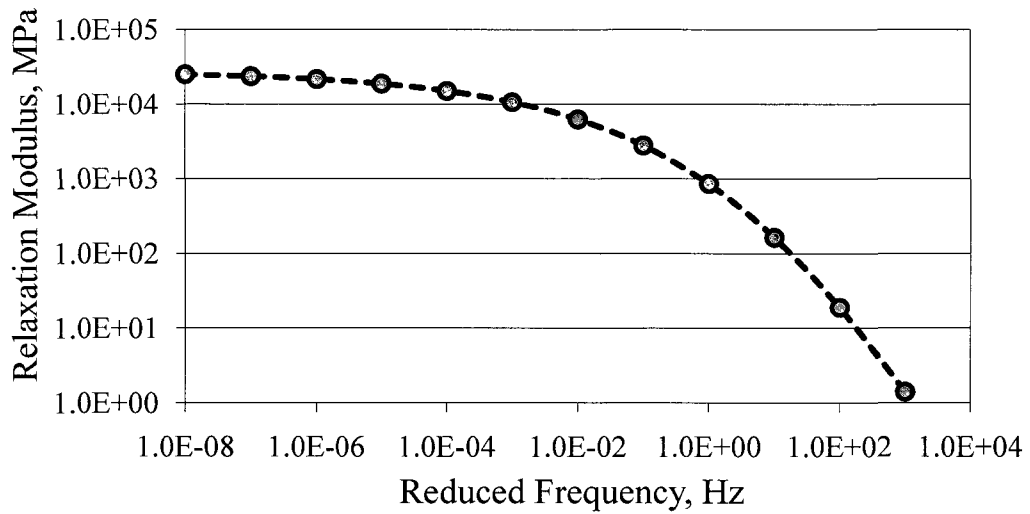
Figure 4-6: Typical relaxation modulus mastercurve

4.2.2 Relaxation modulus to creep compliance

Once the relaxation modulus mastercurve was obtained from dynamic modulus and phase angle data, the creep compliance master curve was obtained through an approximate relation given in Equation 4-17 (Daniel 2001).

$$D(t) = \frac{1}{E(t)} \frac{sin\, n\pi}{n\pi} \qquad\qquad 4\text{-}17$$

where $D(t)$ = creep compliance as a function of time;

$E(t)$ = relaxation modulus as a function of time;

t = time variable; and

n = local slope of relaxation modulus mastercurve.

Using the predicted creep compliance values, the Prony series is fit over a range of time. The Prony series for creep compliance is given in Equation 4-18. Figure 4-7 shows a typical creep compliance curve.

$$D(t) = D_0 + \sum_{i=1}^{N} D_i \left(1 - e^{-\frac{t}{\tau_i}}\right) \qquad \text{4-18}$$

where D_0, D_i = material constants;

  t = time variable; and

  τ_i = retardation time of ith Voigt element.
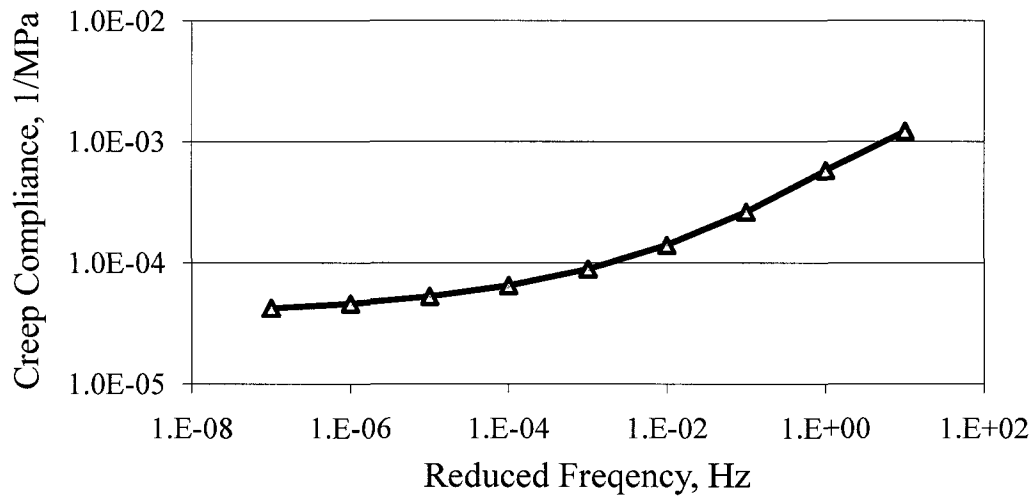
Figure 4-7: Typical creep compliance mastercurve

4.3 Damage inducing tests

The cyclic test and constant crosshead rate test were conducted to capture material behavior under damage inducing loads or strains. These tests aid in characterizing the continuum damage parameters. The following sections describe these tests in detail.

4.3.1 Cyclic loading tests

This test consists of subjecting the specimen to haversine cyclic loading without any rest period between cycles. In this research, cyclic tests were conducted by controlling the crosshead strain amplitude or stress amplitude on the specimen. Hereafter these tests will be referred to as controlled strain amplitude test and controlled stress amplitude test, respectively. The testing frequency of 10 Hz was used for all cyclic tests used to characterize fatigue damage.

In the controlled strain test, the crosshead strain amplitude was held constant. However, due to compliance of the machine and the attached parts, the strain experienced by the specimen will not be the same as crosshead strain (Daniel et al. 2004). To measure the actual strain experienced by the specimen, LVDT's were mounted on the specimen. The variation of axial strain computed using crosshead displacement and LVDT (mounted on specimen) measurements are shown in Figures 4-8 and 4-9, respectively. The strain amplitude computed using the crosshead displacement remained constant throughout the test; whereas the strain values computed using LVDT measurements indicates that the mean strain and the strain amplitude values are increasing as the test progresses. The strain values computed using the LVDT measurements were used in computing pseudostrain values. The variation of stress

response during a controlled strain amplitude test is shown in Figure 4-10. As the damage in specimen increases, the stress amplitude needs to be reduced to keep the strain amplitude the same.
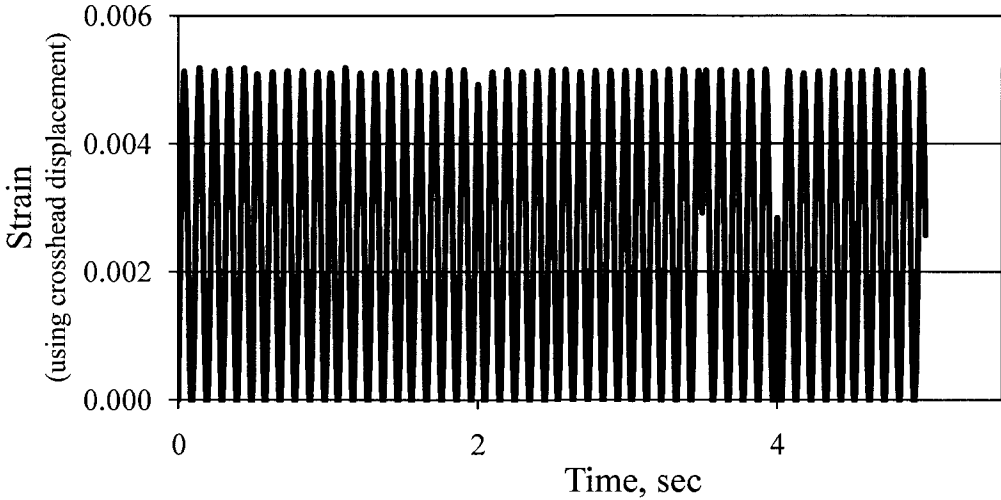
Figure 4-8: Variation of crosshead strain in uniaxial controlled strain amplitude test
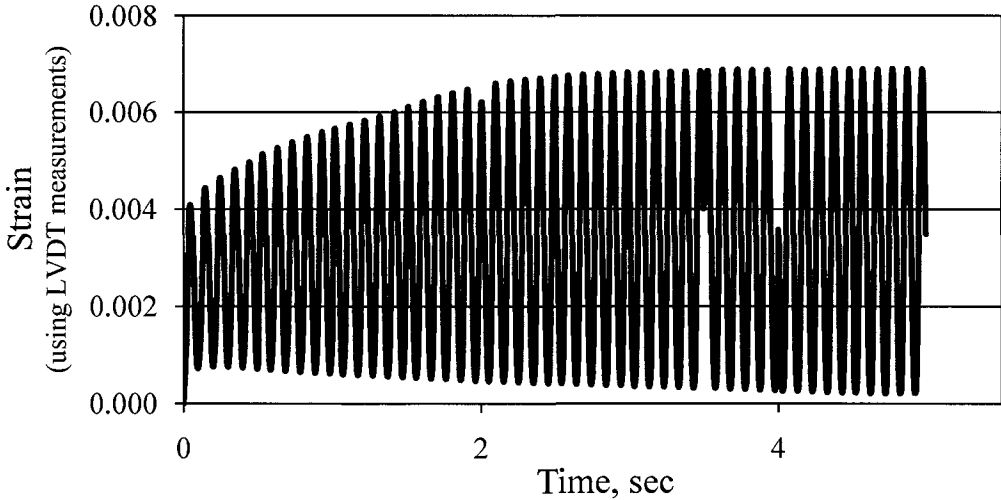
Figure 4-9: Variation of on-specimen strain in uniaxial controlled strain amplitude test
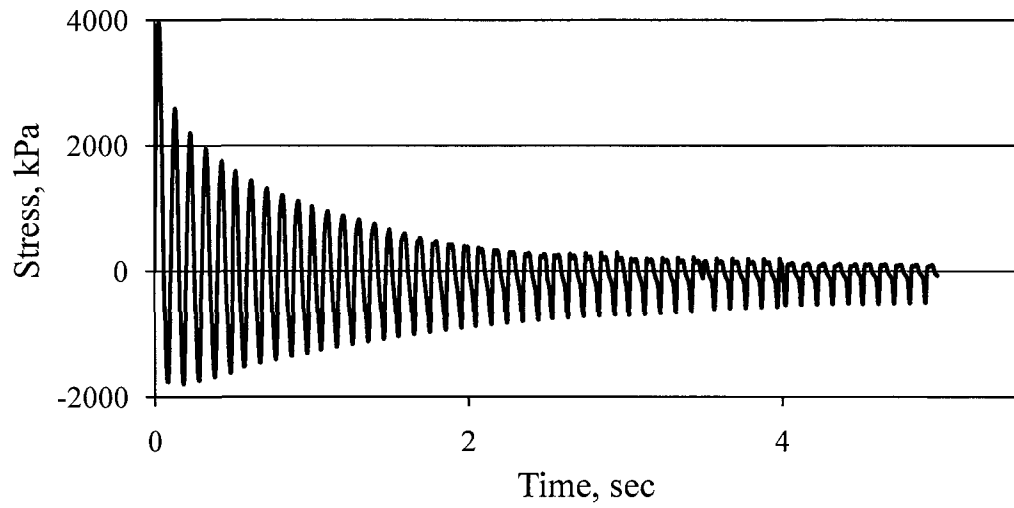
Figure 4-10: Stress response in a uniaxial controlled strain amplitude test

The stress history during a constant stress amplitude test is shown in Figure 4-11. The variation of strain values computed using crosshead displacement and LVDT measurements are shown in Figure 4-12. The strain values calculated using the LVDT measurements were used while computing pseudostrain values.
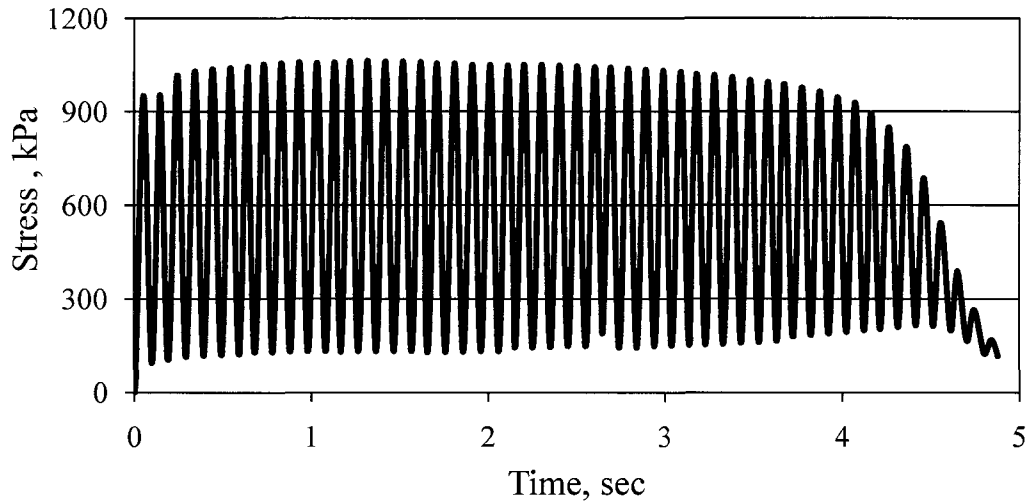
Figure 4-11: Variation of stress in uniaxial controlled stress amplitude test
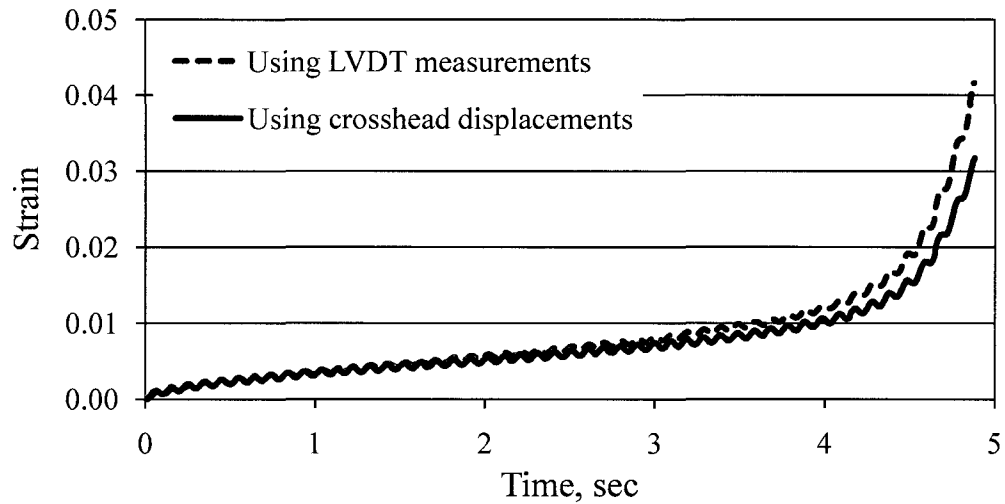
Figure 4-12: Variation of strain response in uniaxial controlled stress amplitude test

4.3.2 Constant crosshead rate test

In this test, a constant rate of loading to failure is used. As mentioned previously, the strain rate experienced by the specimen was not the same as crosshead strain. The strain values computed using LVDT measurements were used in the analysis. In this research, load and displacement values are recorded until the specimen undergoes

complete fracture. Typical variation of strain and stress during a constant crosshead rate test is shown in Figure 4-13. Using the collected strain history, pseudostrain is calculated using Equation 2-10.

Due to inherent spatial variations (imperfections) in the test specimens, a few test specimens failed beyond the measurement zone (i.e. between endplate and LVDT bracket) where as others failed between LVDT brackets. For convenience, these types of failures are referred to as near end failure and mid failure, and examples for both are shown in Figure 4-14 a and b, respectively. Data acquired from mid failure specimens captured damage evolution in specimen during the test. Hence stress, strain data from those specimens were used in further analysis.
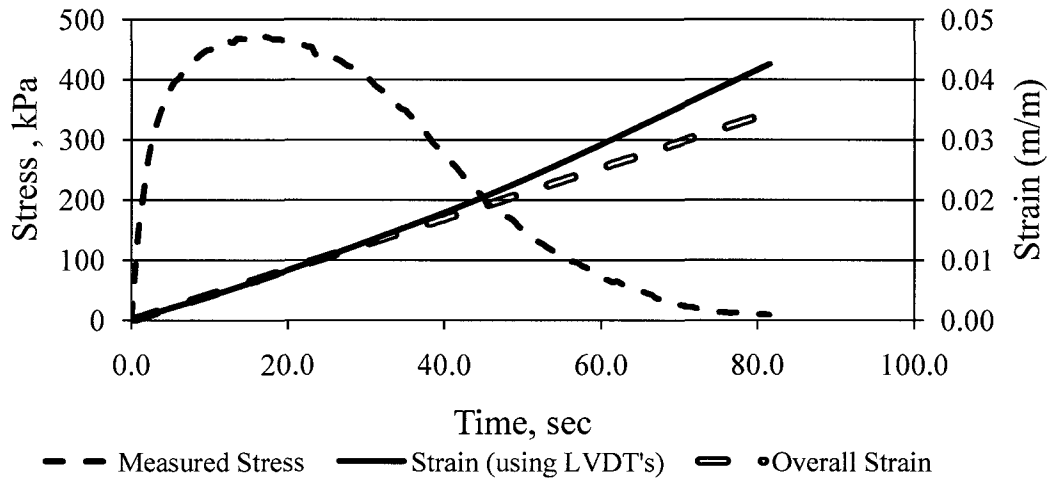
Figure 4-13: Variation of stress and strain during uniaxial constant crosshead rate test
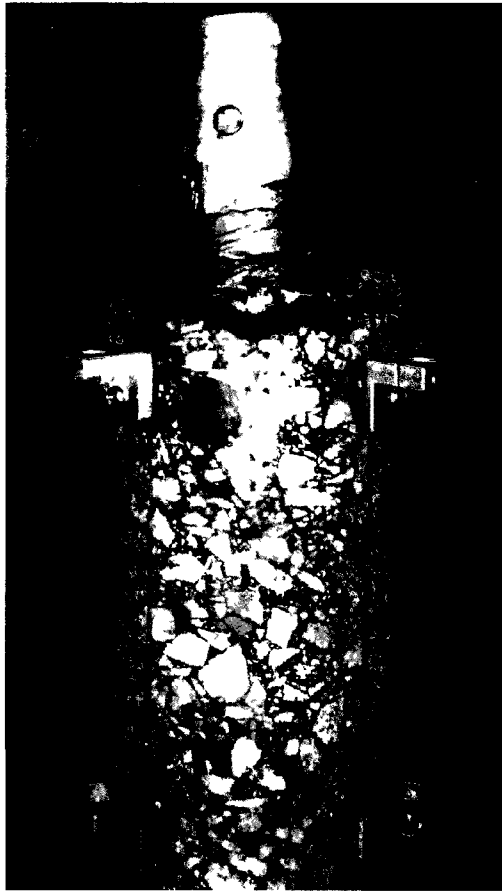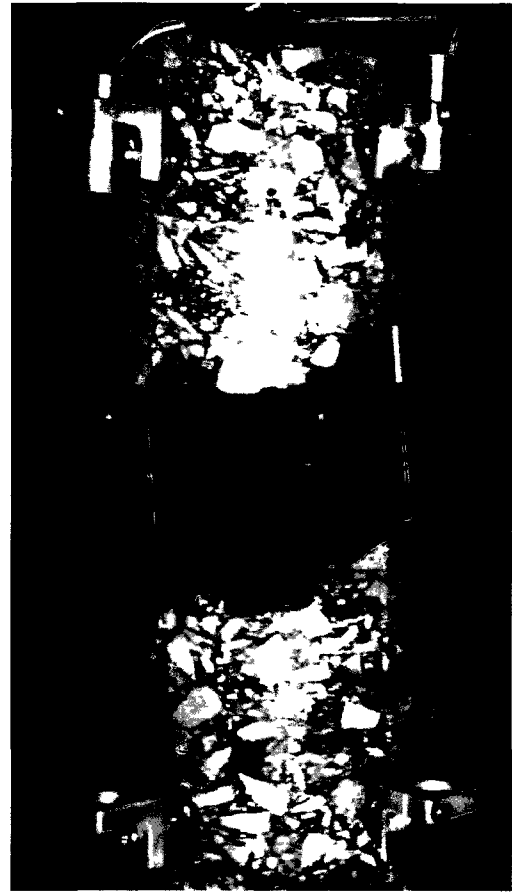
<div align="center">(a)   (b)</div>

Figure 4-14: Typical failure locations in uniaxial test specimens during damage inducing tests

CHAPTER 5

VISCOELASTIC CONTINUUM DAMAGE MODEL FOR FLEXURAL

FATIGUE BEHAVIOR

5.1 AASHTO protocol for flexural fatigue characterization

The AASHTO protocol for fatigue characterization is popular in the engineering community due to its ease with specimen fabrication and simple testing procedure (AASHTO 2003). This protocol adopts a strain based phenomenological approach for fatigue characterization which is a combination of elastic and empirical analysis.

According to the AASHTO specifications, rectangular beams 380 mm × 50 mm × 63 mm are cut and trimmed from asphalt concrete bricks. These beams are kept in an environmental chamber at a constant temperature of 20^0C for at least 2 hours before testing. The specimen is fixed to the flexural fatigue loading frame and is subjected to cyclic loading while keeping the displacement amplitude constant. The load and central deflection of the beam are measured using a load cell and an LVDT, respectively. The stress and strain in the extreme fiber in middle $1/3^{rd}$ region are calculated using Equations 4-9 and 4-10, respectively. Using the computed stress and strain, the stiffness values are calculated for each cycle. The strain and stiffness at 50th cycle are designated as initial tensile strain and initial stiffness value, respectively. The cyclic loading is continued until the stiffness of the specimen reduces to half the initial stiffness value and the corresponding cycle is noted as number of cycles to failure. This process is

repeated at several strain levels to arrive at an empirical relationship between the number of cycles to failure and initial tensile strain. Sometimes the initial stiffness of material is also included in empirical analysis. The relationships generally used in the empirical analysis are presented in Equations 2-1 and 2-2.

5.2   <u>Development of continuum damage model for flexure mode</u>

A typical testing setup for fatigue testing under flexure mode is shown in Figure 3-12. The loading configuration consists of a simply supported beam, point loaded at every third point. The free body diagram for the same testing setup is shown in Figure 5-1. The third point loading generates uniform bending moment and zero shear stress in the middle one third portion. Assuming the beam to be elastic, from the fundamentals of structural mechanics, one can derive relationship among stress, strain, applied load, central deflection and geometry of the beam. The maximum stress and maximum strain in the beam (at time= t) can be calculated using Equations 4-9 and 4-10, respectively. The variation of the maximum strain and the maximum stress in a typical displacement controlled fatigue testing is shown in Figures 5-2 and 5-3, respectively.

Free Body Diagram

Bending Moment Diagram

Shear Force Diagram
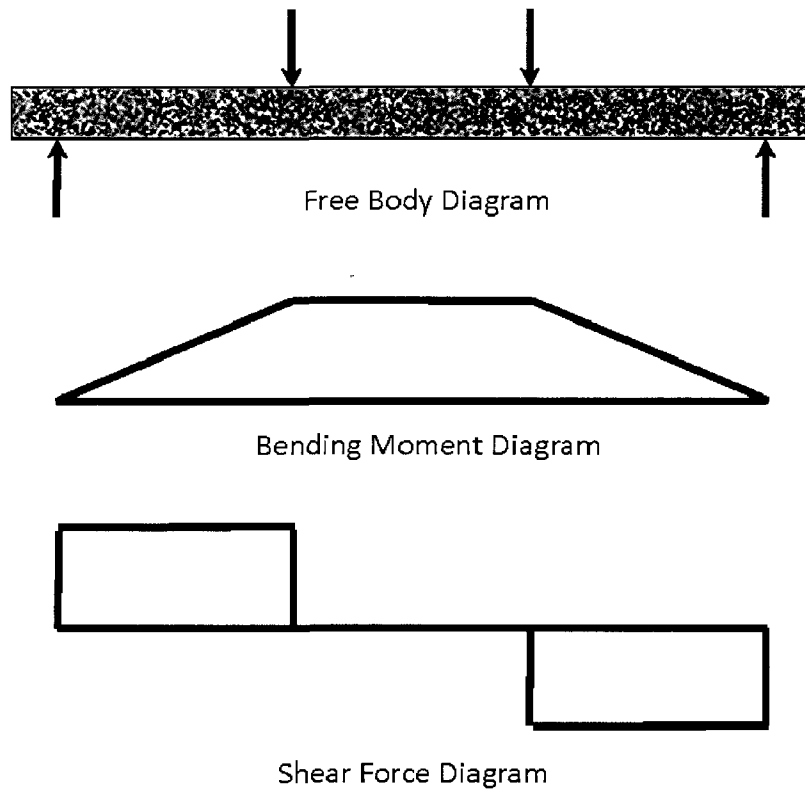
Figure 5-1: Free body diagram, bending moment distribution and shear force distribution in 3rd point loaded beam

68
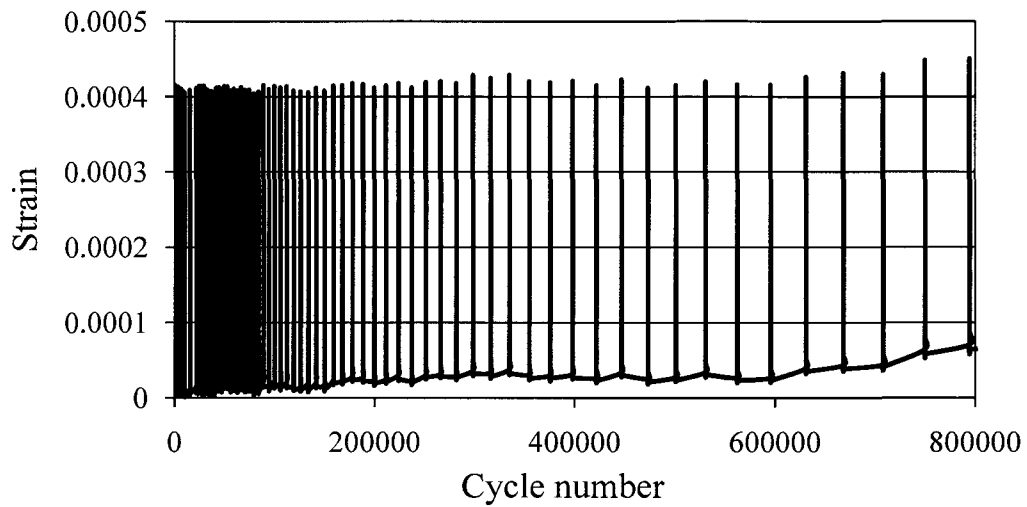
Figure 5-2: Typical strain history in a displacement controlled flexural fatigue test
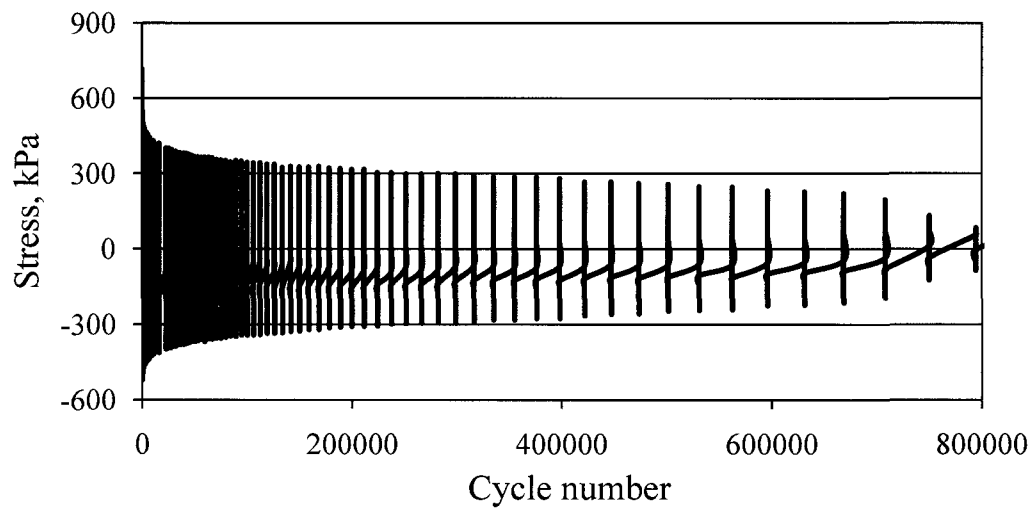
Figure 5-3: Typical stress response in displacement controlled flexural fatigue test

The maximum pseudostrain in beam is calculated by using Equation 2-10. The cross plots of stress vs. strain and stress vs. pseudostrain are shown in Figures 5-4 and 5-5, respectively. Since the specimen is tested at a damage inducing strain level, loops are seen in the stress vs. pseudostrain plots.
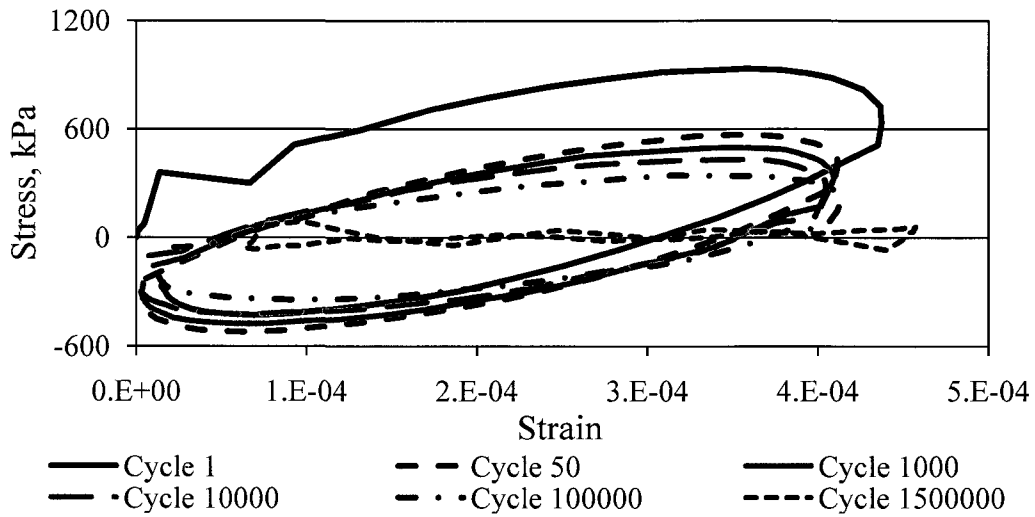
Figure 5-4: Typical plot of stress vs. strain in displacement controlled flexural fatigue test
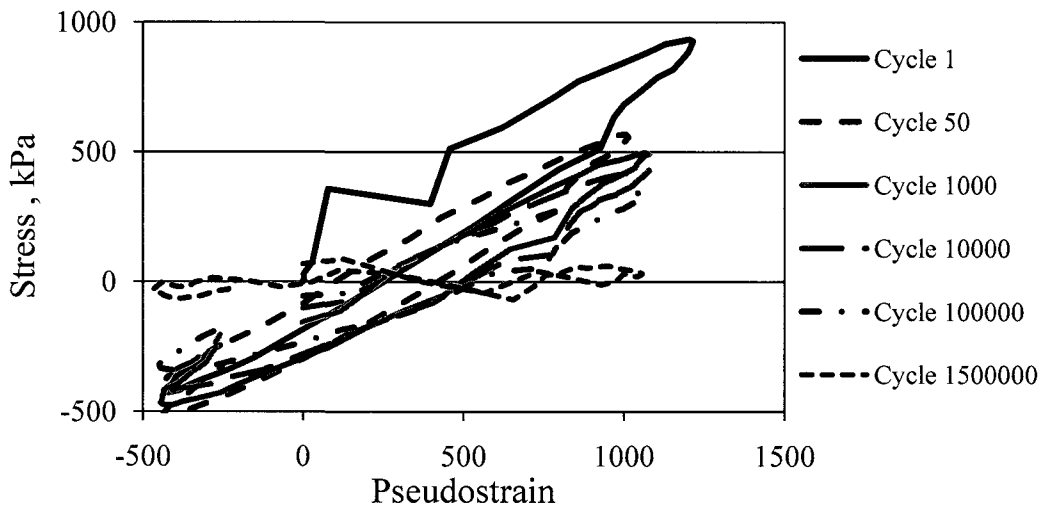
Figure 5-5: Typical plot of stress vs. pseudostrain in displacement controlled flexural fatigue test

The secant pseudostiffness (S_i^R) in any cycle i can be calculated by Equation 5-1. From here onwards for simplicity, secant pseudostiffness will be referred to as

pseudostiffness. The variation of pseudostiffness during a fatigue test is shown in Figure 5-6. To account for the sample to sample variation, the pseudostiffness is normalized using initial pseudostiffness (I). The normalized pseudostiffness is presented in Equation 5-2. The variation of the normalized pseudostiffness during a fatigue test is shown in Figure 5-7. Under the flexural mode of loading, tensile stresses lead to development of cracks. Under compression, rearrangement of aggregate structure takes place. Thus under flexure mode of loading, changes in microstructure take place throughout the test (irrespective of tensile or compressive stress state). Hence, it can be assumed that under flexural loading, damage grows continuously. Thus, the equation to calculate damage parameter ($S1$) takes the form as presented in Equation 5-3.

$$S_i^R = \frac{\sigma_i}{\varepsilon_{max,i}^R} \qquad\qquad 5\text{-}1$$

$$C1_i = \frac{S_i^R}{I} \qquad\qquad 5\text{-}2$$

$$S1_i \cong \sum_{i=1}^{N} \left[\frac{I}{2} \left(\varepsilon_{max,i}^R \right)^2 (C1_{i-1} - C1_i) \right]^{\frac{\alpha}{1+\alpha}} (t_i - t_{i-1})^{\frac{1}{1+\alpha}} \qquad\qquad 5\text{-}3$$

where $\varepsilon_{max,i}^R$ = maximum pseudostrain in cycle i;

σ_i = stress corresponding to maximum pseudostrain in cycle i;

S_i^R = pseudostiffness in cycle i;

I = initial pseudostiffness;

$C1_i$ = normalized pseudostiffness in cycle i;

$S1_i$ = damage parameter in cycle i;

α = material constant; and

t = time to maximum pseudostrain in cycle i.
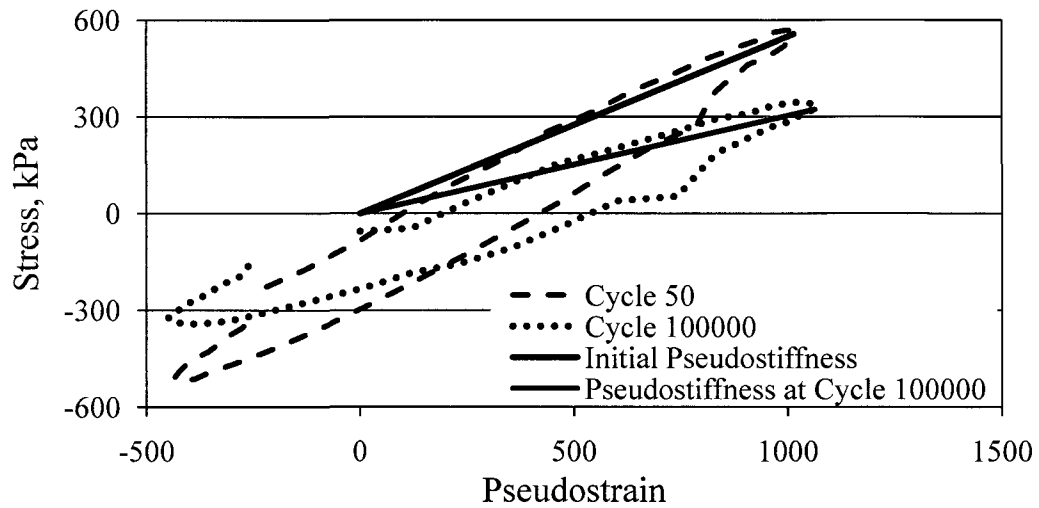
Figure 5-6: Change in pseudostiffness in displacement controlled flexural fatigue test
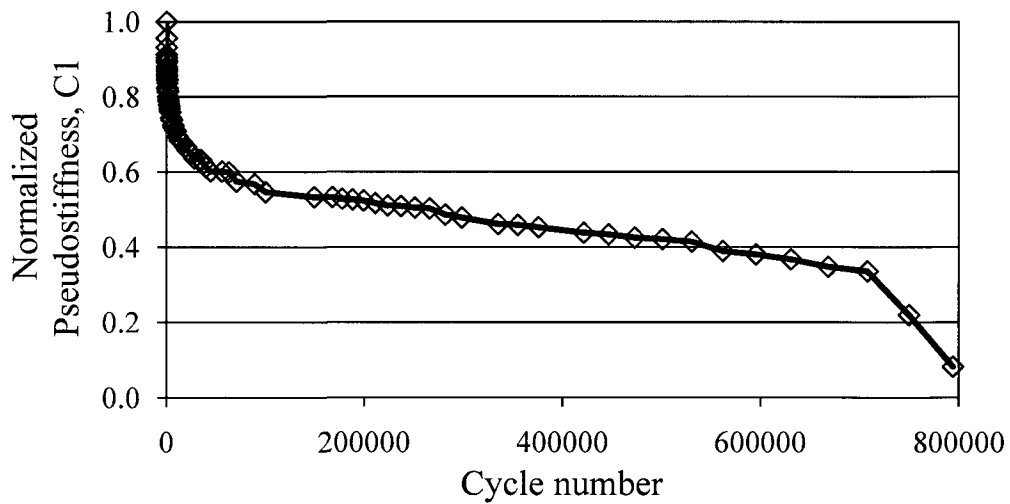
Figure 5-7: Variation of normalized pseudostiffness in displacement controlled flexural fatigue test

Previous studies have reported that damage growth in a specimen is dependent on energy release rate (Lee and Kim 1998b). If the material's fracture energy and failure stress are constant, then the material constant, α equals $1 + 1/n$. On the other hand, if the fracture process zone size and fracture energy are constant, the material constant, α equals $1/n$. Lee and Kim (1998b) suggested that material constant forms $\alpha = 1 + 1/n$, and $\alpha = 1/n$ are more suitable for controlled strain amplitude test and controlled stress amplitude test, respectively. Both forms of material constant expressions were evaluated in the present research. Using both values of α, damage parameter ($S1$) was computed. The variation of damage parameter with time over the course of a fatigue test is shown in Figure 5-8.
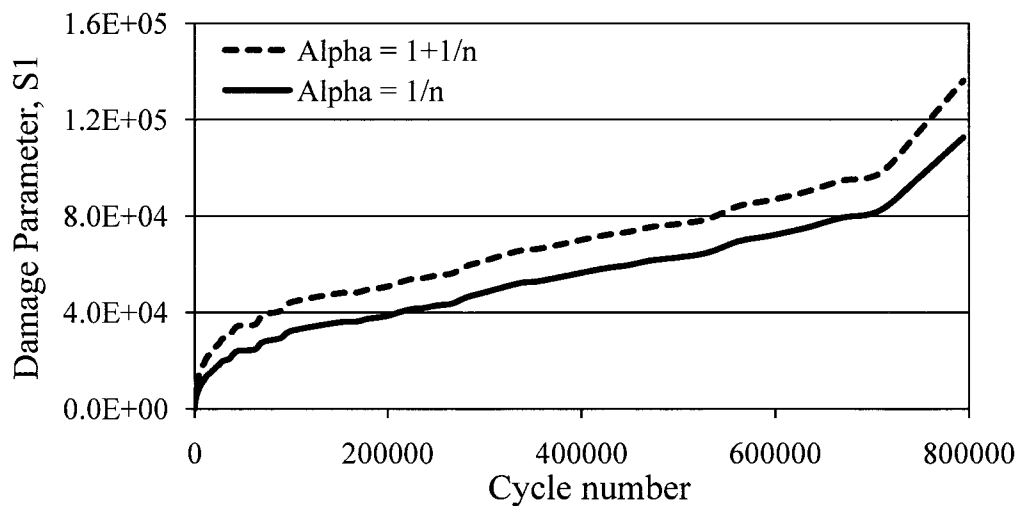
Figure 5-8: Variation of damage parameter in flexural fatigue test

A cross plot of the normalized stiffness vs. the damage parameter is presented in Figure 5-9. Here afterwards the plot of normalized stiffness vs. damage will be referred to as the damage characteristic curve. The Generalized Power Model (GPM) and

Generalized Exponential Model (GEM) were used in the present study to fit the damage characteristic curve are given in Equations 5-4 and 5-5, respectively. A plot of GPM and GEM fitted on damage characteristic curve raw data (using $\alpha = 1 + \frac{1}{n}$) is presented in Figure 5-10.

$$C1 = k_1 - k_2 \times (S1)^{k_3}$$

5-4

$$C1 = e^{k_4 \times (S1)^{k_5}}$$

5-5

where $C1$ = normalized pseudostiffness;

$S1$ = damage parameter; and

k_i = regression coefficients.
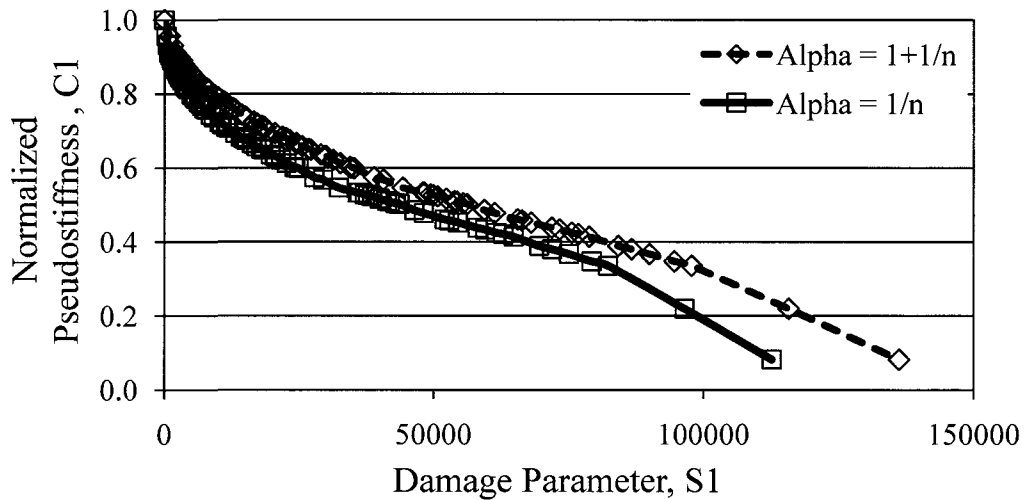
Figure 5-9: Damage characteristic curve at different values of alpha in flexural fatigue test
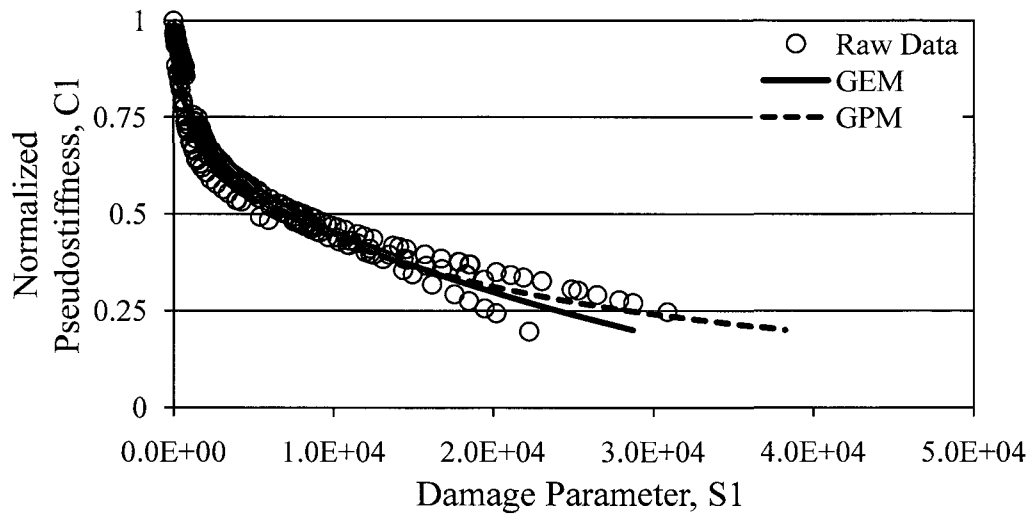
Figure 5-10: Comparison of fitted GPM and GEM on damage characteristic curve data

5.3 Effect of value of material constant on damage characteristic curve

Damage characteristic curve data from tests at a particular test temperature were combined to obtain a master data set and were then fit with analytical functions. The GPM (Equation 5-4) and GEM (Equation 5-5) were fit on the master data set. To measure goodness of fit, the coefficient of determination (R^2) was calculated. The value of R^2 indicates how well the regression fit approximates measured values. The coefficient of determination relates total sum of squares (directly related to sample variance) and sum of squares of residuals, and the relation is given in Equation 5-6.

$$R^2 = 1 - \frac{SS_{res}}{SS_{tot}}$$

5-6

where R^2 = coefficient of determination;

   SS_{res} = sum of squares of residuals; and

SS_{tot} = total sum of squares.

In general, value of R^2 ranges between 0 and 1. The value of 1 indicates regressed values perfectly fits the measured data while the value of 0 indicates complete mismatch between fitted values and measured values. Two values of material constants $(\alpha = 1 + \frac{1}{n}, \alpha = \frac{1}{n})$ were used while calculating the damage parameter. Functional forms namely GPM and GEM were also used. The R^2 obtained for each case using CalTrans mixtures is presented in Table 5-1.

Table 5-1: Summary of coefficient of determination obtained while fitting analytical function to characteristic damage curve data

Mix	Strain Amplitude (10^{-6})	Test Temperature (C)	Generalized Power Model		Generalized Exponential Model	
			alpha = 1 + 1/n	alpha = 1/n	alpha = 1 + 1/n	alpha = 1/n
PG 64-28	370	30	0.955	0.944	0.975	0.966
		20	0.957	0.950	0.958	0.952
		10	0.957	0.937	0.949	0.931
	185	30	0.931	0.916	0.947	0.933
		20	0.974	0.962	0.979	0.966
		10	0.610	0.577	0.589	0.558
PG 64-10	370	30	0.948	0.925	0.944	0.918
		20	0.986	0.978	0.986	0.980
		10	0.983	0.977	0.978	0.972
	185	30	0.982	0.980	0.985	0.983
		20	0.954	0.887	0.961	0.889
		10	0.926	0.903	0.944	0.921
PG 64-16	370	30	0.966	0.950	0.955	0.939
		20	0.979	0.968	0.957	0.945
		10	0.980	0.966	0.972	0.958
	185	30	0.971	0.962	0.965	0.954
		20	0.968	0.949	0.952	0.935
		10	0.936	0.923	0.944	0.932
PG 70-16	370	30	0.972	0.976	0.963	0.968
		20	0.970	0.958	0.957	0.945
		10	0.979	0.970	0.971	0.962
	185	30	0.967	0.967	0.972	0.973
		20	0.939	0.927	0.945	0.934
		10	0.941	0.916	0.954	0.931

In general, higher R^2 were obtained using $\alpha = 1 + 1/n$ when compared to $\alpha = 1/n$. In other words, the material constant $\alpha = 1 + 1/n$ yielded better collapse of all curves when compared to $\alpha = 1/n$. Also, R^2 was higher when the GPM was used, indicating GPM describes the characteristic damage curve in a better way when compared to GEM.

5.4 Effect of strain amplitude on continuum damage parameters

The variation of normalized pseudostiffness with time at different strain amplitudes at 20^0C test temperature for the M1 mixture is shown in Figure 5-11. At lower strain amplitudes, the damage accumulates at a slower rate. Thus, the time required to reach the same pseudostiffness value is more for a smaller strain amplitude test when compared to a higher strain amplitude test. Damage characteristic curves for mixture M1 at 20^0C test temperature using $\alpha = 1 + \frac{1}{n}$ and $\alpha = \frac{1}{n}$ are presented in Figures 5-12 and 5-13, respectively. As seen in Figures 5-12 and 5-13, damage characteristic curves obtained at different strain amplitudes collapse to a single characteristic curve.
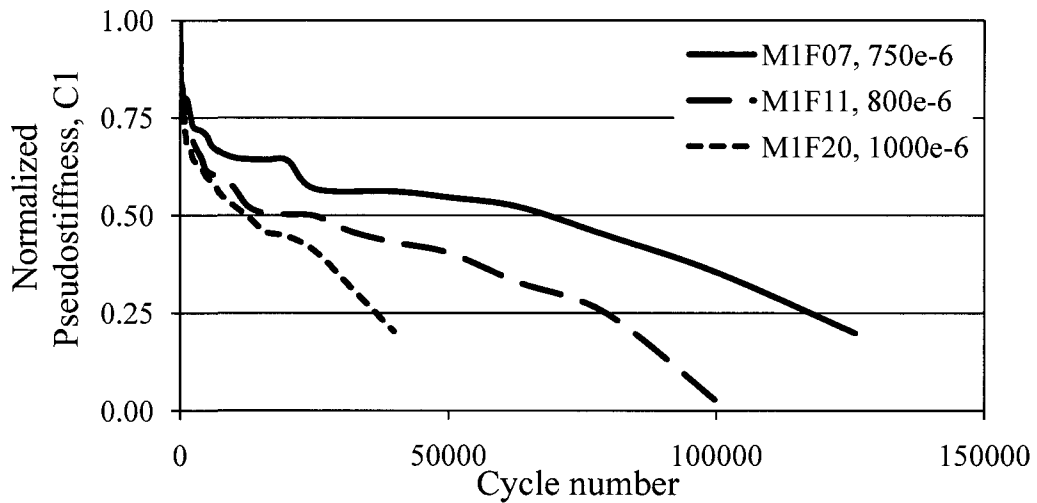
Figure 5-11: Normalized pseudostiffness as a function of cycle number in flexural fatigue test for mixture M1 at 20^0C temperature at three strain amplitudes
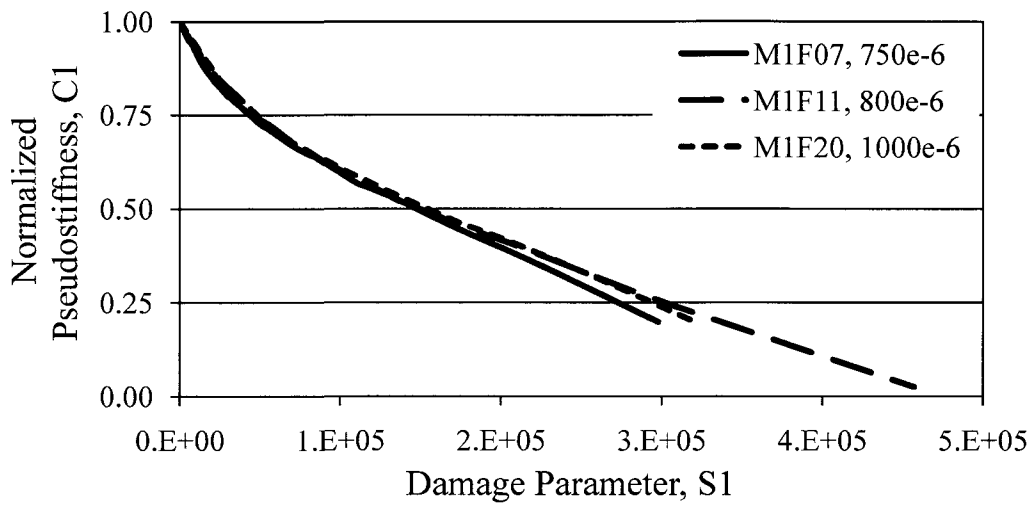
Figure 5-12: Damage characteristic curves in flexural fatigue test for mixture M1 at 20°C temperature with alpha = 1 + 1/n
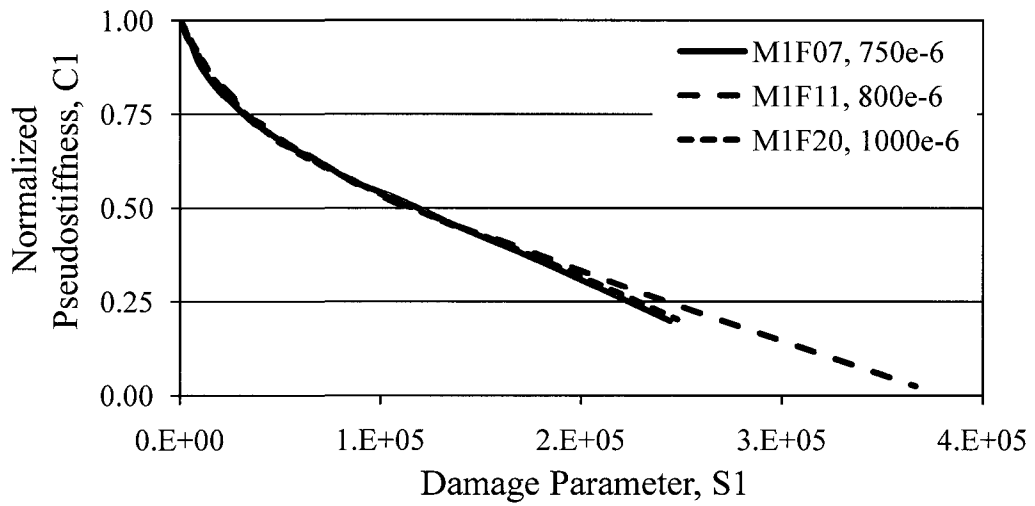
Figure 5-13: Damage characteristic curves in flexural fatigue test for mixture M1 at 20°C temperature with alpha = 1/n

5.5 Effect of test temperature on continuum damage parameter

The variation of normalized pseudostiffness with time at different test temperatures at 370 microstrain amplitude using the PG 64-16 mix is presented in Figure 5-14. At higher test temperatures, due to higher healing rate and relaxation the damage accumulates at a slower rate. Thus the time required to reach same pseudostiffness value is more at higher temperature when compared to low test temperature. Damage characteristic curves for PG 64-16 mix at 370 microstrain amplitude using $\alpha = 1 + \frac{1}{n}$ and $\alpha = \frac{1}{n}$ are presented in Figures 5-15 and 5-16, respectively.
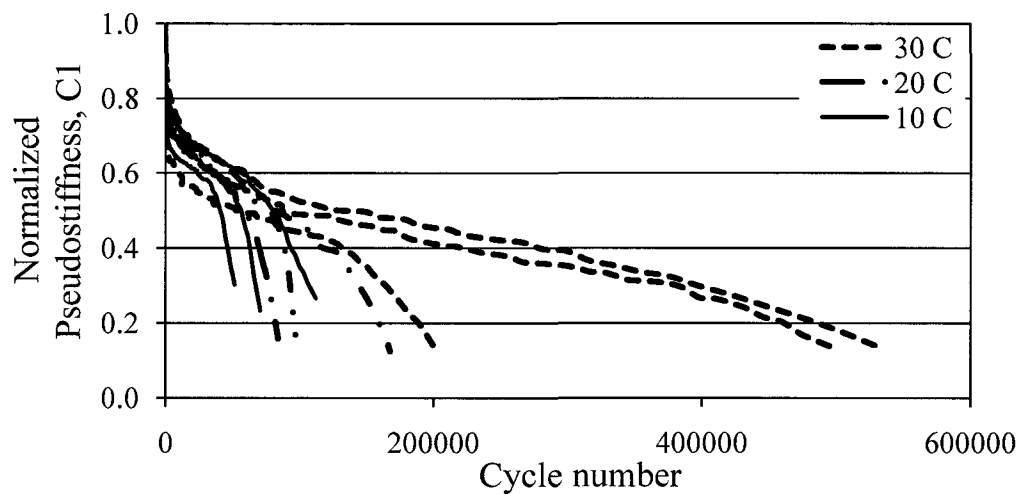
Figure 5-14: Normalized pseudostiffness as a function of cycle number in flexural fatigue test for PG 64-16 mix at 370 microstrain amplitude
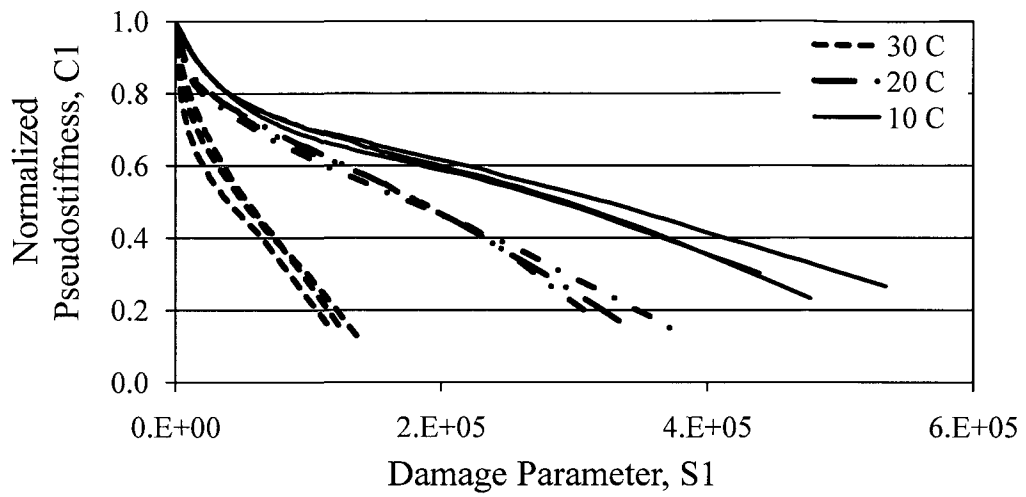
Figure 5-15: Damage characteristic curves in flexural fatigue test for PG 64-16 mix at 370 microstrain amplitude with alpha = 1 + 1/n
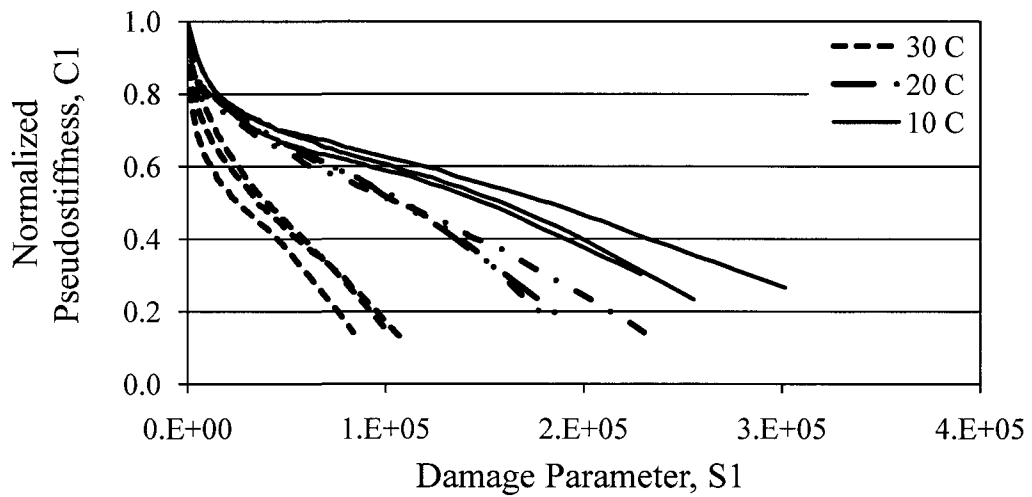
Figure 5-16: Damage characteristic curves in flexural fatigue test for PG 64-16 mix at 370 microstrain amplitude with alpha = 1/n

5.6 Fatigue prediction using damage characteristic curve

This section presents an approach to predict fatigue performance of material at a condition that is completely different than the reference data (testing frequency, temperature). The overall testing and prediction methodology can be divided into the following five stages.

1) Determination of viscoelastic parameters,

2) Testing of the specimen under damage inducing strain amplitude level at reference temperature,

3) VECD analysis and construction of the damage characteristic curve at reference temperature,

4) Shifting of the damage characteristic curve to target temperature using reduced time and time-temperature superposition principle,

5) Prediction of fatigue performance using shifted damage curve and other material parameters at target temperature.

In the first stage, the specimen is tested for its dynamic modulus and phase angle values at multiple strain amplitudes (below damage inducing level) and temperatures. Subsequently, the relaxation modulus mastercurve is constructed using the appropriate inteconversion technique. In the next stage, the sample is subjected to cyclic loading at damage inducing strain levels at a reference temperature. The damage characteristic curve at the reference temperature is constructed using the strain-stress history. Using the histories of the normalized pseudostiffness and the damage parameter at the reference temperature, the damage characteristic curve is shifted to the temperature at

which fatigue prediction is to be made. The pseudostrain and damage parameter at the target temperature are calculated using the following relations:

$$\varepsilon^R(t) = \frac{1}{E_R} \int_0^t E\,(\xi - \xi') \frac{d\xi}{d\xi'}\, d\xi'$$

5-7

$$S1_i \cong \sum_{i=1}^{N} \left[\frac{I}{2} \left(\varepsilon_{m,i}^R\right)^2 (C1_{i-1} - C1_i)\right]^{\frac{\alpha}{1+\alpha}} (\xi_i - \xi_{i-1})^{\frac{1}{1+\alpha}}$$

5-8

$$\xi = \frac{t}{a_t}$$

5-9

where ξ = reduced time;

     a_t = temperature shift factor;

     ε^R = pseudostrain;

     $\varepsilon_{m,i}^R$ = maximum pseudostrain in cycle i;

     I = initial pseudostiffness;

     $C1_i$ = normalized pseudostiffness in cycle i;

     $S1_i$ = damage parameter in cycle i;

     α = material constant; and

     t = time variable.

Prediction of higher temperature behavior from a lower temperature requires a portion of the measured data because the reduced time range is shorter than the measured time range. It is recommended that fatigue testing be conducted at lower temperatures and the data generated used to predict performance at higher temperatures.

For verification of the accuracy of the fatigue prediction models, cyclic tests were conducted on specimens that were not part of preliminary analysis. The damage characteristic curves constructed using the measured data at 20^0C and shifted damage curve from 10^0C for the PG 64-28 mixture using $\alpha = 1 + 1/n$ and $\alpha = 1/n$ are presented in Figures 5-17 and 5-18, respectively. Similar plots for the PG 64-10 mixture are shown in Figures 5-19 and 5-20, respectively. Using the reduced time, reduced pseudostrain and normalized pseudostiffness, stress at 20^0C was predicted. The comparison of predicted stress and measured stress for PG 64-28 and PG 64-10 samples at 20^0C is presented in Figures 5-21 and 5-22, respectively.
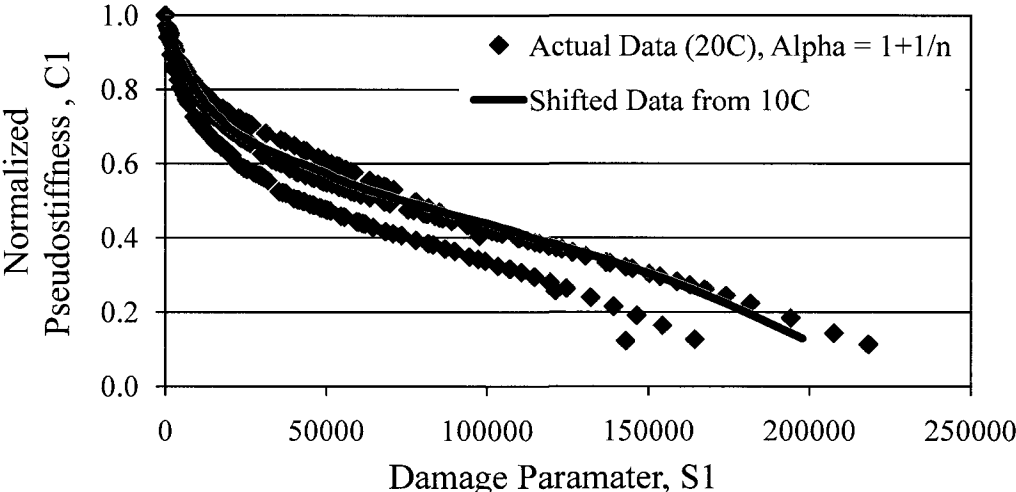
Figure 5-17: Damage characteristic curve shifted to 20^0C for PG 64-28 mix using alpha = 1 + 1/n
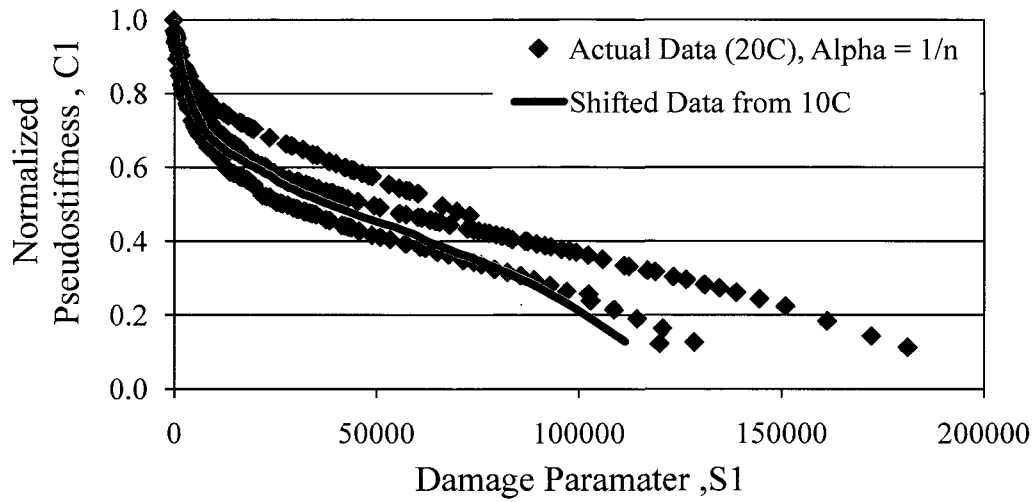
Figure 5-18: Damage characteristic curve shifted to 20°C for PG 64-28 mix using alpha = 1/n
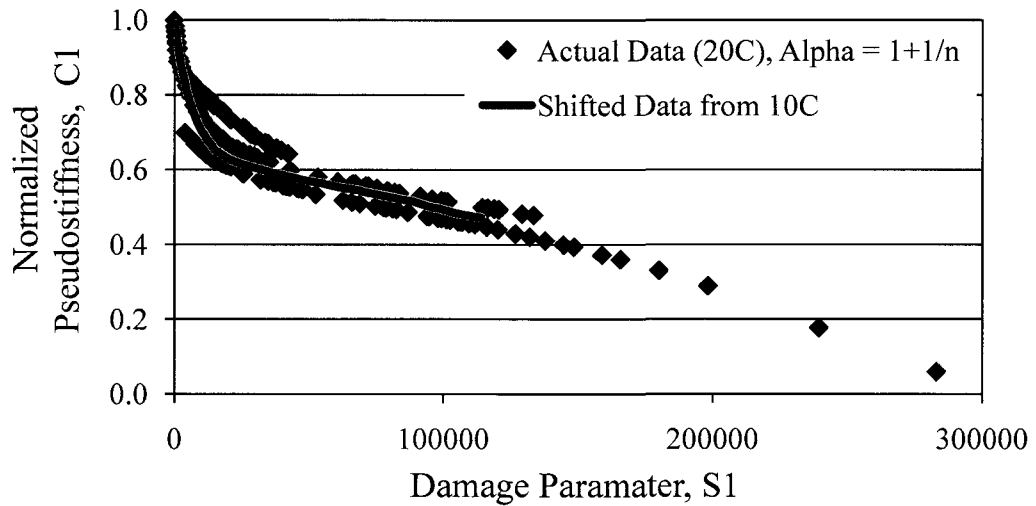
Figure 5-19: Damage characteristic curve shifted to 20°C for PG 64-10 mix using alpha = 1 + 1/n
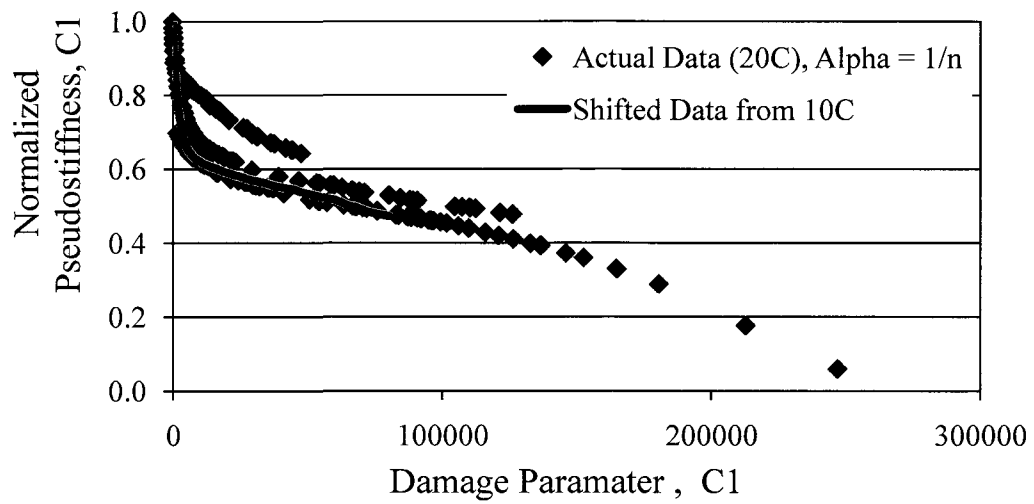
Figure 5-20: Damage characteristic curve shifted to 20°C for PG 64-10 mix using alpha = 1/n
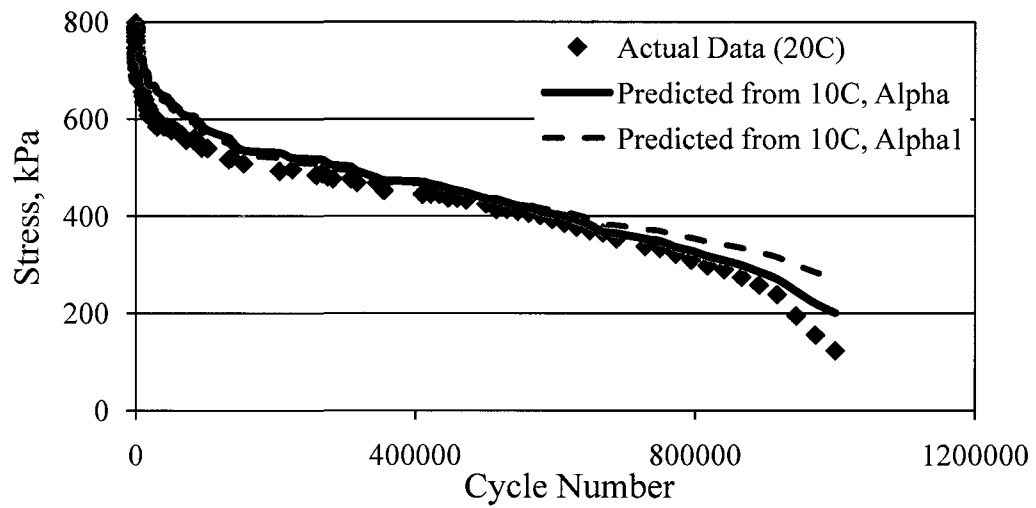
Figure 5-21: Comparison of measured and predicted stress for PG 64-28 mix sample
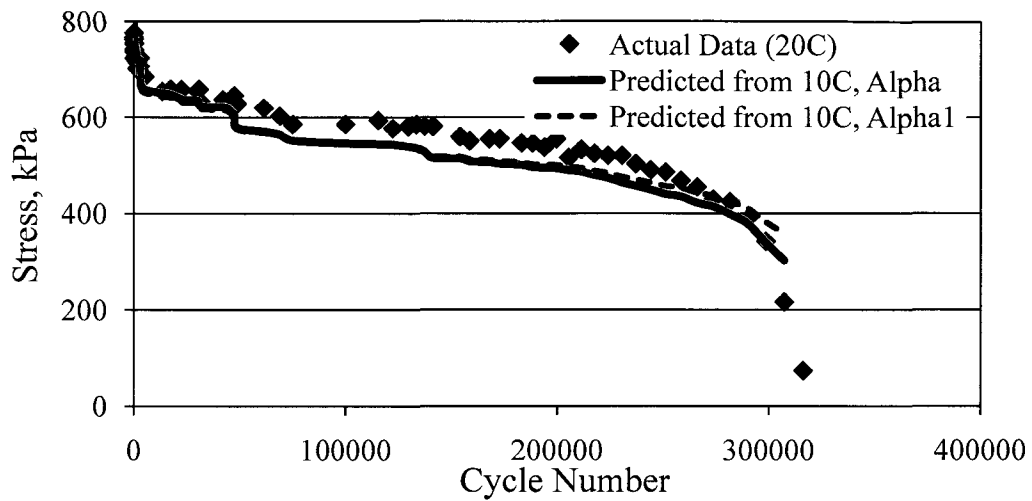
Figure 5-22: Comparison of measured and predicted stress for PG 64-10 mix sample

5.7 Summary

The uniaxial constitutive model has been extended to flexure mode of loading. This extended constitutive model can account for variables like testing temperature, strain rate and testing frequency. Using the extended constitutive model, a method to predict flexural fatigue behavior has been proposed. The proposed methodology combines simplicity of AASHTO protocol with fundamental, mechanics based principles of damage mechanics. The fatigue life predictions made using the continuum damage material constants were well within the range observed from actual measurements.

CHAPTER 6

FATIGUE ENDURANCE LIMIT DETERMINATION

6.1 Introduction

This chapter presents a new approach for the determination of the fatigue endurance limit based upon VECD principles. In the first section, theory behind the proposed incremental amplitude testing approach is presented. The next two sections present the application of the proposed approach to uniaxial and flexural mode of loading. The fifth section presents several automated approaches to evaluate damage and subsequent determination of the fatigue endurance limit. The final section presents the conclusions on qualitative observations about these automated procedures to evaluate the damage.

6.2 Theory behind incremental amplitude test

Asphalt concrete displays hysteretic stress vs. strain loop formation even under small loads or strain due to the combined effect of the damage growth and viscoelastic effects (Kim and Little 1990). Therefore, the viscoelastic effect must be separated from the damage development so that the damage development can be quantified separately. By using the concept of pseudostrain introduced by Schapery (1984), a viscoelastic problem can be converted to an equivalent elastic problem.

As shown in Figure 2-4, when the stress (or strain) levels are small, the stress vs. pseudostrain relationship is linear indicating, removal of linear viscoelastic effects. Any deviation from linearity at this stage indicates the combined effects of nonlinearity and damage. Within the nonlinear viscoelastic region, loops are seen in the cross plot of stress vs. pseudostrain history. However loading and unloading paths of each cycle are the same as in the previous cycle. Thus these loops do not shift their position as cyclic loading is continued. An example for loop formation within nonlinear viscoelastic limits is shown in Figure 6-1. Thus it can be concluded that material is undergoing damage if changes in shape and location are seen in stress-pseudostrain loops as cyclic loading is continued. Examples for change in shape and shift in stress vs. pseudostrain plots indicating damage in controlled strain amplitude test and controlled stress amplitude test are shown in Figures 6-2 and 6-3, respectively.
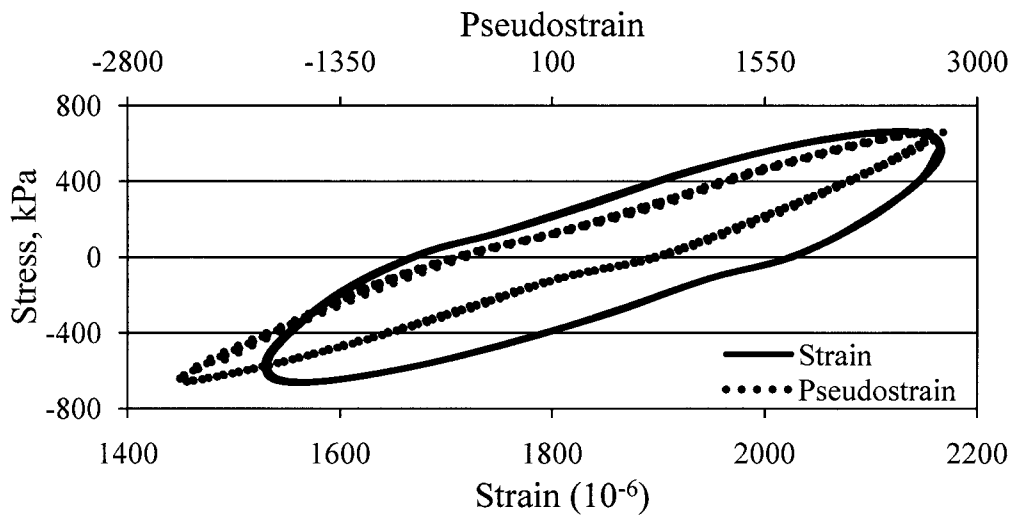
Figure 6-1: Nonlinear viscoelastic behavior in a undamaged viscoelastic material

89
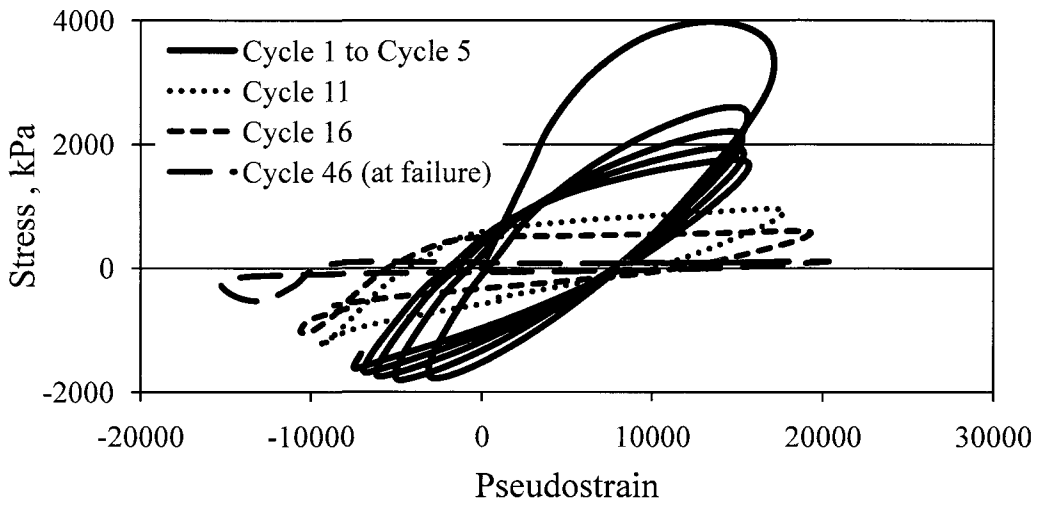
Figure 6-2: Cross plot of stress-pseudostrain at damage inducing level in controlled strain amplitude test
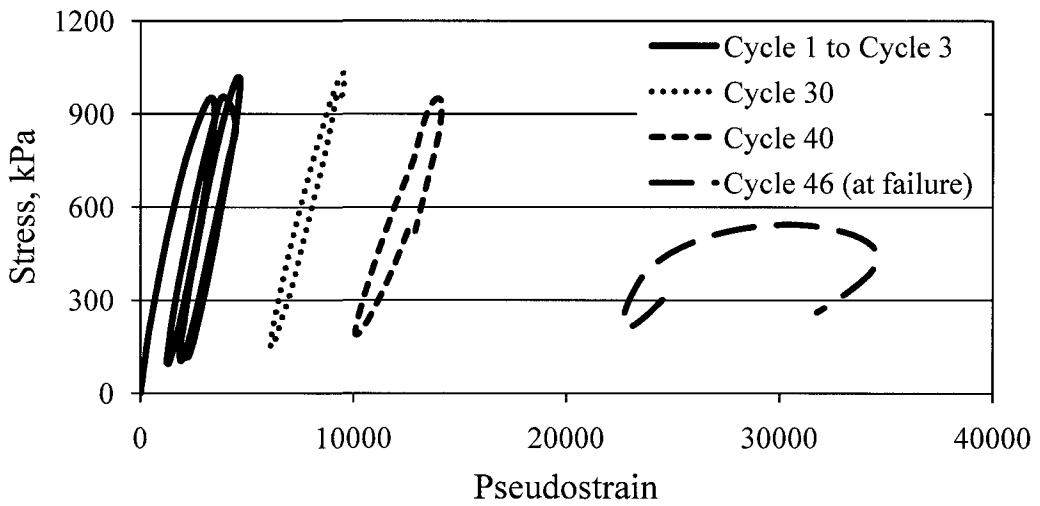
Figure 6-3: Cross plot of stress-pseudostrain at damage inducing level in controlled stress amplitude test

The development of loops and changes in stress vs. pseudostrain plots is used in this research to detect damage in the specimen. If no damage is detected, then the specimen

can sustain load cycles and hence the applied load or strain level can be assumed to be at or below the fatigue endurance limit of the mixture. The proposed testing procedure consists of applying stress or strain blocks of loading. Initially, a relatively low stress or strain amplitude that is thought to be below the fatigue endurance limit is applied. Typically, this is close to the same amplitude at which complex modulus tests are performed. Then the loading block of higher stress or strain amplitude is applied and testing is continued until the specimen fails. A typical incremental stress or strain amplitude input history is shown in Figure 6-4.
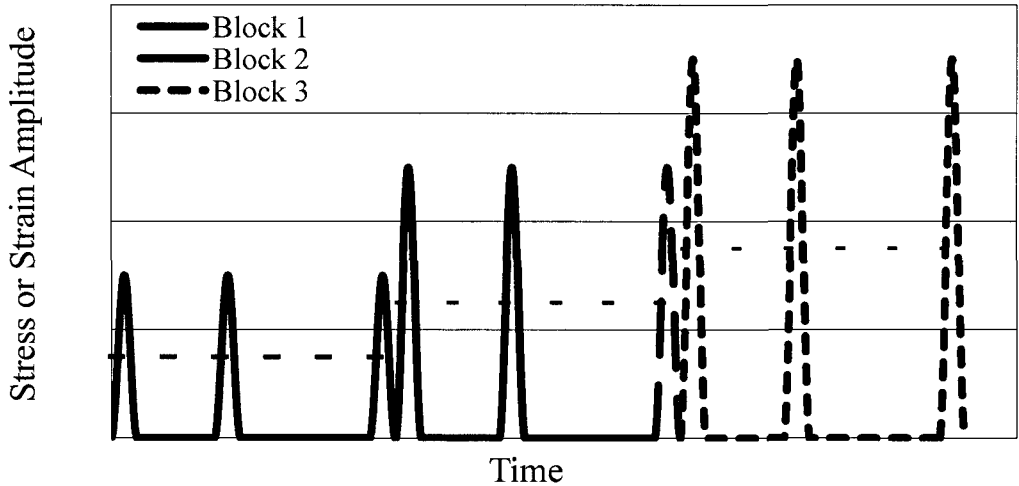
Figure 6-4: Input in a typical incremental amplitude test

Within each loading block, the stress or strain amplitude is held constant and continued until steady state is attained. The number of cycles to attain steady state is dependent on mode of loading. For controlled stress amplitude tests, 2000 cycles were found to be sufficient where as in controlled strain amplitude tests, around 5000 cycles were required. When the average strain and stress attained a plateau value, it was

assumed that steady state was attained for controlled stress amplitude tests and controlled strain amplitude tests, respectively.

6.3 Uniaxial mode of loading

One of the easiest ways to characterize asphalt concrete is in uniaxial mode of loading. This setup gives better control over the loading conditions like controlling stress or crosshead strain, and uniform stress (strain) distribution over the cross sectional area. Under uniaxial loading conditions, samples were tested under two modes of loading i.e. constant stress amplitude and constant strain amplitude within each loading block. Details of these tests are given in the following paragraphs.

6.3.1 Incremental stress amplitude test

In the incremental stress amplitude test, the stress amplitude was held constant within each loading block. A typical input in an incremental stress amplitude test is shown in Figure 6-5.

In an incremental stress amplitude test, crosshead and on specimen strain increase as damage evolves in the specimen. This will be case even within each loading block. This is due to fact that as damage occurs, the load carrying capacity of the specimen decreases and the crosshead ram has to move more in order to keep the stress amplitude the same within each loading block. The increase in strain and computed pseudostrain for a typical incremental stress amplitude test is shown in Figure 6-6. A plot of stress vs. pseudostrain

in an incremental strain amplitude test until failure is shown in Figure 6-7. This indicates

the pseudostiffness of the sample is continuously decreasing with time or load cycles.
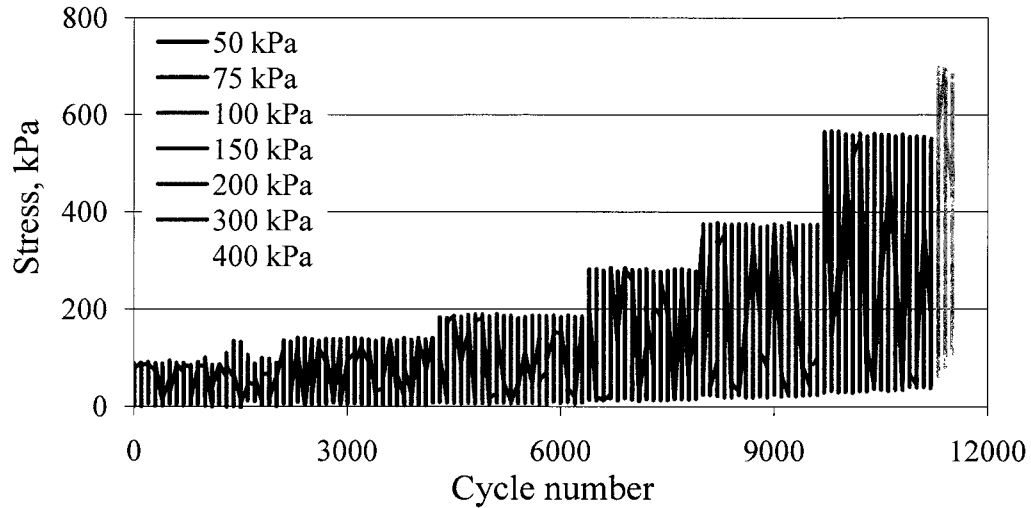
Figure 6-5: Loading blocks in an incremental stress amplitude test under uniaxial test conditions
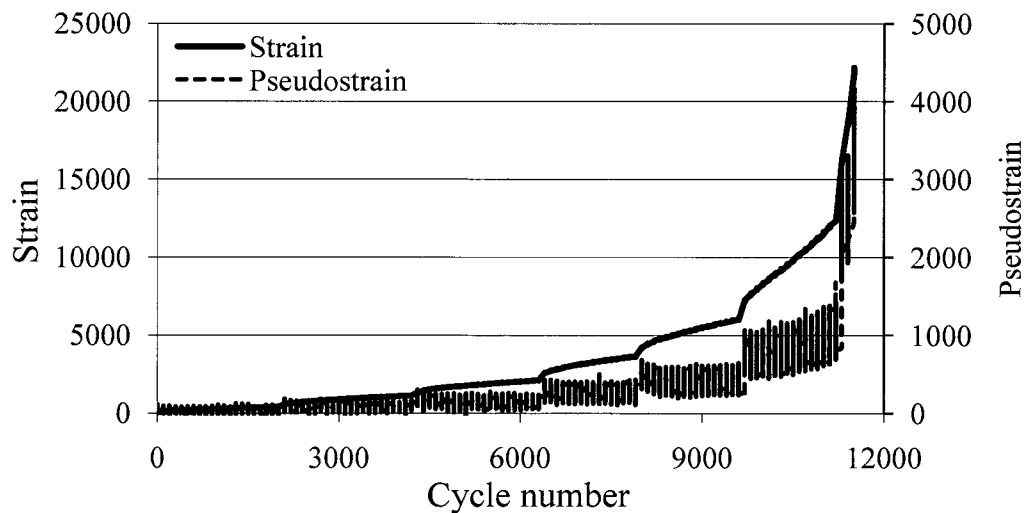
Figure 6-6: Strain response and computed pseudostrain as a function of cycle number in an incremental stress amplitude test under uniaxial test conditions
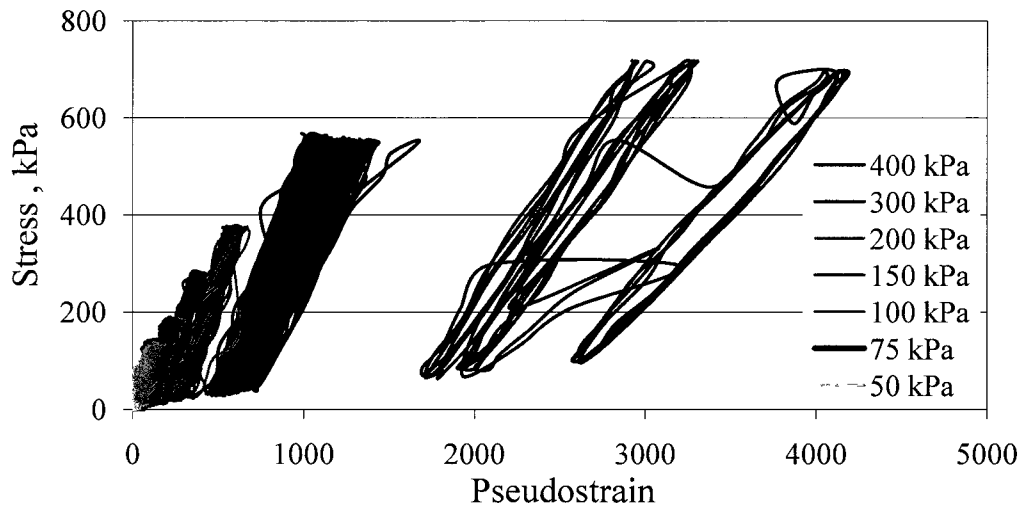
Figure 6-7: Crossplot of stress vs. pseudostrain in an uniaxial incremental stress amplitude test under uniaxial test conditions

6.3.2 Incremental strain amplitude test

In the incremental strain amplitude test, the crosshead strain amplitude was held constant within each loading block. A typical input in an incremental strain amplitude test is shown in Figure 6-8; the crosshead and measured LVDT strains are shown.
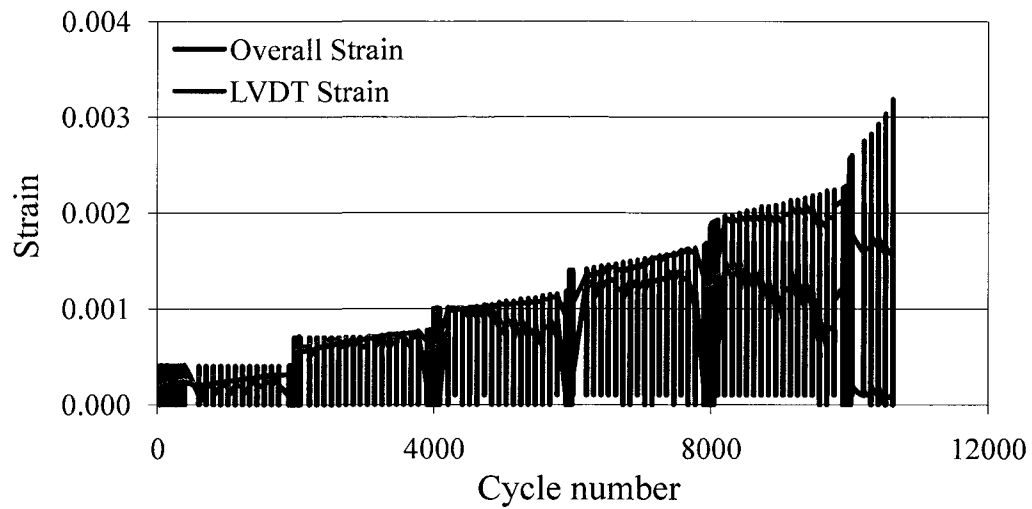
Figure 6-8: Loading blocks in an incremental strain amplitude test under uniaxial test conditions

As damage develops in an incremental strain amplitude test, cracks form in the specimen. Also, due to the viscoelastic nature of material, the specimen relaxes and increases in length. Thus, compressive stress develops in the specimen, while the tensile stress amplitude and the stiffness of the material decreases. Due to an increase in gage length and cyclic displacement input, the value of mean strain increases. Thus, the value of computed pseudostrain also increases. Decrease in stress and simultaneous increase in pseudostrain within each loading block is shown in Figures 6-9 and 6-10, respectively. Just after localization in the test specimen, the macro crack propagates, effectively decreasing the cross-sectional area of the test specimen. Thus as loading progresses, the maximum stress and the minimum stress in each cycle decreases. The same is seen in last loading block in Figure 6-9. A plot of stress vs. pseudostrain in an incremental strain amplitude test until failure is shown in Figure 6-11.
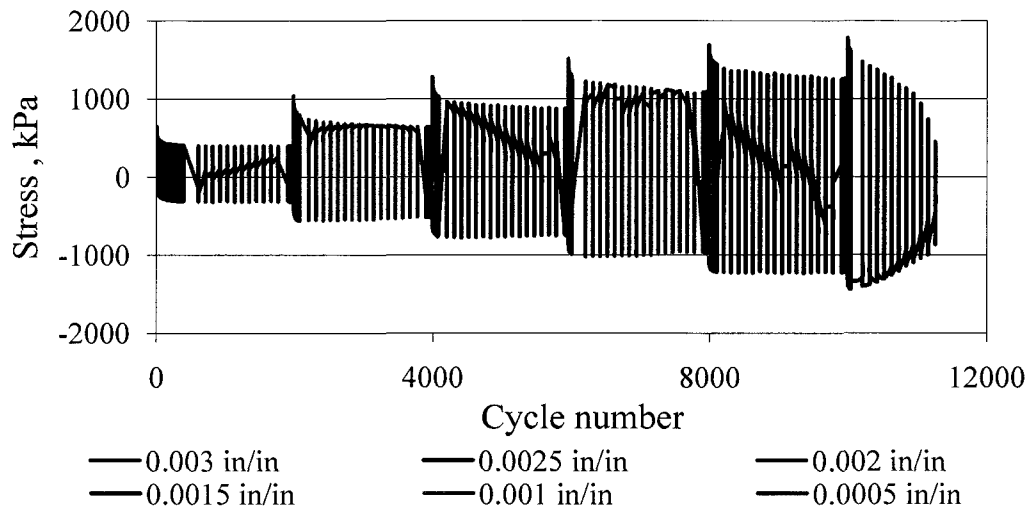
Figure 6-9: Stress response in an incremental strain amplitude test under uniaxial test conditions
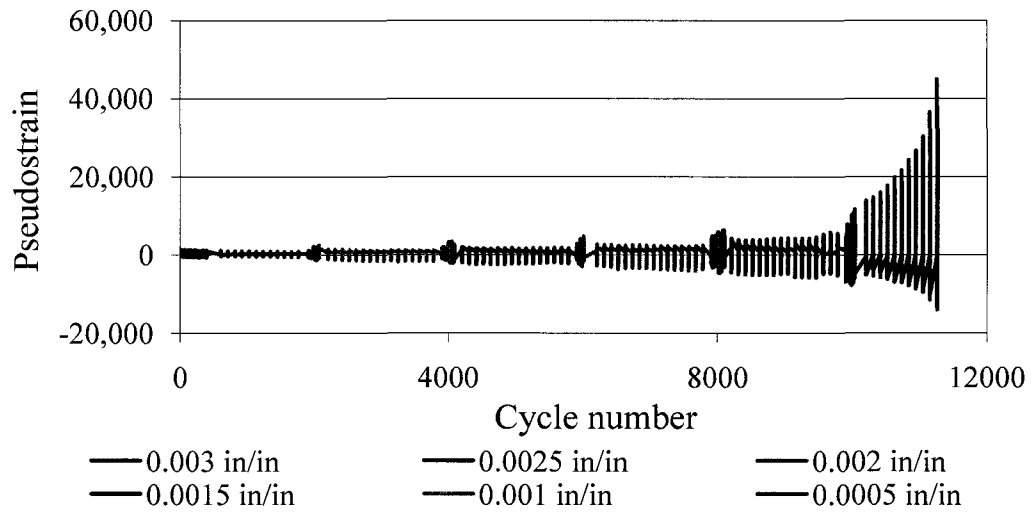
Figure 6-10: Computed pseudostrain as a function of cycle number in an incremental strain amplitude test under uniaxial test conditions
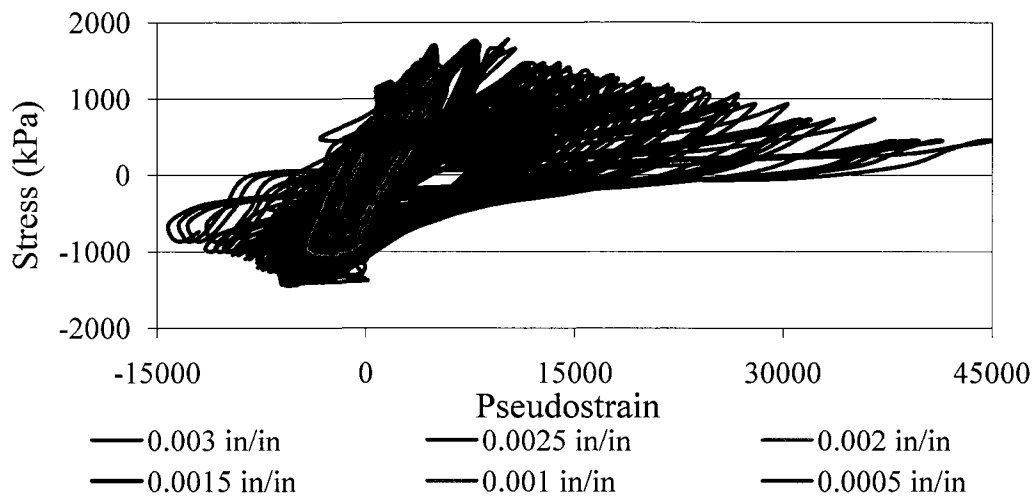
Figure 6-11: Crossplot of stress vs. pseudostrain in an uniaxial incremental strain amplitude test under uniaxial test conditions

6.4 Flexure mode of loading

In flexure mode of loading, beams were tested under displacement controlled mode only. Due to data acquisition issues, load and displacement data from each loading block was acquired separately and then combined for analysis. Detailed descriptions about the test and analysis are presented in the following paragraphs.

A typical input in an incremental strain amplitude test under flexure mode of loading is shown in Figure 6-12. In the absence of a suitable mechanism to measure strain physically, crosshead displacement measurements were used to calculate the maximum strain. Under cyclic loading, the magnitudes of maximum stress in the beam (top and bottom) are equal but have opposite signs (tensile and compressive). Also, due to simultaneous relaxation and damage, the value of maximum stress decreases under damage inducing load levels. The damage in the specimen is symmetric, thus the value of mean stress is approximately zero. A typical stress response during an incremental strain

amplitude test is shown in Figure 6-13. The variation of computed pseudostrain is presented in Figure 6-14. A plot of stress vs. pseudostrain in an incremental strain amplitude test under flexural mode of loading is shown in Figure 6-15.
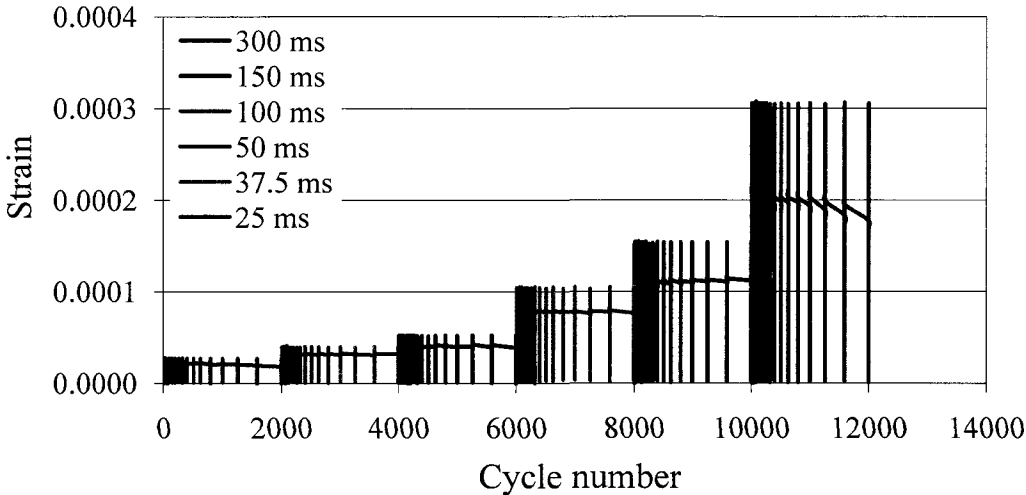
Figure 6-12: Loading blocks in an incremental strain amplitude test under flexure mode of loading
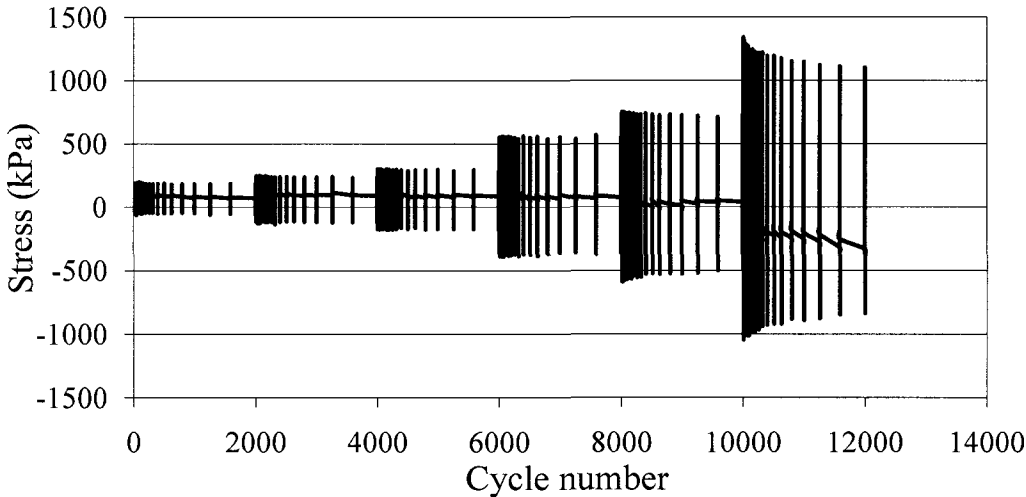
Figure 6-13: Stress response in an incremental strain amplitude test under flexure mode of loading
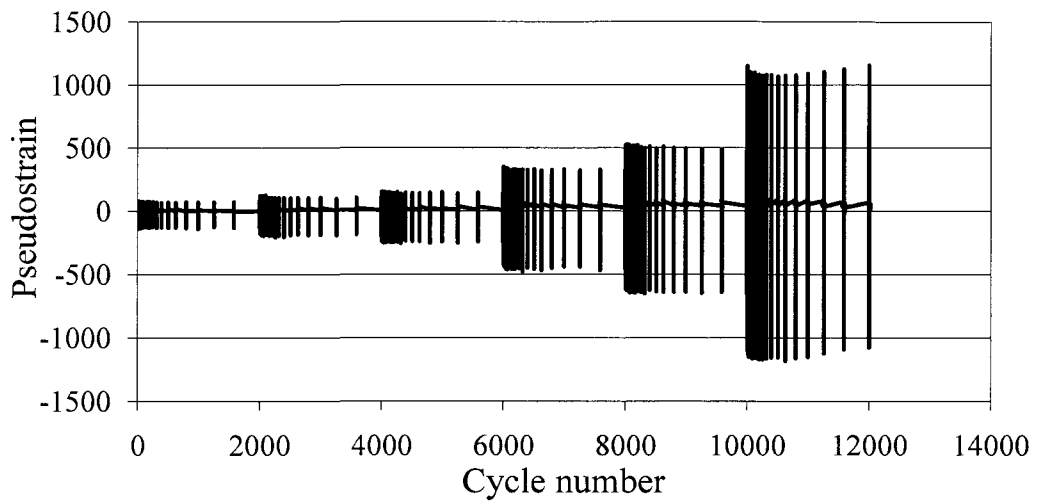
Figure 6-14: Computed pseudostrain as a function of cycle number in an incremental strain amplitude test under flexure mode of loading
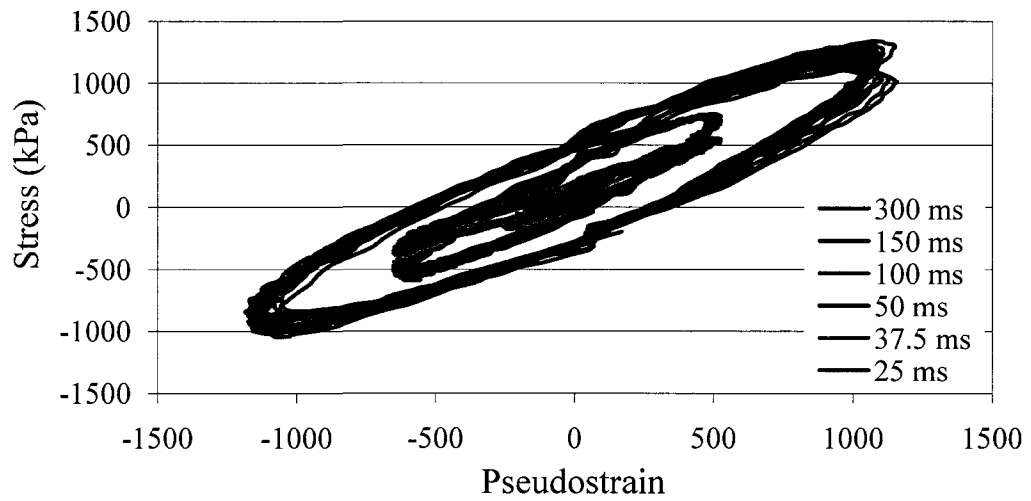
Figure 6-15: Crossplot of stress vs. pseudostrain in an uniaxial incremental strain amplitude test under flexure mode of loading

6.5 Detection of damage development

This section presents different techniques that were evaluated to detect damage in the specimen. The techniques range from visual interpretation technique which is manually intensive to automated techniques that can be implemented in a computer program.

6.5.1 Visual interpretation of stress vs. pseudostrain plots

One of easiest ways to detect damage is to plot stress vs. pseudostrain and visually check for the formation and shifting of any pseudo-hysteresis loop. Typical stress-pseudostrain plots in an incremental strain amplitude test and incremental stress amplitude test are presented in Figures 6-16 and 6-17, respectively. The figures show different stages of damage evolution in the specimen.

Figure 6-16 presents plots of stress-pseudostrain at three strain levels in an incremental strain amplitude test. At the lowest strain level (68 microstrain) the loading path and unloading path data are overlapping, while at the intermediate strain level (163 microstrain) the loop is just visible. At 2259 microstrain (just before failure) the loop is wide open. Thus it can be inferred that the fatigue endurance limit is somewhere between 68 and 163 microstrain. Similarly, the stress vs. pseudostrain plots at three stress amplitude levels are shown in Figure 6-17. The development and shifting of stress vs. pseudostrain loops are seen at the 178 microstrain level (when compared to the lowest stress amplitude level of 61 microstrain). Thus it can be concluded that damage development would start somewhere between 61 and 178 microstrain.
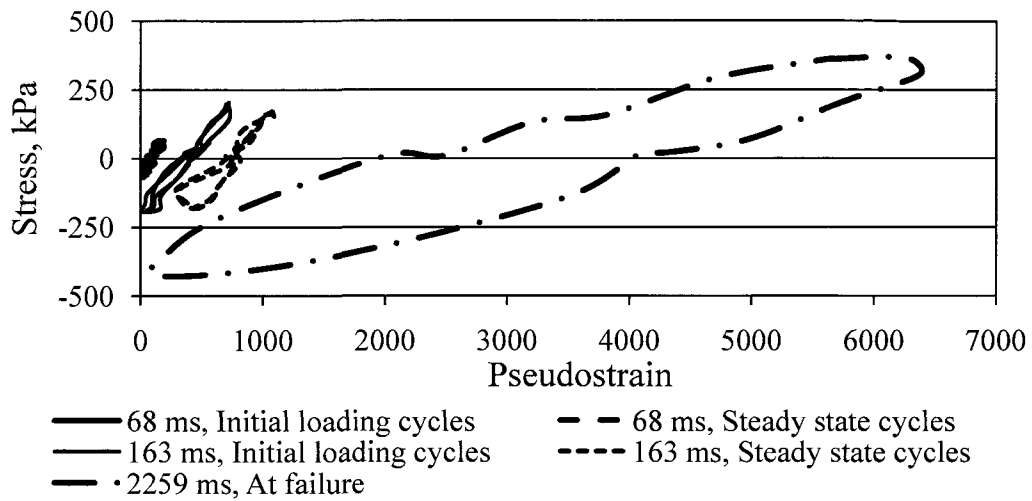
Figure 6-16: Detection of damage in incremental strain amplitude test
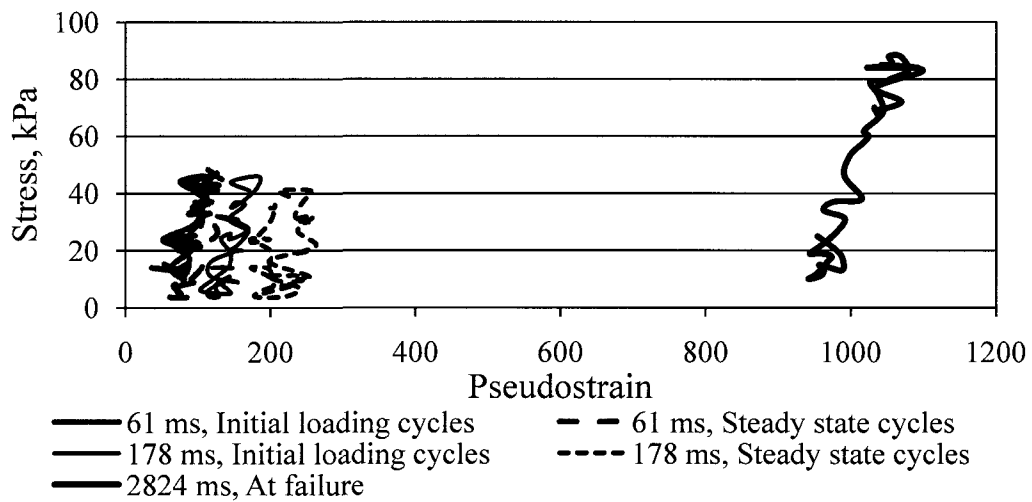
Figure 6-17: Detection of damage in incremental stress amplitude test

Even though visual interpretation is simple, this approach is time consuming. The main drawback is this approach is highly subjective; i.e., if the same plots are given to two designers they can come up with different fatigue endurance limit values. Also it is subjected to bias (from previous experience with similar mixtures). This process gives a

101

range of strain where fatigue endurance limit lies, however more testing has to be done within this range to narrow down and obtain a single value.

6.5.2 Change in dynamic modulus

Using stress and strain histories, the dynamic modulus value can be computed using Equation 4-3. When the applied stress or strain is very small, there will no change in microstructure and hence negligible damage. Thus the dynamic modulus of the material remains the same. Once applied stress or strain is more than a threshold level, damage occurs, leading to deterioration of material integrity. Thus, the dynamic modulus value changes.

Figures 6-18 and 6-19 present changes in dynamic modulus with increase in strain and stress amplitude level under uniaxial testing conditions, respectively. The dynamic modulus decreases over the course of a test and at faster rate at higher stress or strain levels. Any deviation in dynamic modulus value when compared to undamaged dynamic modulus can be interpreted as damage in the specimen.
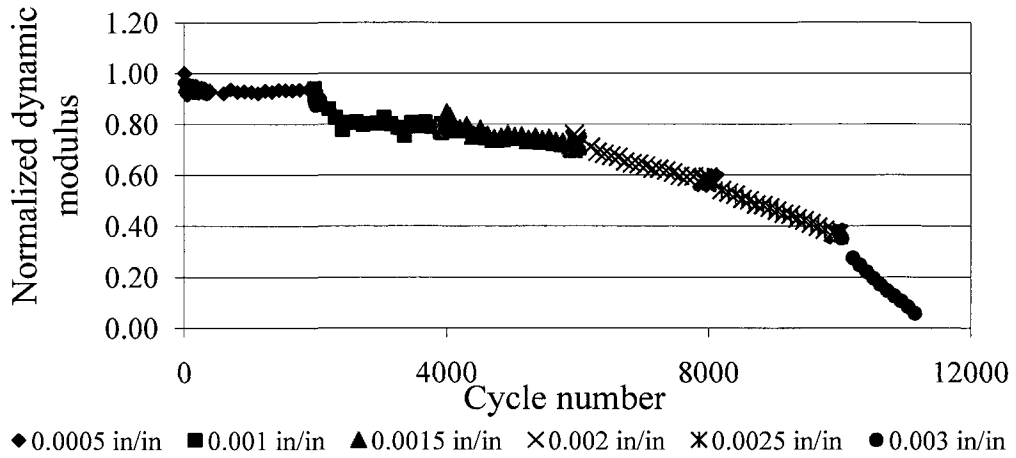
Figure 6-18: Variation of normalized dynamic modulus in uniaxial incremental strain amplitude test
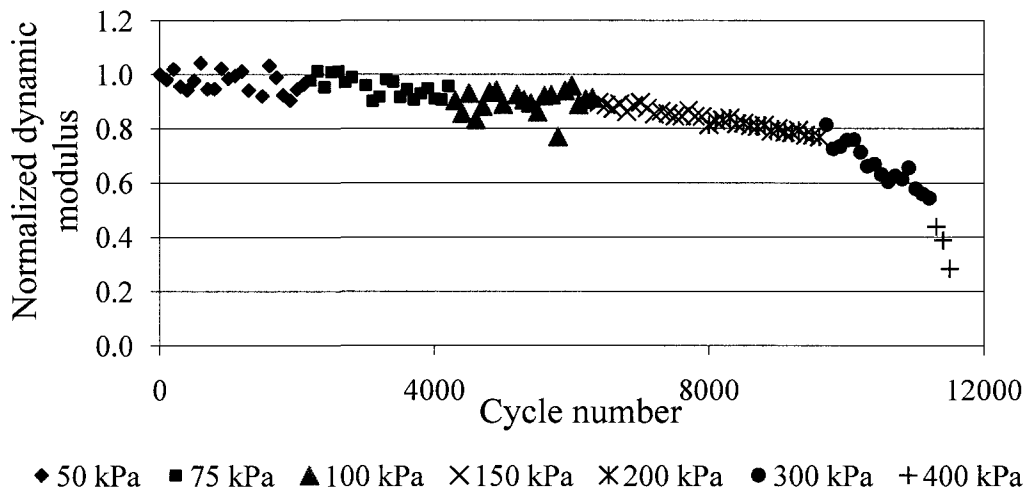
Figure 6-19: Variation of normalized dynamic modulus in uniaxial incremental stress amplitude test

As can be seen in Figures 6-18 and 6-19, the dynamic modulus value started to decrease in second load level. Thus it can be interpreted damage started occurring in specimen somewhere in between 0.0005 and 0.001 in/in and 50 kPa and 75 kPa under strain controlled mode and stress controlled mode, respectively.

By definition, dynamic modulus fails to take permanent deformation into account. That means, one can calculate same dynamic modulus values, even though the sample has undergone substantial permanent deformation. Also dynamic modulus does not account for viscoelastic effects. Hence arriving at conclusions using dynamic modulus might be erroneous.

6.5.3 Change in pseudostiffness

Time and rate dependency of viscoelastic analysis can be removed by using pseudostrain instead of the physical strain. Thus, the computed pseudostiffness (Equation 5-1) removes time dependency in the stiffness parameter calculation. Figures 6-20 and 6-21 present changes in pseudostiffness with increase in strain and stress amplitude level for strain controlled and stress controlled tests, respectively.

◆ 0.0005 in/in   ■ 0.001 in/in   ▲ 0.0015 in/in   ✕ 0.002 in/in   ✳ 0.0025 in/in   ● 0.003 in/in
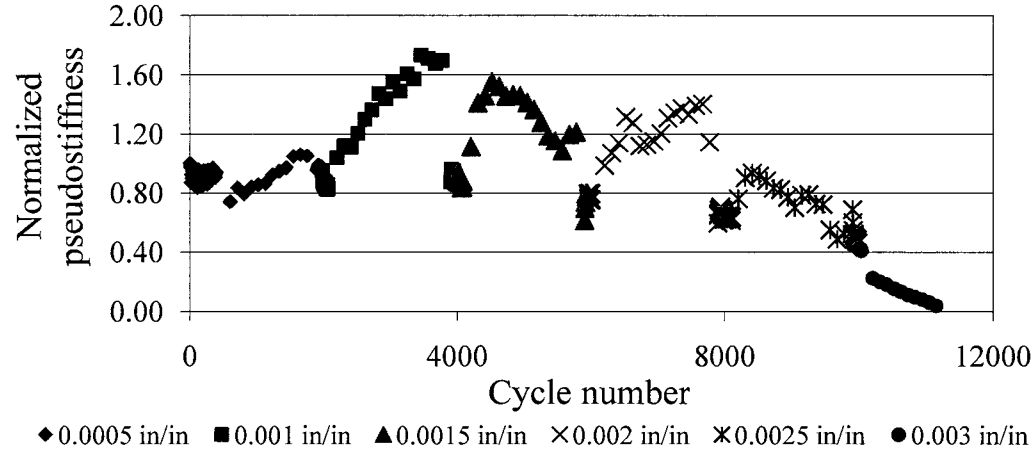
Figure 6-20: Variation of normalized pseudostiffness in uniaxial incremental strain amplitude test
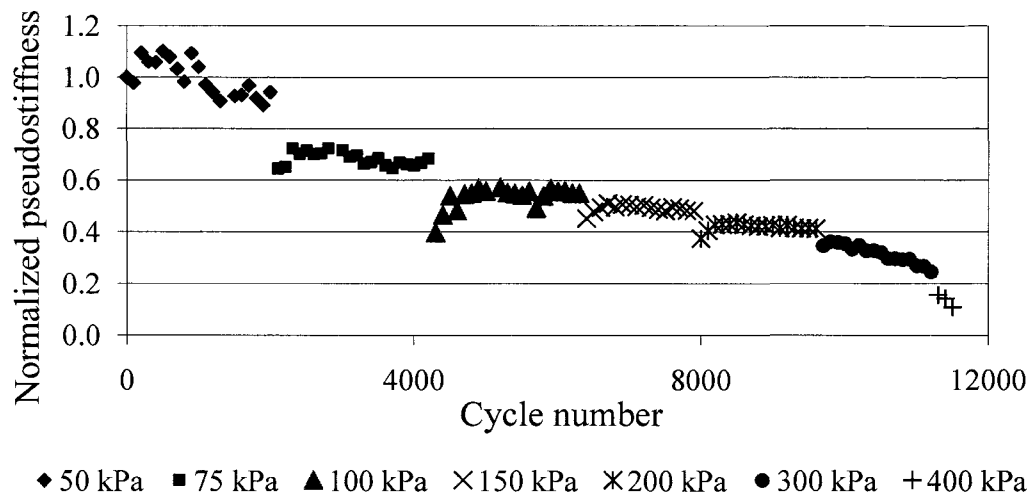
Figure 6-21: Variation of normalized pseudostiffness in uniaxial incremental stress amplitude test

As seen in Figures 6-20 and 6-21, with increase in damage the pseudostiffness deviates from the initial value (at undamaged state). By definition pseudostiffness is stress corresponding to maximum pseudostrain divided by maximum pseudostrain within each cycle. Thus, any error in acquiring this data point or electrical noise can lead to improper conclusions.

While conducting incremental strain amplitude test, strain amplitude was held constant within each loading block. Due to testing difficulties, approximately 2000 cycles of loading were applied within each loading block. Further, due to issues in computer memory and handling the acquired data, only snapshots of measurements were taken and stored. Typically measurements of the first 100 cycles, every 100th cycle there after untill 1800 cycles and the last 100 cycles within each loading block were stored. During analysis of data it was found that LVDT measurements were not smooth between different acquired cycles. Due to presence of these spikes in data, abnormally high values

105

of calculated pseudostrain data were found. Hence an increasing trend in computed pseudostrain is seen between cycle 200 and cycle 1800 within each loading block. These data points can be ignored during analysis.

6.5.4 Change in phase angle between stress and strain

Figures 6-22 and 6-23 present the phase angle evolution in incremental strain and stress amplitude tests, respectively. With an increase in damage, the phase angle is expected to change. From Figures 6-22 and 6-23, it is clear that the incremental strain amplitude test is more sensitive when compared to the incremental stress amplitude test.
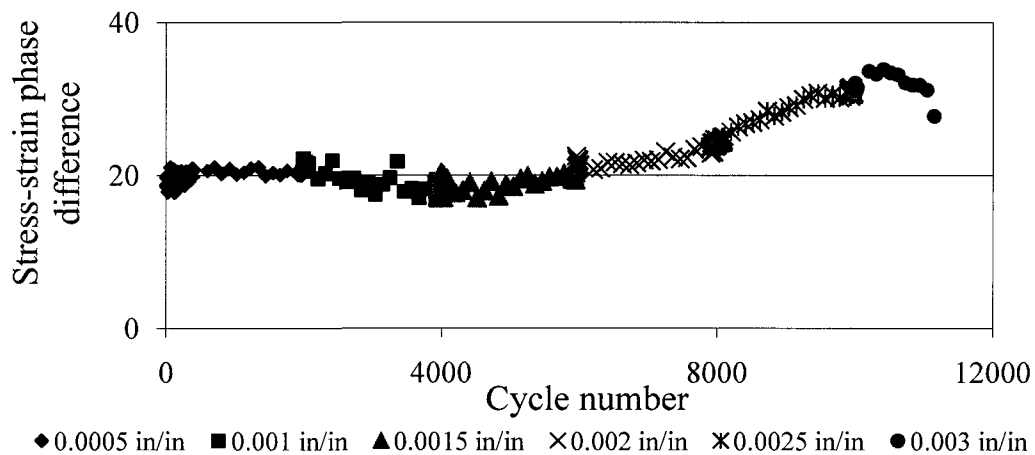
Figure 6-22: Variation of phase angle in uniaxial incremental strain amplitude test
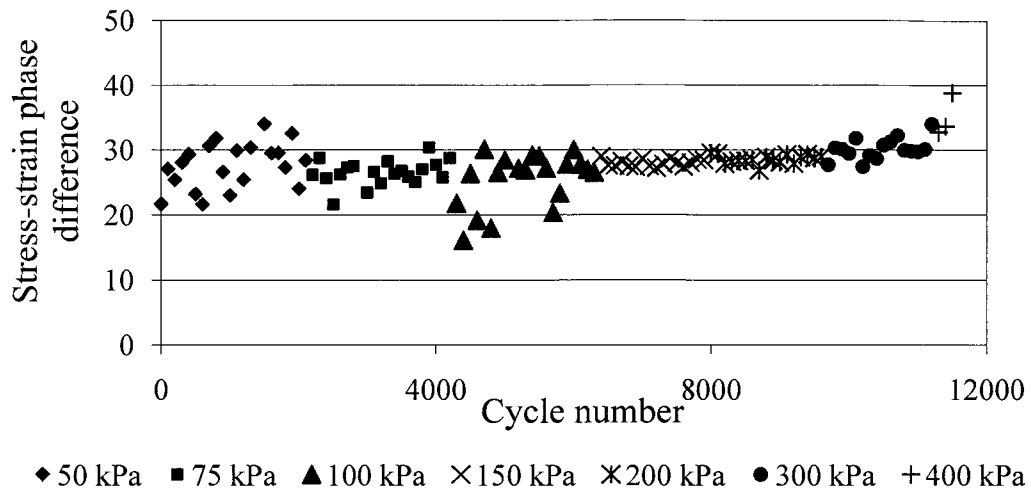
Figure 6-23: Variation of phase angle in uniaxial incremental stress amplitude test

It was found that computation of phase angle is more sensitive to data acquisition rate and quality of data acquired. Also, as seen in Figure 6-23, phase difference might not be sensitive to damage in the specimen.

6.5.5 Change in dissipated energy

Dissipated energy is the amount of energy lost during each loading and unloading cycle. This lost energy can be due to damage and/or viscoelastic hysteresis. The dissipated pseudostrain energy separates energy lost due to damage and viscous effects and dissipated strain energy combines both. In either case, with an increase in stress or strain amplitude, the amount of energy dissipated also increases. The variation of dissipated strain energy and pseudostrain energy in an incremental strain amplitude test are shown in Figures 6-24 and 6-25, respectively. Similar plots for an incremental stress amplitude test are shown in Figures 6-26 and 6-27, respectively.
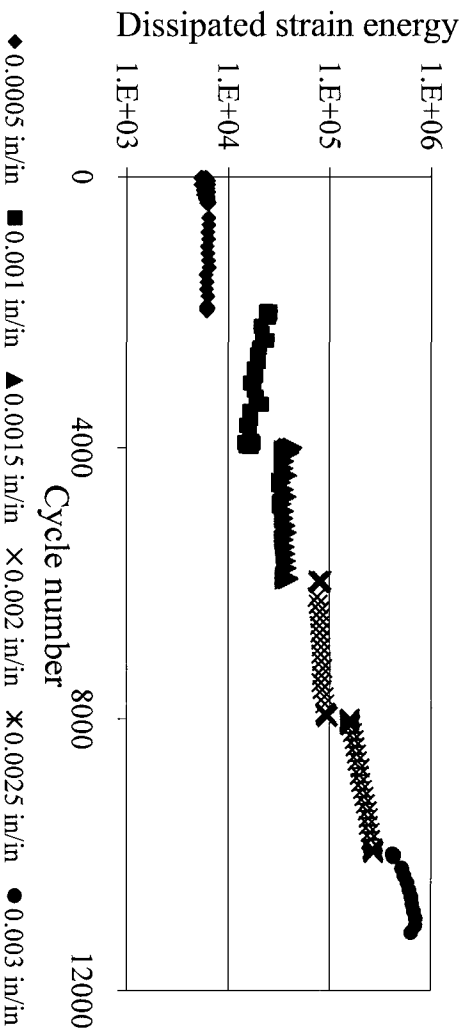
Figure 6-24: Variation of dissipated strain energy in uniaxial incremental strain amplitude test
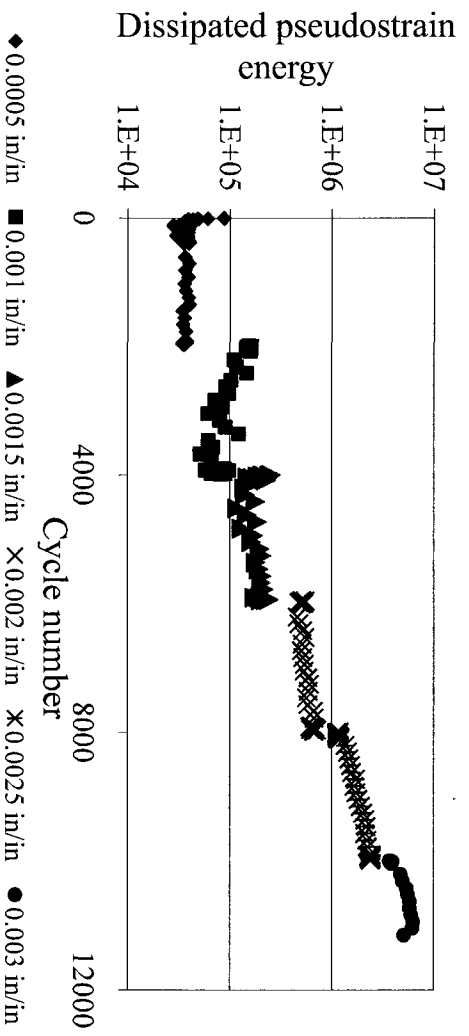
Figure 6-25: Variation of dissipated pseudostrain energy in uniaxial incremental strain amplitude test

108
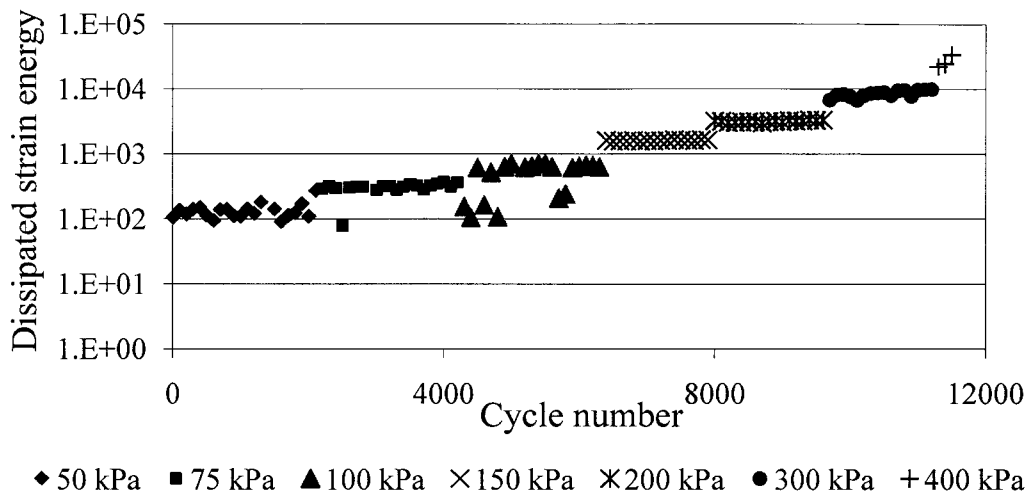
Figure 6-26: Variation of dissipated strain energy in uniaxial incremental stress amplitude test
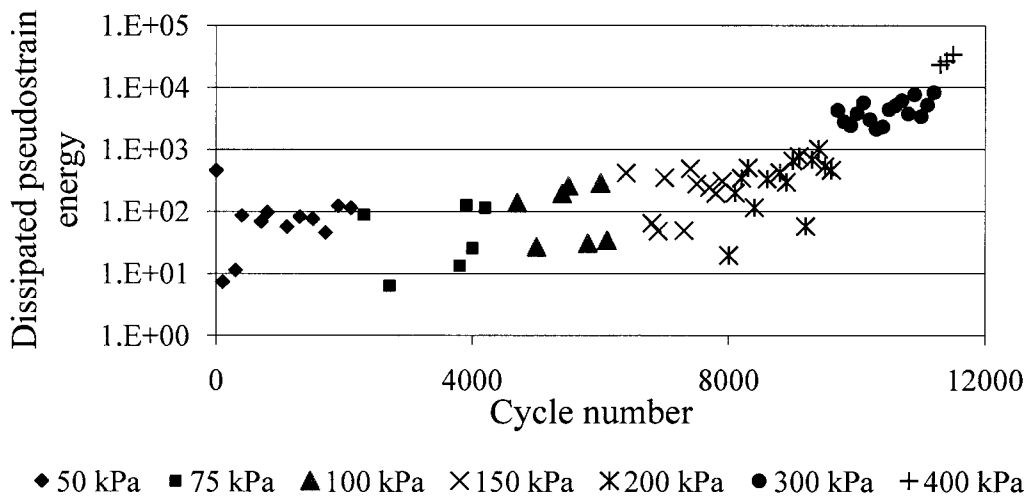
Figure 6-27: Variation of dissipated pseudostrain energy in uniaxial incremental stress amplitude test

In a controlled strain amplitude test, decrease in stress amplitude leads to a decrease in the area of the hysteresis loop and an increase in phase angle increases the area of the

109

hysteresis loop. Thus, the theoretically computed dissipated energy can either increase or decrease depending on the increase or decrease in the sine of phase angle relative to the decrease in stress amplitude. However in controlled stress amplitude test, the strain amplitude and phase angle always increases the area of hysteresis loop. Thus, the computed dissipated energy always increases in controlled stress amplitude test.

6.5.6 Change in properties of fitted straight line for stress-pseudostrain loop

In the case of a strain controlled test, the stress amplitude decreases with an increase in damage. The same can be seen in Figure 6-11. Hence, the maximum pseudostiffness value decreases. If a straight line is fit to the stress-pseudostrain loop, the slope of the straight line decreases. In the case of a stress controlled test, the stain in the specimen continuously increases until complete fracture. If a straight line is fit to stress-pseudostrain loop, the intercept of straight line decreases. A schematic diagram indicating the slope and intercept is shown in Figure 6-28. The slope and intercept of this straight line fit were sensitive in incremental strain amplitude test and incremental stress amplitude test, respectively. Hence the changes in straight line fit to the stress-pseudostrain loop were used as an indicator of damage in specimen.

To obtain the regression coefficients for straight line fit, the two step procedure described below was adopted. In the first step, pesudostrian (dependent variable) was regressed against measured stress, assuming pesudostrian as the dependent variable and measured stress as the independent variable. Thus regression coefficients (m, C) are obtained and the corresponding form of straight line fit is given in Equation 6-1. In the second step, the straight line fit obtained previously is inverted to obtain slope (S) and

intercept (*I*) of the stress vs. pseudostrain plot. Variation of slope and intercept in an incremental stress amplitude test and an incremental stress amplitude test are shown in Figures 6-29 and 6-30, respectively.

$$\varepsilon^R = (m \times \sigma_{meas}) + C \qquad \text{6-1}$$

$$S = \frac{1}{m} \qquad \text{6-2}$$

$$I = -\frac{C}{m} \qquad \text{6-3}$$

where ε^R = computed pseudostrain;

σ_{meas} = measured stress;

m = slope of straight line fit assuming measured stress as independent variable and pseudostress as dependent variable;

C = intercept of straight line fit assuming measured stress as independent variable and pseudostress as dependent variable;

S = slope of straight line fit assuming measured stress as dependent variable and pseudostress as independent variable; and

I = intercept of straight line fit assuming measured stress as dependent variable and pseudostress as independent variable.
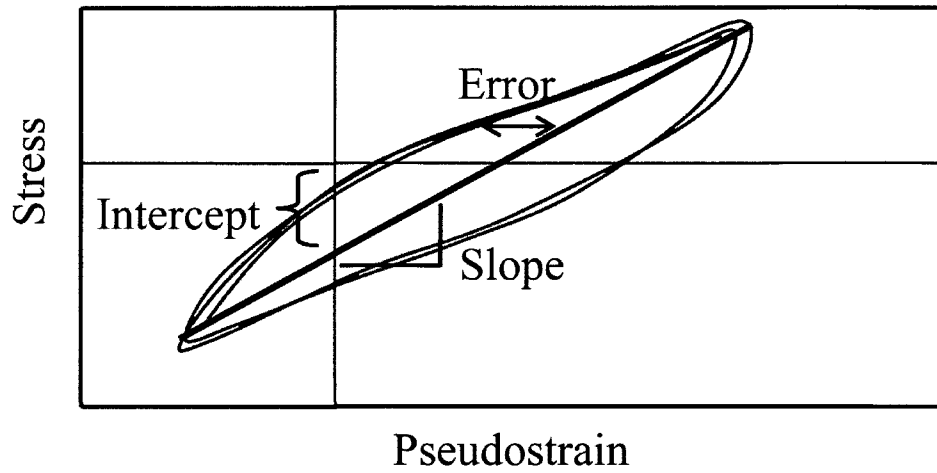
Figure 6-28: Slope and intercept in straight line fit to stress-pseudostrain loop

◆ 0.0005 in/in   ■ 0.001 in/in   ▲ 0.0015 in/in   ✕ 0.002 in/in   ✳ 0.0025 in/in   ● 0.003 in/in
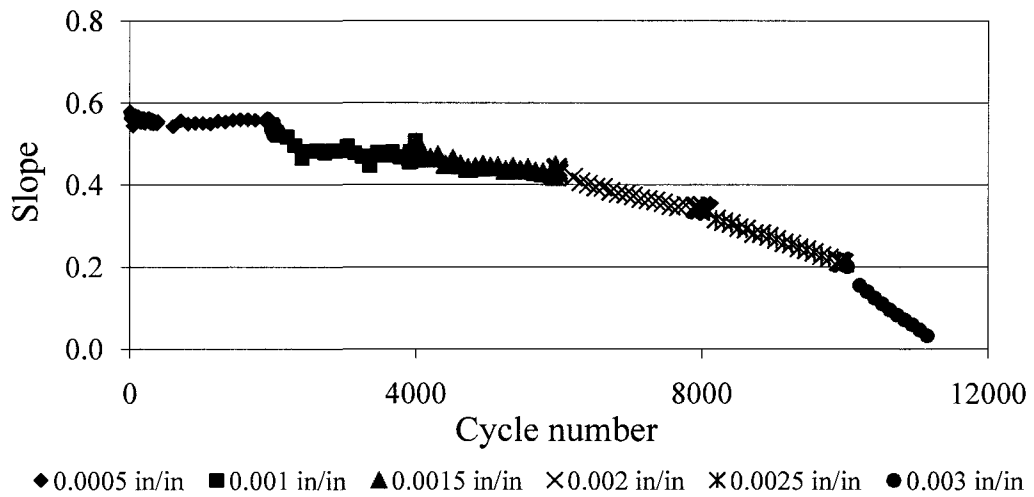
Figure 6-29: Variation of slope in incremental strain amplitude test
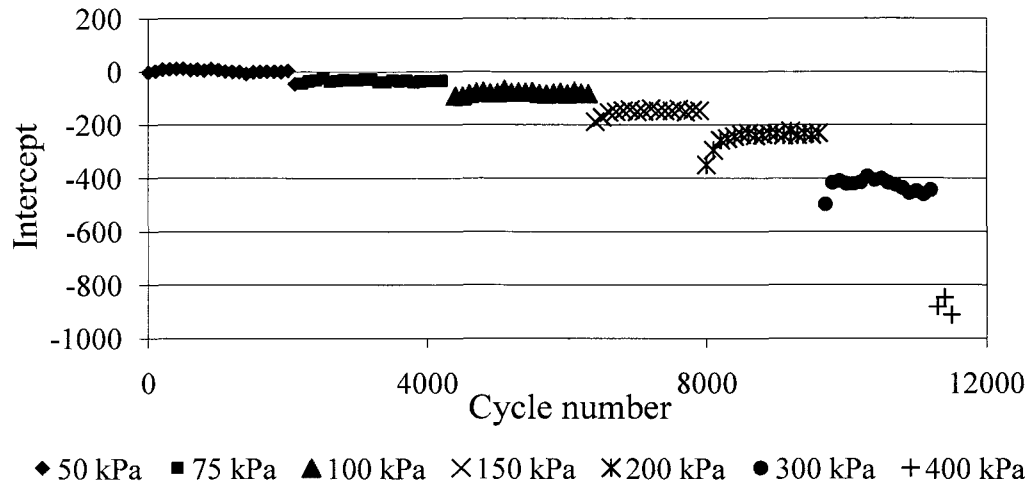
Figure 6-30: Variation of intercept in incremental stress amplitude test

6.6 Proposed test procedure

This section discusses the proposed test procedure for determining the endurance limit of asphalt mixtures based upon the methodology discussed in previous sections. Incremental amplitude tests can only give a range of values within which the endurance limit value lies. Thus the proposed procedure consists of conducting incremental amplitude tests at multiple stages so that the endurance limit value obtained converges to a particular value. The number of stages of testing depends on repeatability of tests, accuracy of endurance limit and sensitivity of mixture to fatigue damage. Flowcharts for the proposed testing procedure and associated analysis are shown in Figures 6-31 and 6-32, respectively.

The proposed test procedure begins with the characterization of the linear viscoelastic properties of the desired mixture using a few specimens (around three in number). Dynamic modulus and phase angle measurements are obtained at multiple temperatures

113

and frequencies. These individual temperatures and frequencies are chosen such that it covers the complete range of behavior of asphalt concrete. In the next stage, incremental amplitude tests are conducted on these specimens. The testing amplitude within each loading block is chosen such that it covers complete range of expected endurance limit values. Then data generated is post processed using analysis procedure presented in Figure 6-32. Thus, a range of values within which the endurance limit lies is obtained. In the next stage, a few more specimens (around three in number) are tested for linear viscoelastic properties and incremental amplitude tests are conducted. The testing amplitude within each loading block is chosen based on the range of endurance limit obtained previously. In other words, more tests are conducted with testing amplitude that was determined previously. Further the data collected is post processed using proposed analysis procedure. Thus the endurance limit value obtained in second stage is well within the range obtained previously. The same procedure is repeated until an endurance limit value with sufficient accuracy is obtained.

```
┌─────────────────────────────────────────────┐
│           Specimen Fabrication                │
│                                               │
│  Mix, compact, trim and instrument the specimen │
└─────────────────────────────────────────────┘
                      │
                      ▼
┌─────────────────────────────────────────────┐
│        LVE Property Characterization          │
│                                               │
│     Perform complex modulus tests at multiple │
│        frequencies and temperature            │
└─────────────────────────────────────────────┘
                      │
                      ▼
                  ◇ First set of ◇
                  ◇ specimen ?   ◇
          Yes                        No
```

Increasing Amplitude Test	Increasing Amplitude Test
Conduct increasing amplitude test	Conduct increasing amplitude test
1) Starting from an amplitude well within LVE limit,	1) Starting from a lower limit of endurance limit determined previously,
2) Amplitude increment between loading blocks approximately 100 µs (corresponding stress)	2) Amplitude increment between loading blocks approximately $1/5^{th}$ of amplitude range determined previously

Figure 6-31: Flowchart for proposed test procedure

```
┌─────────────────────────────────────────────────────┐
│           LVE Property Characterization             │
│                                                     │
│  Calculate dynamic modulus and phase angle          │
│   at different temperatures and frequencies         │
└─────────────────────────────────────────────────────┘
                          ↓
┌─────────────────────────────────────────────────────────────┐
│                 Master Curve Generation                     │
│                                                             │
│ Plot isothermal curves, shift isothermal curves to reference temparature │
│  and generate mastercurve for both dynamic modulus and phase angle │
└─────────────────────────────────────────────────────────────┘
                          ↓
┌─────────────────────────────────────────────────────┐
│             Relaxation Modulus Prediction           │
│                                                     │
│  Using generated dynamic modulus and phase angle    │
│ master curves, predict relaxation modulus for mixture │
└─────────────────────────────────────────────────────┘
                          ↓
┌─────────────────────────────────────────────────────────────────┐
│                  Pseudostrain Calculation                       │
│                                                                 │
│ Using measured strain history from incremental amplitude test and predicted │
│   relaxation modulus, calculate pseudostrains for entire loading history │
└─────────────────────────────────────────────────────────────────┘
                          ↓
┌─────────────────────────────────────────────────────┐
│            Damage Indicator Calculation             │
│                                                     │
│  Calculate damage indicators, plot related graphs   │
│     to detect damage and arrive at conclusion       │
└─────────────────────────────────────────────────────┘
```
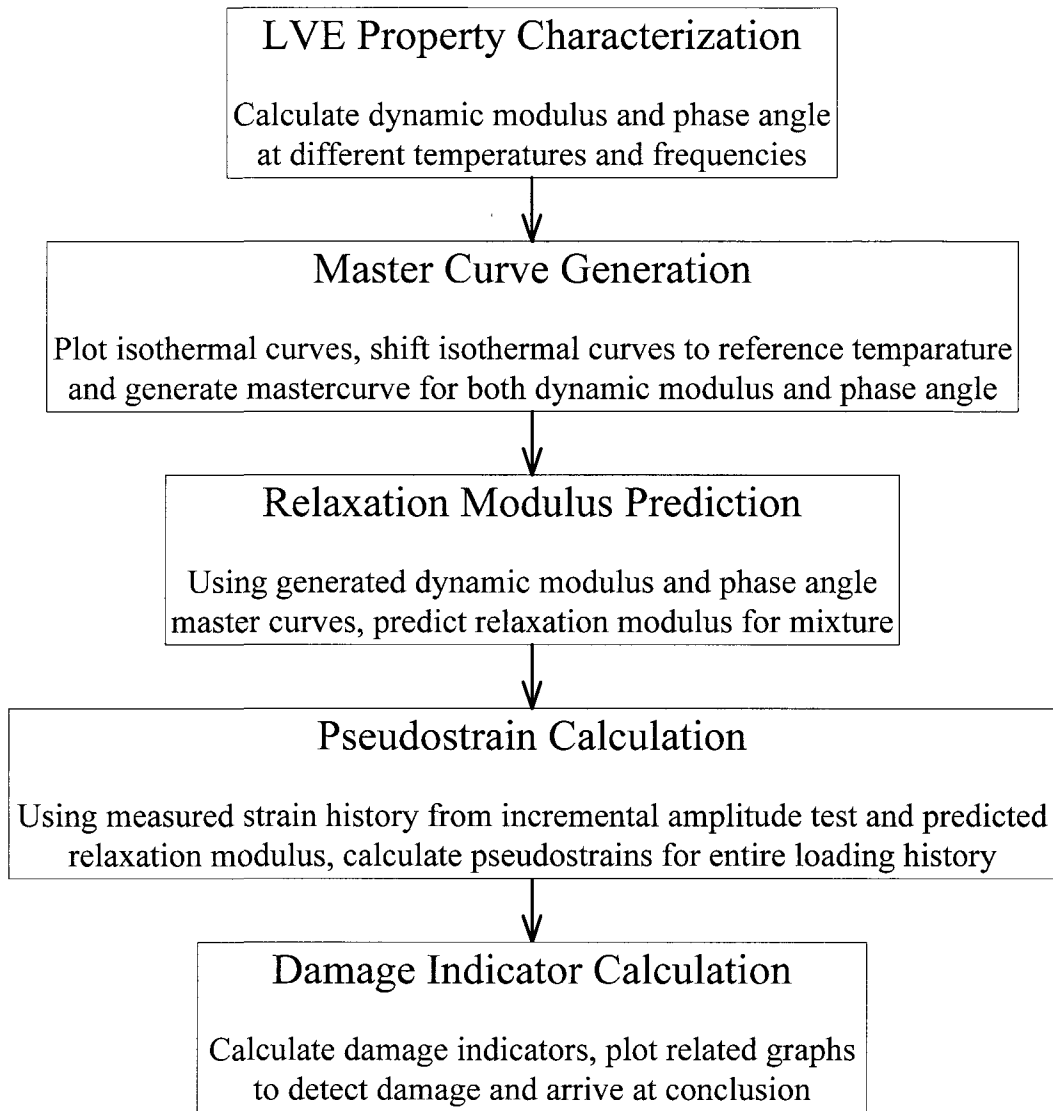
Figure 6-32: Flowchart for proposed test procedure analysis

6.7 <u>Summary</u>

This chapter presented a new approach to determine the fatigue endurance limit in asphalt concrete using continuum damage principles. Also, various approaches to detect damage were presented. It is easier to detect loop formation visually using incremental strain amplitude test when compared to incremental strain amplitude test. However noise level in the incremental strain amplitude test is more when compared to the incremental stress amplitude test. Also, time required to conduct the incremental stress amplitude test is substantially less than that required to conduct the incremental strain amplitude test.

Evaluating elastic parameters (dynamic modulus, dissipated strain energy) is faster when compared to viscoelastic analysis (pseudostiffness, dissipated pseudostrain energy). However, elastic parameters do not account for viscoelastic effects in asphalt concrete.

Indicators like dynamic modulus, pseudostiffness and phase difference are point based evaluation schemes which require computation at one point in stress vs. strain or stress vs. pseudostrain loops. Any noise or error in acquiring and evaluating the numerical values at these places can have a significant effect on the overall evaluation procedure. However dissipated energy, dissipated pseudostrain energy and regression coefficients of fitted straight line account for all points in each stress-pseudostrain loop. Thus the effect of any outlier on overall evaluation scheme will be negligible. It is recommended to conduct increasing amplitude tests and use loop based evaluation schemes for evaluating the damage in the specimen.

CHAPTER 7

EFFECT OF MODE OF LOADING ON VISCOELASTIC AND

CONTINUUM DAMAGE PARAMETERS

Three mixtures (M1, E1 and S1) were tested under uniaxial mode and flexure mode of loading for linear viscoelastic properties and damage characterization. Mix M0 was tested under uniaxial and biaxial loading conditions for linear viscoelastic properties. This chapter discusses the effect of mode of loading on different viscoelastic and continuum damage parameters.

7.1 Effect on dynamic modulus

Several specimens with similar volumetrics were used to conduct complex modulus tests. The dynamic modulus and phase angle values at each frequency and temperature were calculated from measured stresses and strains. The individual isotherm curves were then shifted horizontally along the frequency axis to form a master curve for each specimen. The reduced frequency, temperature shift factors, and dynamic modulus values were combined to obtain mix average mastercurves. In this research, a reference temperature of 20^0C was used unless otherwise specified. Discussion and comparison of dynamic modulus mastercurves are presented below.

7.1.1 Comparison between uniaxial and flexural mode of loading

The dynamic modulus values for M1, E1 and S1 mixtures under uniaxial loading

and flexural loading are presented in Figures 7-1, 7-2, and 7-3, respectively.
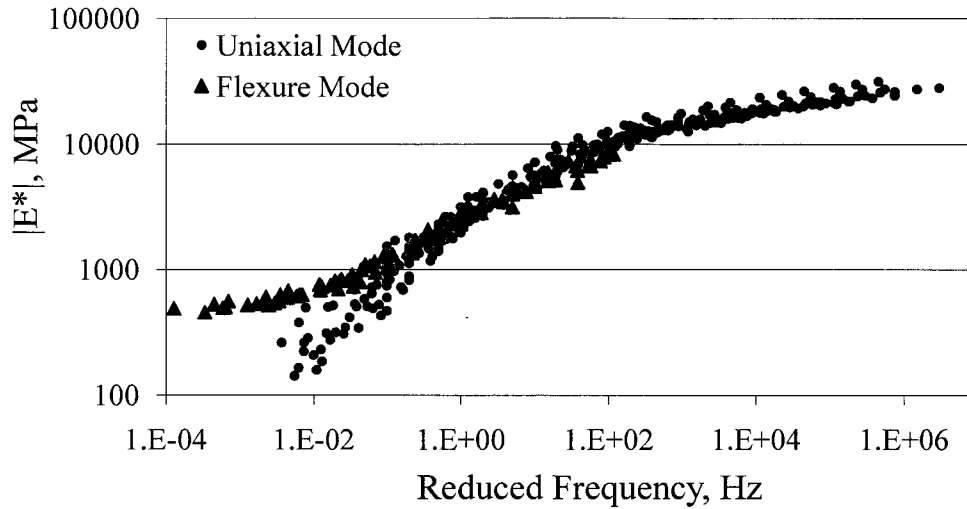

Figure 7-1: Comparison of dynamic modulus values under uniaxial mode and flexural mode of loading for M1 mix
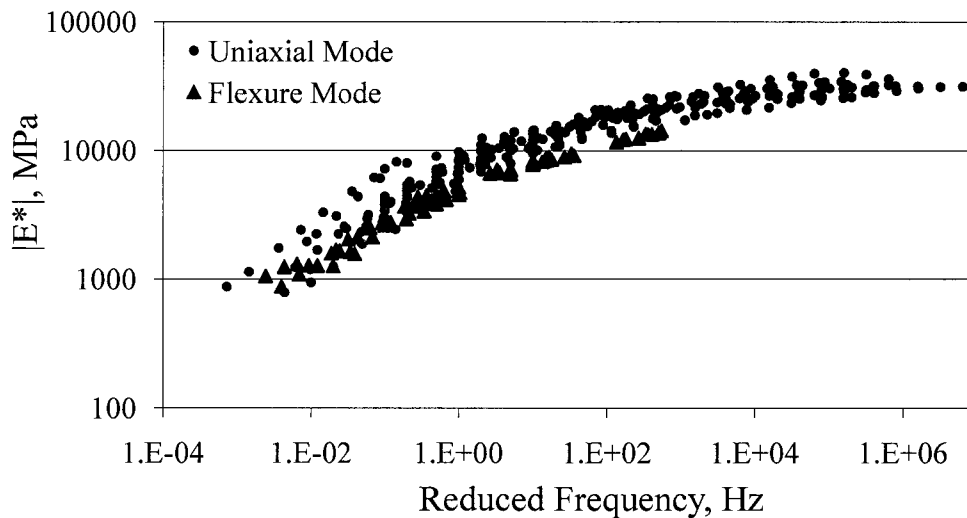

Figure 7-2: Comparison of dynamic modulus values under uniaxial mode and flexural mode of loading for E1 mix
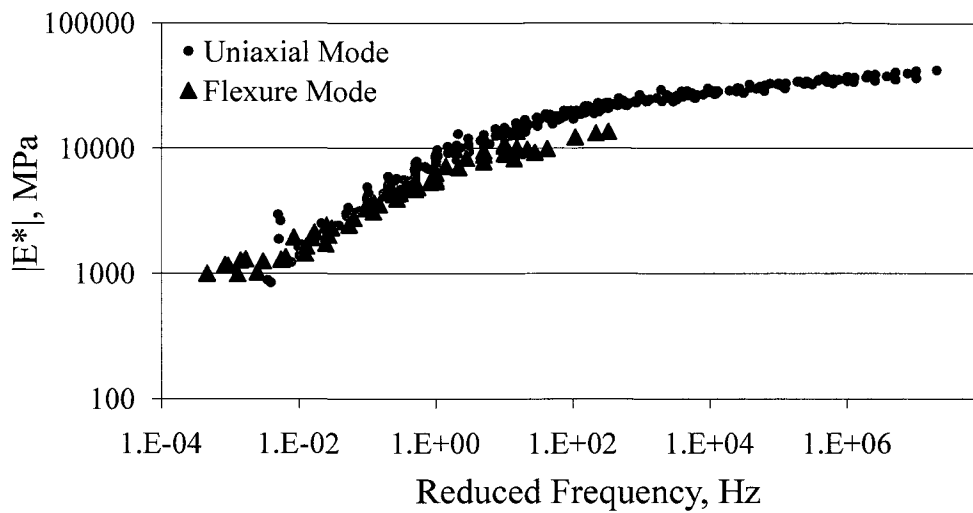
Figure 7-3: Comparison of dynamic modulus values under uniaxial mode and flexural mode of loading for S1 mix

Visual inspection of these plots indicates that the dynamic modulus values are different under uniaxial and flexural mode of loading. The mean, maximum, minimum and standard deviation of dynamic modulus values at 10 Hz under uniaxial and flexural mode of loading were computed at the common test temperatures i.e. 10^0C, 20^0C and 30^0C. A summary of these calculated values for mixture M1 is given in Table 7-1 and is graphically shown in 7-4.

Table 7-1: Summary of dynamic modulus values for M1 mix

Testing Mode/Temperature	Average (MPa)	Maximum (MPa)	Minimum (MPa)	Standard Deviation (MPa)
Uniaxial, 10^0C	11490	15032	9434	1954
Flexure, 10^0C	6919	7464	6163	604
Uniaxial, 20^0C	5686	8989	4769	1268
Flexure, 20^0C	4978	5551	4582	414
Uniaxial, 30^0C	2228	3176	1768	460
Flexure, 30^0C	1561	1763	1068	330

120

From Figures 7-1 through 7-4, it is clear that the difference between flexural dynamic modulus and uniaxial dynamic modulus values increases as the reduced frequency increases and testing temperature decreases. As seen in Figure 7-4, uniaxial dynamic modulus is higher than flexural dynamic modulus at all given temperatures. Statistical analysis using two tailed t-test was performed on the dynamic modulus data over a range of reduced frequencies to determine if there is significant difference between the uniaxial and flexural loading modes. Details about t-test and obtaining the moduli from regression coefficients are explained in the following paragraphs.
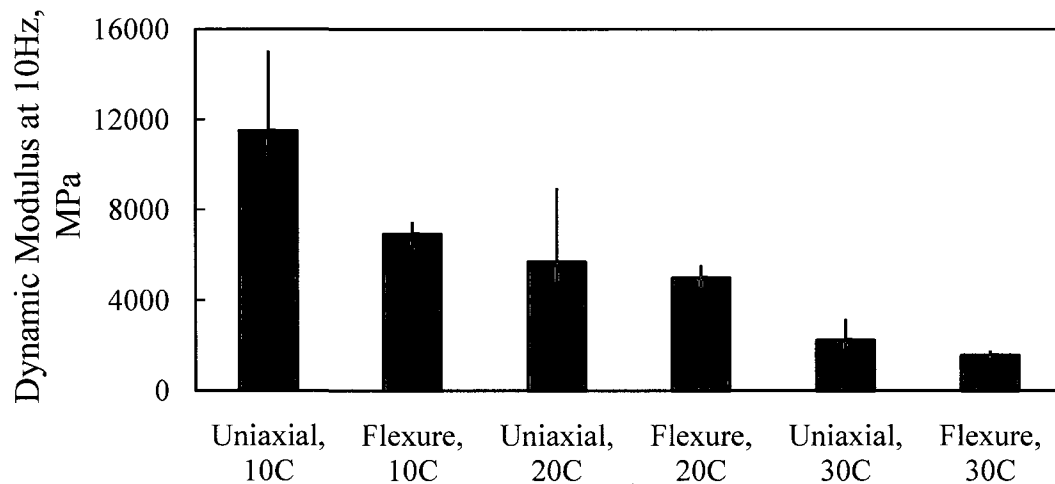

Figure 7-4: Comparison of dynamic modulus values at different temperatures and loading modes

Using the sigmoidal function regression coefficients for the master curves of individual samples, dynamic values at evenly spaced reduced frequency intervals were calculated. This range of reduced frequency values was chosen based on a common region of reduced frequencies between uniaxial and flexure mode. The common reduced frequencies were between 0.001 Hz and 1000 Hz. This exercise was repeated on all samples and both modes of loading to obtain a master data set. The two tailed t-

test was performed on the dynamic modulus data at these common frequencies to check if there is significant difference between the loading modes. A p-value below 0.05 indicates a significant difference at that particular frequency. If the majority of t-test values at these intervals were significantly different, then the dynamic modulus mastercurve under uniaxial mode was considered significantly different than dynamic modulus mastercurve under flexural mode.

The p-values obtained while comparing dynamic modulus obtained under uniaxial mode with flexural mode are presented in Table 7-2. The statistically significant values have been shaded for convenience. As seen in Table 7-2 significant differences exist at higher reduced frequencies for E1 and S1 mixtures (>0.1 Hz). However for mix M1, statistically significant differences were observed throughout common frequency range except at 1 Hz and 10 Hz.

Table 7-2: t-test results from comparison of dynamic modulus under uniaxial mode with flexural mode

Reduced Frequency, Hz	p-value		
	M1 Mix	E1 Mix	S1 Mix
0.001	<0.0001	0.1573	0.5928
0.01	<0.0001	0.473	0.5978
0.1	0.0186	0.0901	0.0216
1	0.8485	0.0248	0.0091
10	0.1978	0.0071	0.0051
100	0.0038	0.0018	0.0111
1000	0.0001	0.0005	0.0257

It is clear that there is significant difference between dynamic modulus mastercurve obtained under uniaxial and flexural mode of loading. The Percentage Difference (PD) between uniaxial dynamic modulus and flexural dynamic modulus ($|E^*| PD$) (Equation 7-1) was computed at regular intervals of reduced frequencies to check if there exists

any systematic variation between these mastercurves. Similarly, the ratio between flexural dynamic modulus and uniaxial dynamic modulus was also computed (Equation 7-2). Here after this ratio will be referred to as Dynamic Modulus Ratio (DMR).

$$|E^*| \, PD_{1D,flex} = \frac{100 \times \left(|E^*|_{flex} - |E^*|_{1D}\right)}{|E^*|_{flex}}$$ 7-1

$$DMR_{1D,flex} = \frac{|E^*|_{flex}}{|E^*|_{1D}}$$ 7-2

where $|E^*|_{flex}$ = flexural dynamic modulus;

$|E^*|_{1D}$ = uniaxial dynamic modulus;

$|E^*| \, PD_{1D,flex}$ = percentage difference between uniaxial and flexural dynamic modulus; and

$DMR_{1D,flex}$ = dynamic modulus ratio computed using uniaxial and flexural dynamic modulus.

The percentage difference and dynamic modulus ratios computed over range of reduced frequencies using dynamic modulus data for all three mixtures (M1, E1 and S1) are presented in Table 7-3, Figures 7-5 and 7-6, respectively.

Table 7-3: Dynamic modulus ratio and |E*| percentage difference computed for M1, E1 and S1 mixtures

Reduced Frequency, Hz	Dynamic Modulus Ratio			|E*| Percentage Difference		
	M1 Mix	E1 Mix	S1 Mix	M1 Mix	E1 Mix	S1 Mix
0.001	5.70	1.49	1.18	82.4	32.6	15.4
0.01	2.57	0.83	0.93	61.0	-21.1	-7.7
0.1	1.34	0.67	0.82	25.4	-48.3	-21.5
1	1.02	0.67	0.79	1.8	-50.2	-27.2
10	0.90	0.68	0.75	-10.6	-46.2	-34.0
100	0.76	0.68	0.71	-31.4	-46.2	-41.0
1000	0.63	0.66	0.68	-58.2	-50.9	-46.1

Comparison of the dynamic modulus ratio under flexural and uniaxial mode of loading indicates that these values are mixture dependent and are a function of testing frequency. At a given value of reduced frequency, the percentage difference and the dynamic modulus ratio are different for all three mixes. Thus it can be concluded that dynamic modulus ratios are mixture dependent. Also, the differences between the mean values under uniaxial and flexural mode of loading were statistically different at the higher frequency range for mixtures E1 and S1. From Figure 7-6 and Table 7-3, it can be concluded that the modular ratio is approaching an asymptotic value at around 1,000,000 Hz.
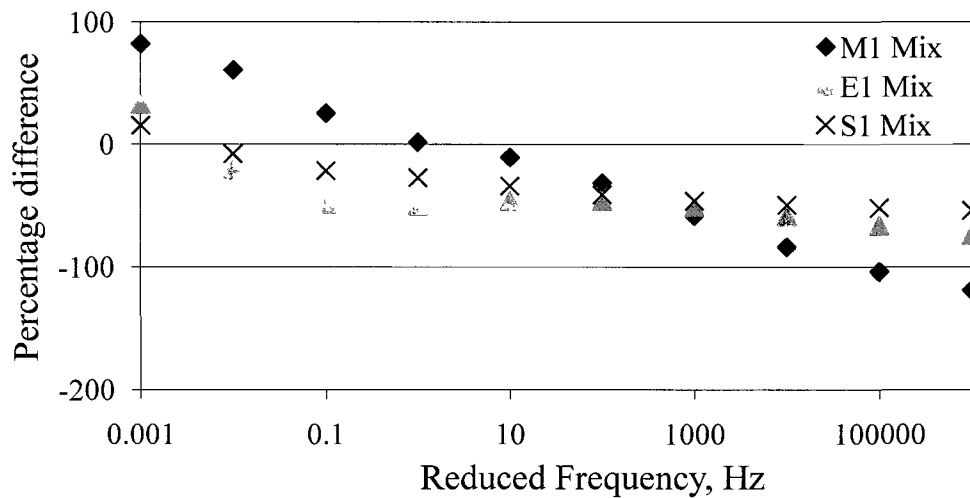

Figure 7-5: Percentage difference between uniaxial dynamic modulus and flexural dynamic modulus as a function of frequency for M1, E1 and S1 mixtures
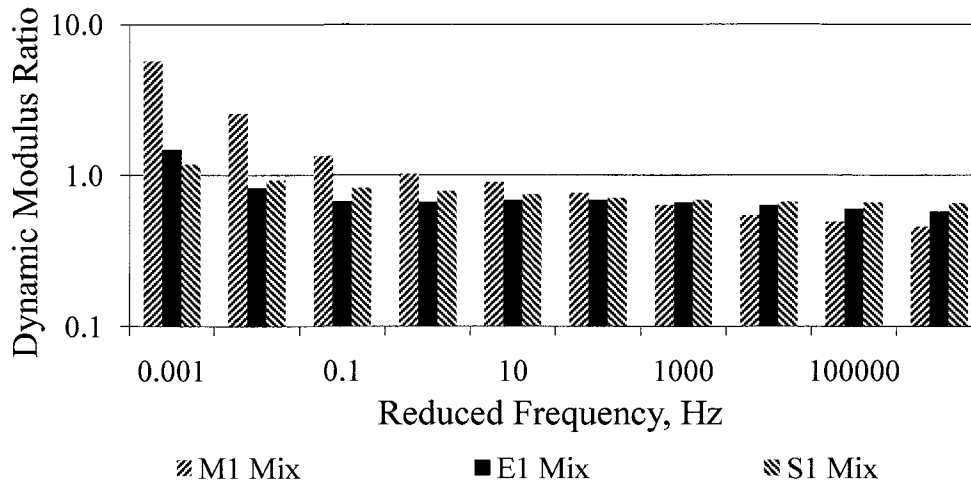
Figure 7-6: Dynamic modulus ratio as a function of frequency for M1, E1 and S1 mixtures

7.1.2 Comparison between uniaxial and biaxial mode of loading

The dynamic modulus values under uniaxial and biaxial mode of loading for mix M0 are shown in Figure 7-7. To check whether there exists any statistically significant difference between uniaxial and biaxial mode of loading, t-test was conducted. Also, the percentage difference (Equation 7-3) and dynamic modulus ratio (Equation 7-4) were computed at regular intervals of frequency. These results are presented in Table 7-4. The dynamic modulus ratio and percentage difference between biaxial dynamic modulus and uniaxial dynamic modulus are graphically presented in Figure 7-8.

$$|E^*| \, PD_{\ 1D,2D} = \frac{100 \times (|E^*|_{2D} - |E^*|_{1D})}{|E^*|_{2D}} \qquad 7\text{-}3$$

$$DMR_{1D,2D} = \frac{|E^*|_{2D}}{|E^*|_{1D}} \qquad 7\text{-}4$$

where $|E^*|_{2D}$ = biaxial dynamic modulus;

$|E^*|_{1D}$ = uniaxial dynamic modulus;

$|E^*| \, PD_{1D,2D}$ = percentage difference between uniaxial and biaxial dynamic

modulus; and

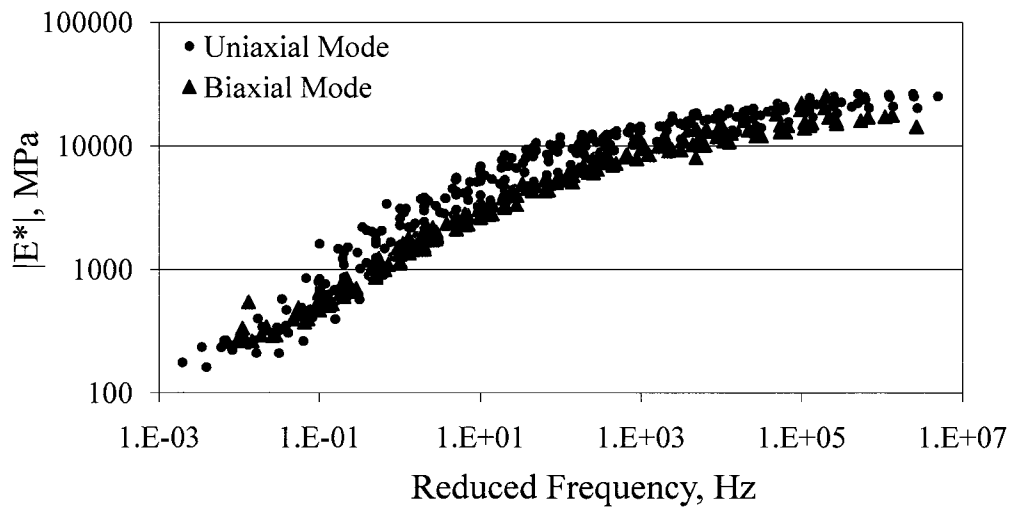$DMR_{1D,2D}$ = dynamic modulus ratio computed using uniaxial and biaxial

dynamic modulus.

Figure 7-7: Comparison of dynamic modulus values under uniaxial and biaxial mode of loading for M0 mix

Statistically significant differences between mean values of uniaxial dynamic modulus and biaxial dynamic modulus were found at frequencies higher than 10 Hz. The ratio between biaxial dynamic modulus and uniaxial dynamic modulus was approximately unity (minimum 0.77, maximum 1.06). Hence it can be concluded that uniaxial dynamic modulus and biaxial dynamic modulus are comparable in magnitude.

Table 7-4: Summary of results obtained while comparing uniaxial and biaxial dynamic modulus

Reduced Frequency, Hz	p-value	Dynamic Modulus Ratio	Percentage Difference
0.01	0.7709	1.06	5.2
0.1	0.4440	0.85	-18.1
1	0.0986	0.70	-42.6
10	0.2230	0.64	-56.9
100	0.0063	0.64	-56.0
1000	0.0016	0.68	-47.4
10000	0.0013	0.72	-39.0
100000	0.0082	0.75	-33.0
1000000	0.0240	0.77	-29.4
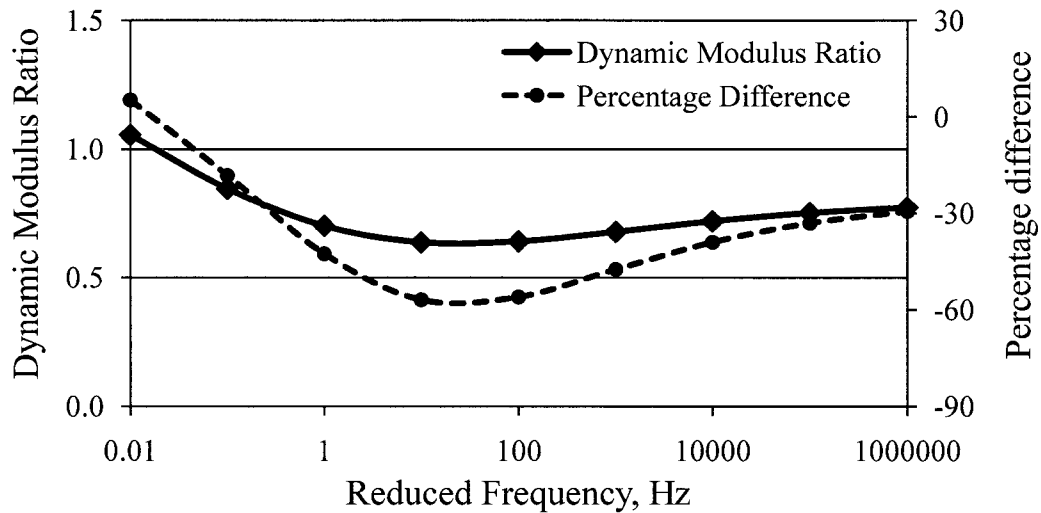
Figure 7-8: DMR and percentage difference as a function of frequency for M0 mix

7.2 Effect on temperature shift factors

Since asphalt is a thermorheologically simple material, the dynamic modulus isotherms at different temperatures can be shifted horizontally relative to a reference temperature to obtain a smooth curve. Any horizontal shift in isotherm can be quantified using a time-temperature shift factor, $log(a_t)$. The same shift factors can be used in

shifting isotherms of other viscoelastic parameters. Also, these temperature shift factors can be used to shift mastercurves at any desired temperature. This section compares the temperature shift factors obtained under different modes of loading.

The average temperature shift factors, $log(a_t)$ computed while shifting dynamic modulus mastercurves of all four mixtures under different modes of loading are presented in Table 7-5. A straight line was fit for $log(a_t)$ vs. test temperature for all four mixtures. The regression coefficients for the straight line are also presented in Table 7-5. A t-test was conducted to check whether the temperature shift factors obtained under different modes of loading are comparable or not. The t-test results are presented in Table 7-6.

Table 7-5: Temperature shift factors obtained during construction of dynamic modulus mastercurve

Mixture	Loading Mode	Testing Temperature, C					Linear Fit	
		-10	0	10	30	40	Slope	Intercept
M0 Mix	Uniaxial	4.25	2.99	1.23	-1.18	--	-0.157	3.32
	Biaxial	4.33	2.81	1.15	-0.93	--	-0.134	2.81
M1 Mix	Uniaxial	4.20	2.58	1.25	-1.14	--	-0.133	2.71
	Flexure	--	--	0.69	-1.70	-2.46	-0.112	1.92
E1 Mix	Uniaxial	4.68	2.82	1.40	-1.23	--	-0.147	3.00
	Flexure	--	--	1.49	-1.24	-1.58	-0.105	2.29
S1 Mix	Uniaxial	4.44	2.62	1.16	-1.29	--	-0.141	2.79
	Flexure	--	--	0.88	-1.85	-2.51	-0.129	2.43

Table 7-6: t-test results from comparison of temperature shift factors

Mixture	Temperature, C				Linear Fit	
	-10	0	10	30	Slope	Intercept
M0 Mix	0.79	0.28	0.75	0.25	0.67	0.81
M1 Mix	--	--	0.0005	0.0023	0.007	0.0001
E1 Mix	--	--	0.11	0.97	0.02	0.03
S1 Mix	--	--	0.27	0.12	0.65	0.47

The slope of fitted straight line was more for uniaxial mode when compared to biaxial and flexure mode of loading. As seen in Table 7-6, temperature shift factors under uniaxial mode are statistically comparable to those obtained under biaxial mode of loading for mixture M0. However temperature shift factors under uniaxial mode are statistically different that their flexural mode counterparts for mixtures M1 and E1. This indicates that mixture specific properties and mode of loading have significant effect on temperature shift factors.

7.3 **Effect on phase angle**

The temperature shift factors determined while constructing dynamic modulus mastercurves were used to shift the phase angle isotherms for each specimen. Comparisons of phase angles obtained under different modes of loading are discussed in the following paragraphs.

Figure 7-9 shows the comparison of measured phase angles under uniaxial mode and biaxial mode of loading for mixture M0. Visual inspection of Figure 7-9 indicates overlap of phase angles obtained under both modes of loading. Phase angles measured under biaxial mode of loading exhibits more scatter than uniaxial mode of loading. At frequencies less than 1 Hz, phase angle values under biaxial mode decrease more with the decrease in frequency. This indicates aggregate structure has more effect on biaxial mode testing when compared to uniaxial mode of testing. Also, the location of peak phase angle under biaxial mode (~1 Hz) is greater than under uniaxial mode of loading (~0.1 Hz). This indicates that aggregate structure plays a dominant role under biaxial mode at lower temperature (high frequency) when compared to uniaxial mode of

loading. However low temperature (high frequency) behavior under uniaxial mode and biaxial mode is similar.
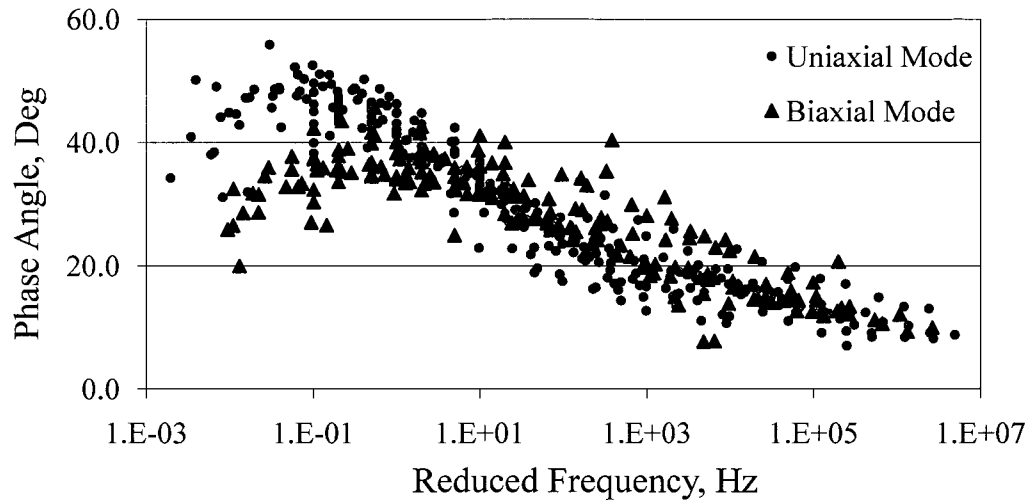
Figure 7-9: Comparison of phase angle values measured under uniaxial and biaxial mode of loading for M0 mix

The measured phase angles under flexure mode and uniaxial mode of loading for mixtures M1, E1 and S1 are presented in Figures 7-10, 7-11 and 7-12, respectively. From all three figures, it is clear that phase angles measured under flexure mode overlaps those measured under uniaxial testing conditions at higher frequencies. Thus it can be concluded that low temperature behavior under uniaxial mode and flexure mode of loading is similar. At frequencies less than 0.1 Hz, phase angle values under flexural mode decrease with the decrease in frequency. However measurements under uniaxial mode for S1 mixture still exhibits an increasing trend whereas M1 and E1 mixture exhibits a plateau value. Also below 0.1 Hz, the drop in phase angle under flexure mode of loading is more when compared to uniaxial mode of loading. This indicates flexural

mode is more influenced by aggregate structure when compared to uniaxial mode of loading.
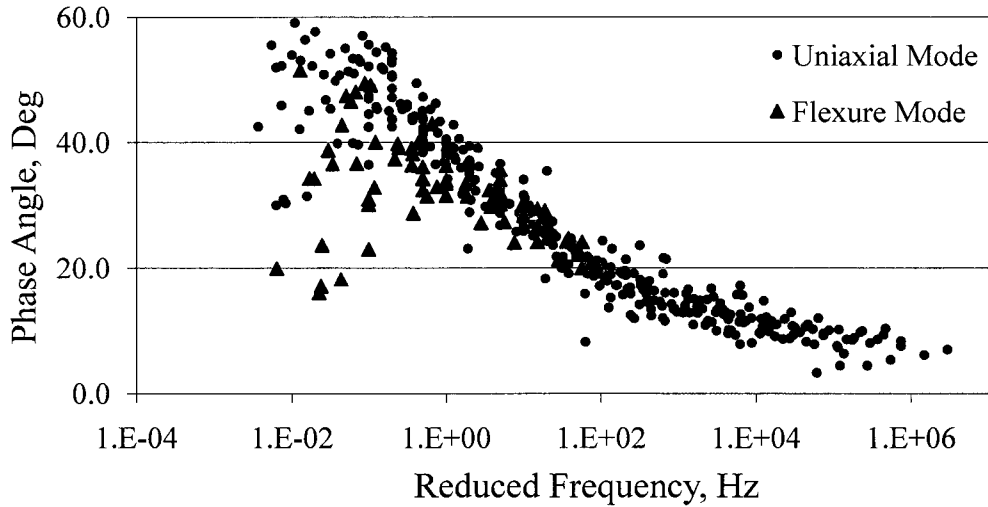
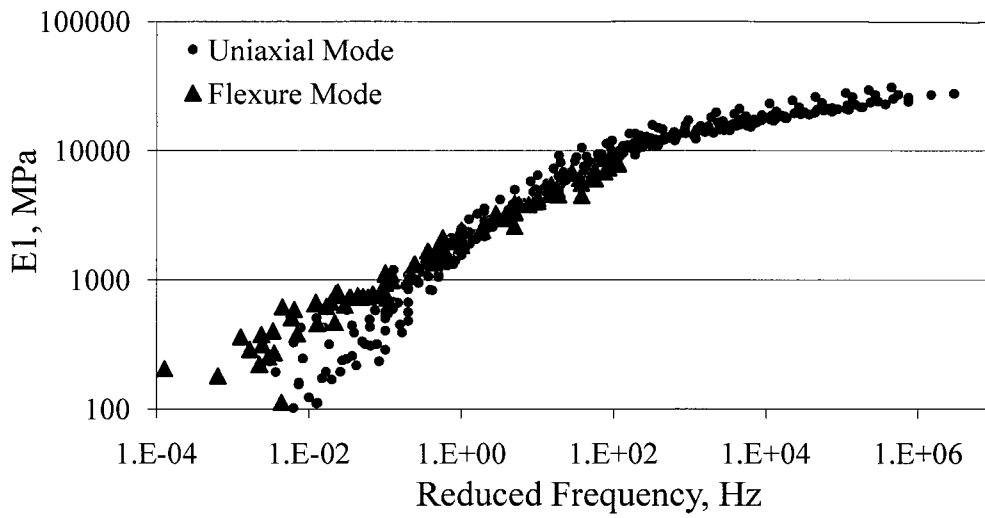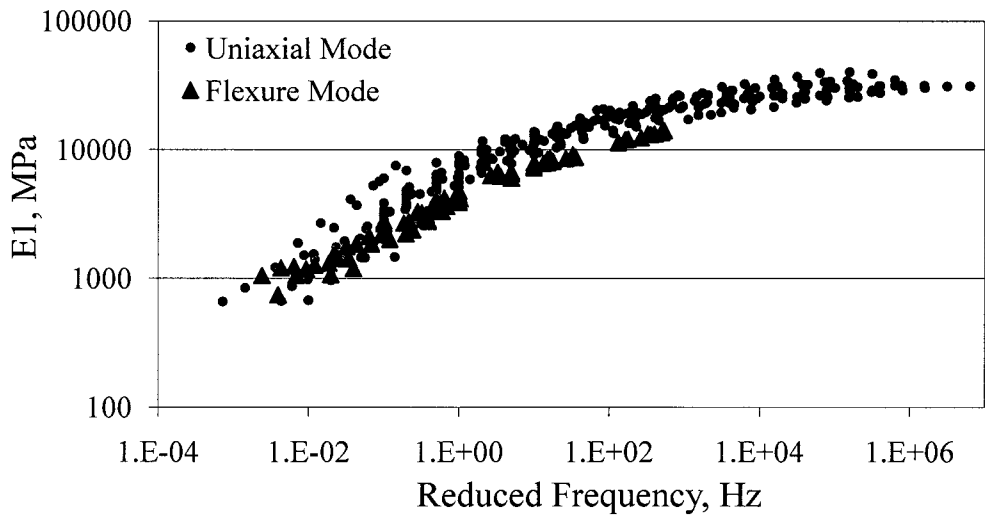Figure 7-10: Comparison of phase angle values measured under uniaxial and flexural mode of loading for M1 mix
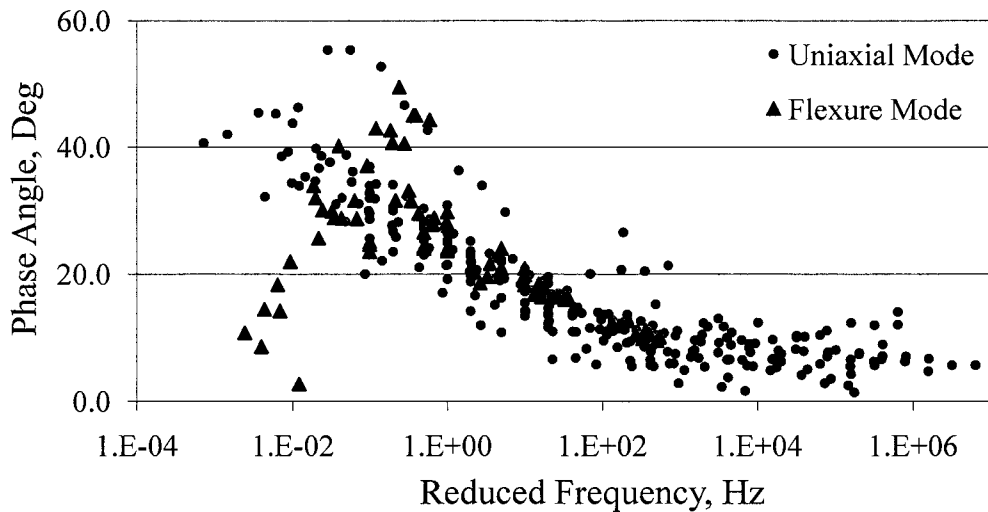
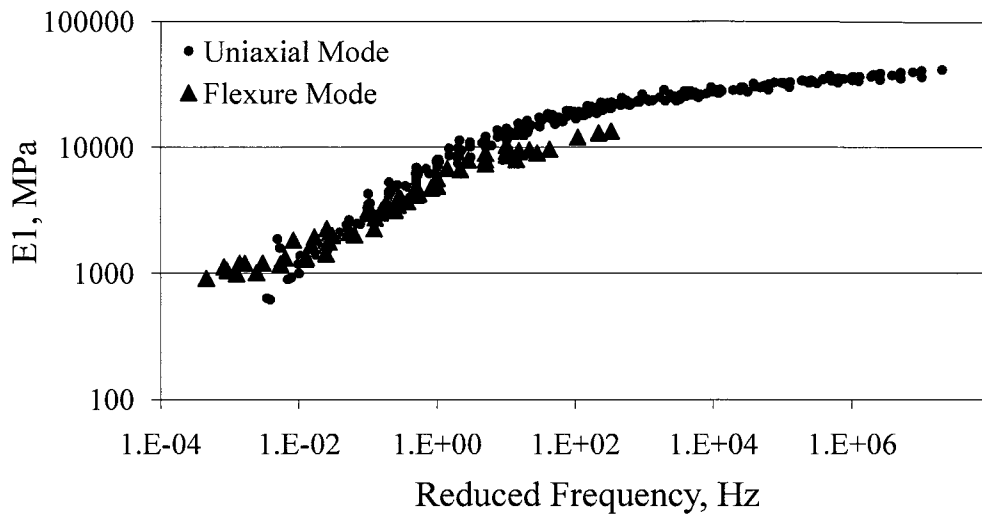Figure 7-11: Comparison of phase angle values measured under uniaxial and flexural mode of loading for E1 mix

131
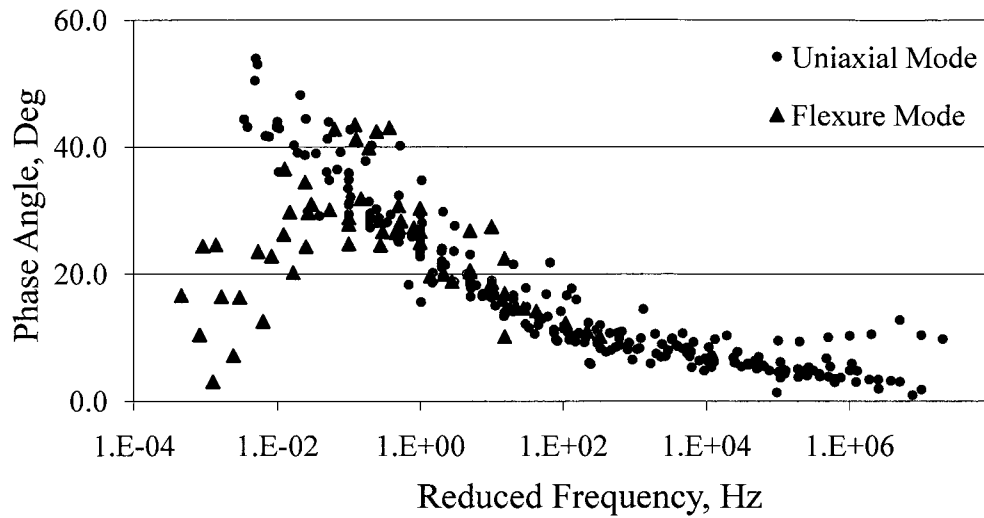
Figure 7-12: Comparison of phase angle values measured under uniaxial and flexural mode of loading for S1 mix

7.4 Effect on storage modulus

The previous sections showed that uniaxial dynamic modulus values are significantly different than flexural dynamic modulus values. However phase angle data indicated overlap in certain range of frequencies (temperatures). Storage modulus combines effects of dynamic modulus and phase angle, so the effect of loading mode on storage modulus mastercurve was evaluated.

7.4.1 Comparison between uniaxial mode and flexural mode of loading

Storage modulus mastercurves obtained under uniaxial and flexural mode of loading for all three mixtures (M1, E1 and S1) are presented in Figures 7-13, 7-14 and 7-15, respectively.

132

Figure 7-13: Comparison of storage modulus values measured under uniaxial and flexural mode of loading for M1 mix

Figure 7-14: Comparison of storage modulus values measured under uniaxial and flexural mode of loading for E1 mix

133

Figure 7-15: Comparison of storage modulus values measured under uniaxial and flexural mode of loading for S1 mix

Since the visual inspection indicated very few regions of overlap, a t-test was conducted to check if statistically significant differences existed between storage modulus values obtained under different modes of loading. A similar procedure to that described in Section 7.1 was used to obtain storage modulus values at regular intervals of reduced frequencies. The p-values obtained while comparing uniaxial storage modulus with flexural storage modulus for all three mixtures are presented in Table 7-7. The percentage difference between uniaxial storage modulus and flexural storage modulus ($E1\ PD$) (Equation 7-5), and Storage Modulus Ratio (SMR) (Equation 7-6) was computed. These values for all three mixtures (M1, E1, S1) are presented in Table 7-8. The percentage difference between flexural storage modulus and uniaxial storage modulus is shown graphically in Figure 7-16. The variation of storage modulus ratio as a function of frequency as bar chart and scatter plot are shown Figures 7-17 and 7-18, respectively.

$$E1\ PD_{1D,flex} = \frac{100 \times (E1_{flex} - E1_{1D})}{E1_{flex}} \qquad 7\text{-}5$$

$$SMR_{1D,flex} = \frac{E1_{flex}}{E1_{1D}} \qquad 7\text{-}6$$

where $E1_{flex}$ = flexural storage modulus;

$E1_{1D}$ = uniaxial storage modulus;

$E1\ PD_{1D,flex}$ = percentage difference between uniaxial and flexural storage modulus; and

$SMR_{1D,flex}$ = storage modulus ratio computed using uniaxial and flexural storage modulus.

Table 7-7: t-test results from comparison of storage modulus under uniaxial mode with flexural mode

Reduced Frequency, Hz	p-value		
	M1 Mix	E1 Mix	S1 Mix
0.001	<0.0001	0.9248	0.2988
0.01	<0.0001	0.9346	0.2578
0.1	<0.0001	0.3412	0.179
1	0.03	0.1468	0.0075
10	0.7728	0.0773	0.0022
100	0.0091	0.0344	0.0068
1000	0.0001	0.0125	0.0592

Table 7-8: Storage modulus ratio and E1 percentage difference computed for M1, E1 and S1 mixtures

Reduced Frequency, Hz	Storage Modulus Ratio			E1 Percentage Difference		
	M1 Mix	E1 Mix	S1 Mix	M1 Mix	E1 Mix	S1 Mix
0.001	8.70	2.30	1.85	88.5	56.6	45.9
0.01	3.82	1.03	1.18	73.8	3.0	15.2
0.1	1.75	0.72	0.89	42.7	-39.7	-12.9
1	1.19	0.67	0.79	15.8	-49.2	-26.9
10	0.98	0.69	0.73	-2.1	-45.0	-37.5
100	0.76	0.69	0.69	-32.2	-45.2	-44.8
1000	0.58	0.66	0.70	-73.2	-51.6	-42.5
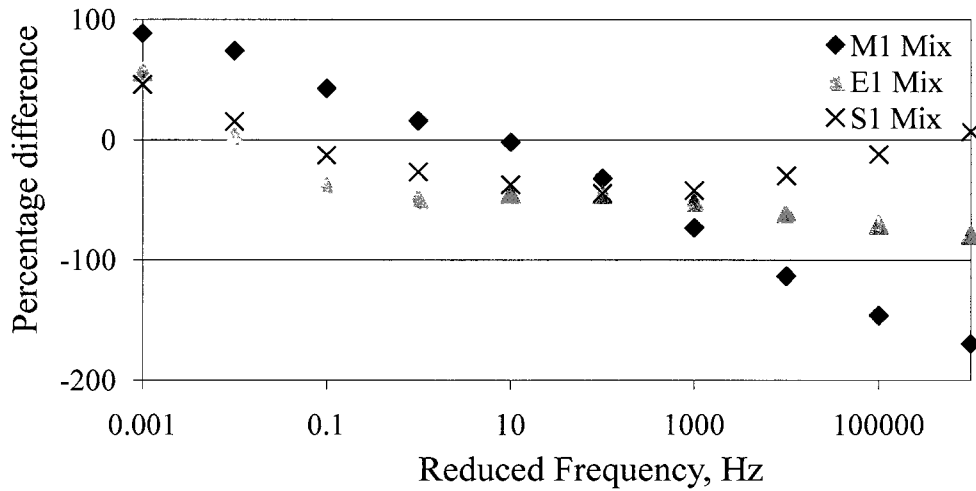
Figure 7-16: Percentage difference between uniaxial storage modulus and flexural storage modulus as a function of frequency for M1, E1 and S1 mixtures
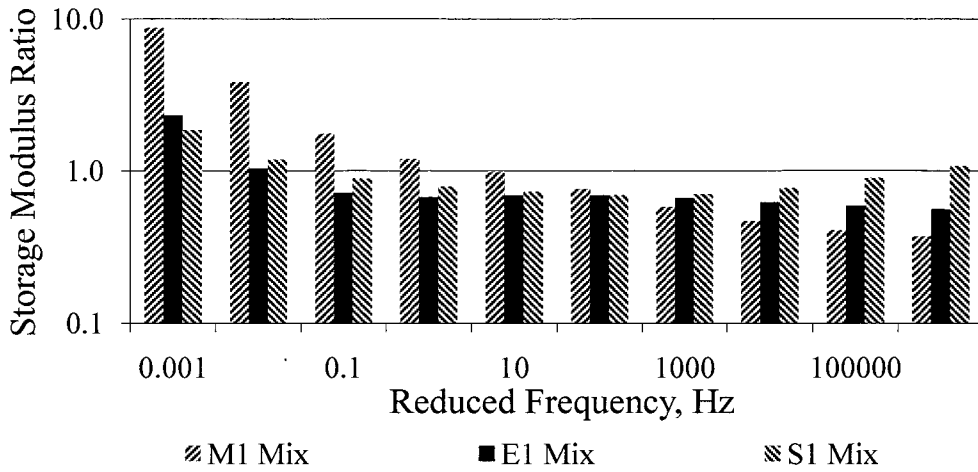
Figure 7-17: Variation of storage modulus ratio with frequency for M1, E1 and S1 mixtures (as bar chart)
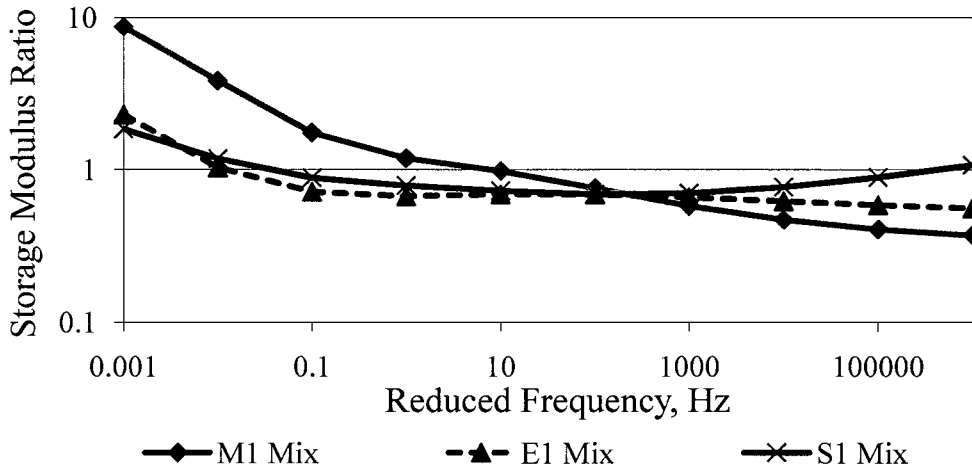
Figure 7-18: Variation of storage modulus ratio with frequency for M1, E1 and S1 mixtures (as scatter plot)

From the t-test results it is clear that there exists a significant difference between uniaxial storage modulus mastercurve and flexural storage modulus mastercurve. The percentage difference between uniaxial storage modulus and flexural storage modulus

and storage modulus ratio is a function of frequency. Again modular ratio values approach an asymptotic value at higher frequencies for mixtures M1 and E1. Higher storage modulus ratio at lower frequencies (higher temperature) indicates that the material is storing more energy under flexure mode than uniaxial mode. In other words, more energy is dissipated under uniaxial mode than under flexure mode at lower frequencies (higher temperatures). One reason for less energy dissipation could be non-uniform stress distribution in flexural mode where certain zones in the beam are subjected to lower stress (strain) variation and hence less damage.

7.4.2 Comparison between uniaxial mode and biaxial mode of loading

The storage modulus values under uniaxial and biaxial mode of loading for mix M0 are shown in Figure 7-19. To check whether if there exists any statistically significant difference between uniaxial and biaxial mode of loading, a t-test was conducted. Also, the percentage difference (Equation 7-7) and Storage Modulus Ratio (SMR) (Equation 7-8) were computed at regular intervals of frequency. These results are presented in Table 7-9. The storage modulus ratio and percentage difference between biaxial storage modulus and uniaxial storage modulus are graphically presented in Figure 7-20.
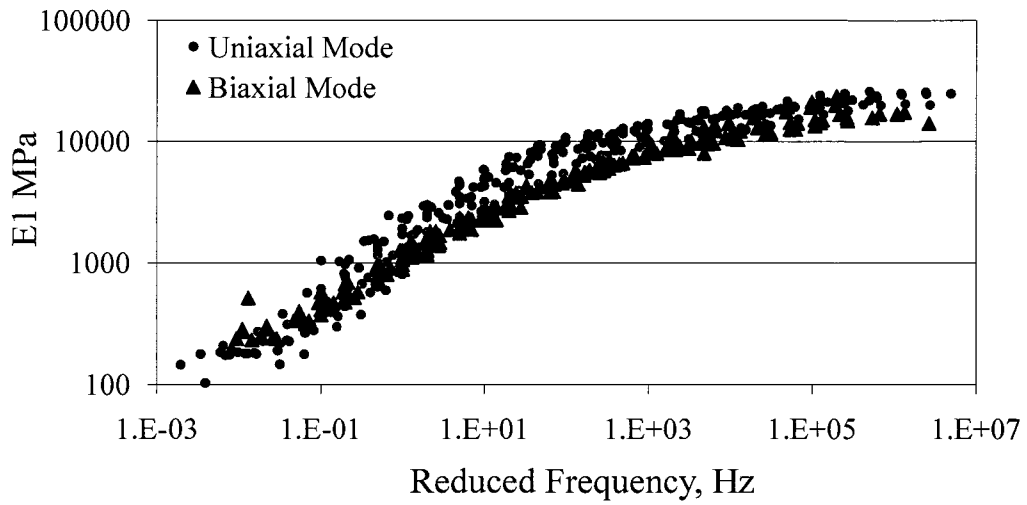
Figure 7-19: Comparison of storage modulus values under uniaxial and biaxial mode of loading for M0 mix

$$E1\ PD_{\ 1D,2D} = \frac{100 \times (E1_{2D} - E1_{1D})}{E1_{2D}} \qquad \text{7-7}$$

$$SMR_{1D,2D} = \frac{E1_{2D}}{E1_{1D}} \qquad \text{7-8}$$

where $E1_{2D}$ = biaxial storage modulus;

$E1_{1D}$ = uniaxial storage modulus;

$E1\ PD_{\ 1D,2D}$ = percentage difference between uniaxial and biaxial storage

modulus; and

$SMR_{1D,2D}$ = storage modulus ratio computed using uniaxial and biaxial

storage modulus.

139

Table 7-9: Summary of results obtained while comparing uniaxial and biaxial storage modulus

Reduced Time, sec	p-value	Storage Modulus Ratio	E1 Percentage Difference
0.01	0.7524	1.11	9.74
0.1	0.5941	0.87	-15.10
1	0.1012	0.69	-44.44
10	0.0106	0.61	-64.65
100	0.0019	0.60	-66.56
1000	0.0004	0.64	-57.03
10000	0.0004	0.68	-46.56
100000	0.0019	0.72	-38.85
1000000	0.0074	0.75	-33.90
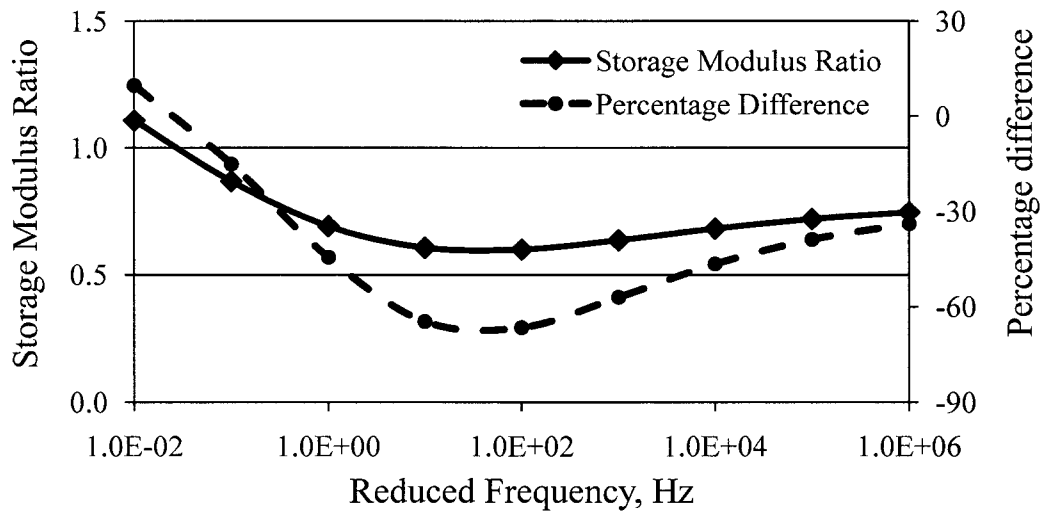
Figure 7-20: SMR and percentage difference between storage modulus as function of frequency from comparison of uniaxial mode and biaxial mode for M0 mix

Statistically significant differences between mean values of uniaxial storage modulus and biaxial storage modulus were found at frequencies higher than 10 Hz. The ratio between biaxial storage modulus and uniaxial storage modulus was approximately unity (minimum 0.75, maximum 1.11). Hence it can be concluded that uniaxial storage

modulus and biaxial storage modulus are comparable in magnitude. The storage modulus ratio reached a plateau value at around 1,000,000 Hz.

7.5   Effect on relaxation modulus mastercurve

Calculation of pseudostrains requires the relaxation modulus values. As mentioned previously, the relaxation modulus is difficult to measure directly in the laboratory and is therefore determined from the storage modulus mastercurve using inteconversion techniques. From previous sections it is clear that mode of loading affects the dynamic modulus, phase angle (at lower frequencies, higher temperature) and storage modulus mastercurve values significantly. Thus, the effect of loading mode on relaxation modulus mastercurve is also evaluated.

7.5.1   Comparison between uniaxial mode and flexural mode of loading

Using the storage modulus mastercurve regression coefficients, the relaxation modulus mastercurve was constructed for individual specimens. Using the common region of reduced frequency from dynamic modulus data, a common region of relaxation time was found. The computed common relaxation time range was 0.0001 to 100s. The procedure described in Section 7.1 was used to obtain relaxation modulus values at regular intervals of reduced time. Relaxation modulus mastercurves obtained under uniaxial and flexure mode of loading for all three mixtures are presented in Figures 7-21, 7-22 and 7-23, respectively. A t-test was conducted using the combined data set of relaxation modulus. The t-test results are presented in Table 7-10.
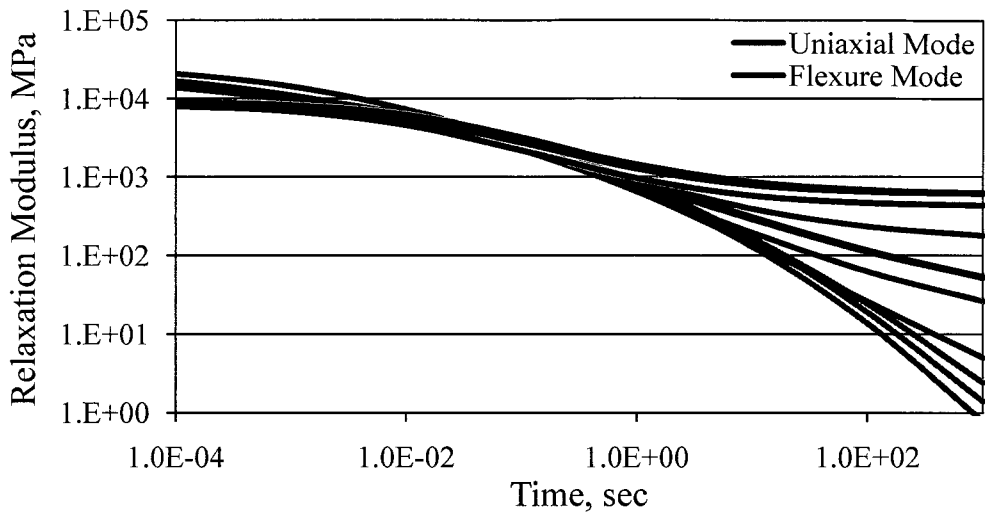
Figure 7-21: Comparison of relaxation modulus values measured under uniaxial and flexural mode of loading for M1 mix
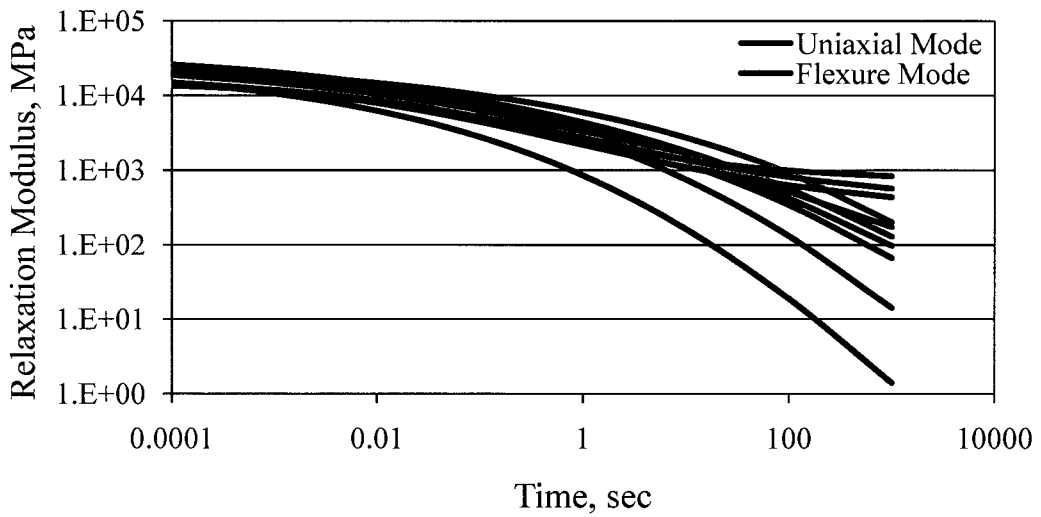
Figure 7-22: Comparison of relaxation modulus values measured under uniaxial and flexural mode of loading for E1 mix
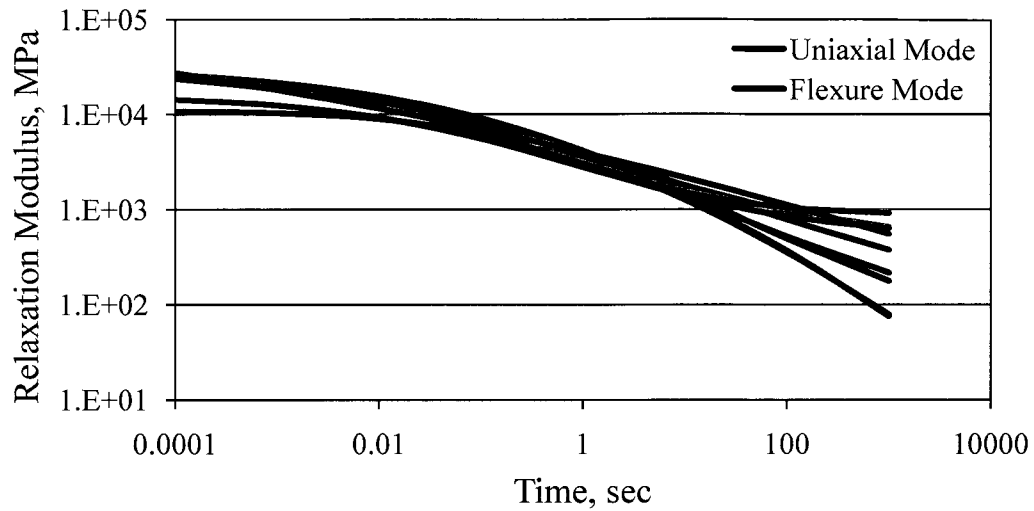
Figure 7-23: Comparison of relaxation modulus values measured under uniaxial and flexural mode of loading for S1 mix

Table 7-10: t-test results from comparison of relaxation modulus under uniaxial mode with flexural mode

Reduced Time, sec	p-value		
	M1 Mix	E1 Mix	S1 Mix
0.0001	<0.0001	0.0106	0.0575
0.001	0.0043	0.0295	0.0086
0.01	0.4533	0.0691	0.0028
0.1	0.0686	0.1312	0.0082
1	0.0002	0.2892	0.1373
10	<0.0001	0.8763	0.4023
100	<0.0001	0.0672	0.0314

The percentage difference between the flexural relaxation modulus and the uniaxial relaxation modulus ($E(t)$ PD) (Equation 7-9) and Relaxation Modulus Ratio (RMR) (Equation 7-10) was computed to check if there exists a trend. These values are presented in Table 7-11. The percentage difference between uniaxial relaxation modulus and flexural relaxation modulus is shown in Figure 7-24. Relaxation modulus

ratio as a function of frequency as bar chart and scatter plot are shown in Figures 7-25 and 7-26, respectively.

$$E(t)\ PD_{1D,flex} = \frac{100 \times \left(E(t)_{flex} - E(t)_{1D}\right)}{E\ (t)_{flex}}$$

7-9

$$RMR_{1D,flex} = \frac{E(t)_{flex}}{E\ (t)_{1D}}$$

7-10

where $E(t)_{flex}$ = flexural relaxation modulus;

$E(t)_{1D}$ = uniaxial relaxation modulus;

$E(t)\ PD_{1D,flex}$ = percentage difference between uniaxial and flexural relaxation modulus; and

$RMR_{1D,flex}$ = relaxation modulus ratio computed using uniaxial and flexural relaxation modulus.

Table 7-11: Relaxation modulus ratio and E(t) percentage difference computed for M1, E1 and S1 mixtures

Reduced Time, sec	Relaxation Modulus Ratio			E(t) Percentage Difference		
	M1 Mix	E1 Mix	S1 Mix	M1 Mix	E1 Mix	S1 Mix
0.0001	0.58	0.65	0.69	-72.41	-53.02	-43.93
0.001	0.76	0.69	0.69	-32.13	-45.86	-45.73
0.01	0.98	0.69	0.72	-2.25	-44.59	-38.35
0.1	1.17	0.67	0.79	14.33	-48.85	-27.34
1	1.62	0.70	0.87	38.43	-43.54	-14.66
10	3.63	0.94	1.12	72.43	-6.05	10.82
100	10.21	1.95	1.72	90.21	48.83	41.92
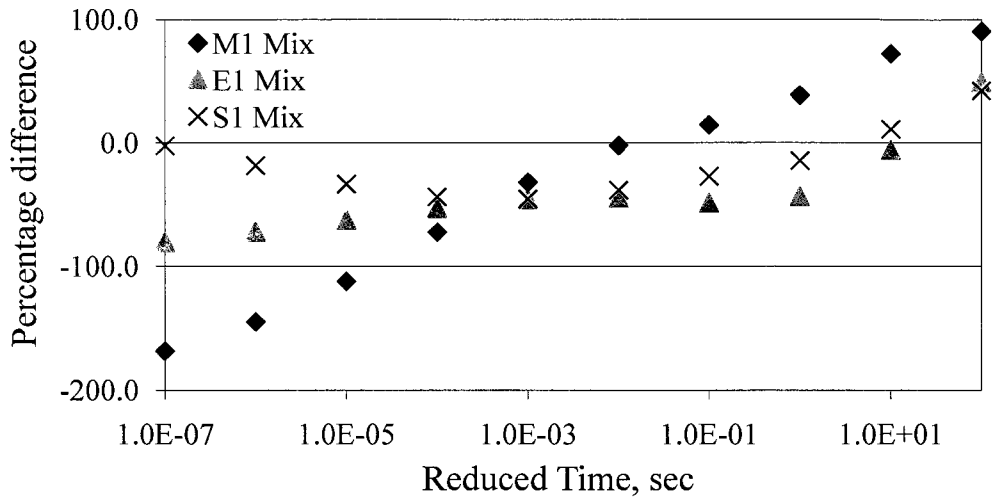
Figure 7-24: Percentage difference between uniaxial and flexural relaxation modulus as a function of time for M1, E1 and S1 mixtures
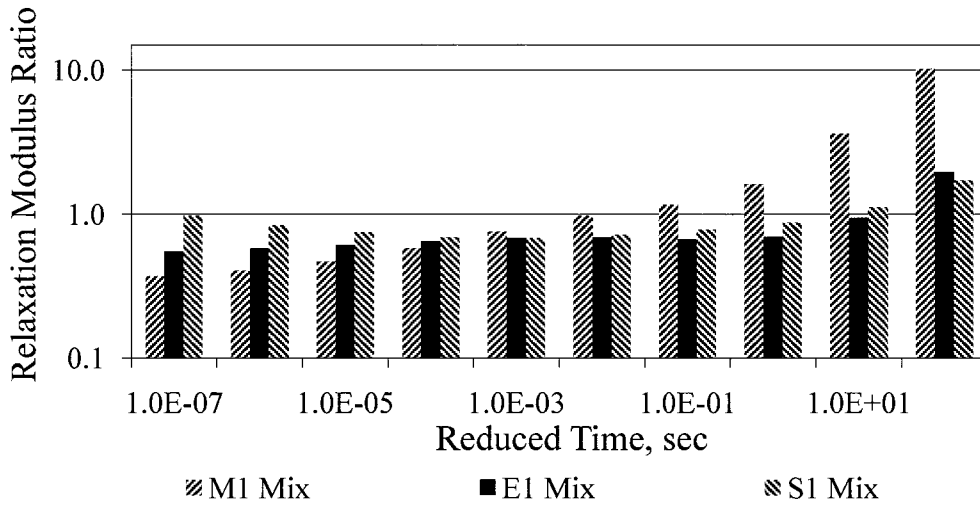
Figure 7-25: Variation of relaxation modulus ratio with time for M1, E1 and S1 mixtures (as bar chart)
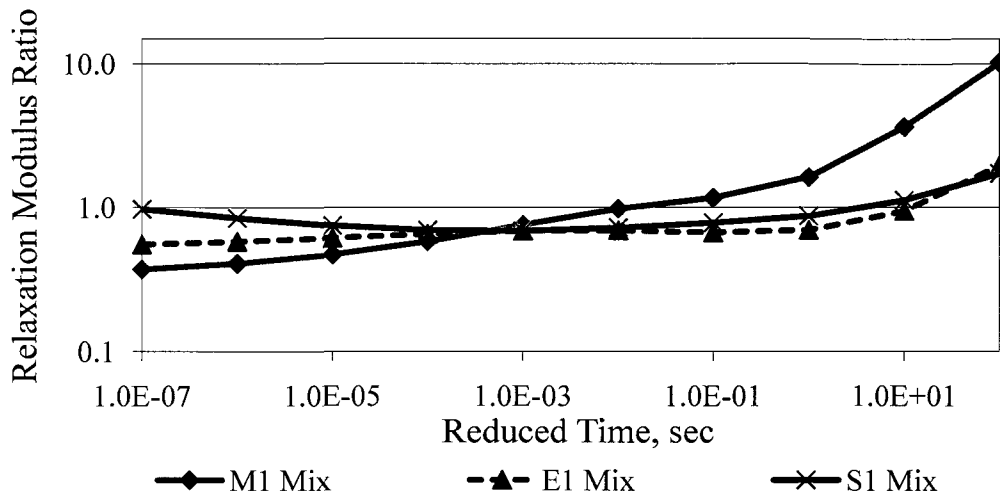
Figure 7-26: Variation of relaxation modulus ratio with time for M1, E1 and S1 mixtures (as scatter plot)

Statistically significant differences were found between uniaxial relaxation modulus and flexural relaxation modulus for M1 and S1 mixtures. However, for mixture E1 statistically significant differences were found only at times less than 0.001 second. As seen in Figures 7-25 and 7-26, the relaxation modulus ratio for mixtures E1 and S1 remains approximately constant up to 1 second; beyond which, the relaxation modulus ratio values starts to increase at faster rate. However for mixture M1, rate of increase of relaxation modulus ratio increases with time. This indicates that the relaxation modulus ratio is dependent on mixture properties.

7.5.2 Comparison between uniaxial mode and biaxial mode of loading

The relaxation modulus values under uniaxial and biaxial mode of loading for mix M0 are shown in Figure 7-27. A t-test was conducted to check if a statistically significant difference existed between uniaxial relaxation modulus mastercurve and biaxial relaxation modulus mastercurve. These results are presented in Table 7-12. The storage percentage difference (Equation 7-11) and Relaxation Modulus Ratio (RMR) (Equation 7-12) were computed at regular intervals. Relaxation modulus ratio and percentage difference between biaxial relaxation modulus and uniaxial relaxation modulus are graphically presented in Figure 7-28.
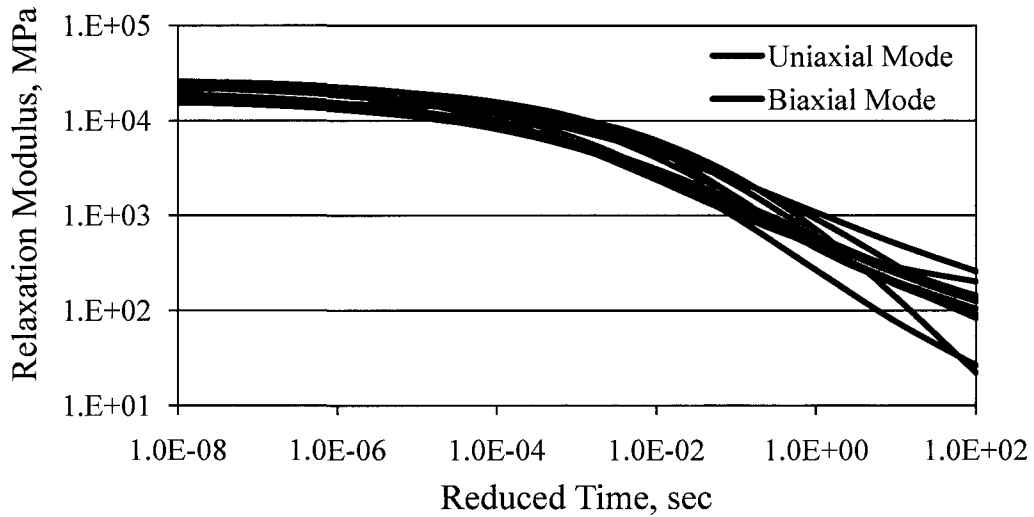
Figure 7-27: Comparison of relaxation modulus values measured under uniaxial and biaxial mode of loading for M0 mix

$$E(t) \ PD_{1D,2D} = \frac{100 \times (E(t)_{2D} - E(t)_{1D})}{E\ (t)_{2D}}$$

$$\hspace{10cm} 7\text{-}11$$

$$RMR_{1D,2D} = \frac{E(t)_{2D}}{E\ (t)_{1D}}$$

$$\hspace{10cm} 7\text{-}12$$

where $E(t)_{2D}$ = biaxial relaxation modulus;

$E(t)_{1D}$ = uniaxial relaxation modulus;

$E(t) PD_{1D,2D}$ = percentage difference between uniaxial and biaxial relaxation modulus; and

$RMR_{1D,2D}$ = relaxation modulus ratio computed using uniaxial and biaxial relaxation modulus.

Table 7-12: Summary of results obtained while comparing uniaxial and biaxial relaxation modulus for M0 mixture

Reduced Time, sec	p-value	Relaxation Modulus Ratio	E(t) Percentage Difference
0.000001		0.70	-43.27
0.00001		0.67	-48.83
0.0001	0.001	0.64	-56.28
0.001		0.61	-63.70
0.01		0.60	-65.38
0.1	0.067	0.65	-53.23
1	0.379	0.79	-26.00
10	0.899	1.04	4.25
100	0.483	1.35	25.66
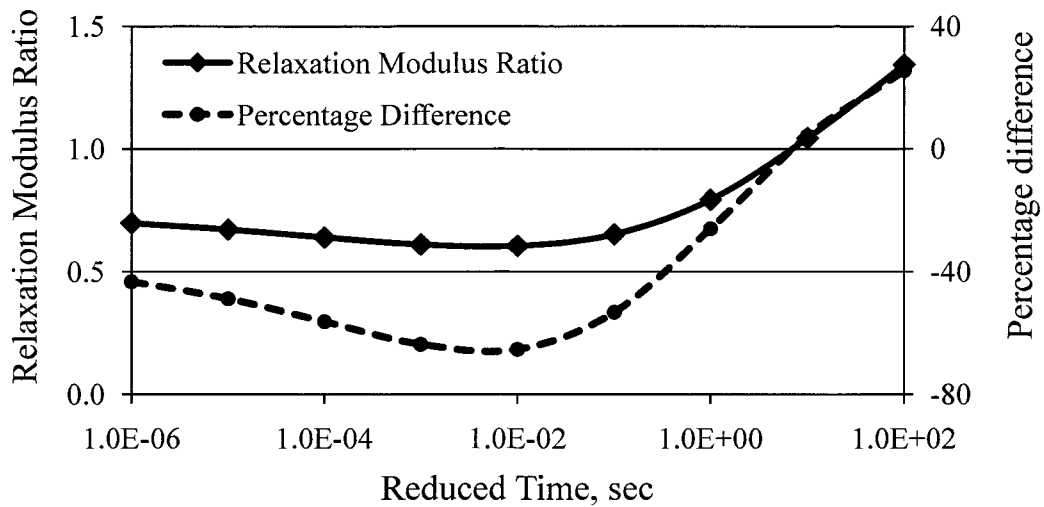
Figure 7-28: Variation of percentage difference between uniaxial relaxation modulus and biaxial relaxation modulus, and RMR with time for M0 mix

As seen in Figure 7-28, the relaxation modulus ratio remains approximately constant up to 0.1 second and then starts to increase at a faster rate. This indicates that this relaxation modulus ratio can be used as conversion factor for short term behavior prediction.

7.6 Effect on creep compliance mastercurve

This section discusses the effect of mode of loading on the creep compliance property. The relaxation modulus values obtained previously were used to compute creep compliance values. The interconversion technique described in Section 4.2.2 was used for this purpose.

7.6.1 Comparison between uniaxial mode and flexural mode of loading

Using the storage modulus data, the creep compliance mastercurve was constructed for individual specimens using an inteconversion technique. Creep compliance mastercurves obtained under uniaxial and flexure mode of loading for M1, E1 and S1 mixtures are presented in Figures 7-29, 7-30 and 7-31, respectively. A t-test was conducted using combined data set of relaxation modulus. The t-test results are presented in Table 7-13.
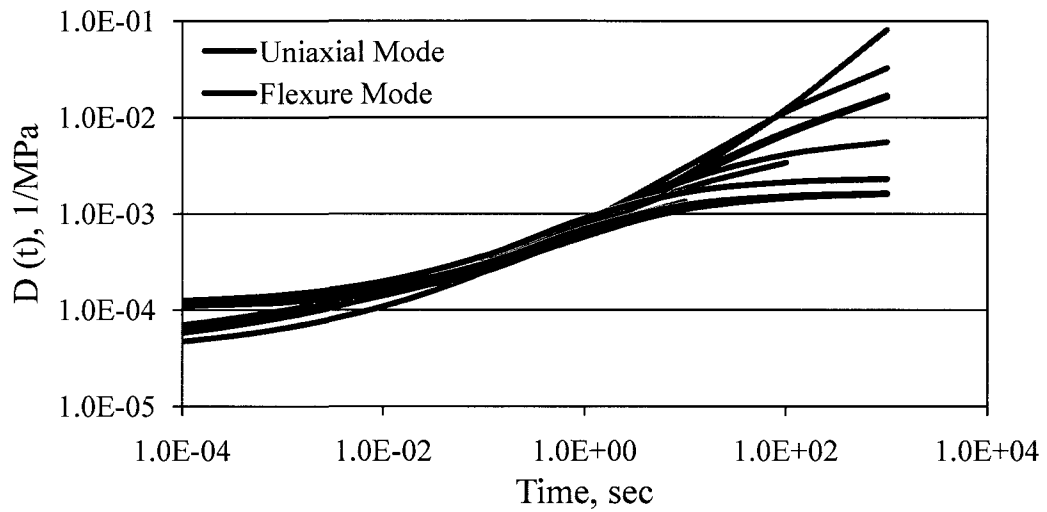
Figure 7-29: Comparison of creep compliance values measured under uniaxial and flexural mode of loading for M1 mix
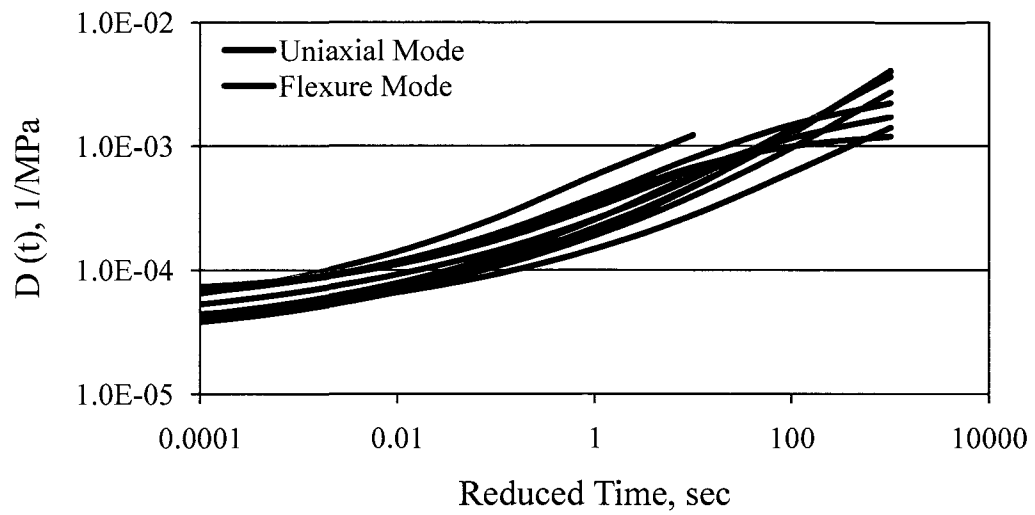
Figure 7-30: Comparison of creep compliance values measured under uniaxial and flexural mode of loading for E1 mix
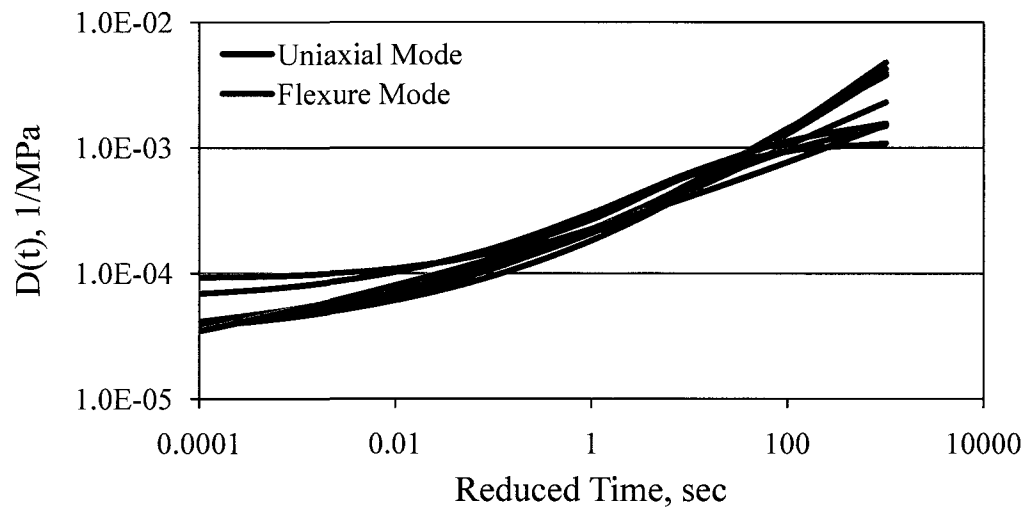
Figure 7-31: Comparison of creep compliance values measured under uniaxial and flexural mode of loading for S1 mix

Table 7-13: t-test results from comparison of creep compliance under uniaxial mode with flexural mode

Reduced Time, sec	M1 Mix	E1 Mix	S1 Mix
0.0001	<0.0001	0.0037	0.0489
0.001	<0.0001	0.022	0.0181
0.01	0.0507	0.0957	0.0031
0.1	0.9319	0.2081	0.002
1	0.4053	0.328	0.0178
10	0.0199	0.4711	0.2344
100	0.0082	0.5982	0.0657

The percentage difference between the flexural creep compliance and the uniaxial creep compliance $(D(t)\ PD)$ (Equation 7-13) and Creep Compliance Ratio (CCR) (Equation 7-14) was computed to check if there exists a trend. These values are presented in Table 7-14. The percentage difference between uniaxial creep compliance and flexural creep compliance is shown in Figure 7-32. Creep Compliance Ratio as a function of frequency as bar chart and scatter plot are shown in Figure 7-33 and 7-34, respectively.

$$D(t)\ PD_{1D,flex} = \frac{100 \times \left(D(t)_{flex} - D(t)_{1D}\right)}{D(t)_{flex}} \qquad \text{7-13}$$

$$CCR_{1D,flex} = \frac{D(t)_{flex}}{D(t)_{1D}} \qquad \text{7-14}$$

where $D(t)_{flex}$ = flexural creep compliance;

$D(t)_{1D}$ = uniaxial creep compliance;

$D(t)\ PD_{1D,flex}$ = percentage difference between uniaxial and flexural creep compliance; and

$CCR_{1D,flex}$ = creep compliance ratio computed using uniaxial and flexural creep compliance.

Table 7-14: Creep compliance ratio and D(t) percentage difference computed for M1, E1 and S1 mixtures

Reduced Time, sec	Creep Compliance Ratio			D(t) Percentage Difference		
	M1 Mix	E1 Mix	S1 Mix	M1 Mix	E1 Mix	S1 Mix
0.0001	1.77	1.50	1.67	43.59	33.23	40.27
0.001	1.40	1.41	1.55	28.81	29.11	35.48
0.01	1.12	1.36	1.42	10.59	26.35	29.77
0.1	0.97	1.35	1.32	-2.94	25.66	24.03
1	0.93	1.34	1.25	-7.10	25.51	19.94
10	0.61	1.25	1.13	-63.70	19.87	11.71
100	0.21	1.09	0.76	-380.74	8.62	-31.25
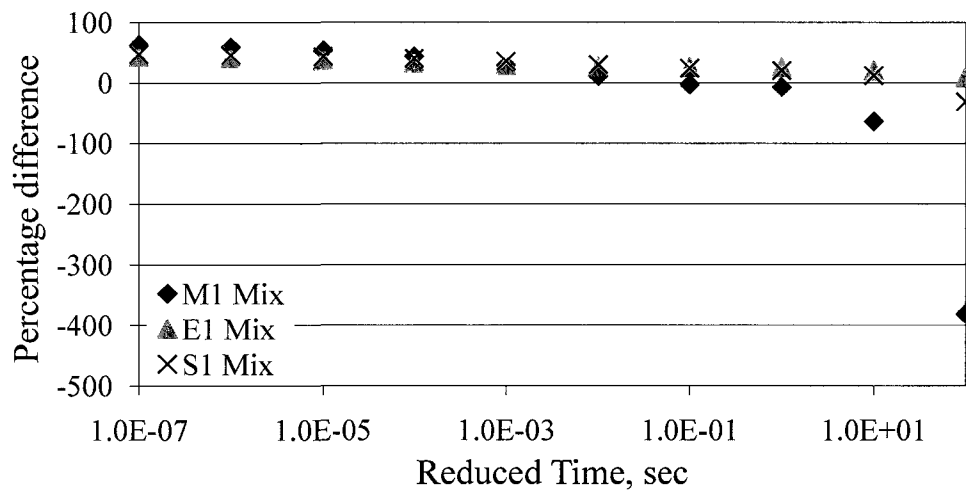
Figure 7-32: Percentage difference between uniaxial and flexural creep compliance as a function of time for M1, E1 and S1 mixtures
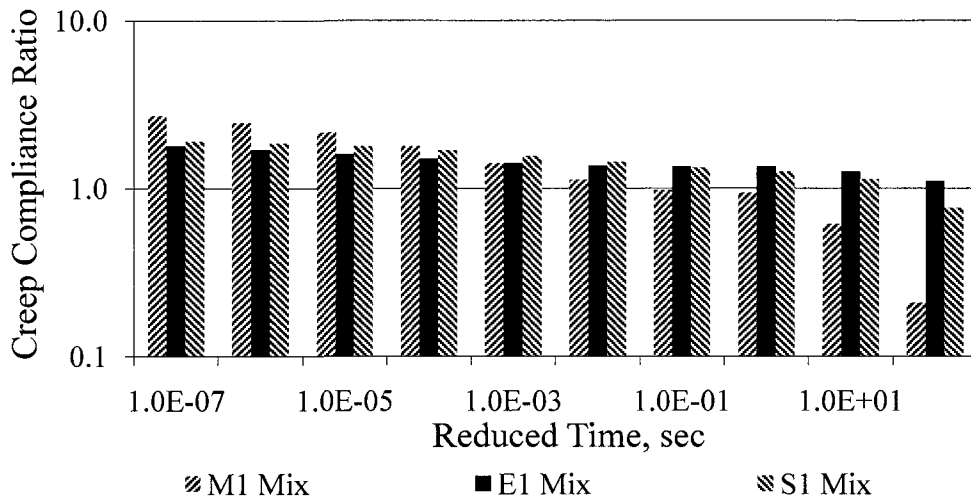
Figure 7-33: Variation of creep compliance ratio with time for M1, E1 and S1 mixtures (as bar chart)
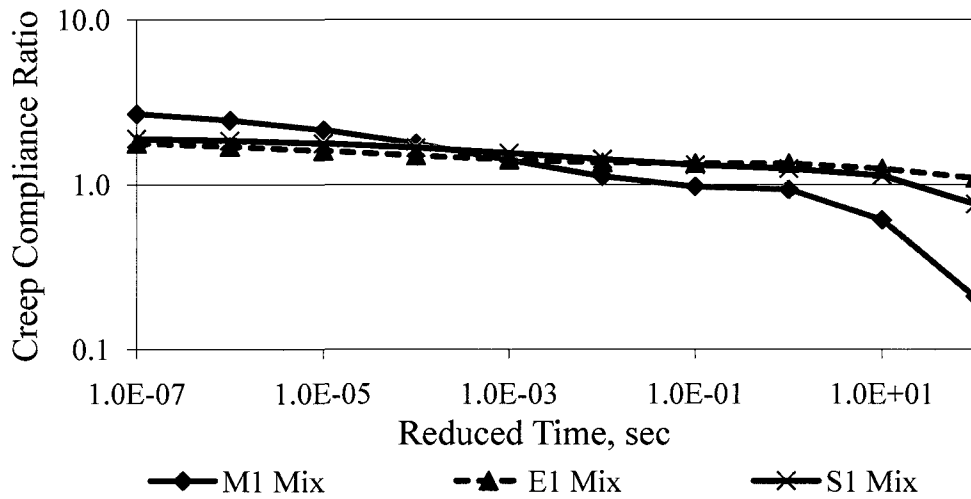
Figure 7-34: Variation of creep compliance ratio with time for M1, E1 and S1 mixtures (as scatter plot)

Statistically significant differences were found between uniaxial creep compliance and flexural creep compliance for E1 and S1 mixtures especially at lower reduced time.

However, for mixture M1 statistically significant differences were found at all times except between 0.01 and 1 second. As seen in Figures 7-33 and 7-34, creep compliance ratio for all mixtures shows a monotonically decreasing trend with increasing time. Also, beyond 1 second time, the creep compliance ratio values starts to decrease at faster rate. This indicates that the creep compliance ratio is dependent on mixture properties and is sensitive to mixture properties and testing mode.

`

7.6.2 Comparison between uniaxial mode and biaxial mode of loading

The creep compliance values under uniaxial and biaxial mode of loading for mix M0 are shown in Figure 7-35. A t-test was conducted to check if statistically significant difference existed between uniaxial relaxation modulus mastercurve and biaxial creep compliance mastercurve. These results are presented in Table 7-15. The creep compliance percentage difference (Equation 7-15) and Creep Compliance Ratio (CCR) (Equation 7-16) were computed at regular intervals. Creep Compliance Ratio and percentage difference between biaxial creep compliance and uniaxial creep compliance are graphically presented in Figure 7-36.
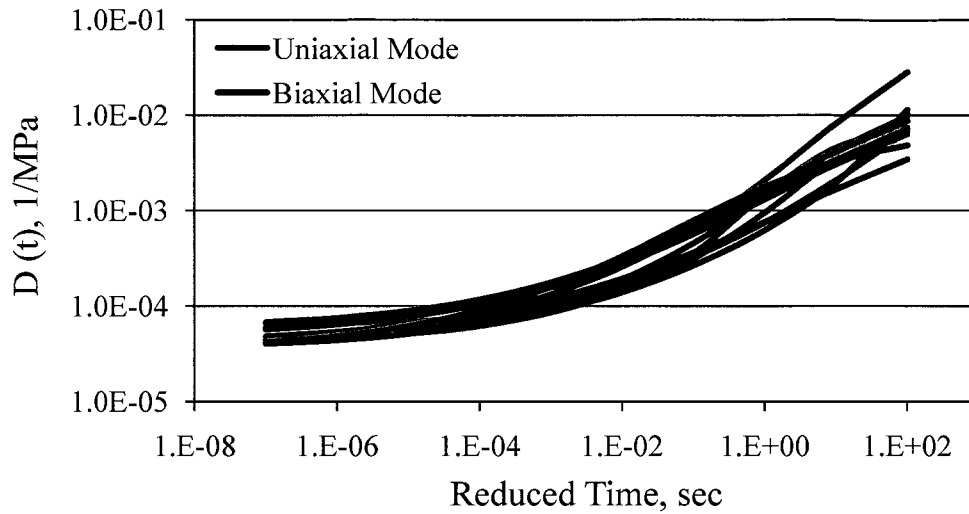
Figure 7-35: Comparison of creep compliance values measured under uniaxial and biaxial mode of loading for M0 mix

$$D(t)\ PD_{\ 1D,2D} = \frac{100 \times (D(t)_{2D} - D(t)_{1D})}{D(t)_{2D}}$$

7-15

$$CCR_{1D,2D} = \frac{D(t)_{2D}}{D\ (t)_{1D}}$$

7-16

where $D(t)_{2D}$ = biaxial creep compliance;

$D(t)_{1D}$ = uniaxial creep compliance;

$D(t)\ PD_{\ 1D,2D}$ = percentage difference between uniaxial and biaxial creep compliance; and

$CCR_{1D,2D}$ = relaxation modulus ratio computed using uniaxial and biaxial creep compliance.

Table 7-15: Summary of results obtained while comparing uniaxial and biaxial creep compliance values for M0 mixture

Reduced Time, sec	t-test result	Creep Compliance Ratio	D(t) Percentage Difference
0.000001	<0.0001	1.43	30.04
0.00001	<0.0001	1.48	32.21
0.0001	<0.0001	1.53	34.72
0.001	0.000	1.59	37.05
0.01	0.001	1.62	38.31
0.1	0.014	1.57	36.45
1	0.232	1.34	25.58
10	0.930	0.97	-3.44
100	0.340	0.61	-63.20
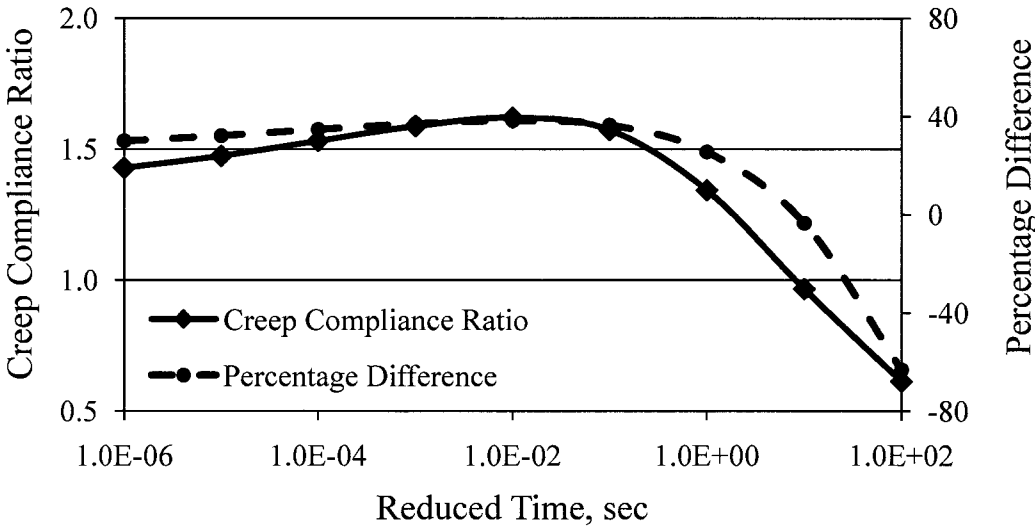
Figure 7-36: Variation of percentage difference between uniaxial creep compliance and biaxial creep compliance, and CCR with time for M0 mix

As seen in Figure 7-36, the creep compliance ratio remains approximately constant up to 0.1 second and then starts to decrease at a faster rate. This indicates that this creep compliance ratio can be used as conversion factor for short term behavior prediction.

7.7 Effect on damage characteristic curve

Several specimens were tested under monotonic or cyclic test conditions by applying damage inducing loads or displacement. These test data were used to calculate continuum damage parameters and subsequent construction of the damage characteristic curve. However, under flexural mode of loading, specimens were tested under cyclic loading only. This section discusses the effect of mode of loading on the damage characteristic curves.

The damage characteristic curves for M1, E1 and S1 mixtures using different values of material constant (alpha) are presented in Figures 7-37 through 7-42. Visual inspection of these plots indicates that the damage characteristic curves are different under uniaxial and flexural mode of loading. From Figures 7-37 through 7-42, it is clear that the difference between damage parameter at a given value of pseudostiffness increases as the pseudostiffness value decreases.
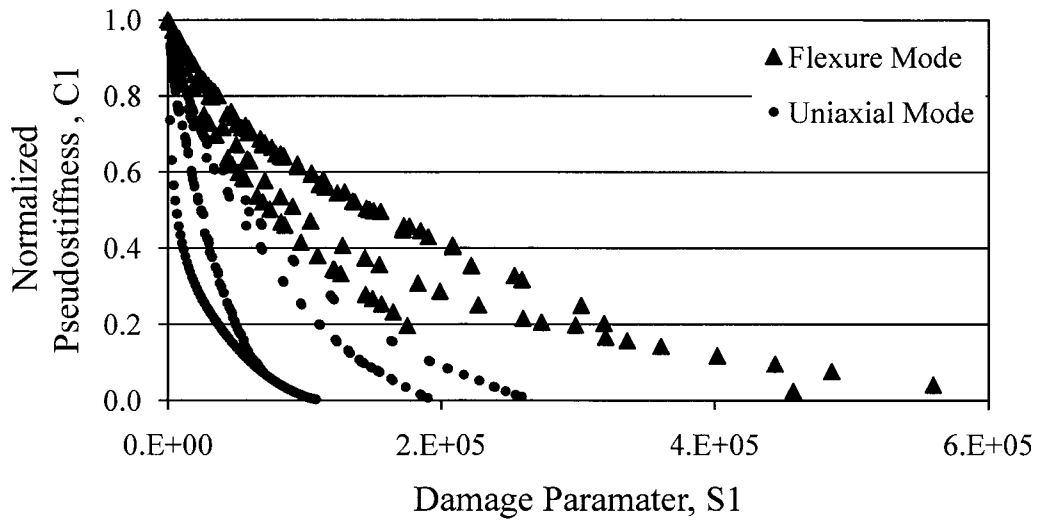
Figure 7-37: Damage characteristic curves for M1 mix with alpha = 1 + 1/n
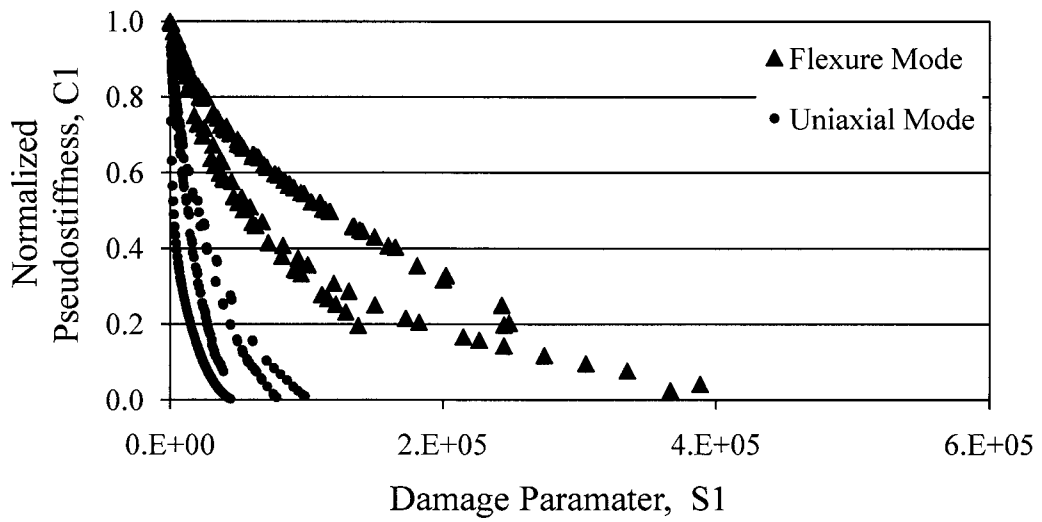
Figure 7-38: Damage characteristic curves for M1 mix with alpha = 1/n
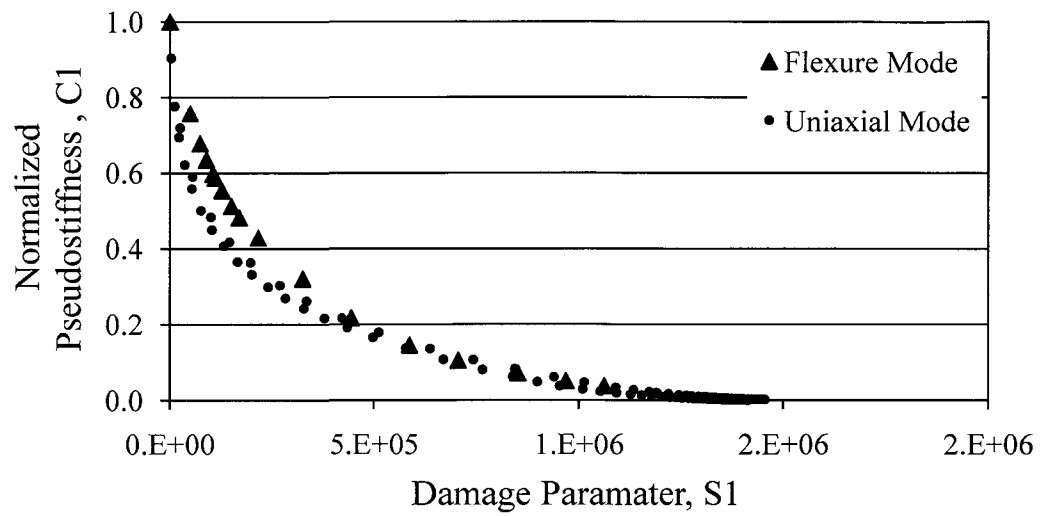
Figure 7-39: Damage characteristic curves for E1 mix with alpha = 1 + 1/n
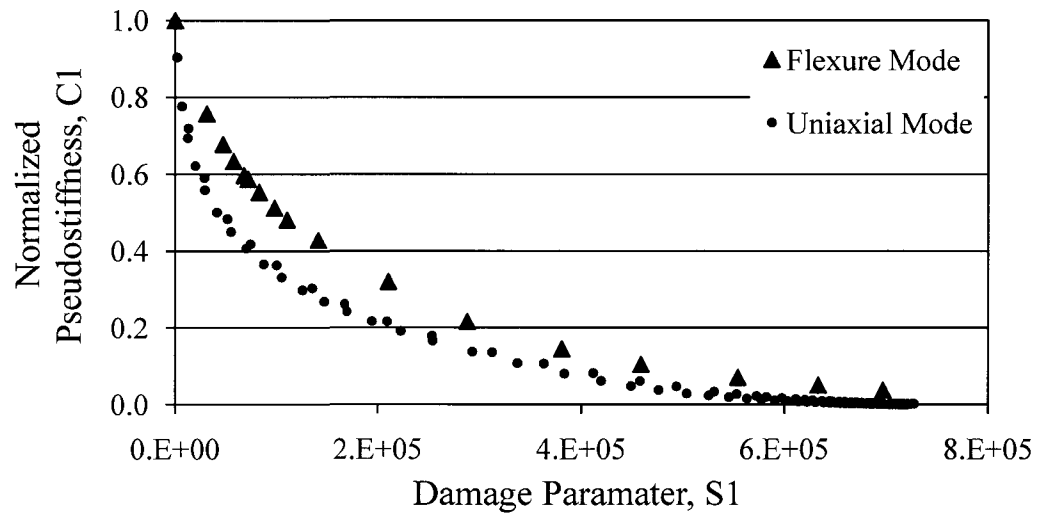
Figure 7-40: Damage characteristic curves for E1 mix with alpha = 1/n

160
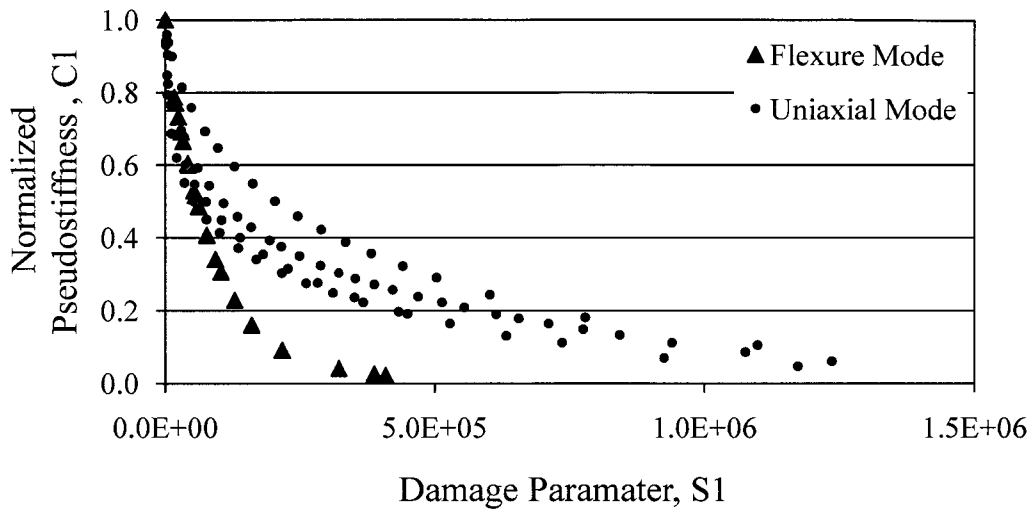
Figure 7-41: Damage characteristic curves for S1 mix with alpha = 1 + 1/n
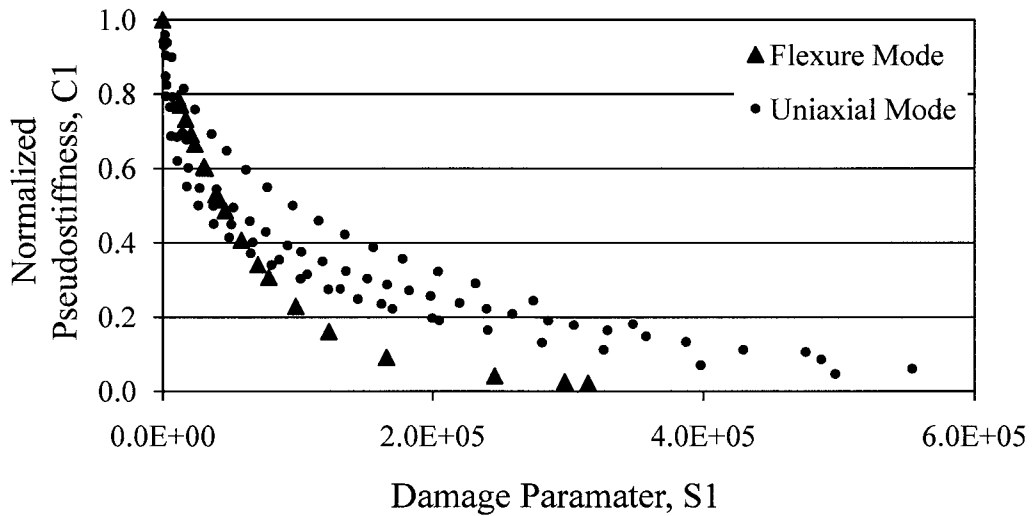
Figure 7-42: Damage characteristic curves for M1 mix with alpha = 1/n

Since it was clear that damage characteristic curves under uniaxial mode are different than under flexure mode of loading, analysis was done to check whether there exists any systematic variation between the damage parameters at a given value of pseudostiffness. Initially, normalized pseudostiffness was regressed against damage parameter to obtain regression coefficients of the damage characteristic curve from each specimen. Both GPM and GEM (Equations 5-4 and 5-5) were used during this analysis. In the next stage, the regression coefficients were used to backcalculate damage parameter values at predetermined values of normalized pseudostiffness. The predetermined values of normalized pseudostiffness ranged from 0.1 to 0.9 in 0.1 increments. In the third stage, the average values of damage parameters at predetermined pseudostiffness values were calculated for a given mode of loading and mixture. These averaged damage parameter values were used to calculate Damage Parameter Ratio (DPR) and percentage difference between uniaxial and flexural damage parameter ($S1\ PD$). The equations to calculate damage parameter ratio and percentage difference are given in Equations 7-17 and 7-18, respectively.

$$DPR = \frac{S1_{c,flex}}{S1_{c,1D}} \qquad \text{7-17}$$

$$S1\ PD = \frac{100 \times \left(S1_{c,flex} - S1_{c,1D}\right)}{S1_{c,flex}} \qquad \text{7-18}$$

where $S1_{c,flex}$ = damage parameter in flexure mode at a given value of c;

$S1_{c,1D}$ = damage parameter in uniaxial mode at a given value of c;

DPR = damage parameter ratio computed using uniaxial and flexural damage parameter; and

$S1\ PD$ = percentage difference between uniaxial and flexural damage parameter.

The damage parameter ratio and percentage difference computed over a range of normalized pseudostiffness for all three mixtures (M1, E1 and S1) backcalculated from GPM and GEM are presented in Tables 7-16 through 7-19. The percentage difference between damage parameter as a function of normalized pseudostiffness using GPM and GEM are presented graphically in Figures 7-43 and 7-44, respectively. The variation of damage parameter ratio with normalized pseudostiffness using material constant $\alpha = 1 + \frac{1}{n}$ and $\alpha = \frac{1}{n}$ backcalculated from GPM regression coefficients are shown in Figures 7-45 and 7-46, respectively. Similar plots obtained using GEM are presented in Figures 7-47 and 7-48, respectively.

Table 7-16: Damage parameter ratio and percentage difference computed using GPM with alpha = 1 + 1/n

Normalized Pseudostiffness	Percentage Difference,S1			Damage Parameter Ratio		
	M1 Mix	E1 Mix	S1 Mix	M1 Mix	E1 Mix	S1 Mix
0.9	67.80	86.82	58.08	3.11	7.59	2.39
0.8	67.91	75.94	27.07	3.12	4.16	1.37
0.7	67.96	65.77	-6.27	3.12	2.92	0.94
0.6	67.94	56.03	-42.81	3.12	2.27	0.70
0.5	67.84	46.60	-82.82	3.11	1.87	0.55
0.4	67.66	37.40	-126.39	3.09	1.60	0.44
0.3	67.32	28.40	-173.60	3.06	1.40	0.37
0.2	66.53	19.56	-249.30	2.99	1.24	0.29
0.1	63.68	7.49	-295.27	2.75	1.08	0.25

Table 7-17: Damage parameter ratio and percentage difference computed using GPM with alpha = 1/n

Normalized Pseudostiffness	Percentage Difference,S1			Damage Parameter Ratio		
	M1 Mix	E1 Mix	S1 Mix	M1 Mix	E1 Mix	S1 Mix
0.9	84.73	87.24	51.68	6.55	7.84	2.07
0.8	84.14	78.42	35.51	6.30	4.63	1.55
0.7	83.78	70.62	18.96	6.16	3.40	1.23
0.6	83.49	63.43	1.63	6.06	2.73	1.02
0.5	83.23	56.65	-16.59	5.96	2.31	0.86
0.4	83.02	50.18	-35.71	5.89	2.01	0.74
0.3	82.80	43.95	-60.40	5.81	1.78	0.62
0.2	82.33	37.93	-100.65	5.66	1.61	0.50
0.1	73.96	30.76	-217.11	3.84	1.44	0.32

Table 7-18: Damage parameter ratio and percentage difference computed using GEM with alpha = 1 + 1/n

Normalized Pseudostiffness	Percentage Difference,S1			Damage Parameter Ratio		
	M1 Mix	E1 Mix	S1 Mix	M1 Mix	E1 Mix	S1 Mix
0.9	68.21	80.18	55.55	3.15	5.05	2.25
0.8	68.78	70.19	25.64	3.20	3.35	1.34
0.7	69.03	61.49	-4.84	3.23	2.60	0.95
0.6	69.13	53.14	-38.13	3.24	2.13	0.72
0.5	69.13	44.61	-76.19	3.24	1.81	0.57
0.4	69.22	35.45	-121.77	3.25	1.55	0.45
0.3	69.33	25.01	-179.82	3.26	1.33	0.36
0.2	70.02	12.04	-250.55	3.34	1.14	0.29
0.1	73.72	4.56	-353.03	3.81	1.05	0.22

Table 7-19: Damage parameter ratio and percentage difference computed using GEM with alpha = 1/n

Normalized Pseudostiffness	Percentage Difference,S1			Damage Parameter Ratio		
	M1 Mix	E1 Mix	S1 Mix	M1 Mix	E1 Mix	S1 Mix
0.9	85.25	82.30	64.80	6.78	5.65	2.84
0.8	84.79	74.38	45.35	6.57	3.90	1.83
0.7	84.44	67.69	26.52	6.43	3.10	1.36
0.6	84.12	61.41	6.73	6.30	2.59	1.07
0.5	83.81	55.11	-15.19	6.18	2.23	0.87
0.4	83.71	48.45	-40.69	6.14	1.94	0.71
0.3	83.77	40.97	-72.23	6.16	1.69	0.58
0.2	84.37	31.82	-108.83	6.40	1.47	0.48
0.1	79.87	29.04	-172.52	4.97	1.41	0.37
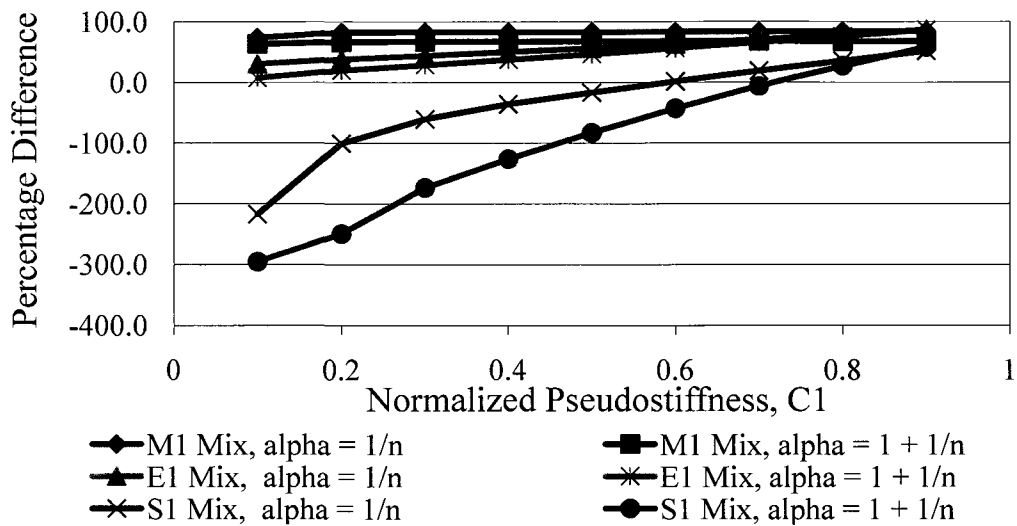
Figure 7-43: Percentage difference between uniaxial and flexural damage parameter as a function of normalized pseudostiffness (using GPM)
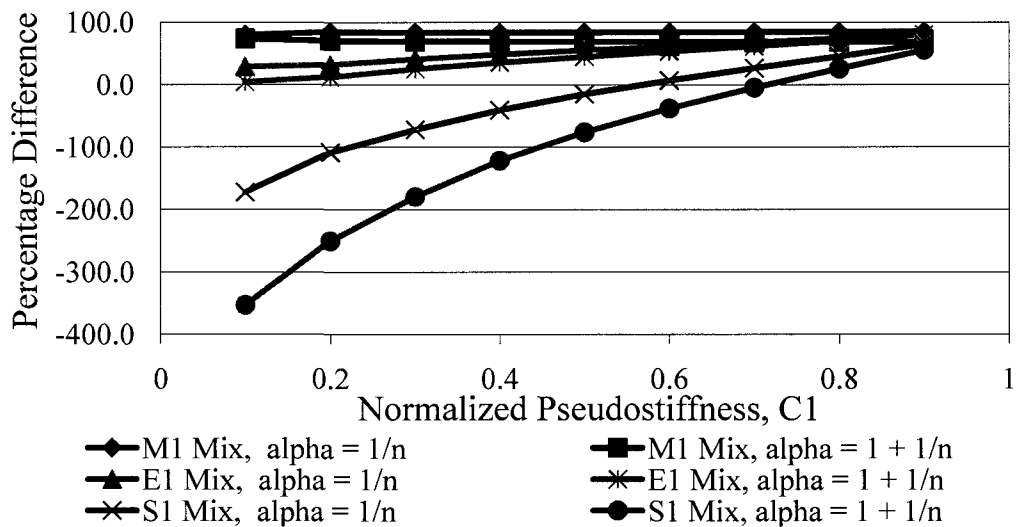
Figure 7-44: Percentage difference between uniaxial and flexural damage parameter as a function of normalized pseudostiffness (using GEM)

Damage Parameter Ratio
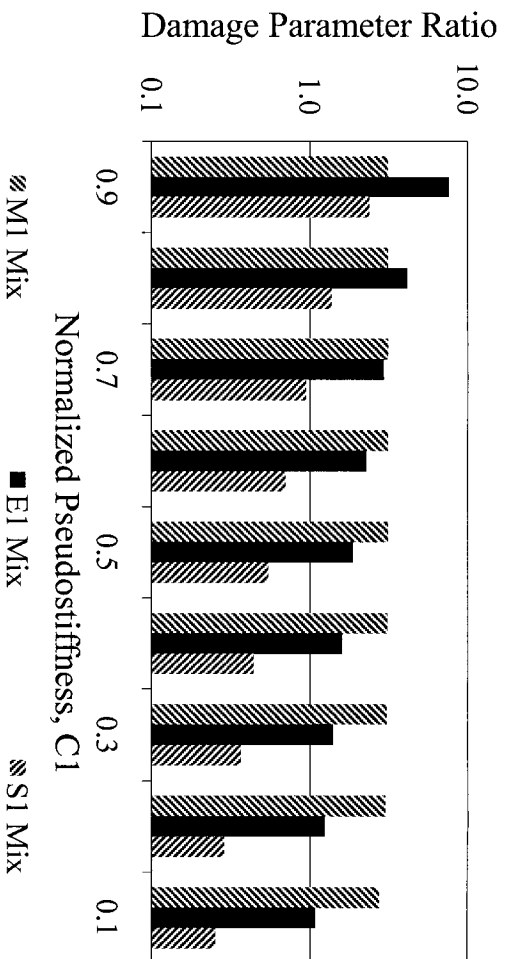
Figure 7-45: Variation of DPR with normalized pseudostiffness backcalculated from GPM with alpha = 1 + 1/n

Damage Parameter Ratio
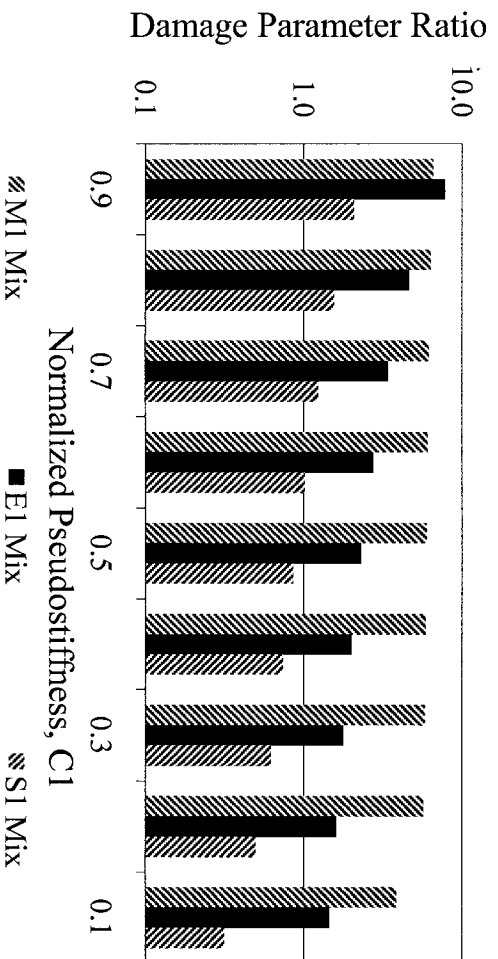
Figure 7-46: Variation of DPR with normalized pseudostiffness backcalculated from GPM with alpha = 1/n

167
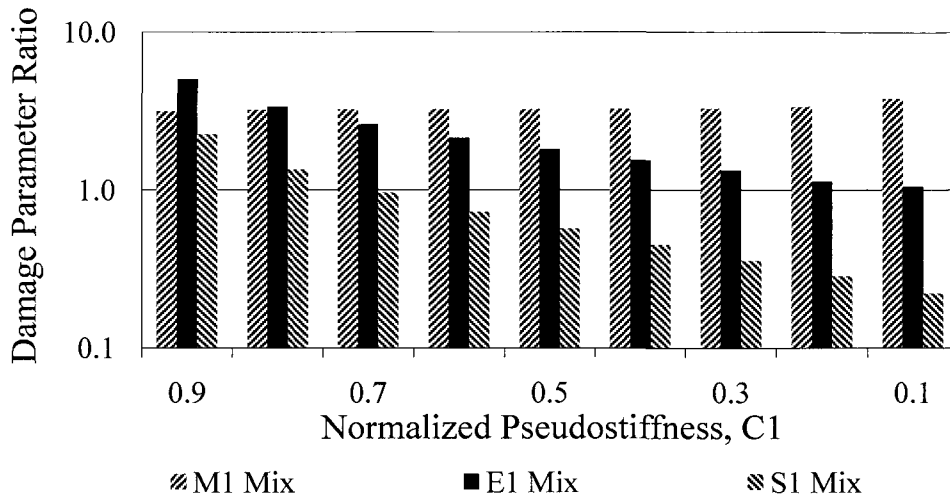
Figure 7-47: Variation of DPR with normalized pseudostiffness backcalculated from GEM with alpha = 1 + 1/n
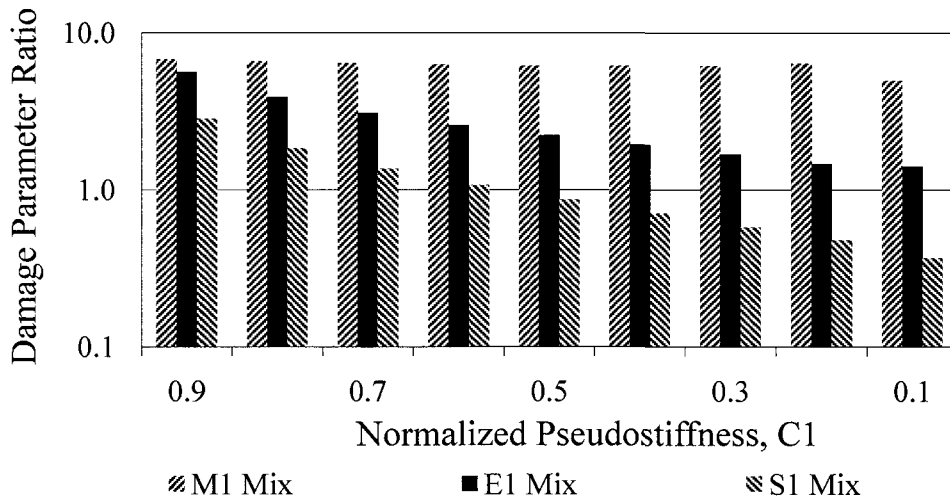
Figure 7-48: Variation of DPR with normalized pseudostiffness backcalculated from GEM with alpha = 1/n

From Tables 7-16 through 7-19, and Figures 7-43 through 7-48 it is clear that damage parameter ratio and percentage difference is dependent on mixture properties.

For mixture M1, percentage difference and damage parameter ratio remained fairly constant while for mixtures E1 and S1, percentage difference increased with decrease in normalized pseudostiffness while damage parameter ratio decreased with simultaneous decrease in normalized pseudostiffness.

For a given value of strain, fatigue life under flexure mode of loading was always more than fatigue life under uniaxial mode of loading. One reason for such difference is difference in stress (strain) field. Under flexure mode, the stress (strain) varies linearly from neutral axis to extreme fiber where as under uniaxial mode stress (or strain) distribution is constant throughout the specimen. Since the strain (stress) amplitude is different at different places, the damage is different at these places.

7.8 <u>Summary</u>

Viscoelastic properties under different modes of loading were compared and it was found that these properties are dependent on mode of loading, material properties and testing frequency. Comparison of the dynamic modulus ratio under flexural and uniaxial mode of loading indicated that at lower frequencies (higher temperature) uniaxial dynamic modulus is less than its counterparts under flexure and biaxial mode of loading. Also, uniaxial dynamic modulus is more sensitive to testing frequency. The dynamic modulus ratio is a function of testing frequency. The differences between the mean values under uniaxial and flexural mode of loading were statistically different especially at the higher frequency range. Comparison of the dynamic modulus ratio under uniaxial and flexural mode of loading, and dynamic modulus ratio under uniaxial and biaxial mode of loading indicated that the modular ratio assumes an asymptotic

value at frequency of 1,000,000 Hz and statistically significant differences were found at the higher frequency range.

Sufficient overlap was found among measured phase angle under uniaxial and flexural mode of loading at frequencies greater than 0.1 Hz. At frequencies less than 1 Hz under biaxial mode and 0.1 Hz under flexure mode of loading, the decrease in phase angle was more when compared to uniaxial counterparts. This indicates aggregate structure has a significant effect on phase angle measurements, especially at higher temperature under flexure and biaxial mode of loading.

Since storage modulus values combined effect of both dynamic modulus and phase angle, it was used as an indicator to check whether mode of loading had any effect on measured viscoelastic properties. Storage modulus ratio and percentage difference indicated these values are dependent on testing frequency and mean values under different modes were statistically different. Also, the ratios were comparable for all three mixtures. Similar observations were made from the relaxation modulus comparison.

Comparison of damage characteristic curves under uniaxial and flexural mode of loading indicated both are visually different. Damage parameter under flexure mode was always greater than under uniaxial mode for a given value of normalized pseudostiffness. This indicated damage evolution mechanisms are different and material under goes damage at a faster rate under uniaxial mode than under flexure mode of loading. In the case of flexure mode, a specimen loses its stiffness at a faster rate at pseudostiffness of around 0.3 (presence of inflection point) where as under uniaxial mode, the rate of reduction in pseudostiffness remains approximately the same. For a

170

given mixture, damage parameter ratio tended to reach a plateau value near failure (normalized pseudostiffness value = 0).

A systematic variation (in terms of percentage differences and ratios) of material properties have been found between different modes of loading (uniaxial vs flexure). The differences in properties (viscoelastic and damage parameters) found between different modes of loading can be attributed to properties of individual mixture components. In principle, these ratios can be used as correction factors to account for the effect of mode on viscoelastic parameters and fatigue testing. This will be of significant advantage when the comparison has to be made.

CHAPTER 8

CONCLUSIONS AND FUTURE WORK

The uniaxial constitutive model has been extended to the flexure mode of loading. The analysis of flexural fatigue data using the extended constitutive model indicated that a unique relationship exists between the normalized pseudostiffness and the damage parameter at a given temperature. A fatigue prediction methodology that uses the extended constitutive model method was proposed. This methodology used data generated from the existing AASHTO testing protocol without any additional effort and instrumentation. Thus, the proposed methodology combines simplicity of the AASHTO protocol with fundamental, mechanics based principles of damage mechanics.

A new method to determine the fatigue endurance limit based on VECD principles was proposed. This new procedure was based on an energy based mechanistic approach and hence is applicable to different testing conditions. This approach is a faster and more efficient method when compared to the traditional approach and essentially removes empiricism in the testing and analysis procedure.

Viscoelastic properties under different modes of loading were measured and predicted. It was found that values of these viscoelastic properties are dependent on mode of loading and mixture properties. The differences between the mean values of dynamic modulus and storage modulus under uniaxial and flexural mode of loading were statistically different especially at the higher frequency range. Modulus ratios for

different viscoelastic properties are suggested. These modulus values are dependent on frequency and modes of loading being compared. It was found that flexure and biaxial mode of loading properties are more influenced by the aggregate microstructure especially at lower frequencies (higher temperature).

Comparison of damage characteristic curves under uniaxial and flexural mode of loading indicated both are visually different. Damage parameter under flexure mode was always greater than under uniaxial mode for a given value of normalized pseudostiffness. This indicated damage evolution mechanisms are different and material under goes damage at a faster rate under uniaxial mode than under flexure mode of loading. For a given mixture, damage parameter ratio tended to attain plateau value near failure (normalized pseudostiffness value = 0).

A systematic variation of material properties have been found between different modes of loading. In principle, these ratios can be used as correction factors to account for the effect of mode on viscoelastic parameters and fatigue testing. This will be of significant advantage and becomes handy when the comparison has to be made.

Recommendations for further study are as follows.

1. Due to limitations in testing equipment and the environmental chamber, the minimum testing temperature under flexure mode of loading was 10 ^{0}C. However, dynamic modulus and storage modulus mastercurves did not show any trends of attaining limiting modulus at low temperature. This in turn affected the overall quality of the master curve and the subsequent extrapolations made. Also, the common region of reduced frequency (time) decreased. Thus it is recommended to conduct complex modulus testing to

obtain dynamic modulus and phase angle measurements at temperatures less than 10 ^{0}C.

2. In this research, increasing amplitude tests were conducted at 20 ^{0}C. It is suggested to conduct these tests at other temperatures to verify the applicability of the proposed approach and compare the damage threshold levels at different temperatures.

3. In this research, damage characteristic curves were constructed using cyclic loading data under flexure mode of loading where as damage was characterized using monotonic test data under uniaxial mode of loading (for mixtures E1 and S1). E1 mixture indicated better overlap between uniaxial and flexure mode than the S1 mixture. Results from mixture M1 indicated that damage characteristic curves obtained from cyclic data was different from damage characteristic curves obtained from monotonic test results. Also, the number of specimens tested using E1 and S1 mixtures were limited. Thus it is recommended to test more specimens under different modes of loading and different testing conditions to make reliable predictions.

4. Previous researches have indicated different compaction methods can produce different aggregate structure and orientation but with similar volumetric properties. Gyratory compaction results in more circumferential oriented aggregate particles due to vertical compressive and horizontal shear force. Slab compaction method results in more randomly oriented aggregate particles due to greater degree of freedom. This aggregate structure can

affect overall properties of mixture. Influence of compaction method has been ignored in this research. Thus it is recommended to obtain specimens of different geometrics from the slab compaction method and test those specimens to evaluate compaction method effect on mechanical properties of asphalt concrete.

LIST OF REFERENCES

AASHTO Standard (2003). Standard Test Method for Determination of Fatigue Life of Compacted Hot Mix Asphalt (HMA) Subjected to Repeated Flexural Bending. TP321-03.

Adhikari, S., and You, Z. (2010). "Fatigue Evaluation of Asphalt Pavement using Beam Fatigue Apparatus." *Technology Interface Journal.*,10(3).

Arambula, E., Masad, E., and Martin, A.E. (2007). "Moisture Susceptibility of Asphalt Mixtures with Known Field Performance: Evaluated with Dynamic Analysis and Crack Growth Model." *Transportation Research Record: Journal of the Transportation Research Board.*, 2007, 20-28.

Bennert, T. (2010). "*SBS vs Elvaloy Modified PG76-22: Evaluation of Asphalt Binder and Mixtures Properties*" Center for Advanced Infrastructure and Transportation, Rutgers University, Piscataway, NJ.

Birgisson, B., Montepara, A., Romeo, E., Roque, R., Roncella, R., and Tebaldi, G. (2007). "Determination of Fundamental Tensile Failure Limits of Mixtures." *Journal of Association of Asphalt Paving Technologists.*,76, 303–344.

Brown, S.F. (1974). "A Simplified Fundamental Design Procedure for Bituminous Pavements." The Highway Engineer., 209(8-9), 14–23.

Brunton, J.M., Brown, S.F., and Pell, P.S. (1987). "Development to the Nottingham Analytical Design Method for Asphalt Pavements." In Proceedings of *6th International Conference on structural design of asphalt pavements*, University of Michigan, Ann Arbor, MI.

C333. Development of New Bituminous Pavement Design Method. Technical report, European commission, Directorate general of transport, Brussels, Belgium, 1999.

Carpenter, S.H., Ghuzlan, K.A., and Shen, S. (2003). "Fatigue Endurance Limit for Highway and Airport Pavements." *Transportation Research Record: Journal of the Transportation Research Board.*, 1832, 131-138.

Carpenter, S.H., and Shen, S. (2006). "A Dissipated Energy Approach to Study Hot-Mix Asphalt Healing in Fatigue." *Transportation Research Record: Journal of the Transportation Research Board.*, 1970, 178-185.

Chehab, G.R. (2002). *"Characterization of Asphalt Concrete in Tension Using a Viscoelastoplactic Model."* Doctoral dissertation, North Carolina State University, Raleigh, NC.

Chehab, G.R., O' Quinn, E.N., and Kim, Y.R. (2000). "Specimen Geometry Study for Direct Tension Test Based on Mechanical Tests and Air Void Variation in Asphalt Concrete Specimens Compacted by Superpave Gyratory Compactor." *Transportation Research Record: Journal of the Transportation Research Board.*, 1723, 125-132.

Chehab, G.R., Kim, Y.R., Schapery, R.A., Witczak, M.W., and Bonaquist, R. (2002). "Time-temperature Superposition Principle for Asphalt Concrete Mixtures with Growing Damage in Tension State." *Journal of Association of Asphalt Paving Technologists.*, 71, 559–593.

Chomton, G., and Valayer, P.J. (1972). "Applied Rheology of Asphalt Mixes Practical Application." In Proceedings of *Third international conference on the structural design of asphalt pavements*, London, 214–225.

Daniel, J.S. (2001). *"Development of a Simplified Fatigue Test and Analysis Procedure Using a Viscoelastic, Continuum Damage Model and its Implementation to WesTrack Mixtures."* Doctoral dissertation, North Carolina State University, Raleigh, NC.

Daniel, J.S., and Kim, Y.R. (2002). "Development of a Simplified Fatigue Test and Analysis Procedure Using a Viscoelastic Continuum Damage Model." *Journal of Association of Asphalt Paving Technologists.*, 71, 619–650.

Daniel, J.S., and Mogawer, W. S. (2010). *"Determining the Effective PG Grade of Binder in RAP Mixes."* New England Transportation Consortium, NETC Report No: NETCR78.

Daniel, J.S., Chehab, G.R., and Kim, Y.R. (2004). "Issues Affecting Measurement of Fundamental Asphalt Mixture Properties." *Journal of Materials in Civil Engineering.*, 16 (5), 469-476.

Finn, F.N., Saraf, C., Kulkarni, R., Nair, K., Smith, W., and Abudllah, A. (1977). "Use of Distress Prediction Subsystems in the Design of Pavement Structures." In Proceedings of *Fourth International Conference on the Structural Design of Asphalt Pavements*, University of Michigan, Ann Arbor, MI.

Guzlan, K.A., and Carpenter, S. H. (2000). "Energy-derived, Damage-based Failure Criterion for Fatigue Testing." *Transportation Research Record: Journal of the Transportation Research Board.*, 1723, 141–149.

Ghuzlan, K. (2001). *"Fatigue Damage Analysis in Asphalt Concrete Mixtures Based Upon Dissipated Energy Concepts."* Doctoral dissertation, University of Illinois at Urbana-Champaign, Champaign, IL.

Hondros, G. (1959). "The Evaluation of Poisson's Ratio and the Modulus of Materials of a Low Tensile Resistance by the Brazilian Indirect Tensile Test with Particular Reference to Concrete." *Australian Journal of Applied Science.*, 10(3), 243–268.

Hou, T., Underwood, B.S., and Kim, Y.R. (2010). "Fatigue Performance Prediction of North Carolina Mixtures Using the Simplified Viscoelastic Continuum Damage Model." *Journal of Association of Asphalt Paving Technologists.*, 79, 35–80.

Jacobs, M.M., Hopman, P.C., and Molenaar, A.A.A. (1995). "Application of Fracture Mechanics Principles to Analyze Cracking in Asphalt Concrete." *Journal of Association of Asphalt Paving Technologists.*, 64, 1–36.

Kachanov, L.M. (1958). "Time of Rupture Process under Creep Conditions." *Izvestiya Akademii Nauk.*, 8, 26–31.

Kim, Y.R. (1988). *"Evaluation of Healing and Constitutive Modeling of Asphalt Concrete by Means of Theory of Nonlinear Viscoelasticity and Damage Mechanics."* Doctoral dissertation, Texas A & M University, College Station, TX.

Kim, Y.R., and Little, D.N. (1990). "One-dimensional Constitutive Modeling of Asphalt Concrete." *Journal of Engineering Mechanics.*, 116(4), 751–772.

Kim, Y.R., Lee, Y.C., and Lee, H.J. (1995)."Correspondence Principle for Characterization of Asphalt Concrete." *Journal of Materials in Civil Engineering.*, 7(1), 59–68.

Kim, Y.R., Seo, Y., King, M., and Momen, M. (2004). "Dynamic Modulus Testing of Asphalt Concrete in Indirect Tension Mode." *Transportation Research Record: Journal of Transportation Research Board.*, 1891, 163-173.

Kim, Y.R., Little, D.N., and Lytton, R.L. (2002). "Use of Dynamic Mechanical Analysis (DMA) to Evaluate the Fatigue and Healing Potential of Asphalt Binders in Sand Asphalt Mixtures." *Journal of Association of Asphalt Paving Technologists.*, 71, 176–206.

Kim, Y.R., King, M., and Momen, M. (2005). *"Typical Dynamic Moduli for North Carolina Asphalt Concrete Mixes"* Final report to the North Carolina Department of Transportation, Report No. FHWA/NC/2005-03.

Kutay, M.E., Gibson, N., and Youtcheff, J. (2008). "Conventional and Viscoelastic Continuum Damage (VECD) Based Fatigue Analysis of Polymer Modified Asphalt Pavements." *Journal of Association of Asphalt Paving Technologists.*, 77, 395-434.

Little, D.N., and Bhasin, A. (2008). "Exploring Mechanism of Healing in Asphalt Mixtures and Quantifying its Impact." *Self Healing Materials.*, 100, 205-218.

Lee, H.J. (1996). *"Uniaxial Constitutive Modeling of Asphalt Concrete using Viscoelasticity and Continuum Damage Theory."* Doctoral dissertation, North Carolina State University, Raleigh, NC.

Lee, H.J., and Kim, Y.R. (1998a). "Viscoelastic Constitutive Model for Asphalt Concrete under Cyclic Loading." *Journal of Engineering Mechanics.*, 124(1), 32–40.

Lee, H. J., and Kim, Y. R. (1998b). "Viscoelastic Continuum Damage Model of Asphalt Concrete with Healing." *Journal of Engineering Mechanics.*, 124(11), 1224–1232.

Lemaitre, J., and Desmorat, R. (2005). *"Engineering Damage Mechanics: Ductile, Creep, Fatigue and Brittle Failures."* Springer Verlag, Heidelberg, Germany.

Maupin, G.W., Jr. and Freeman, J.R., Jr. (1976). *"Simple Procedure for Fatigue Characterization of Bituminous Concrete."* Final Report No. FHWA-RD-76-102, Federal Highway Administration, Washington, DC.

Molenaar, A.A.A. (2007). "Prediction of Fatigue Cracking in Asphalt Pavements: Do We Follow the Right Approach?" *Transportation Research Record: Journal of the Transportation Research Board.*, 2001, 155–162.

Molenaar, A.A.A., Scarpas, A., Liu, X., and Erkens, S.M.J.G. (2002). "Semi-circular Bending Test Simple But Useful." *Journal of Association of Asphalt Paving Technologists.*, 71, 794-815.

Masad, E., Castelo-Branco, V.T.F., Little, D.N., and Lytton, R. (2008). "A Unified Method for the Analysis of Controlled-Strain and Controlled-Stress Fatigue Testing." *International Journal of Pavement Engineering.*, 9(4), 233-246.

Monismith, C.L., and McLean, D.B. (1972). "Structural Design Considerations." *Journal of Association of Asphalt Paving Technologists.*, 41, 258–304.

Monismith, C.L., Epps, J.A., and Finn, F.N. (1985). "Improved Asphalt Mix Design." *Journal of Association of Asphalt Paving Technologists.*, 54, 347–407.

Park, S.W. (1994). *"Development of a Nonlinear Thermo-viscoelastic Constitutive Equation for Particulate Composites with Damage."* Doctoral dissertation, University of Texas at Austin, Austin, TX.

Park, S.W., Kim, Y.R., and Schapery, R.A. (1996). "A Viscoelastic Continuum Damage Model and its Application to Uniaxial Behavior of Asphalt Concrete." *Mechanics of materials.*, 24(4), 241–255.

Prowell, B., Brown, E.R., Anderson, M., Daniel, J.S., Krishna Swamy, A., Quintus, H.V., Shen, S., Carpenter, S.H., Bhattacharjee, S., and Maghsoodloo, S. (2008). *"Validating the Fatigue Endurance Limit for Asphalt Concrete"*. NCHRP report 646, Transportation Research Board, Washington D.C.

Pronk, A.C. (1998). "Harmonization of Bending Fatigue Tests: A(n) (Im)possibility?." In Proceedings of *Wenbouwkundige Werkdagen*, CROW, Ede, Netherlands.

Rabotnov, I.N. (1963). "Progress in Applied Mechanics -The Prager Anniversary Volume." MacMillan, New York.

Rowe, G.M. (1993). "Performance of the Asphalt Mixtures in the Trapezoidal Fatigue Test." *Journal of Association of Asphalt Paving Technologists.*, 62, 344-384.

Si, Z., Little, D.N., and Lytton, R.L. (2002). "Evaluation of Fatigue Healing Effect of Asphalt Concrete by Pseudostiffness." *Transportation Research Record: Journal of the Transportation Research Board.*, 1789, 73–79.

Schapery, R.A. (1984). "Correspondence Principles and a Generalized j-integral for Large Deformation and Fracture Analysis of Viscoelastic Media." *International Journal of Fracture.*, 25(3), 195–223.

Schapery, R.A. (1990). "A Theory of Mechanical Behavior of Elastic Media with Growing Damage and Other Changes in Structure." *Journal of the Mechanics and Physics of Solids.*, 38(2), 215–253.

Schapery, R.A. (1999). "Nonlinear Viscoelastic and Viscoplastic Constitutive Equations with Growing Damage." *International Journal of Fracture.*, 97, 33–66.

Shen, S., and Carpenter, S.H. (2005). "Application of Dissipated Energy Concept in Fatigue Endurance Limit Testing." *Transportation Research Record: Journal of the Transportation Research Board.*, 1929, 165–173.

Tayebali, A.A., Deacon, J.A., Coplantz, J.S., and Monismith, C.L. (1993). "Modeling Fatigue Response of Asphalt Aggregate Mixtures." *Journal of Association of Asphalt Paving Technologists.*, 62, 385–421.

Tayebali, A.A., Deacon, J.A., and Monismith, C.L. (1996). "Development and Evaluation of Dynamic Flexural Beam Fatigue Test System." *Transportation Research Record: Journal of the Transportation Research Board.*, 1545, 89-97.

Tayebali, A.A., Deacon, J.A., Coplantz, J.S., Harvey, J.T., and Monismith, C.L. (1994). "Mixture and Mode of Loading Effects on Fatigue Response of Asphalt-Aggregate Mixtures." *Journal of Association of Asphalt Paving Technologists.*, 63, 118-151.

Underwood, B.S., Kim, Y.R., and Guddati, M.N. (2010). "Improved Calculation Method of Damage Parameter in Viscoelastic Continuum Damage Model." *International Journal of Pavement Engineering.*, 11(6), 459-476.

Underwood, B.S., Kim, Y.R., Guddati, M.N., Thirunavukkarasu, S., and Savadatti, S. (2009). "Response and Fatigue Performance Modeling of ALF Pavements using 3-D Finite Element Analysis and a Simplified Viscoelastic Continuum Damage Model." *Journal of Association of Asphalt Paving Technologists.*, 78, 743–776.

Uzan, J., Perl, M., and Sides, A. (1985). "Viscoelastoplastic Model for Predicting Performance of Asphalt Mixtures." *Transportation Research Record: Journal of the Transportation Research Board.*, 1043, 78–79.

Van Dijk, W., and Vesser, W. (1977). "The Energy Approach to Fatigue for Pavement Design." *Journal of Association of Asphalt Paving Technologists.*, 46, 1–40.

APPENDICES

APPENDIX - A

MASTERCURVES OF VISCOELASTIC PARAMETERS
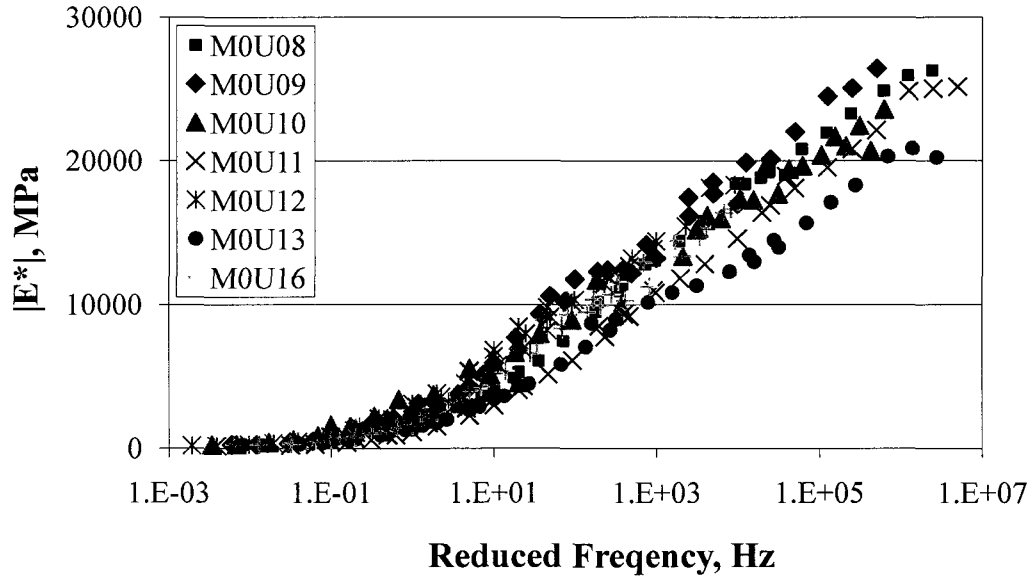
Figure A-1: Dynamic modulus mastercurves for M0 mixture specimens under uniaxial mode
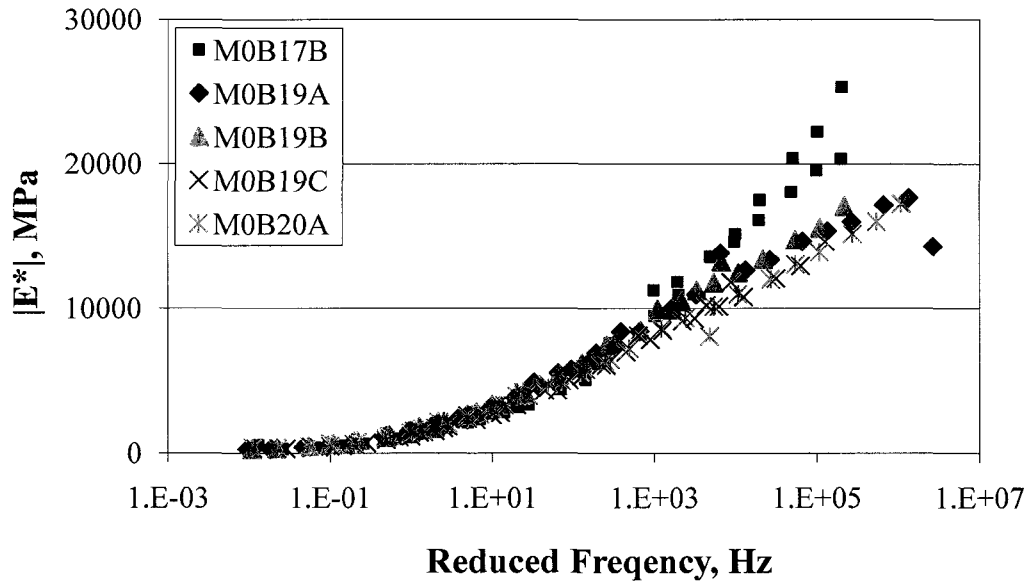
Figure A-2: Dynamic modulus mastercurves for M0 mixture specimens under biaxial mode
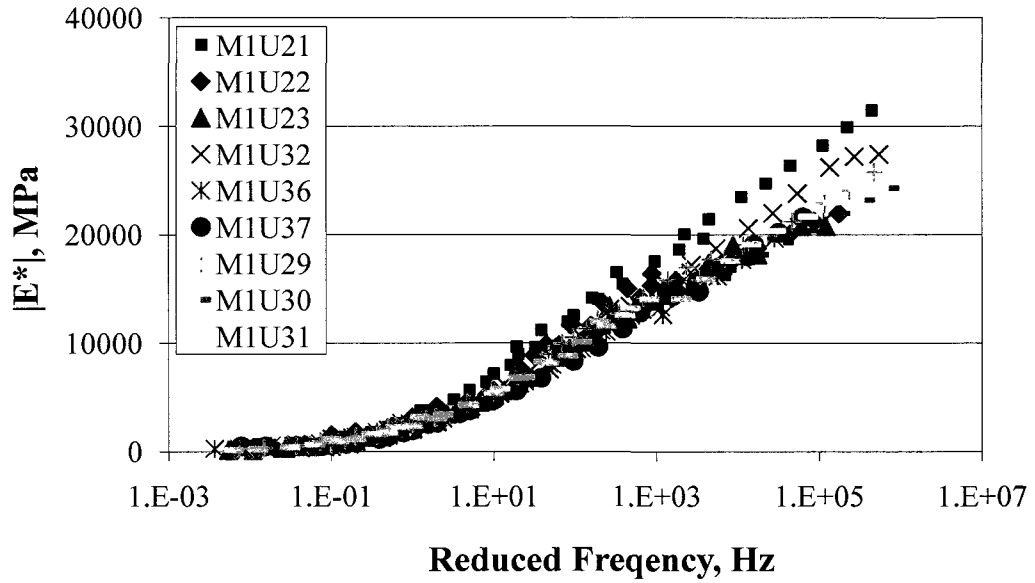
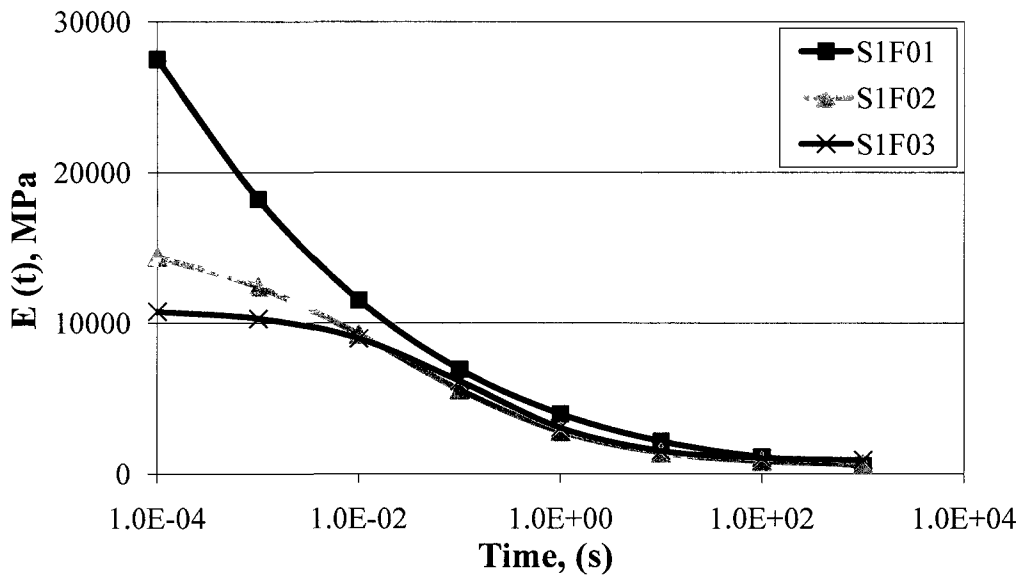**Figure A-3: Dynamic modulus mastercurves for M1 mixture specimens under uniaxial mode**
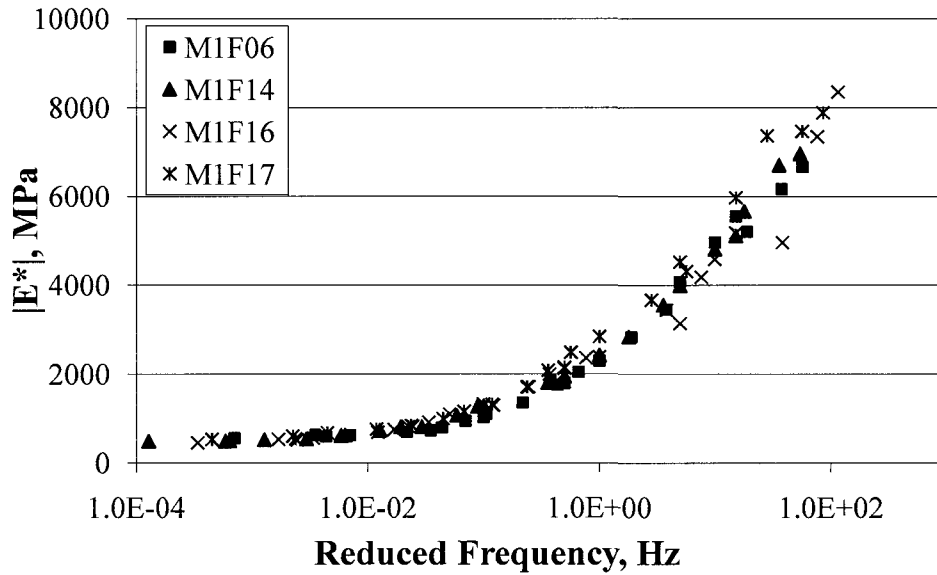
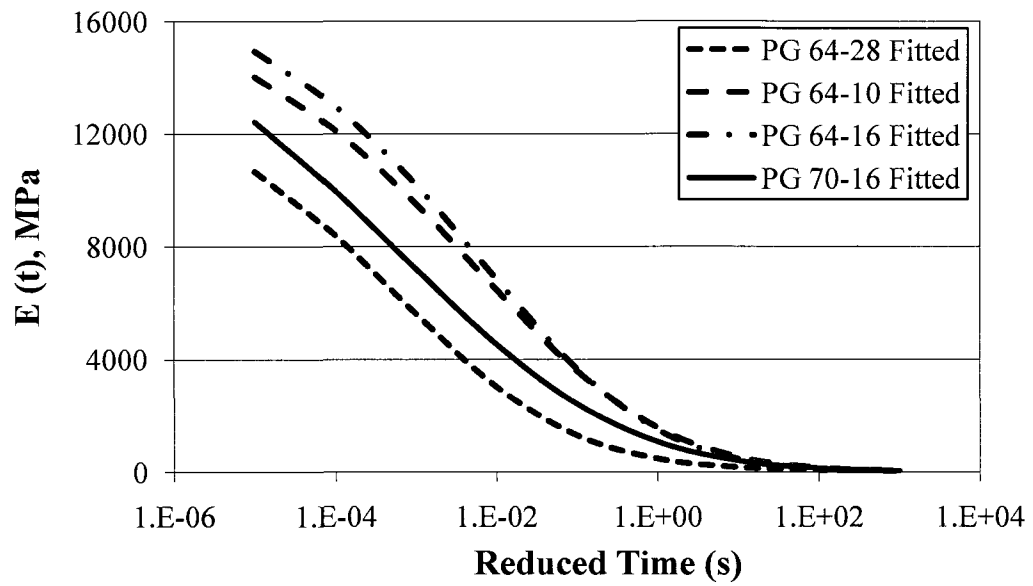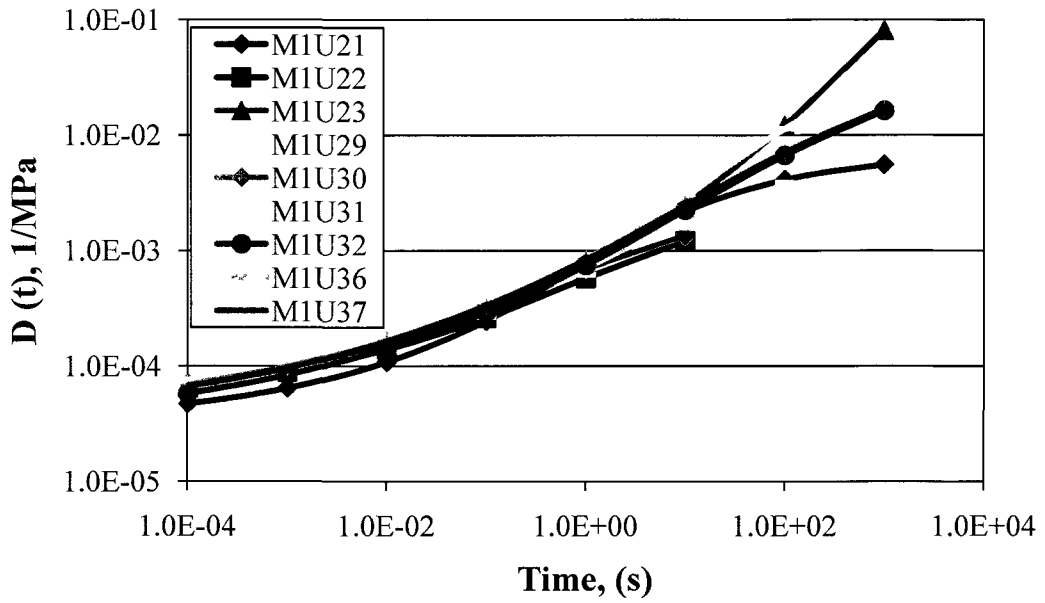**Figure A-4: Dynamic modulus mastercurves for M1 mixture specimens under flexure mode**

186
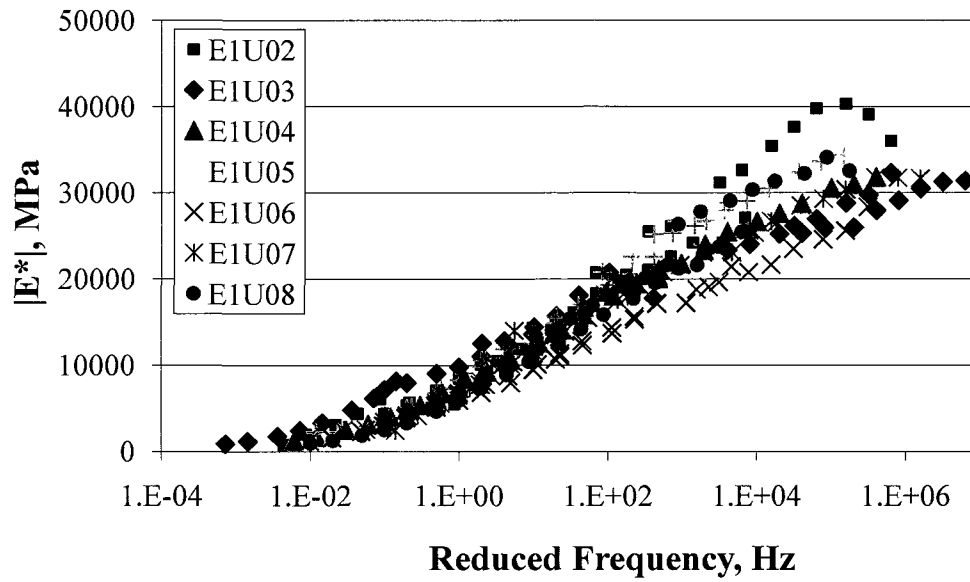
Figure A-5: Dynamic modulus mastercurves for E1 mixture specimens under uniaxial mode
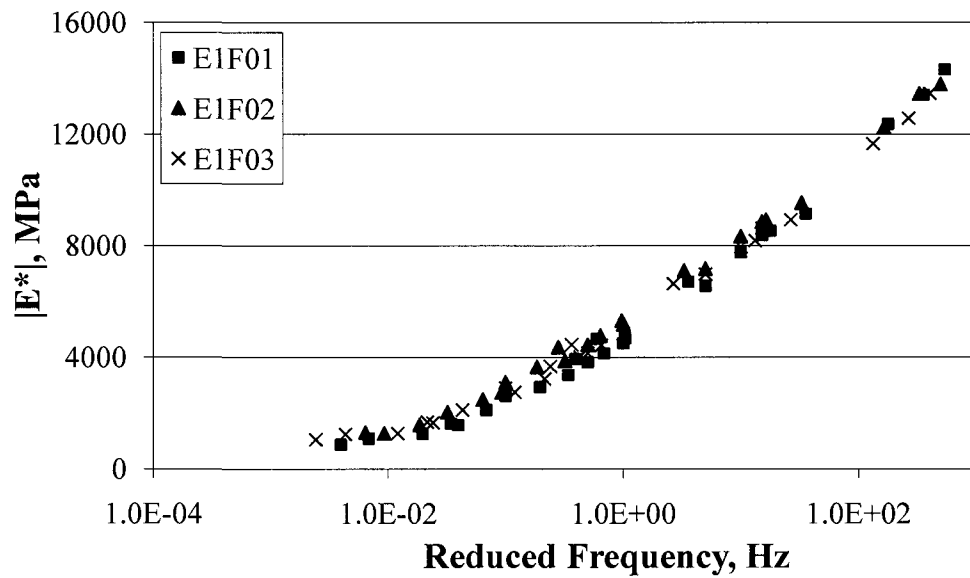
Figure A-6: Dynamic modulus mastercurves for E1 mixture specimens under flexure mode
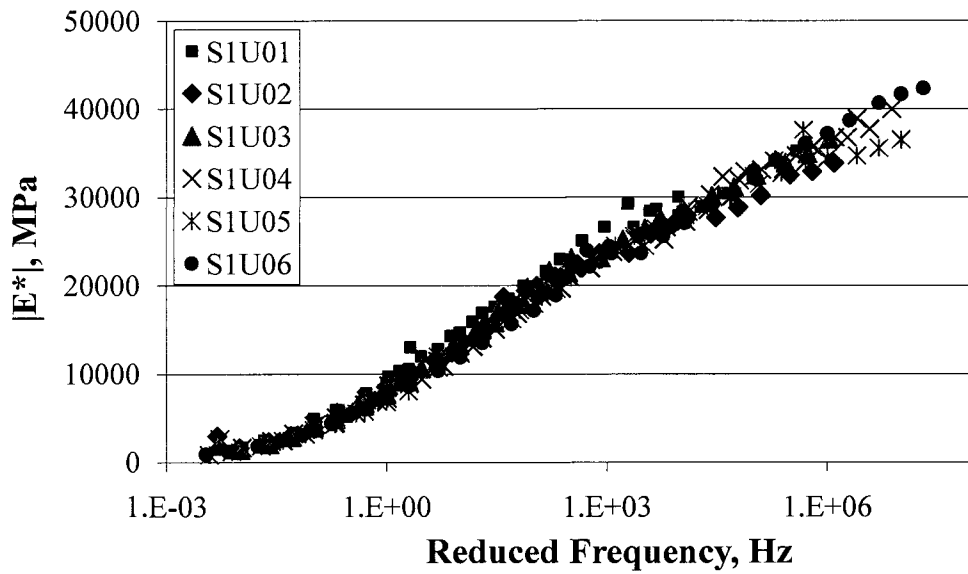
Figure A-7: Dynamic modulus mastercurves for S1 mixture specimens under uniaxial mode
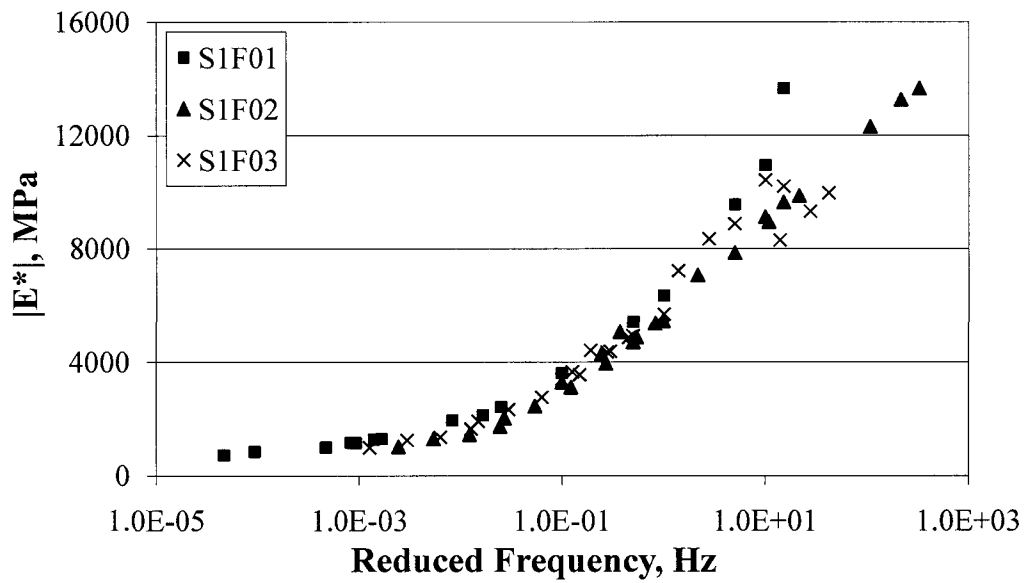
Figure A-8: Dynamic modulus mastercurves for S1 mixture specimens under flexure mode
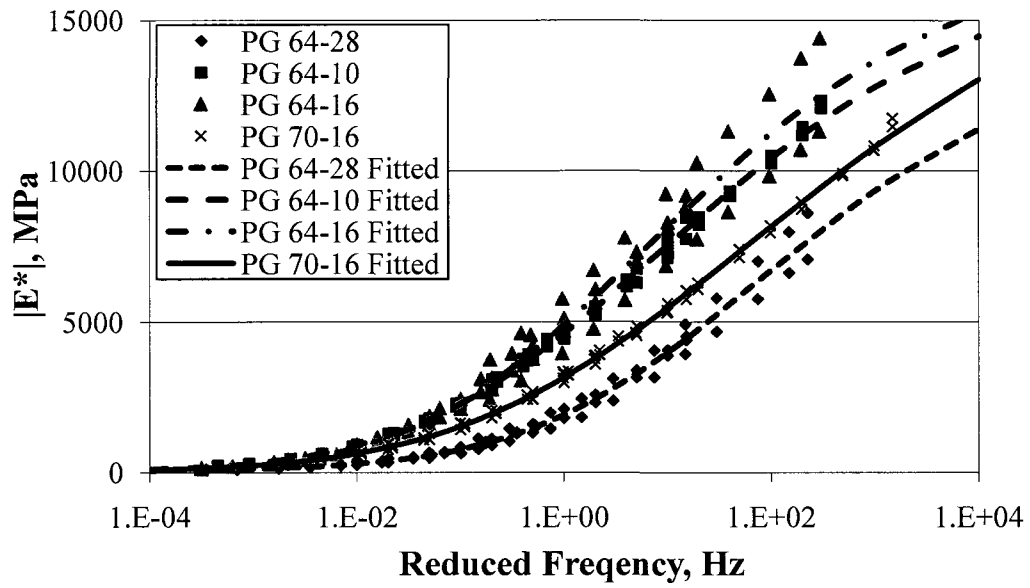
Figure A-9: Dynamic modulus mastercurves for CalTrans mixtures under flexure mode
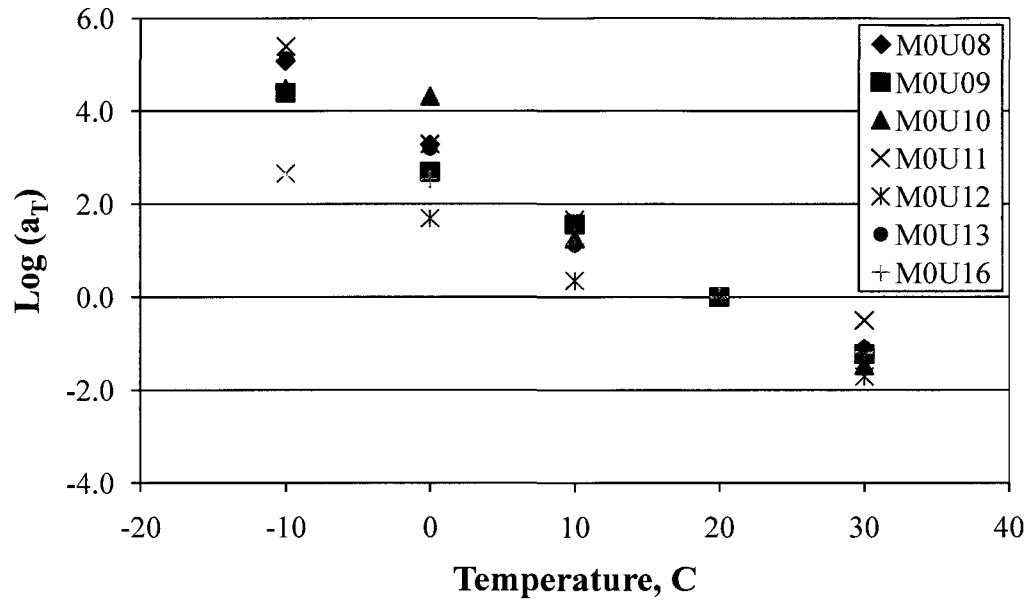
Figure A-10: Temperature shift factors for M0 mixture specimens under uniaxial mode
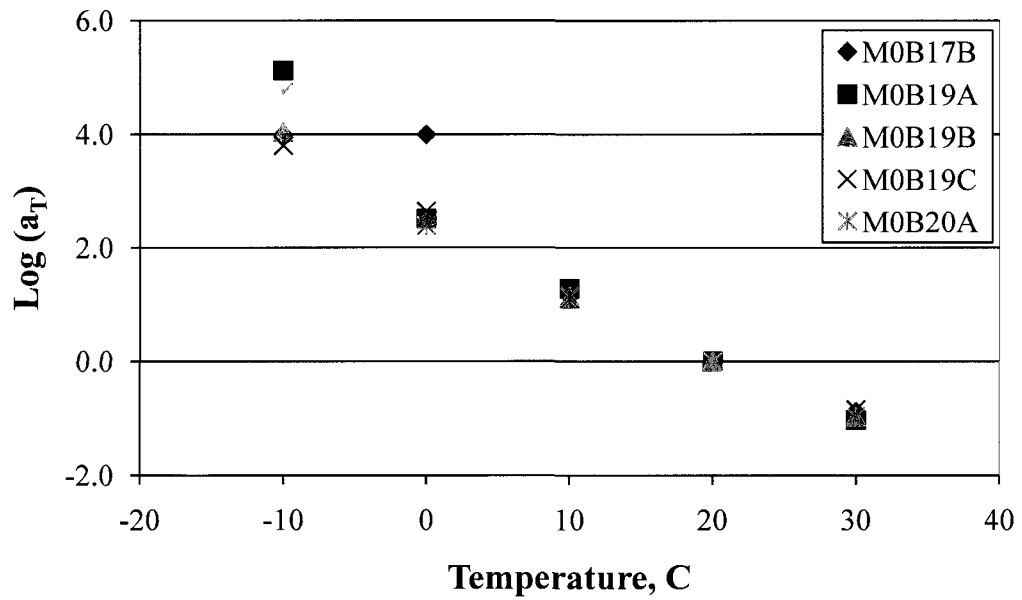
Figure A-11: Temperature shift factors for M0 mixture specimens under biaxial mode
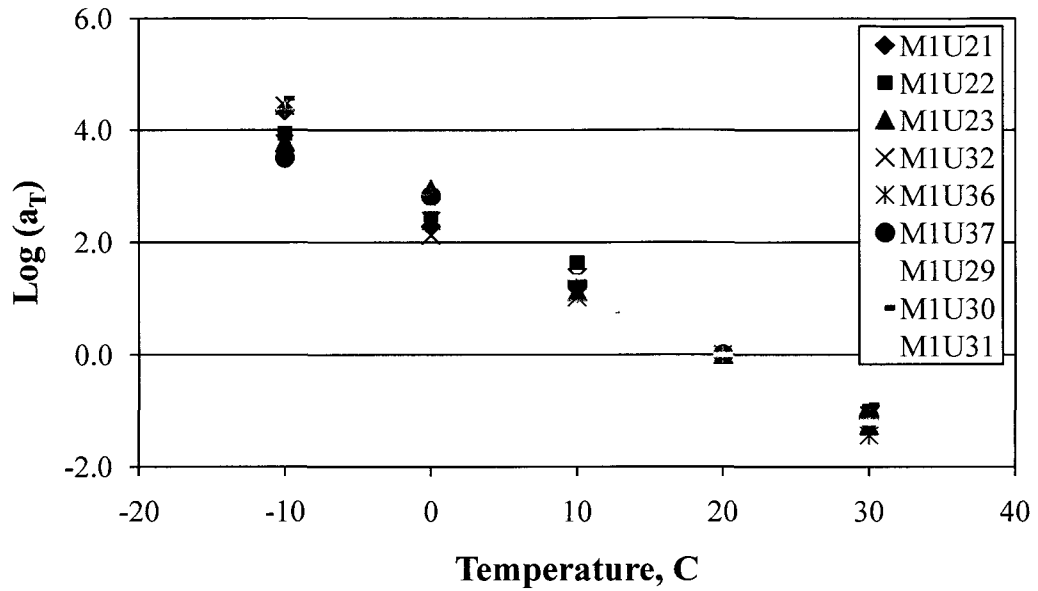
Figure A-12: Temperature shift factors for M1 specimens mixture under uniaxial mode
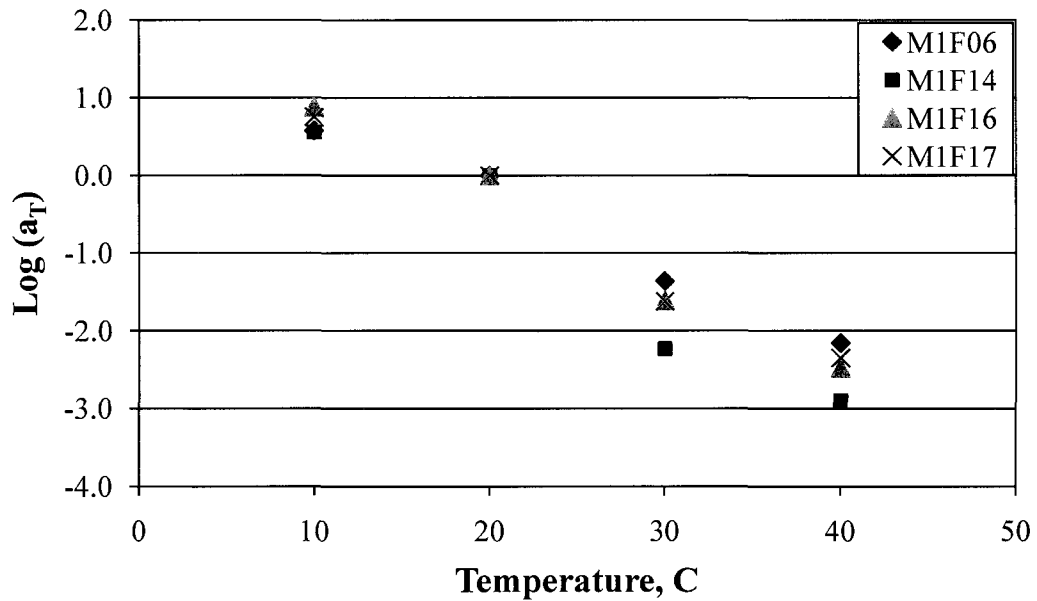
Figure A-13: Temperature shift factors for M1 mixture specimens under flexure mode

191
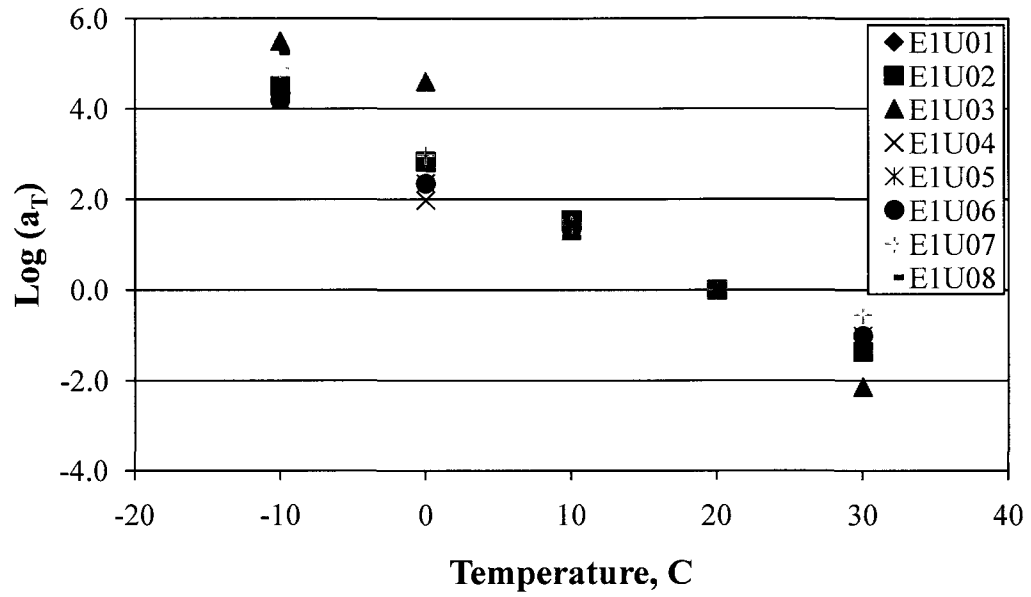
Figure A-14: Temperature shift factors for E1 mixture specimens under uniaxial mode
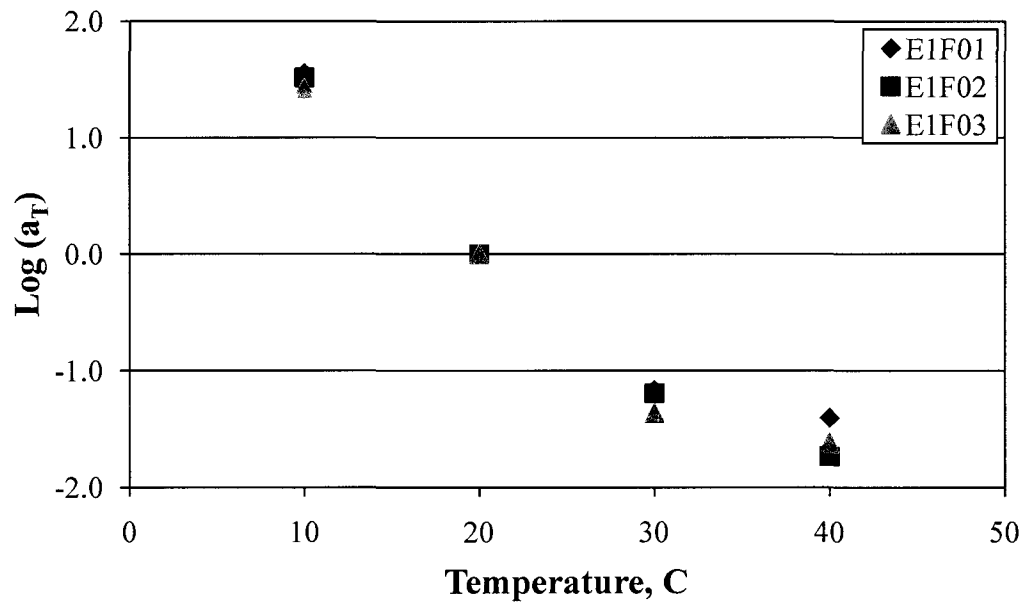
Figure A-15: Temperature shift factors for E1 mixture specimens under flexure mode
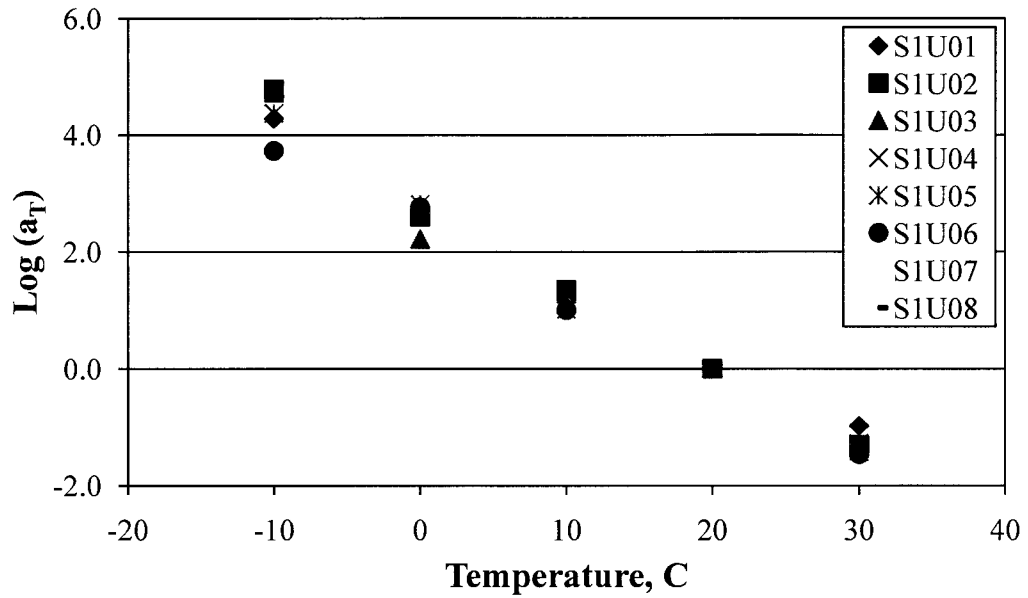
Figure A-16: Temperature shift factors for S1 mixture specimens under uniaxial mode
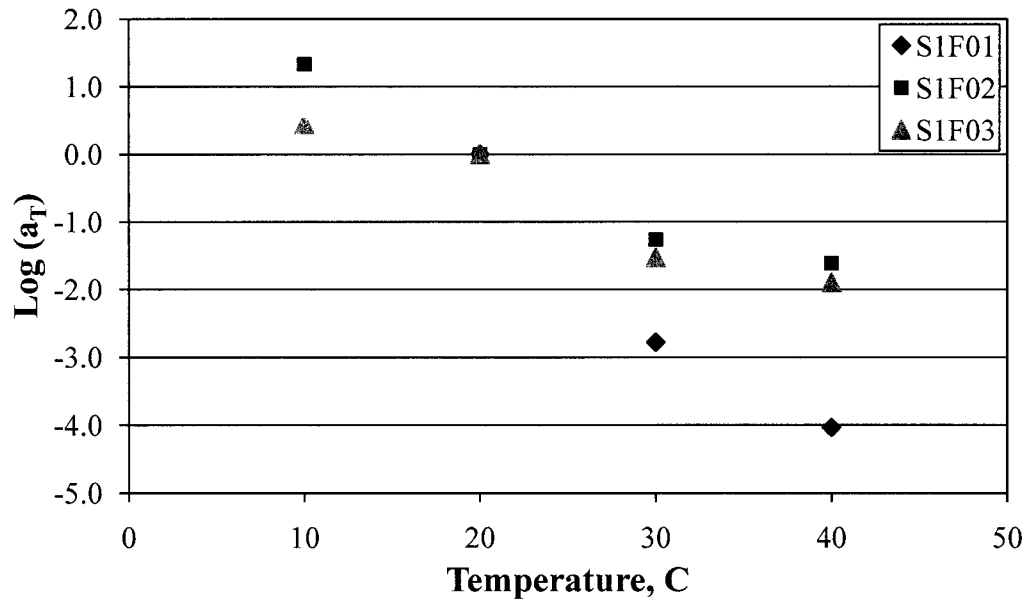
Figure A-17:Temperature shift factors for S1 mixture specimens under flexure mode
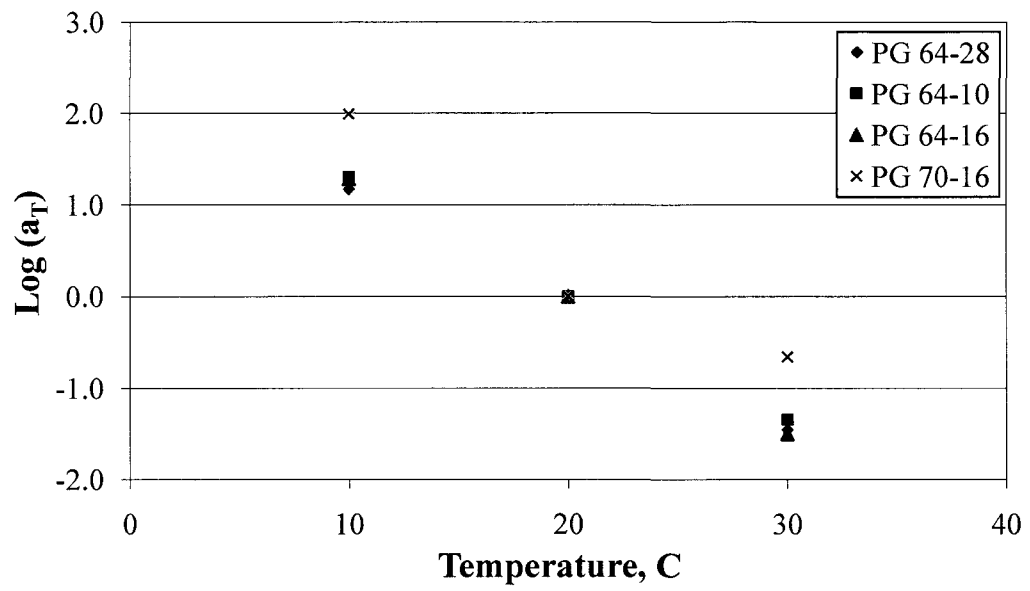
Figure A-18: Temperature shift factors for CalTrans mixtures under flexure mode
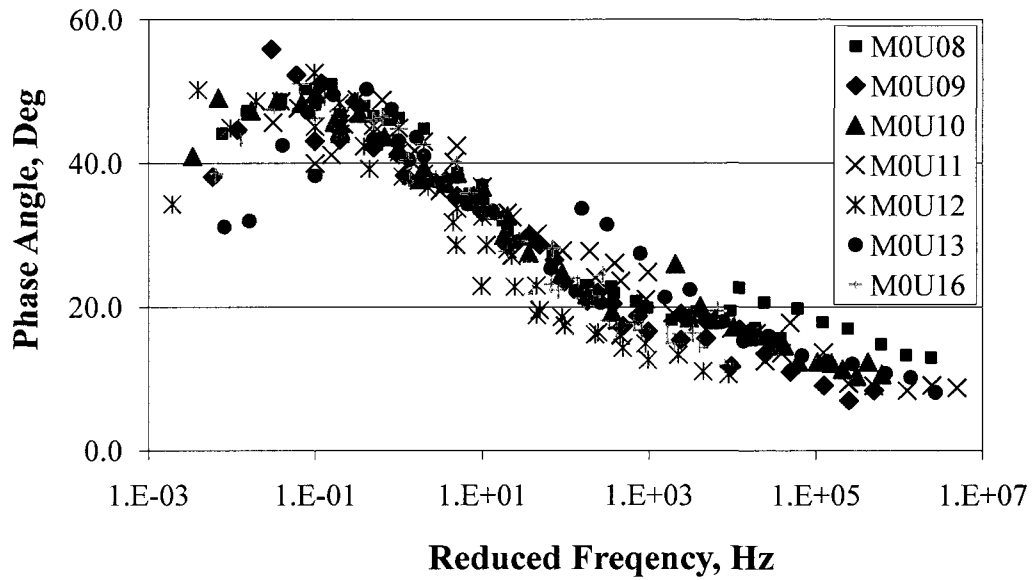
Figure A-19: Phase angle modulus mastercurves for M0 mixture specimens under uniaxial mode
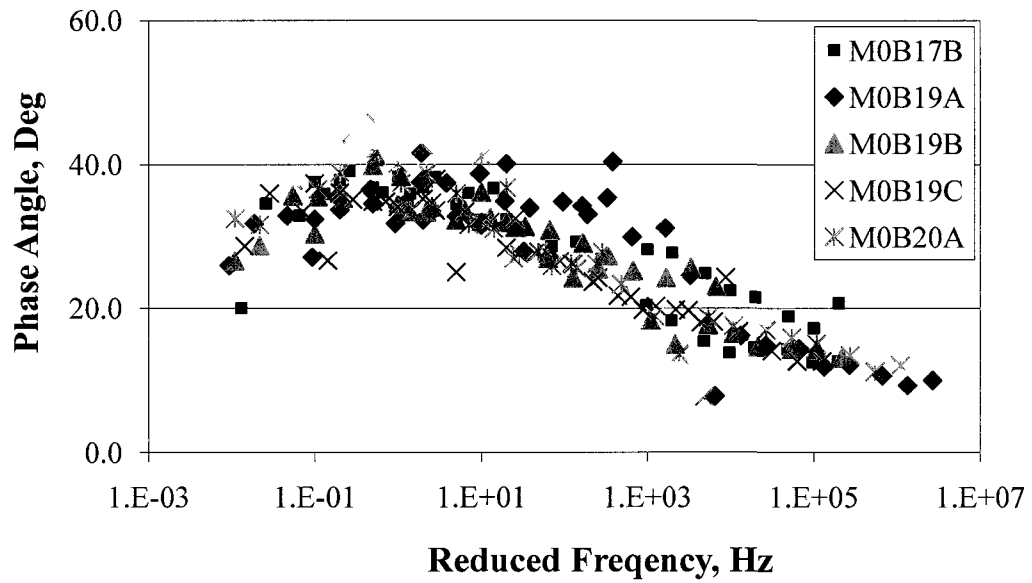
Figure A-20: Phase angle modulus mastercurves for M0 mixture specimens under biaxial mode
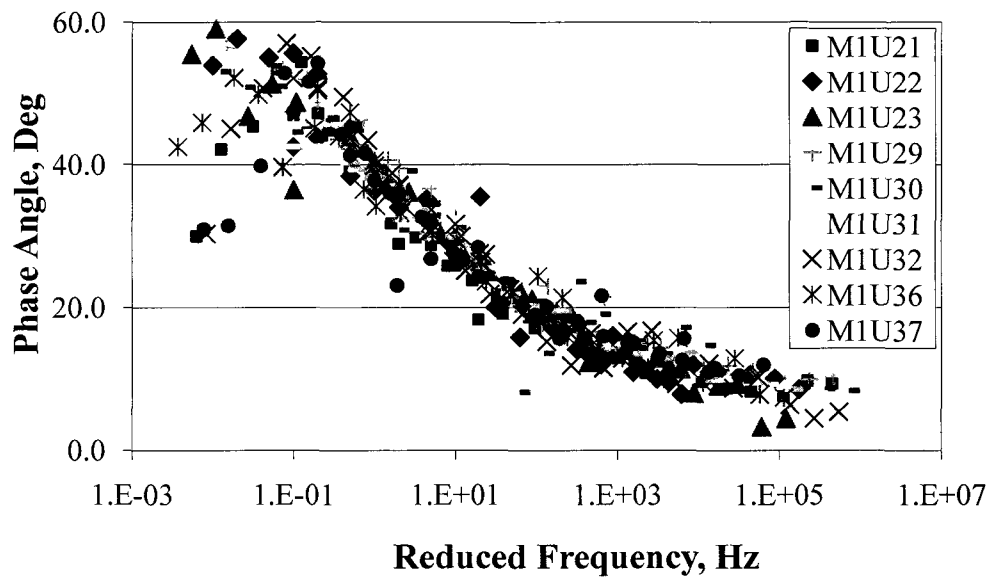
Figure A-21: Phase angle modulus mastercurves for M1 mixture specimens under uniaxial mode
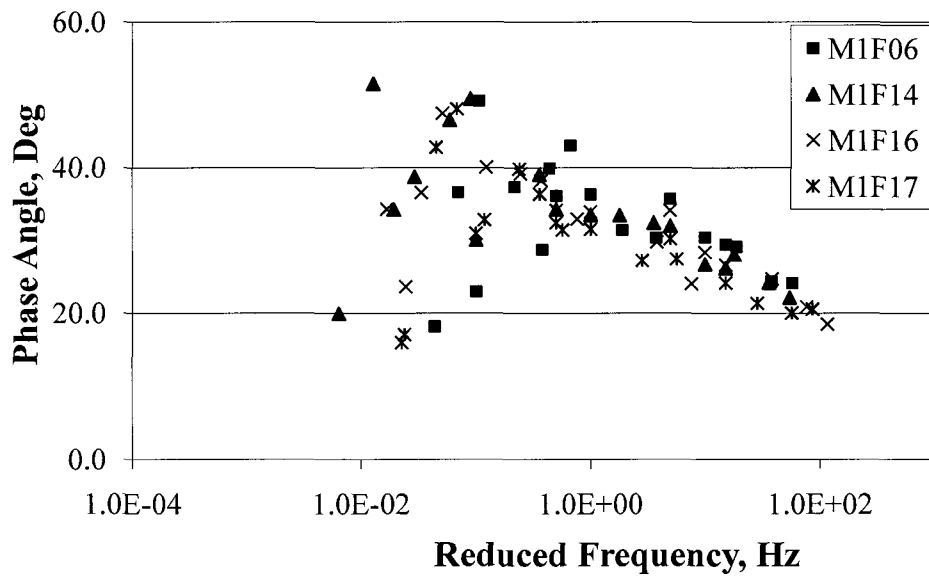
Figure A-22: Phase angle modulus mastercurves for M1 mixture specimens under flexure mode

196
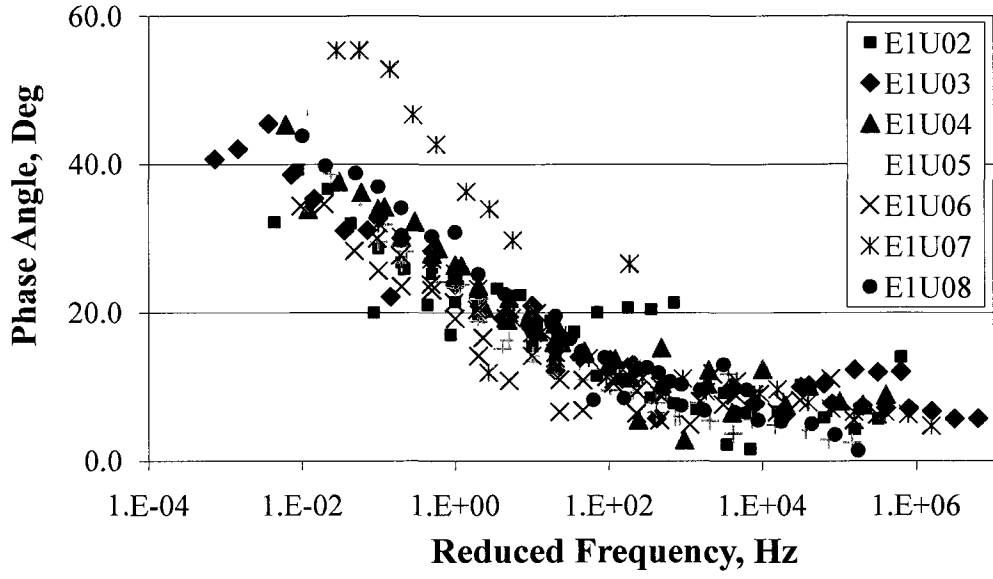
Figure A-23: Phase angle modulus mastercurves for E1 mixture specimens under uniaxial mode
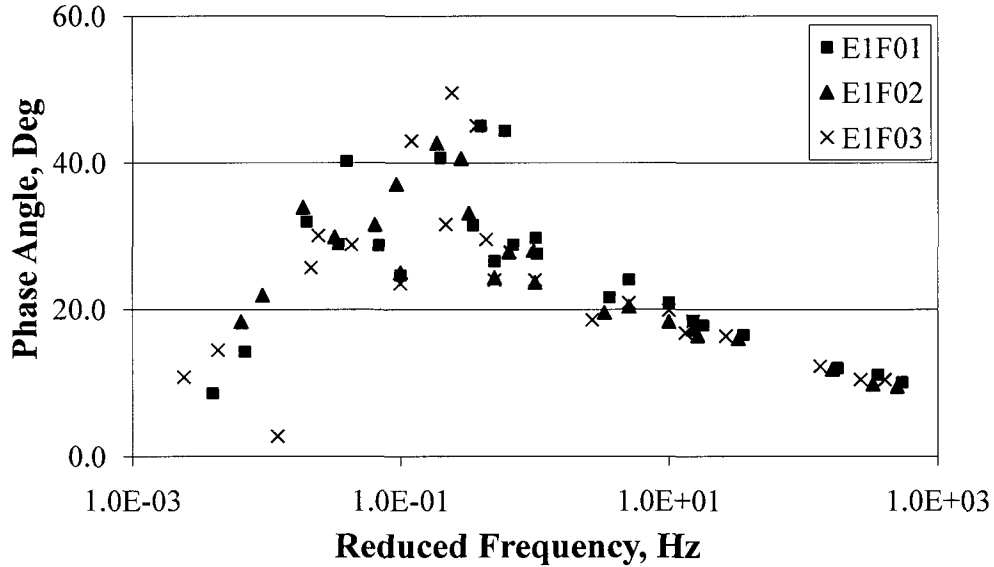
Figure A- 24: Phase angle modulus mastercurves for E1 mixture specimens under flexure mode
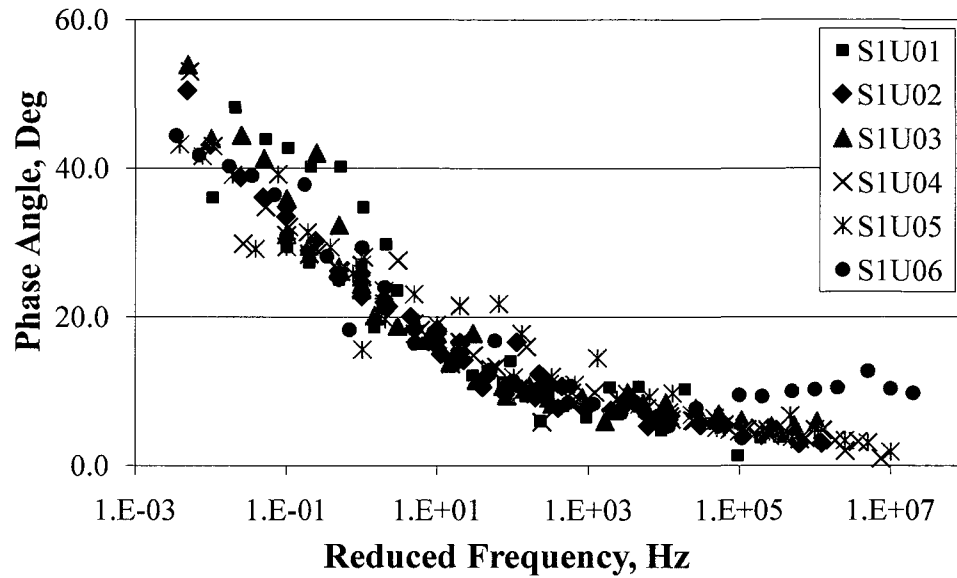
Figure A-25: Phase angle modulus mastercurves for S1 mixture specimens under uniaxial mode
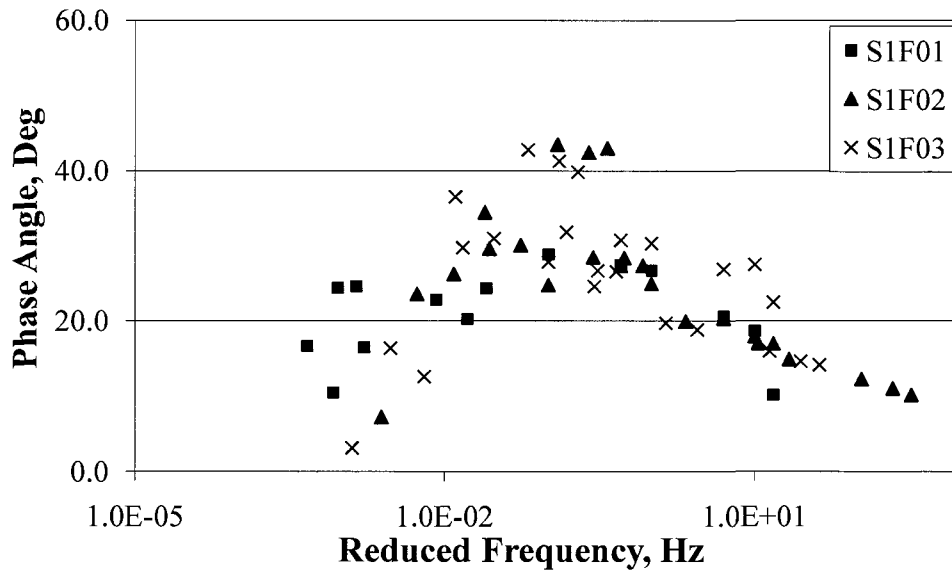
Figure A-26: Phase angle modulus mastercurves for S1 mixture specimens under flexure mode
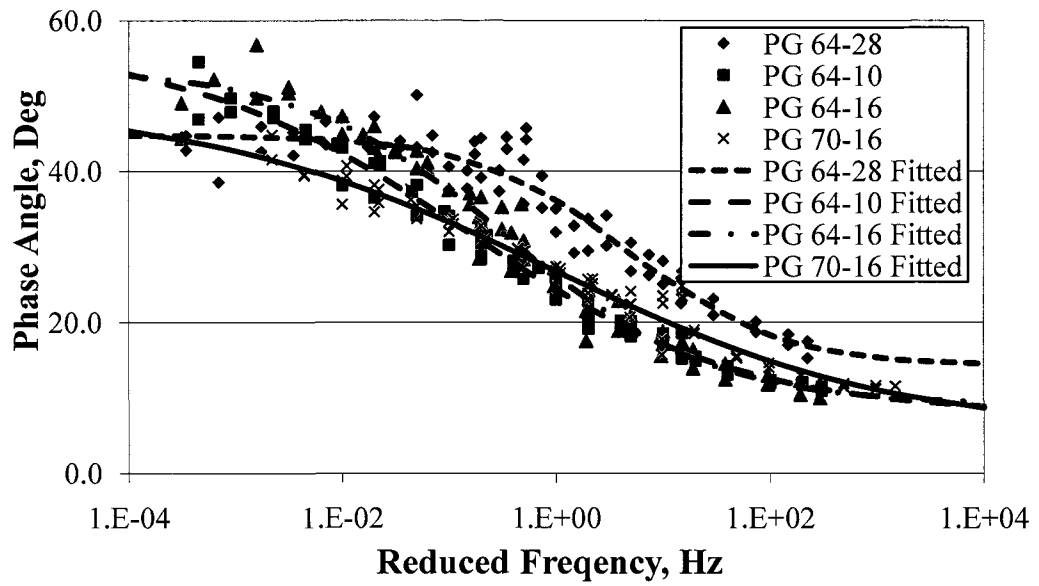
Figure A-27: Phase angle mastercurves for CalTrans mixtures under flexure mode
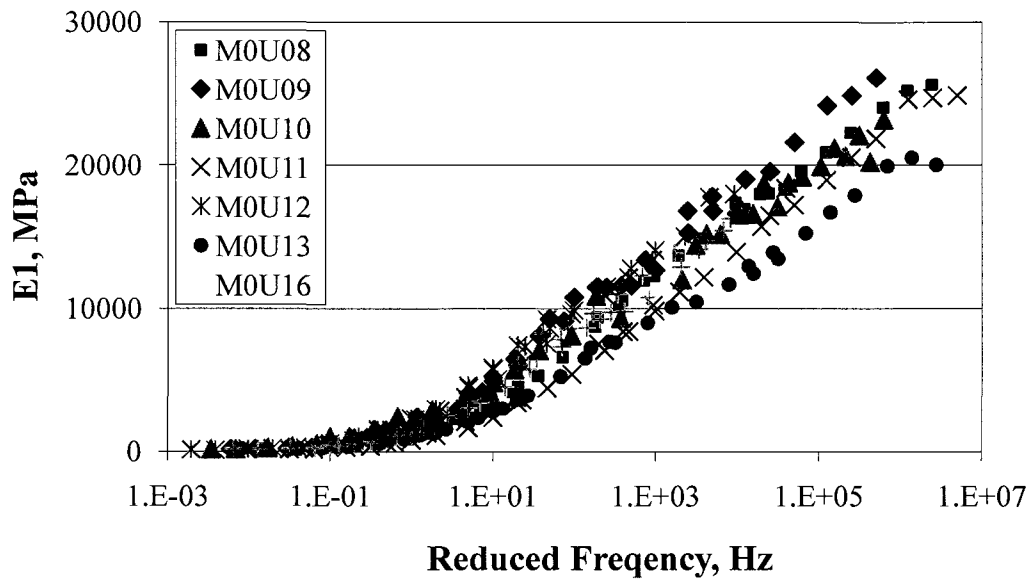
Figure A-28: Storage modulus mastercurves for M0 mixture specimens under uniaxial mode
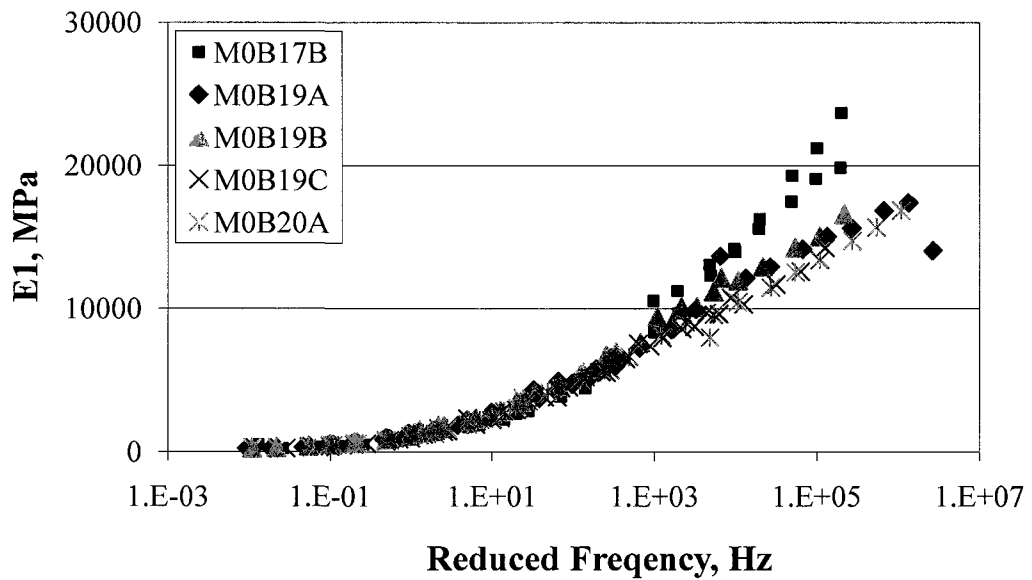
Figure A-29: Storage modulus mastercurves for M0 mixture specimens under biaxial mode
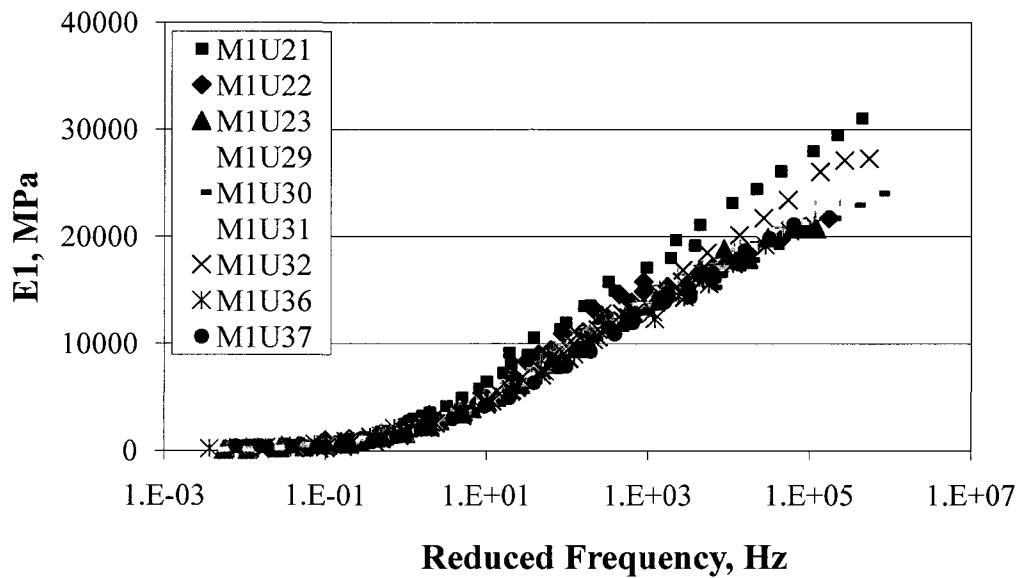
Figure A-30: Storage modulus mastercurves for M1 mixture specimens under uniaxial
mode
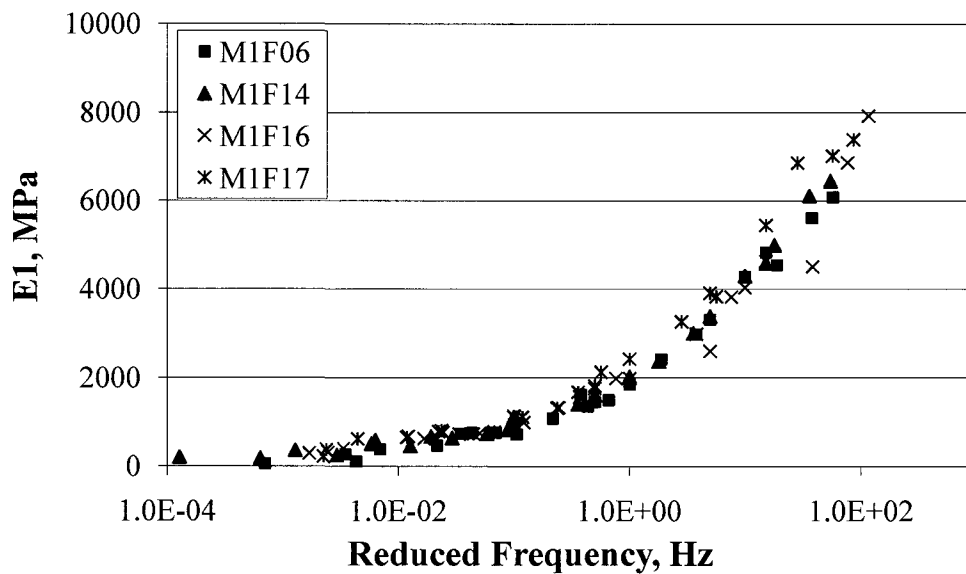
Figure A-31: Storage modulus mastercurves for M1 mixture specimens under flexure
mode
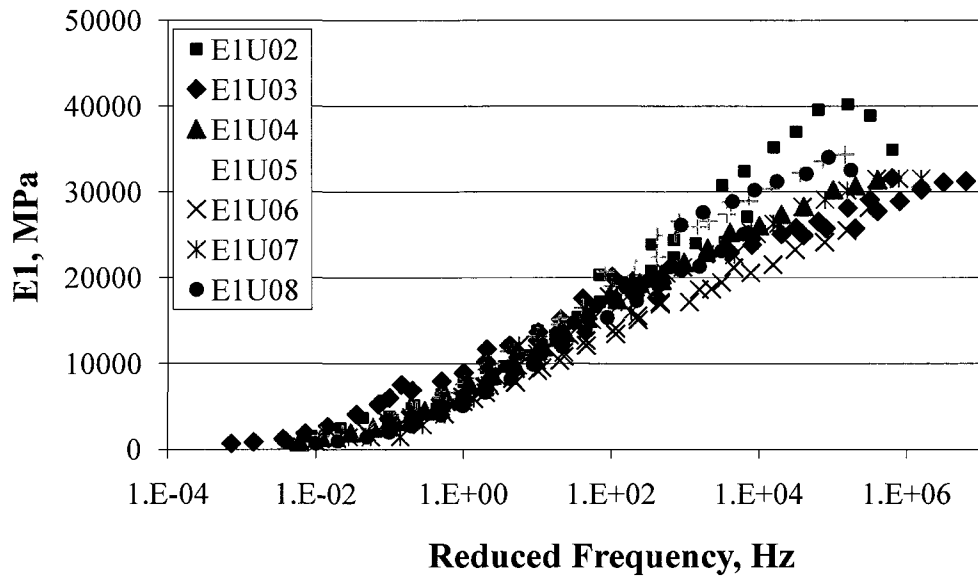
Figure A-32: Storage modulus mastercurves for E1 mixture specimens under uniaxial mode
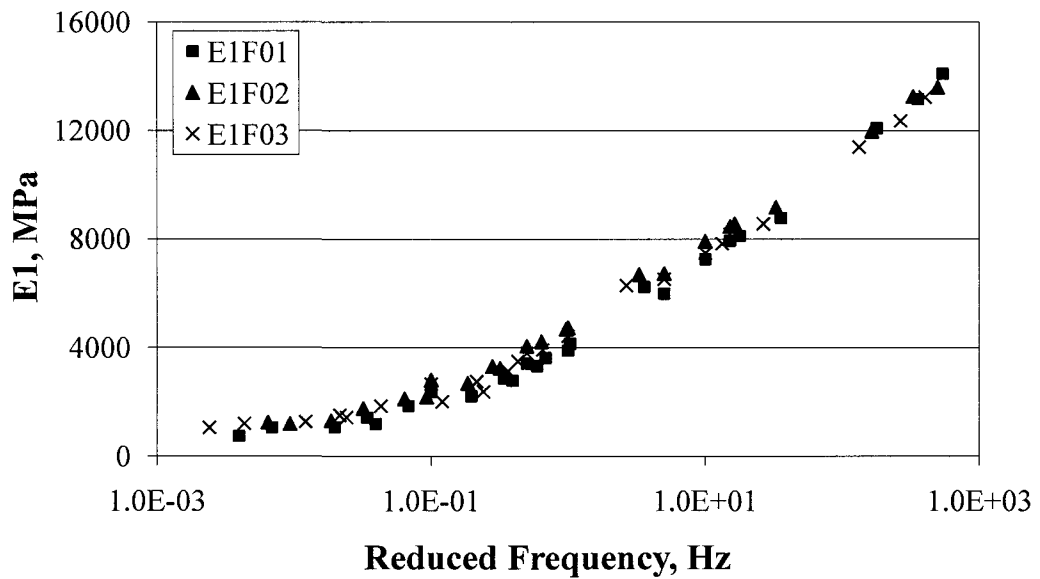
Figure A-33: Storage modulus mastercurves for E1mixture specimens under flexurel mode
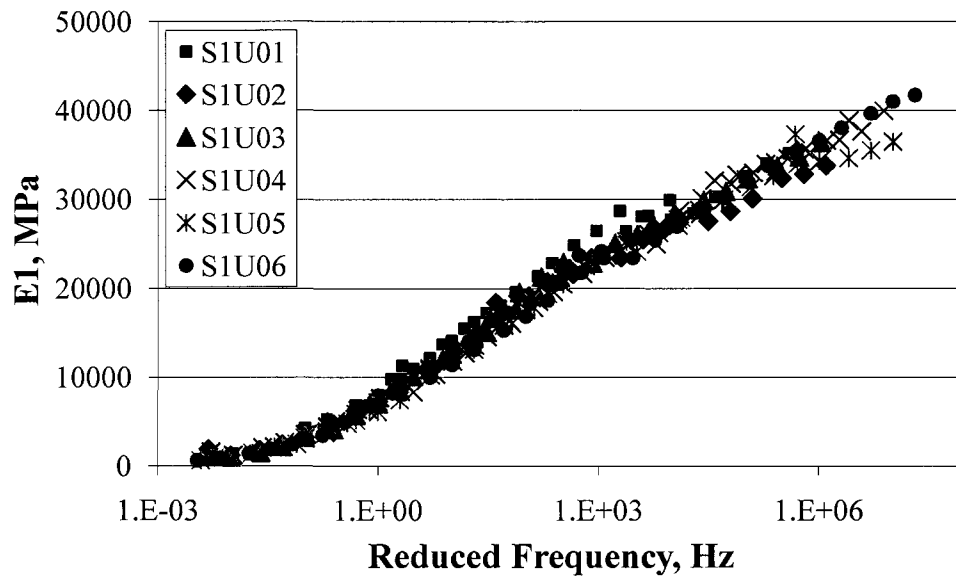
Figure A-34: Storage modulus mastercurves for S1 mixture specimens under uniaxial mode
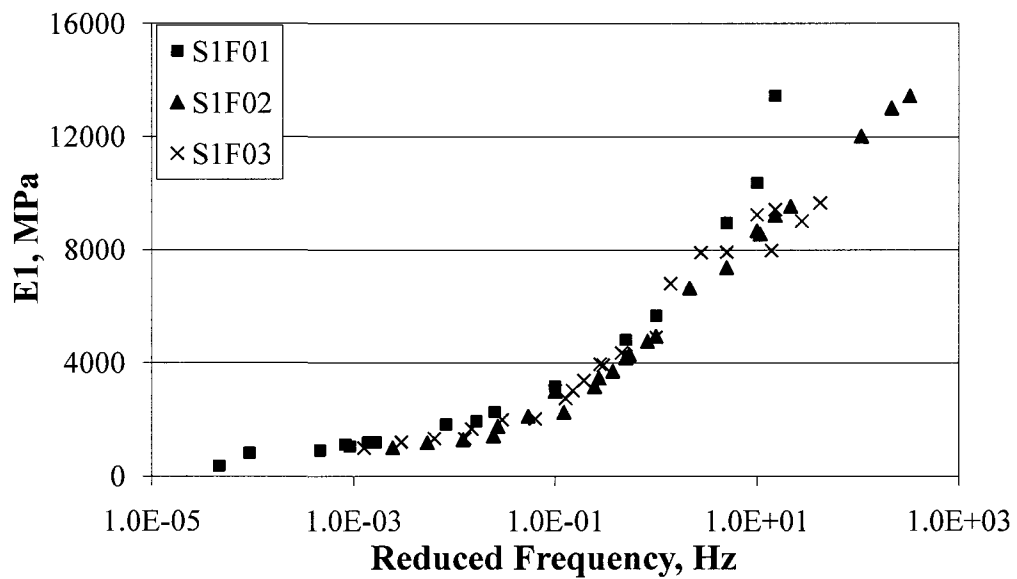
Figure A-35: Storage modulus mastercurves for S1 mixture specimens under flexure mode
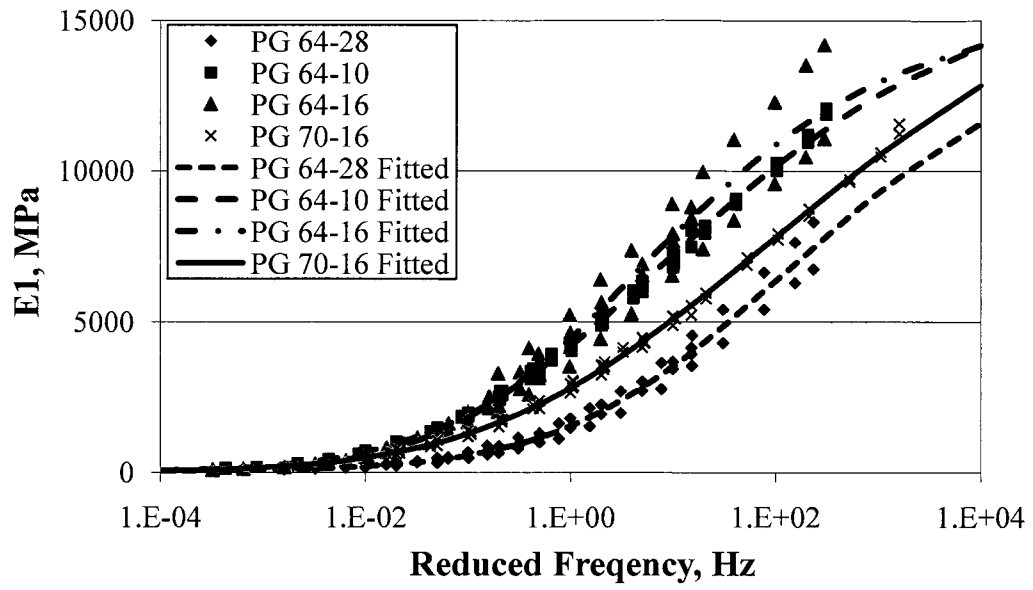
Figure A-36: Storage modulus mastercurves for CalTrans mixtures under uniaxial mode
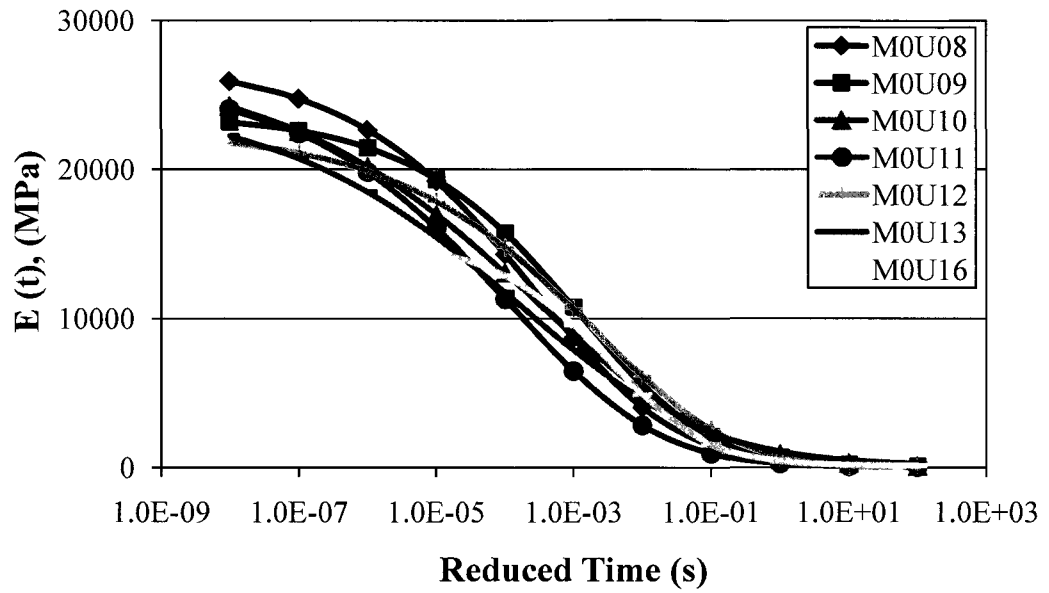
Figure A-37: Relaxation modulus mastercurves for M0 mixture specimens under uniaxial mode
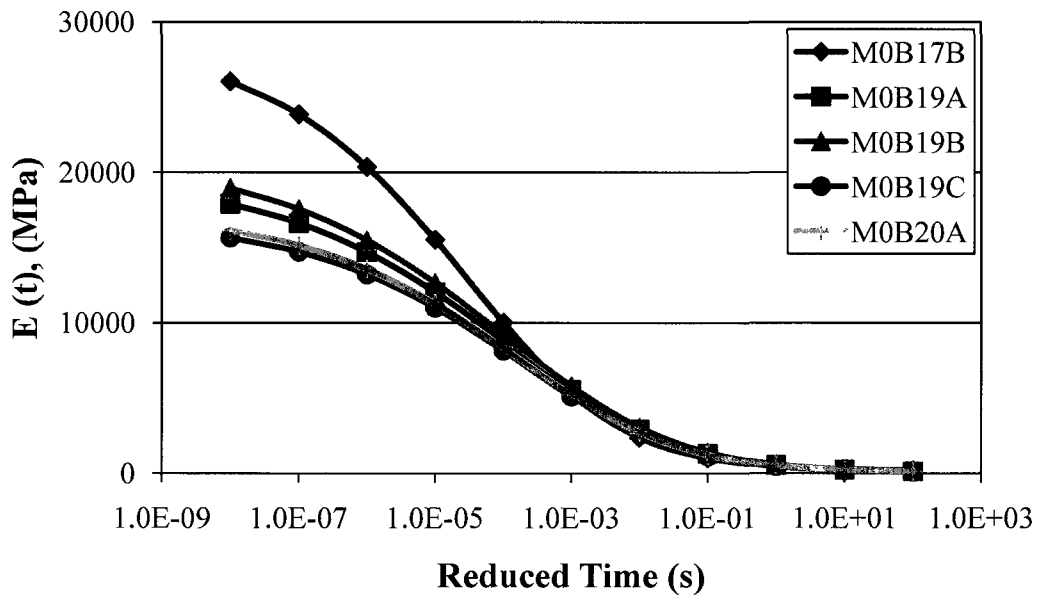
Figure A-38: Relaxation modulus mastercurves for M0 mixture specimens under biaxial mode
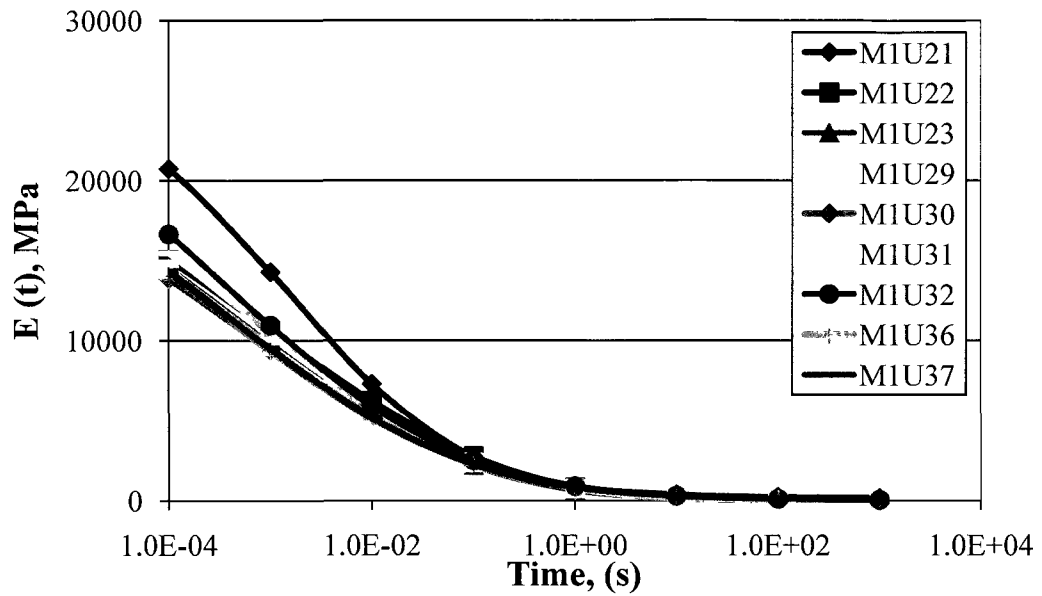
Figure A-39: Relaxation modulus mastercurves for M1 mixture specimens under uniaxial mode
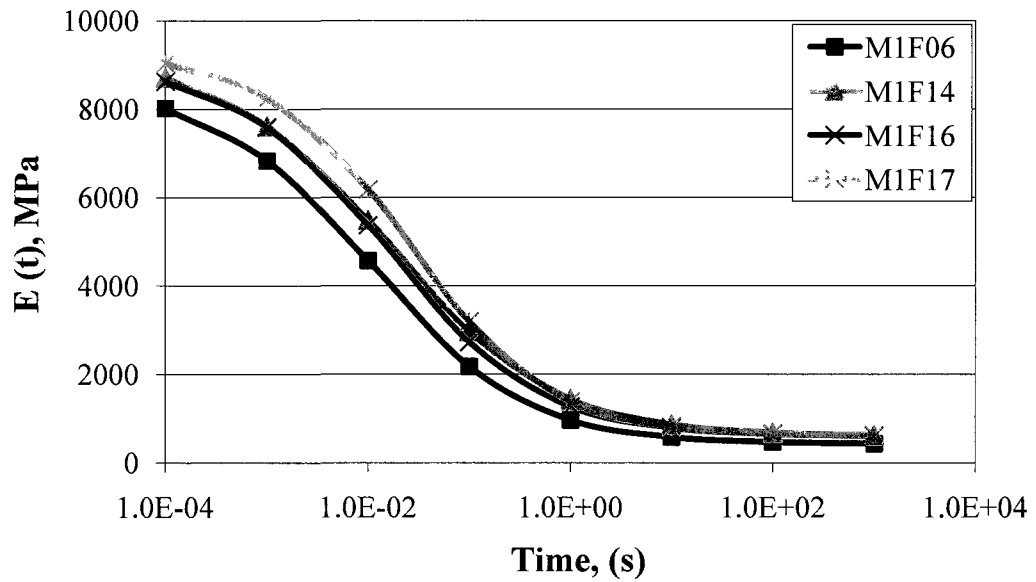
Figure A-40: Relaxation modulus mastercurves for M1 mixture specimens under flexure mode
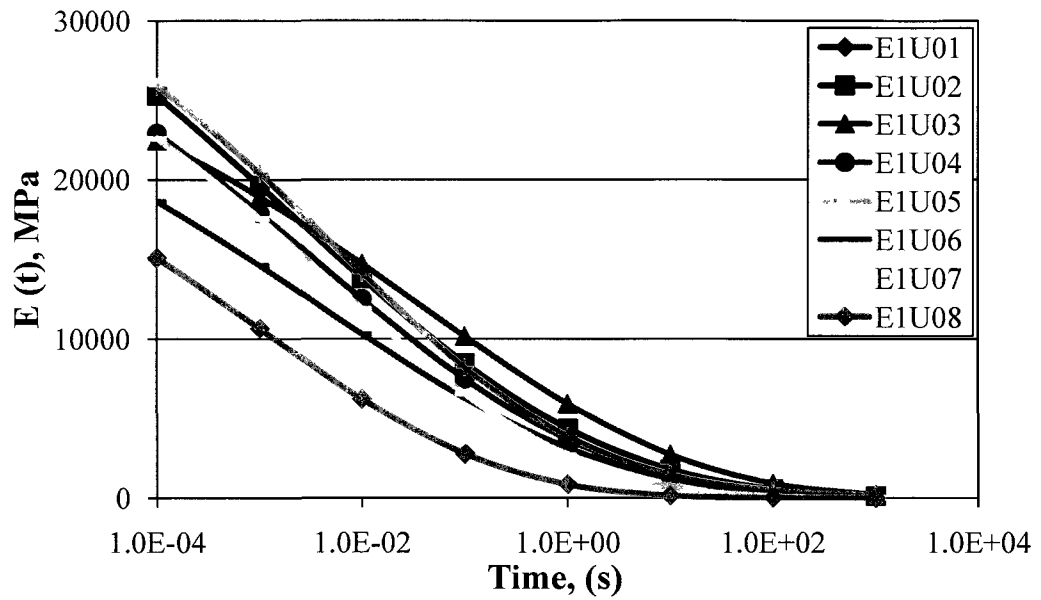
Figure A-41: Relaxation modulus mastercurves for E1 mixture specimens under uniaxial mode
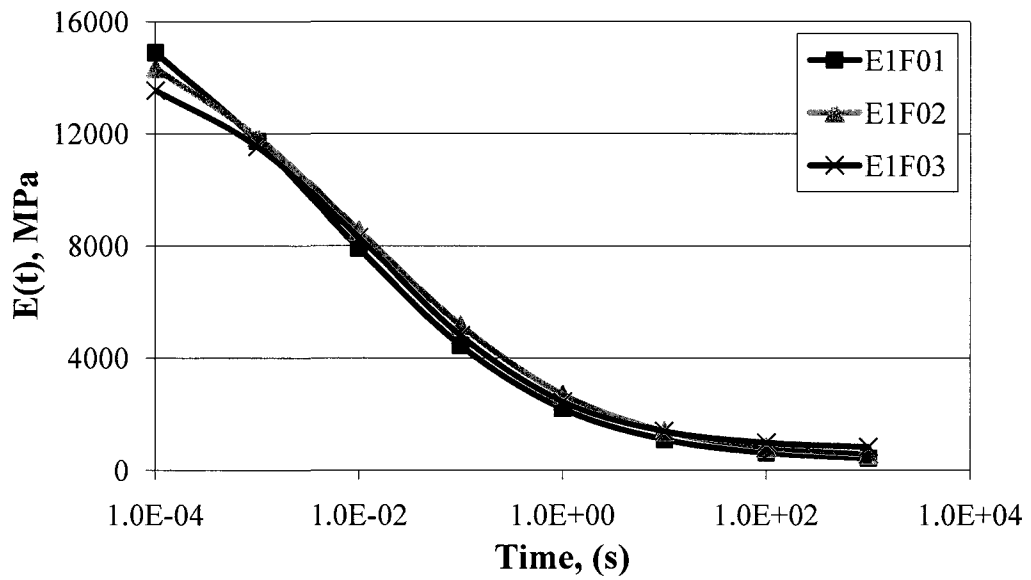
Figure A-42: Relaxation modulus mastercurves for E1 mixture specimens under flexure mode
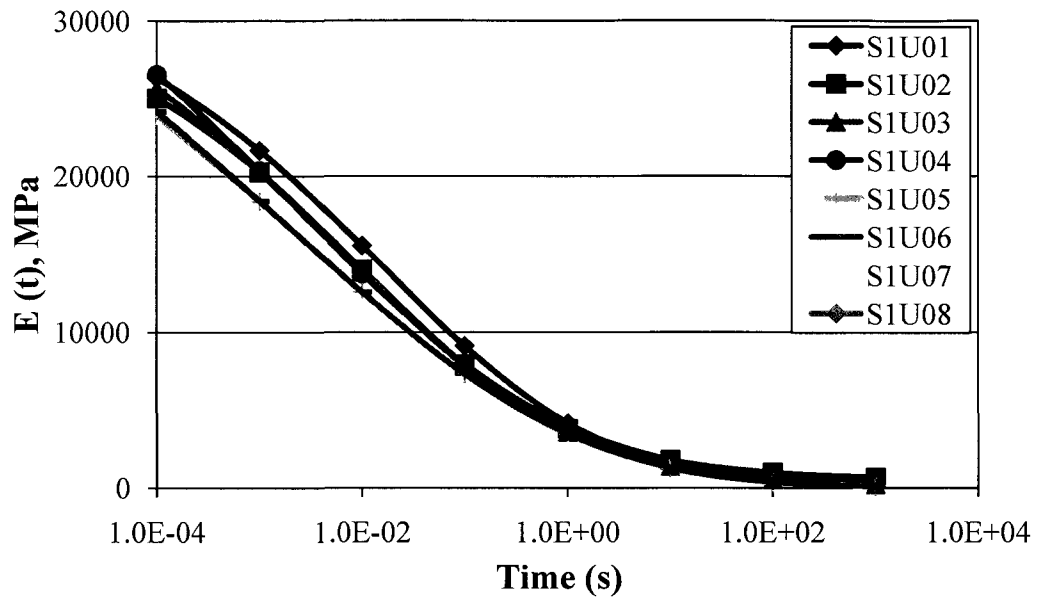
Figure A-43: Relaxation modulus mastercurves for S1 mixture specimens under uniaxial mode

Figure A-44: Relaxation modulus mastercurves for S1 mixture specimens under flexurel mode

Figure A-45: Relaxation modulus mastercurves for CalTrans mixtures under flexurel mode
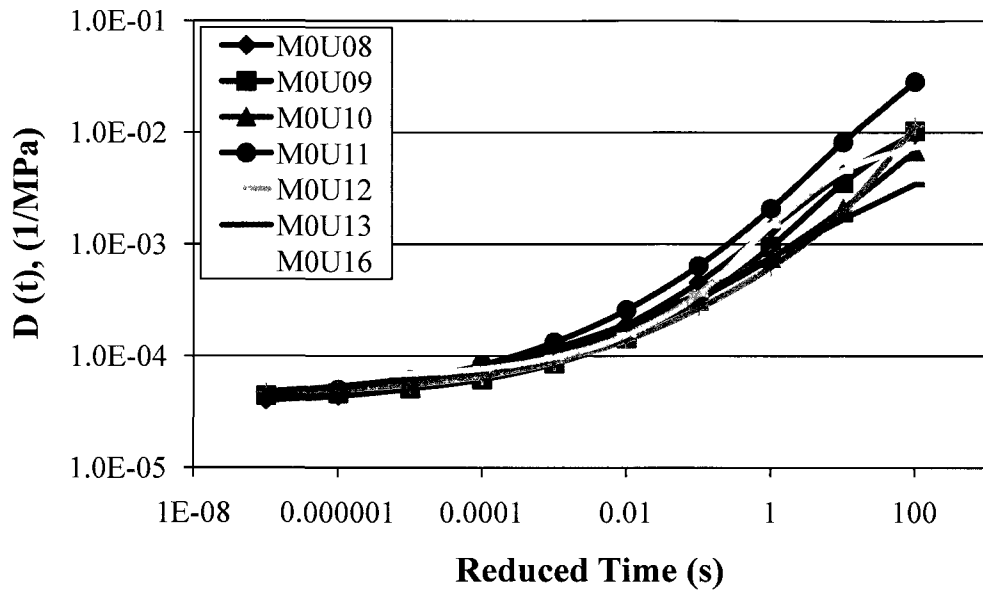
Figure A-46: Creep compliance mastercurves for M0 mixture specimens under uniaxial mode
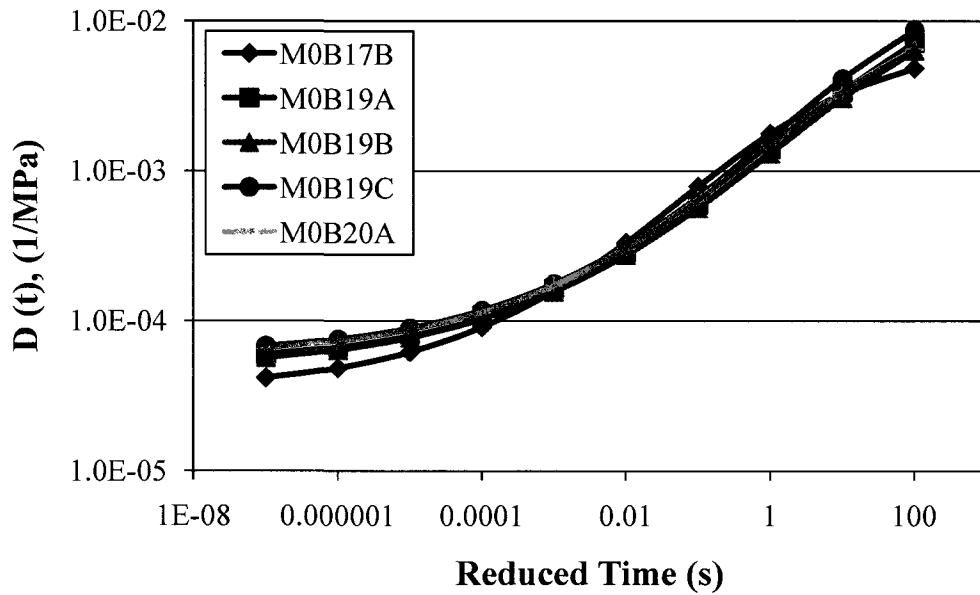
Figure A-47: Creep compliance mastercurves for M0 mixture specimens under biaxial mode

Figure A-48: Creep compliance mastercurves for M1 mixture under uniaxial mode
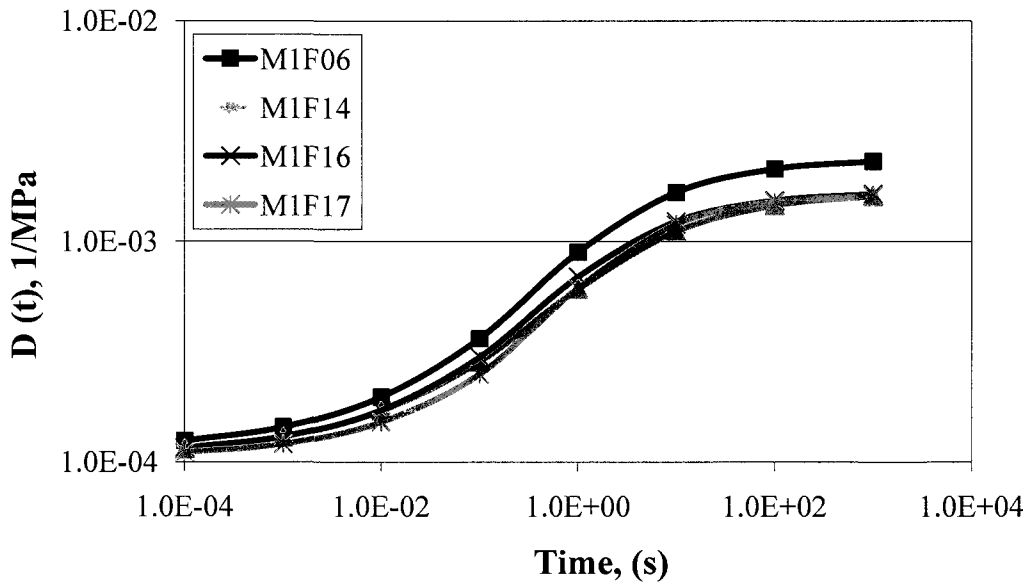
Figure A-49: Creep compliance mastercurves for M1 mixture specimens under flexure mode
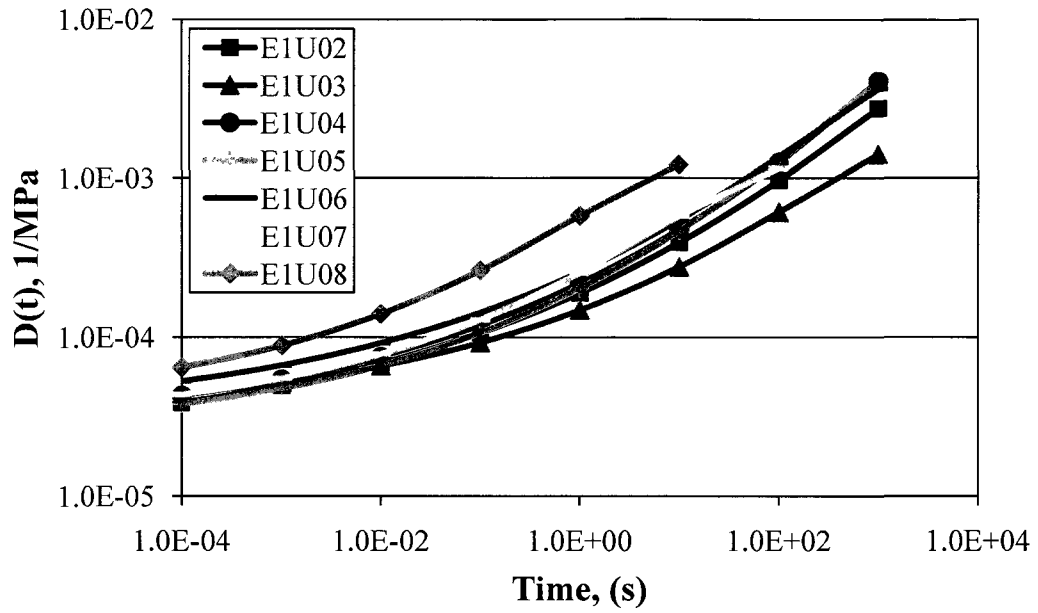
Figure A-50: Creep compliance mastercurves for E1 mixture under uniaxial mode
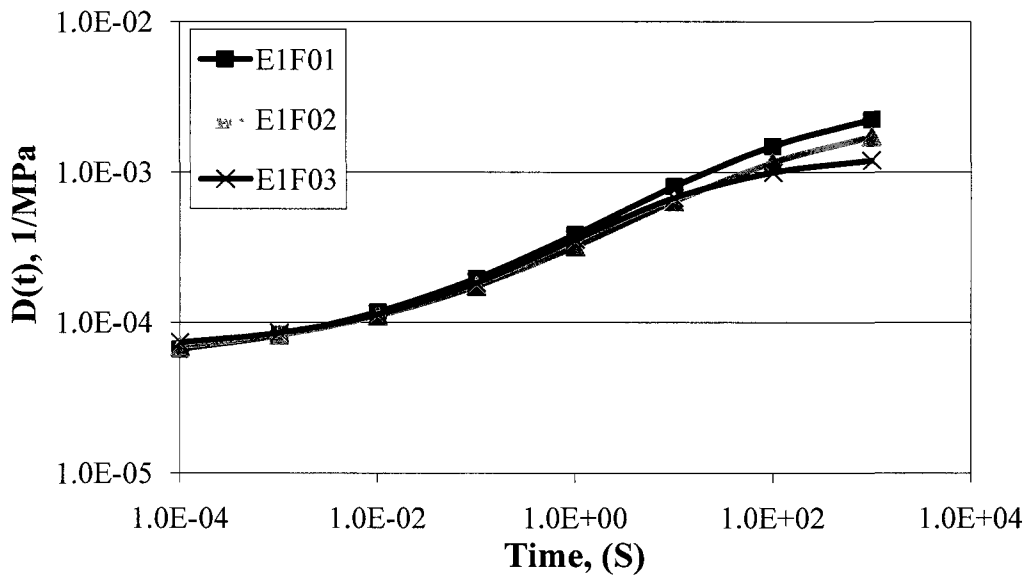
Figure A-51: Creep compliance mastercurves for E1 mixture specimens under flexure mode
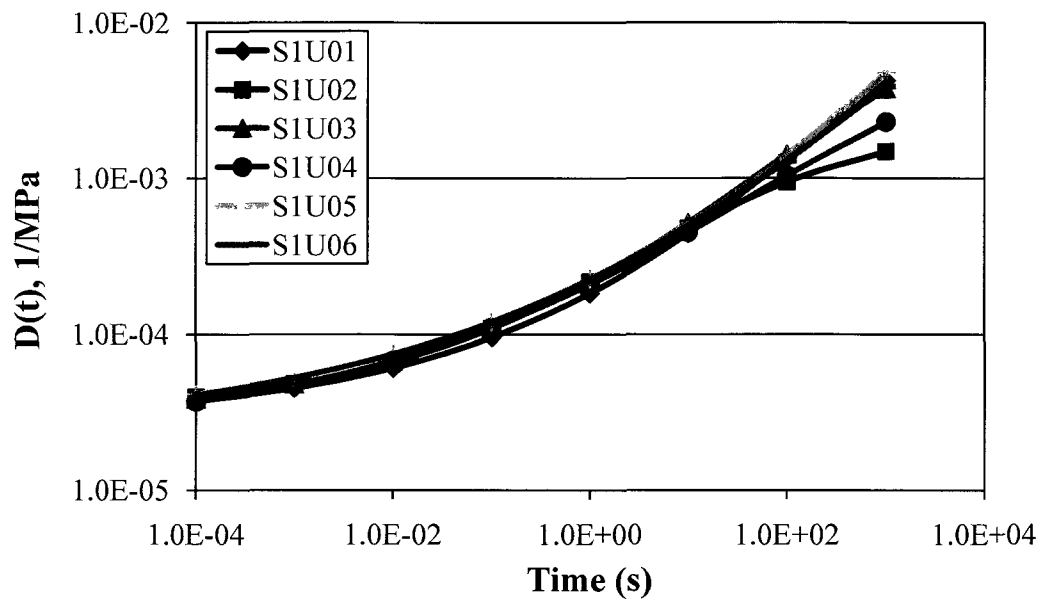
Figure A-52: Creep compliance mastercurves for S1 mixture specimens under uniaxial mode
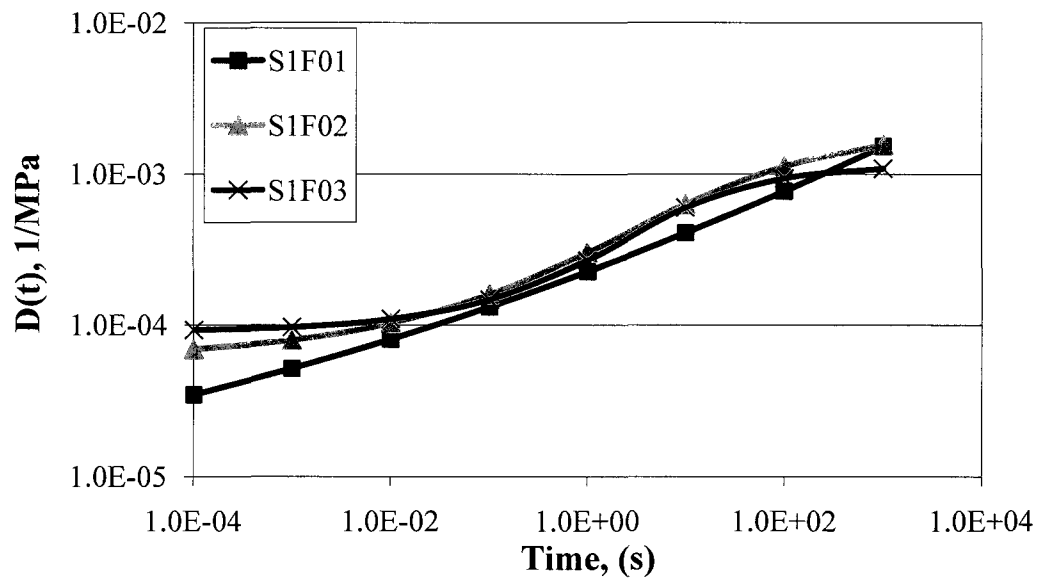
Figure A-53: Creep compliance mastercurves for S1 mixture specimens under flexure mode
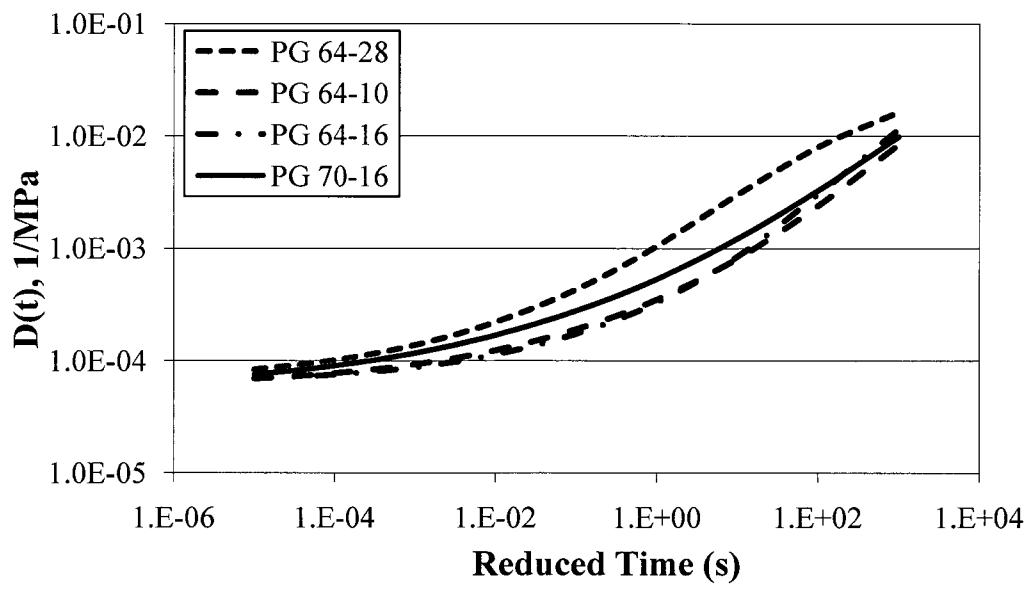
Figure A-54: Creep compliance mastercurves for CalTrans mixtures under flexure mode

APPENDIX - B

DAMAGE CHARACTERISTIC CURVES
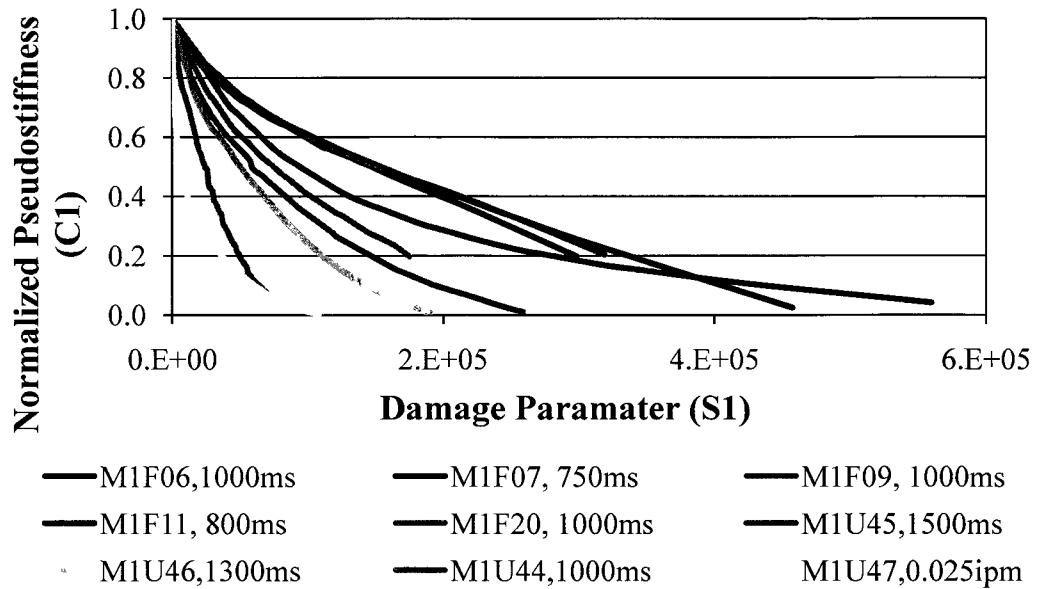
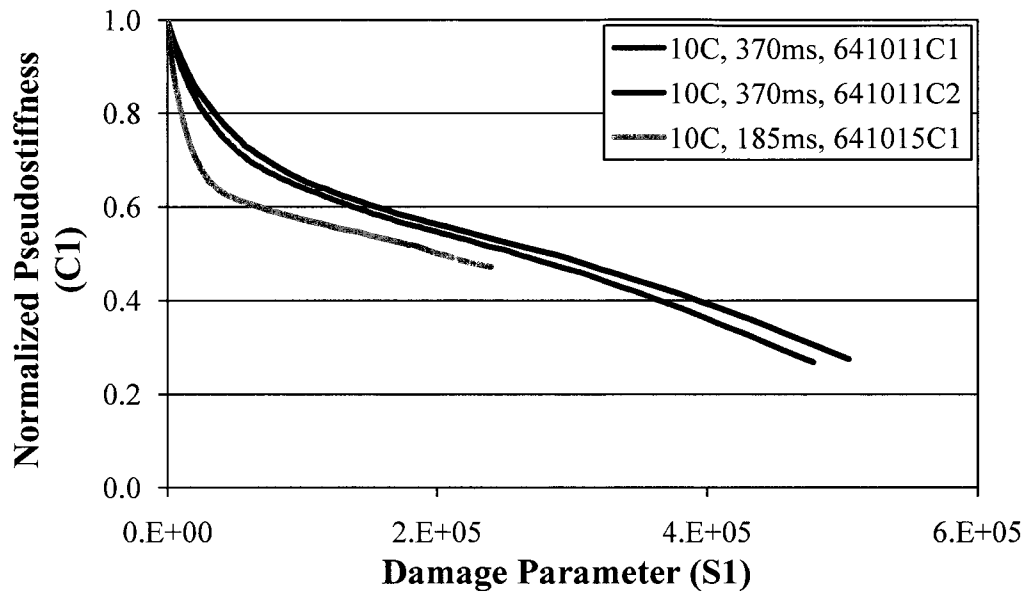**Figure B-1: Damage characteristic curves for M1 mixture using alpha = 1 + 1/n**
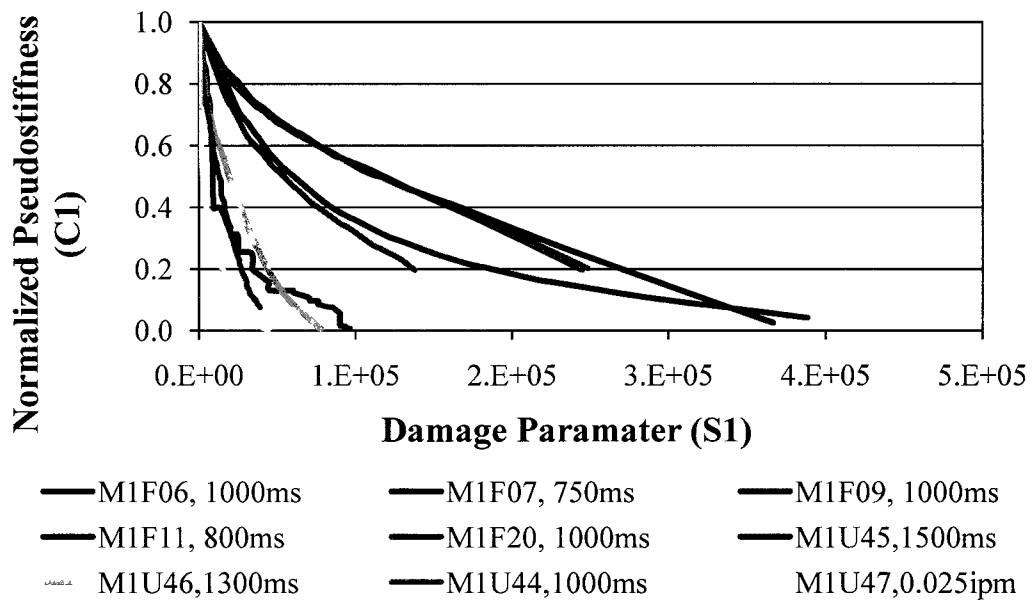
Figure B-2: : Damage characteristic curves for M1 mixture using alpha = 1/n
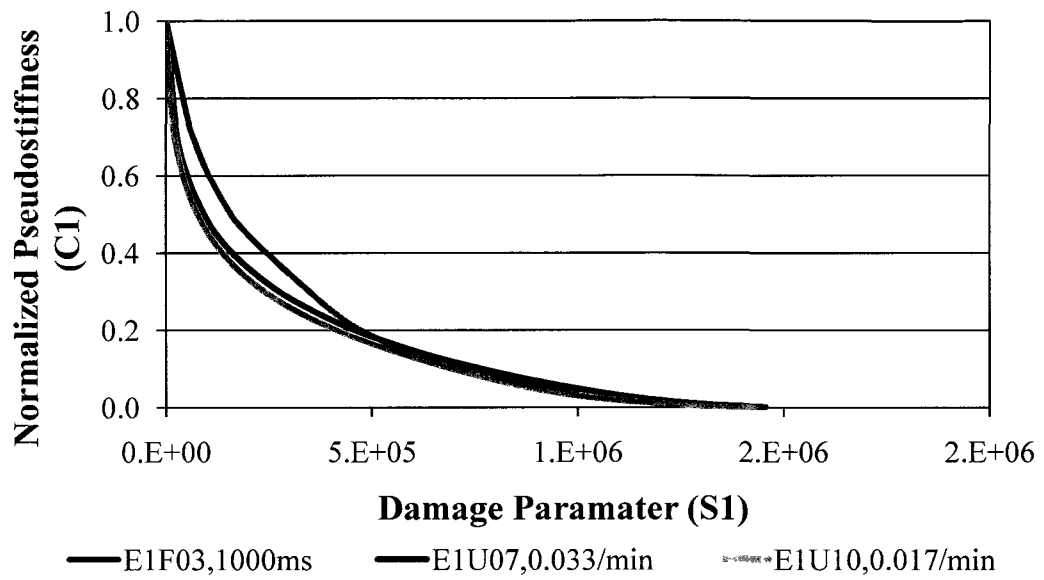
Figure B-3: Damage characteristic curves for E1 mixture using alpha = 1 + 1/n
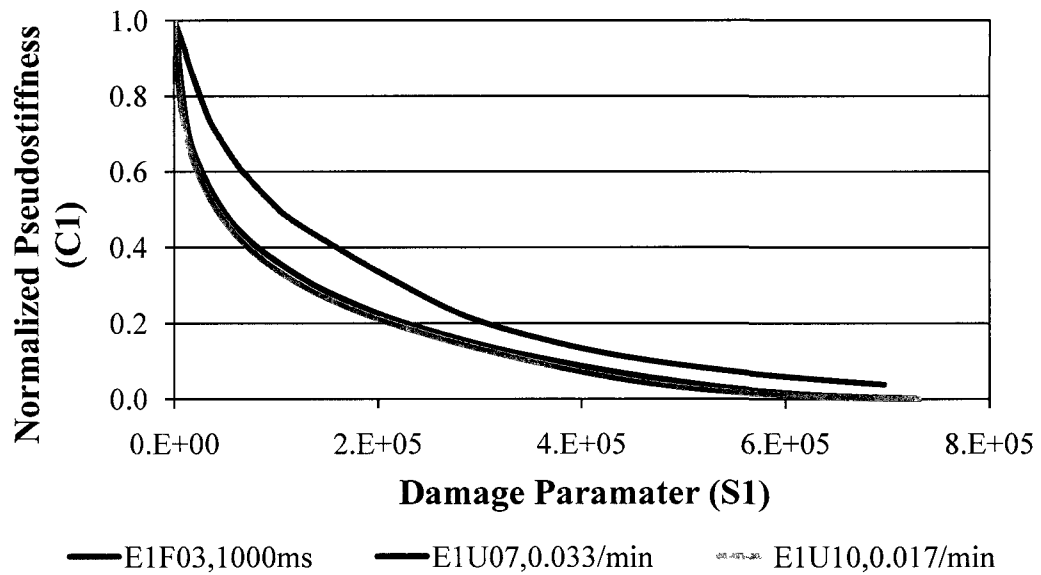
Figure B-4: Damage characteristic curves for E1 mixture using alpha = 1/n

217
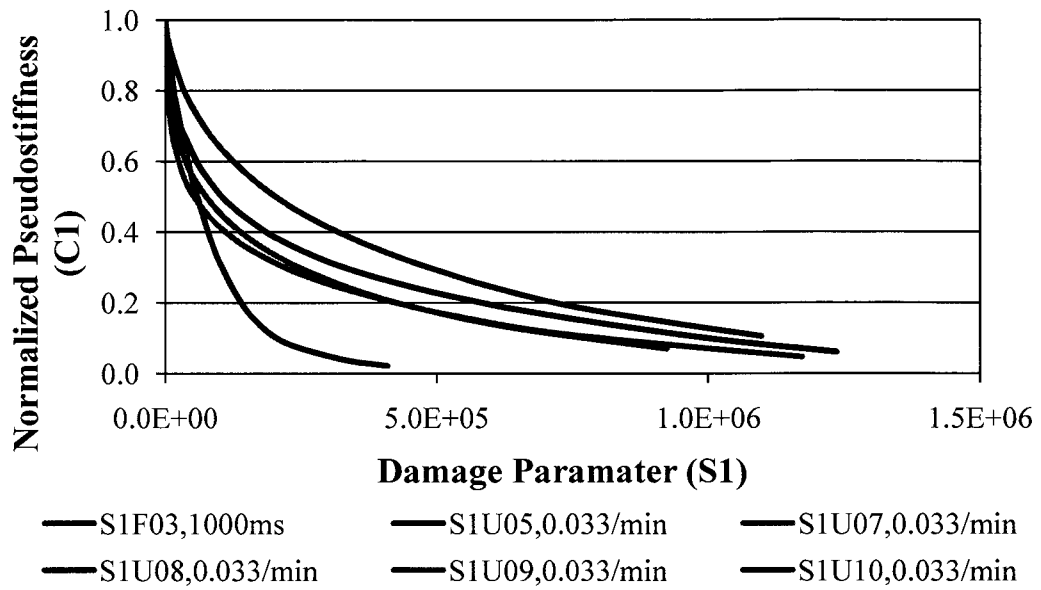
Figure B-5: Damage characteristic curves for S1 mixture using alpha = 1 + 1/n
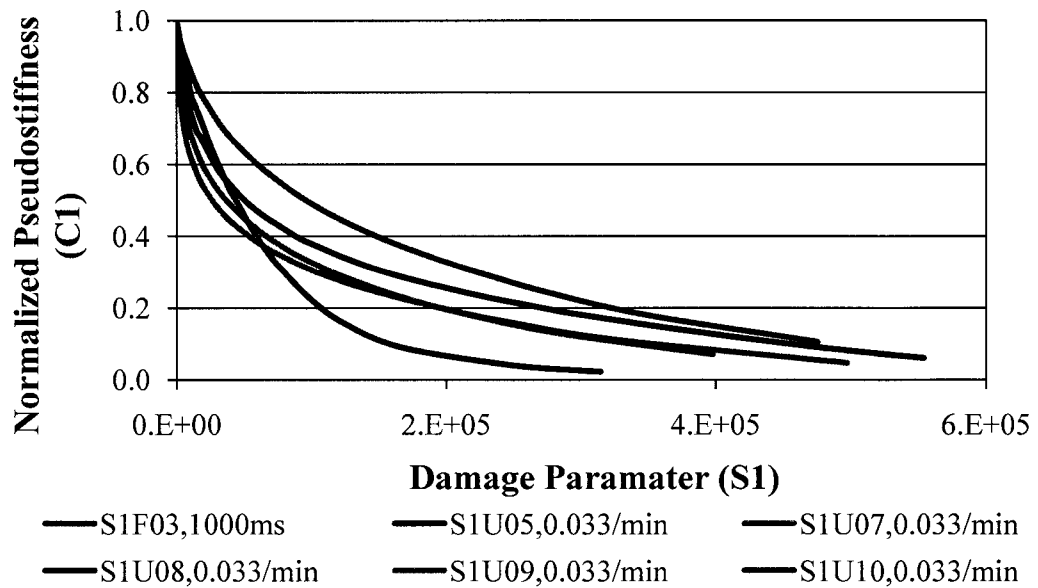
Figure B-6: Damage characteristic curves for S1 mixture using alpha = 1/n
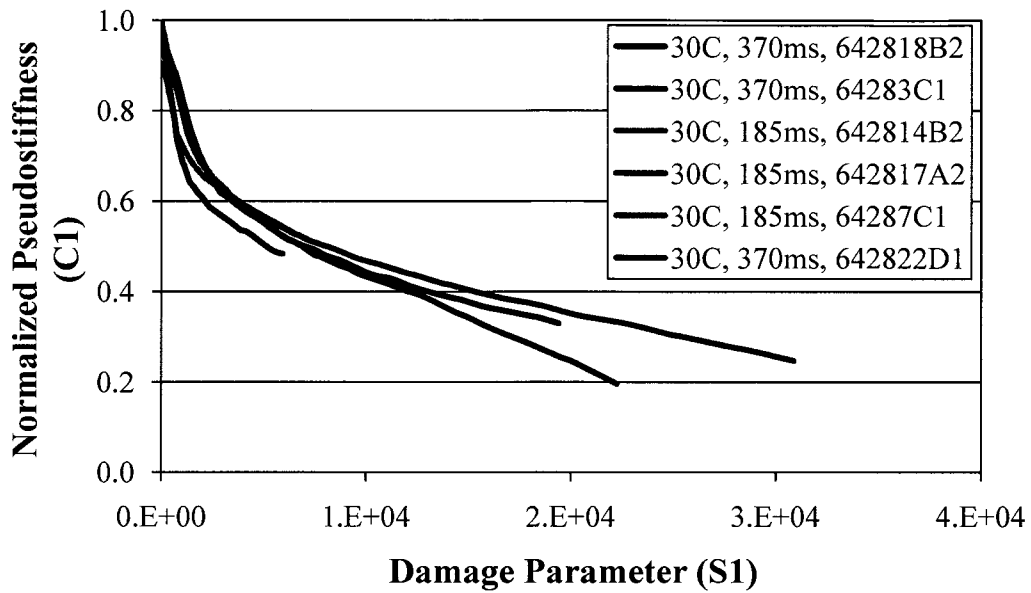
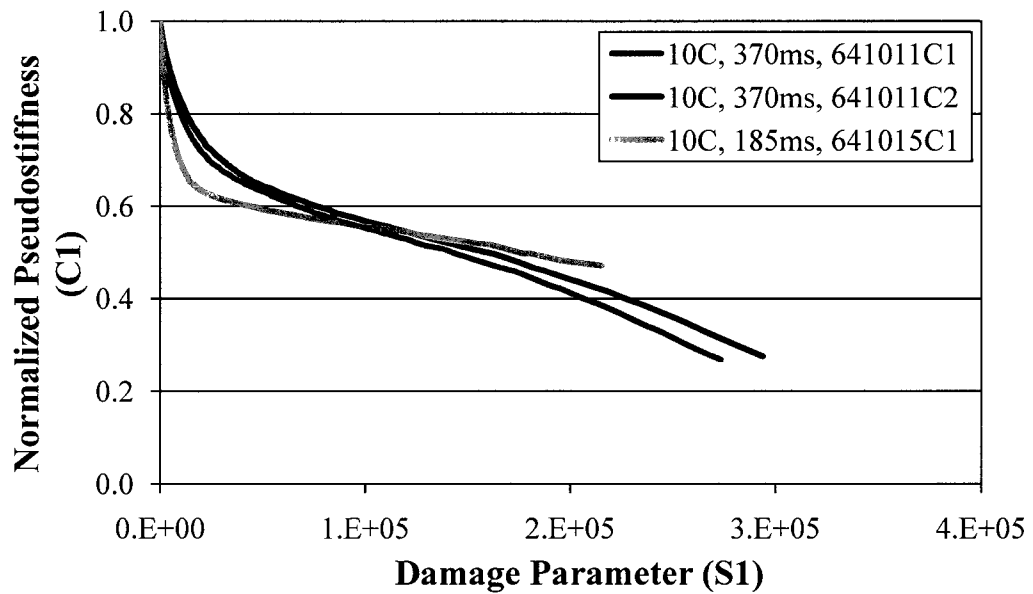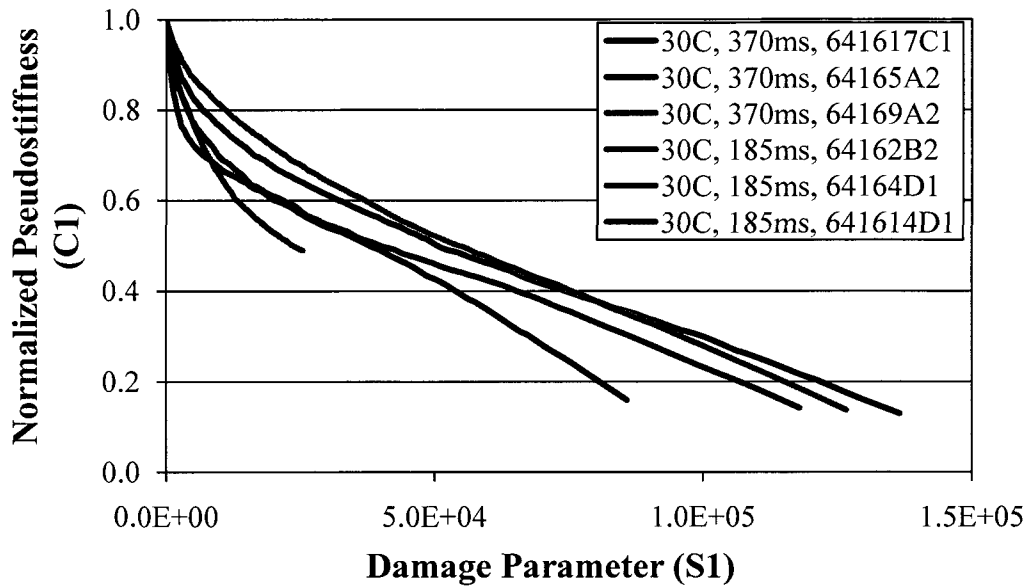Figure B-7: Damage characteristic curves for PG 64-28 mixture specimens using alpha = 1 + 1/n at 30 C
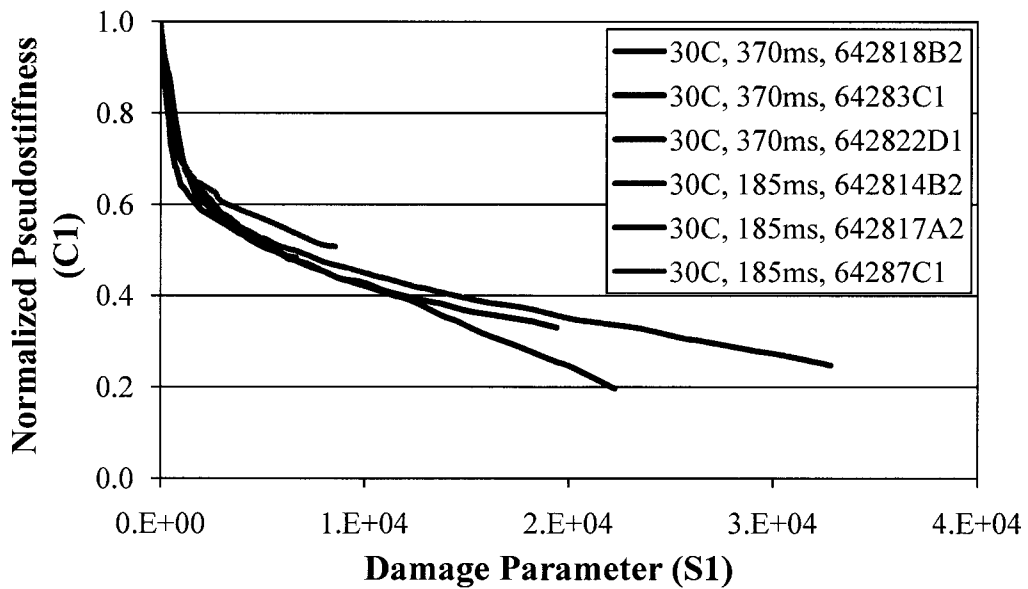
Figure B-8: Damage characteristic curves for PG 64-28 mixture specimens using alpha = 1/n at 30 C
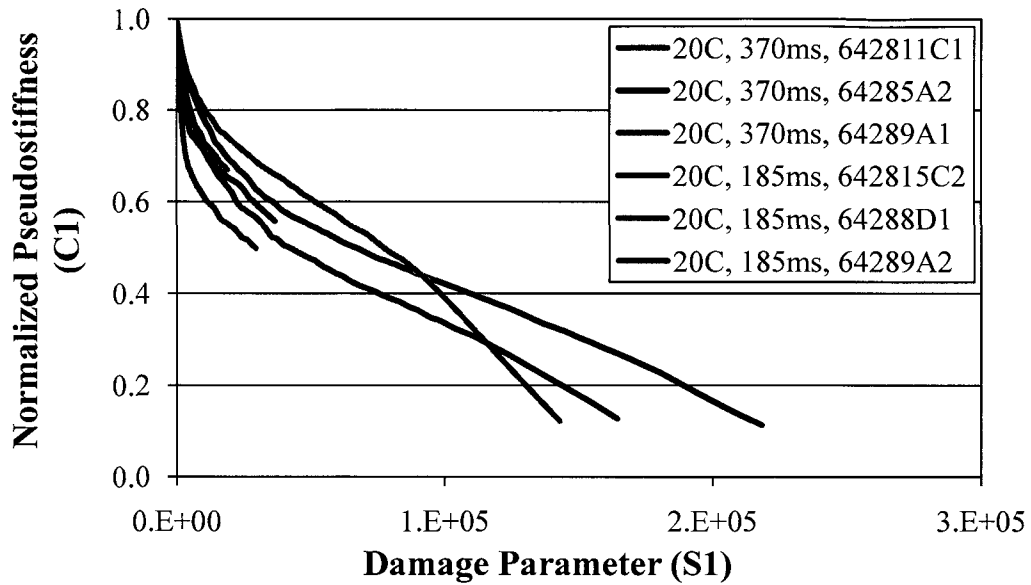
Figure B-9: Damage characteristic curves for PG 64-28 mixture specimens using alpha = 1 + 1/n at 20 C
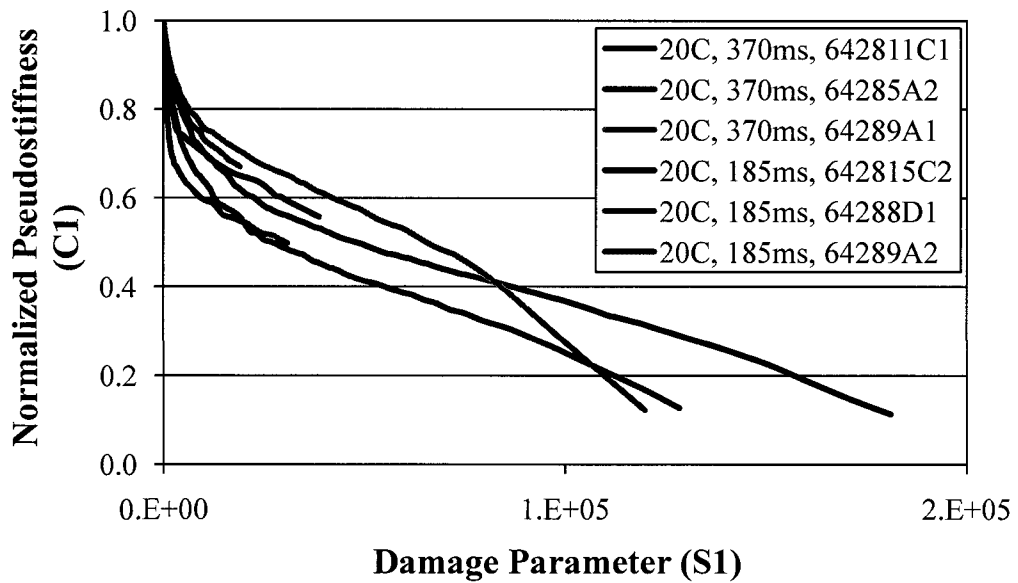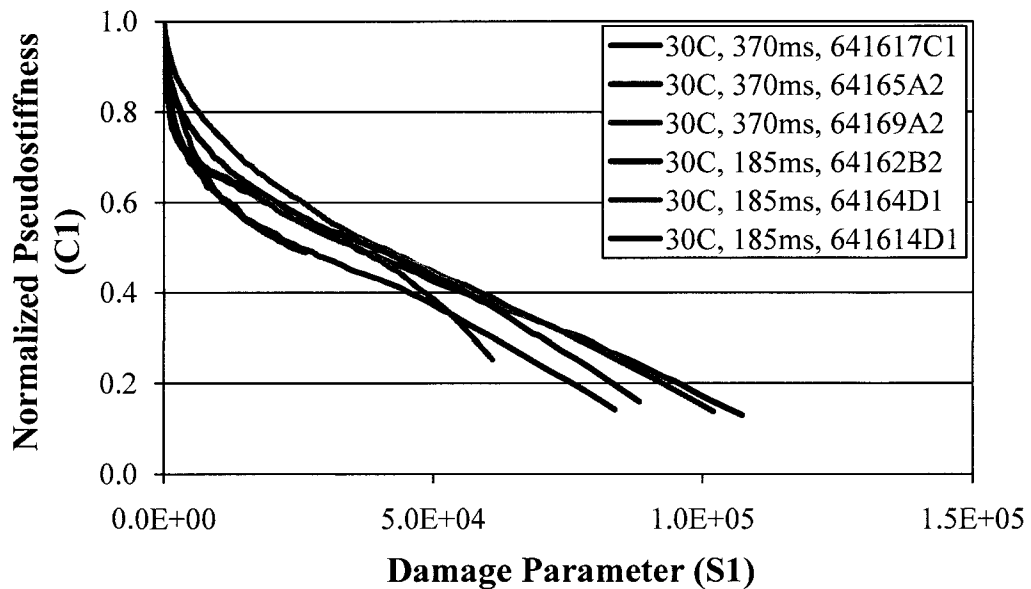

Figure B-10: Damage characteristic curves for PG 64-28 mixture specimens using alpha = 1/n at 20 C
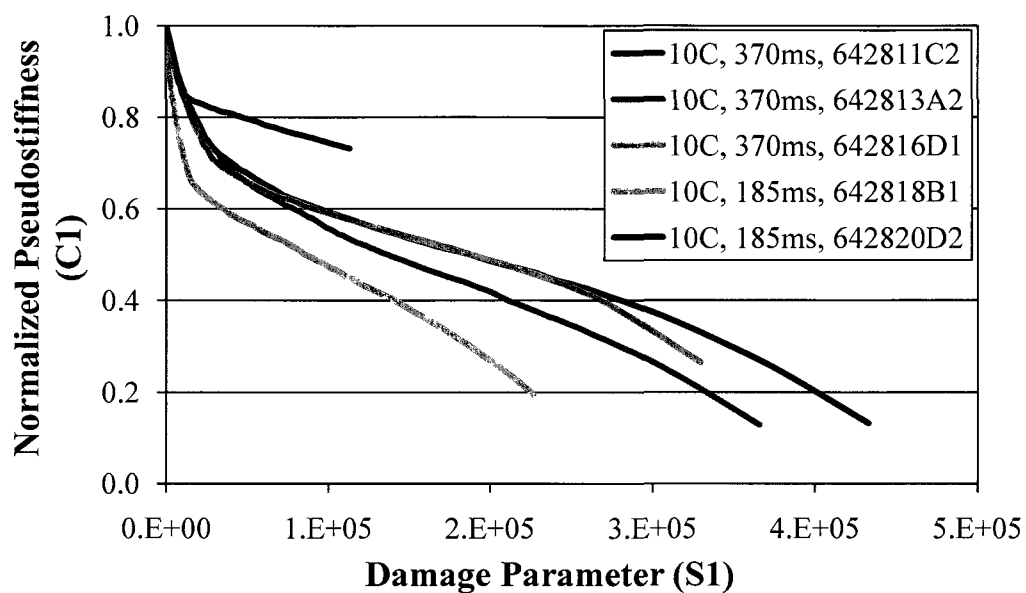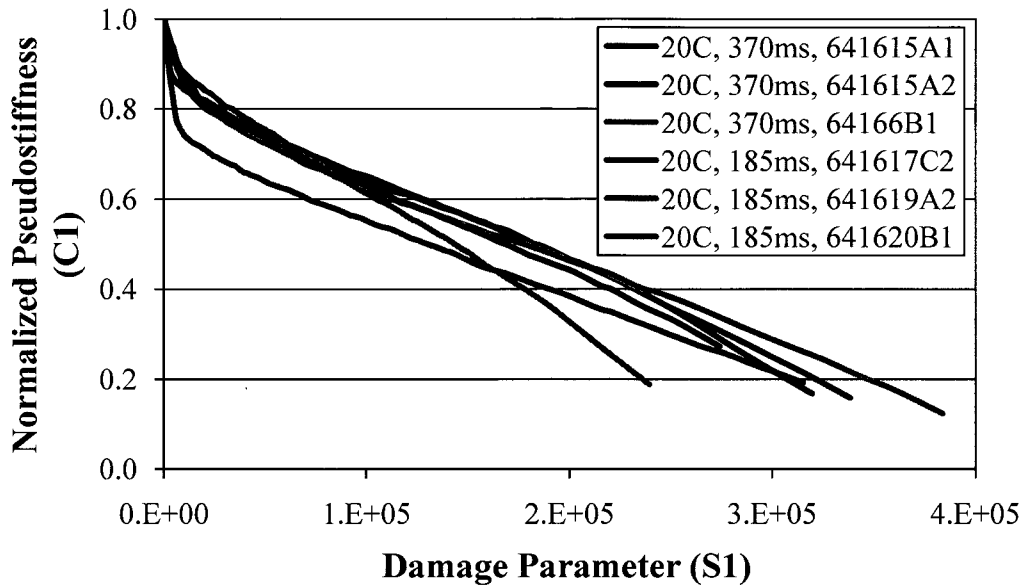
Figure B-11: Damage characteristic curves for PG 64-28 mixture specimens using alpha = 1 + 1/n at 10 C
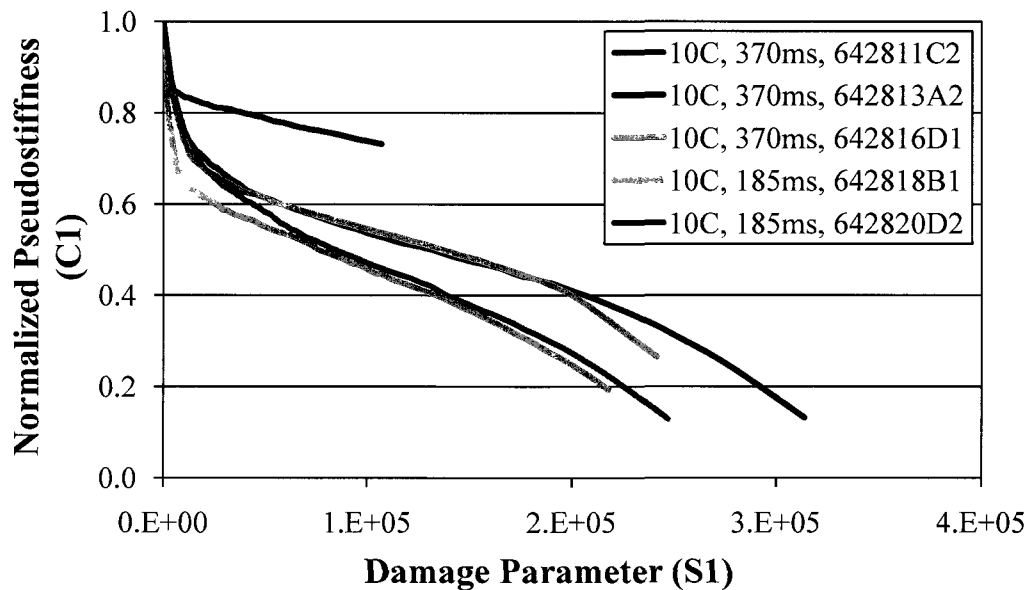
Figure B-12: Damage characteristic curves for PG 64-28 mixture specimens using alpha = 1/n at 10 C
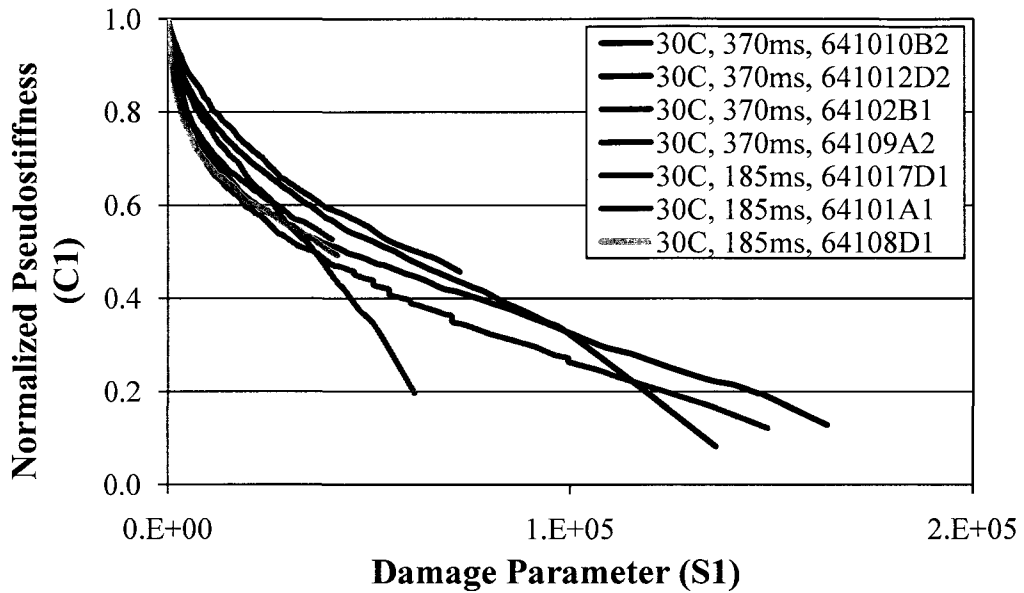
Figure B-13: Damage characteristic curves for PG 64-10 mixture specimens using alpha = 1 + 1/n at 30 C
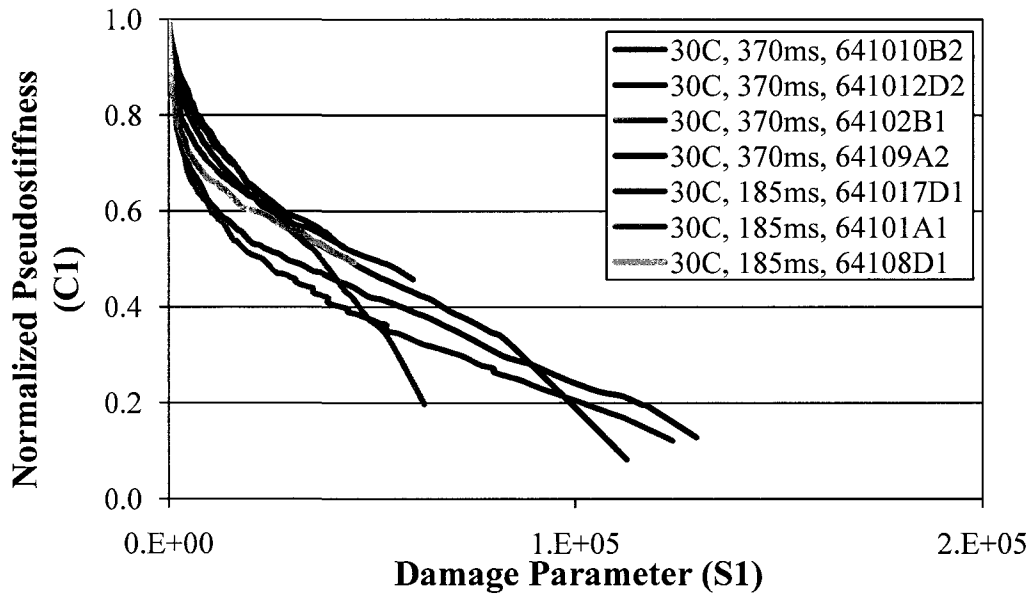
Figure B-14: Damage characteristic curves for PG 64-10 mixture specimens using alpha = 1/n at 30 C
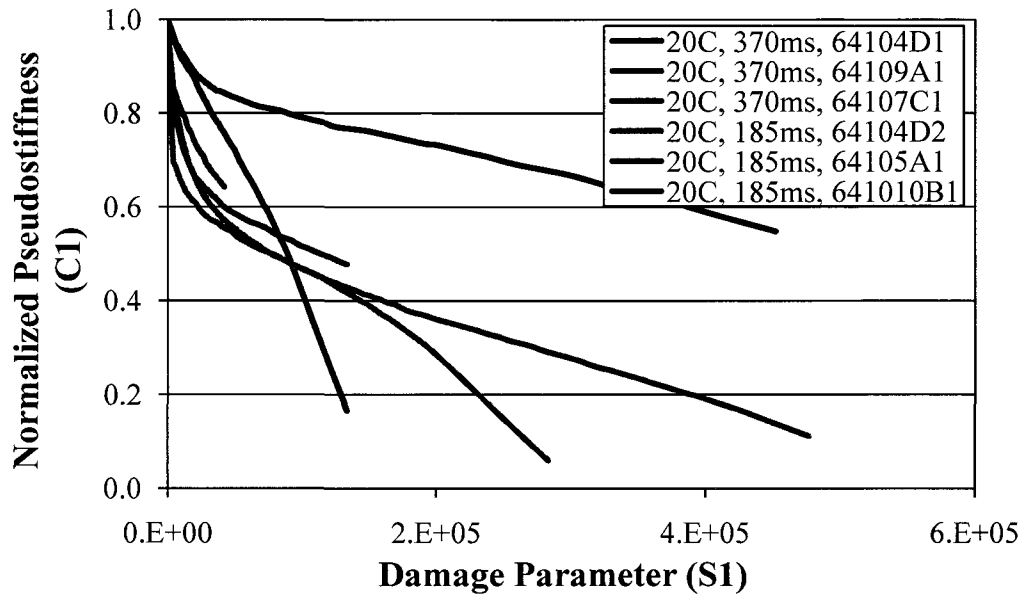
Figure B-15: Damage characteristic curves for PG 64-10 mixture specimens using alpha = 1 + 1/n at 20 C
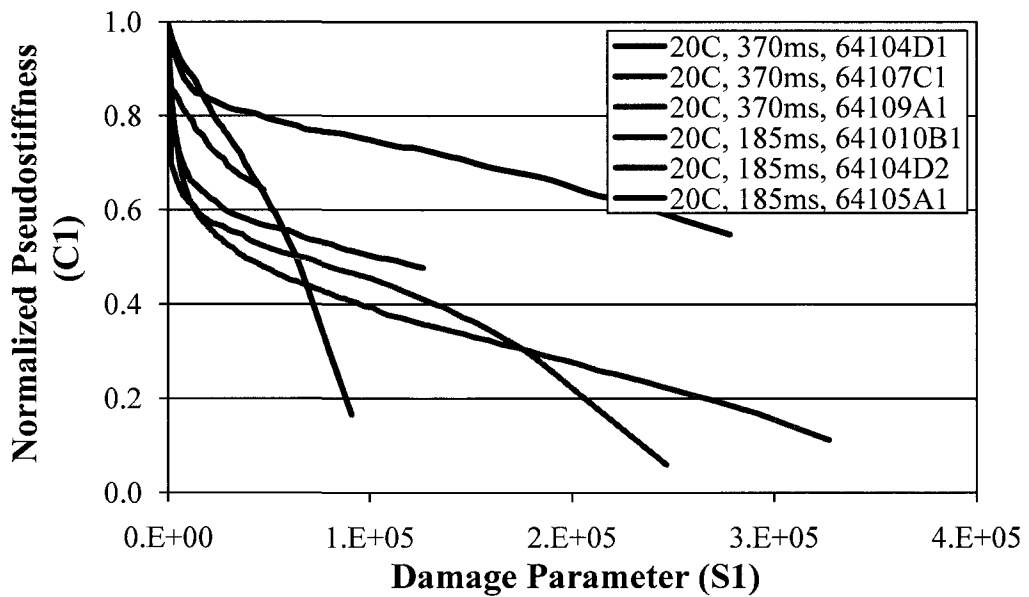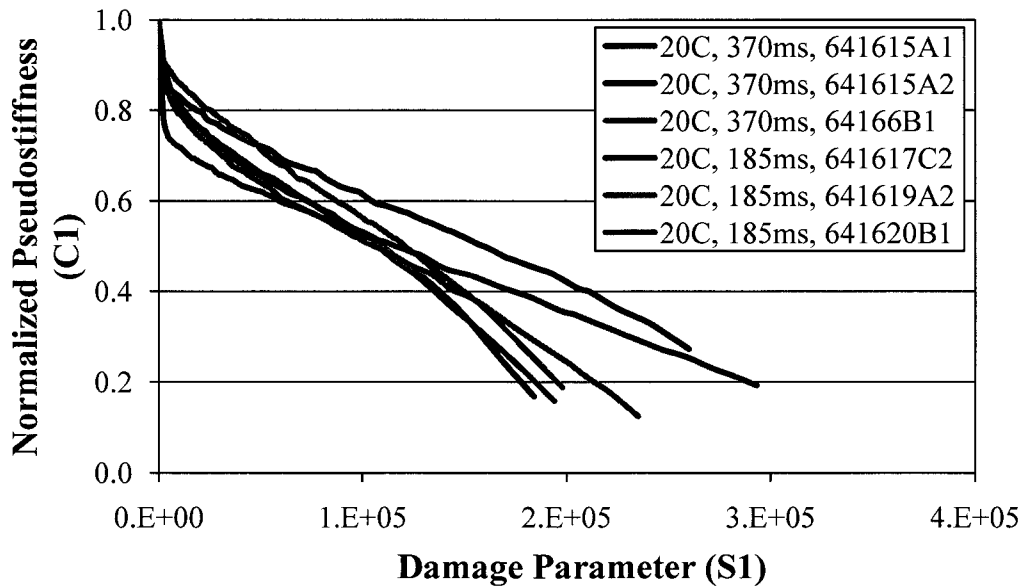

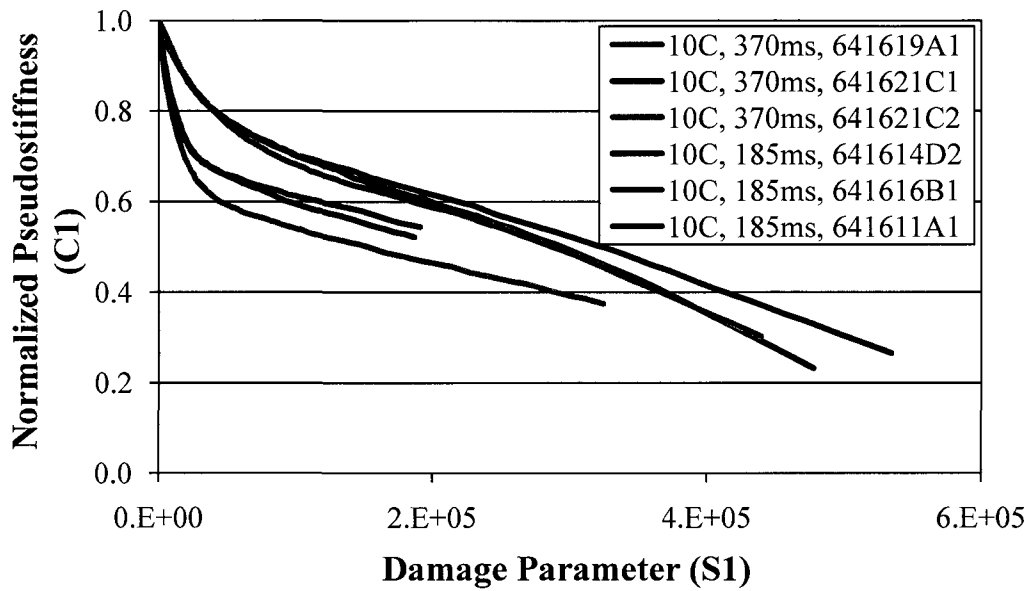**Figure B-16:** Damage characteristic curves for PG 64-10 mixture specimens using alpha = 1/n at 20 C

Figure B-17: Damage characteristic curves for PG 64-10 mixture specimens using alpha = 1 + 1/n at 10 C

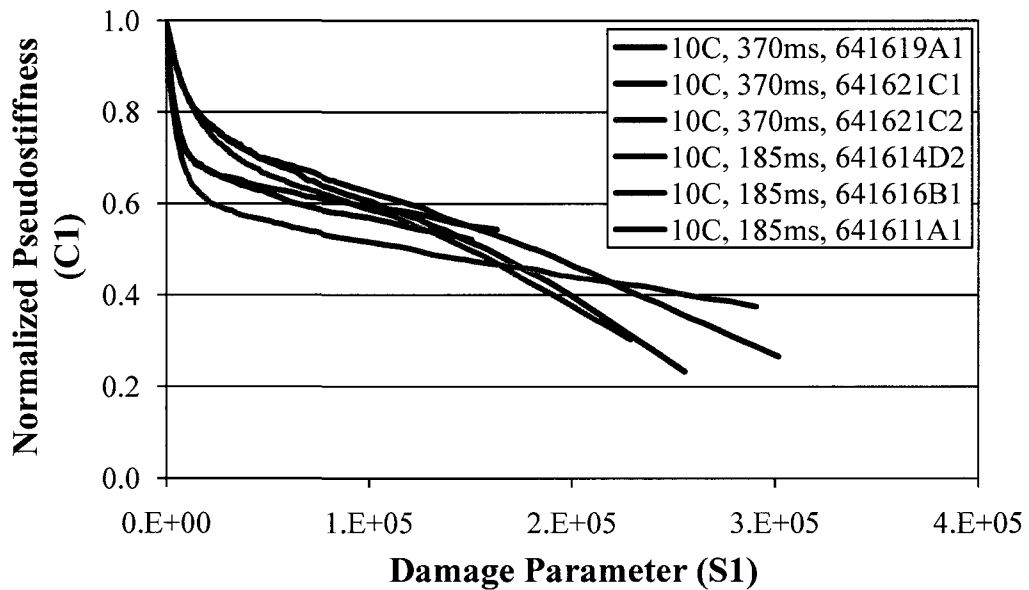

Figure B-18: Damage characteristic curves for PG 64-10 mixture specimens using alpha = 1/n at 10 C

Figure B-19: Damage characteristic curves for PG 64-16 mixture specimens using alpha = 1 + 1/n at 30 C

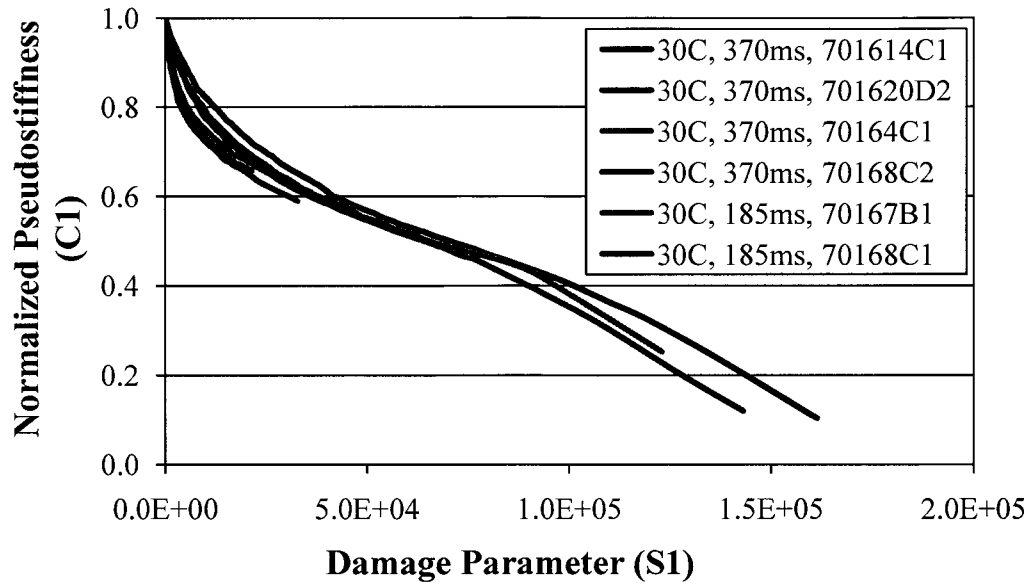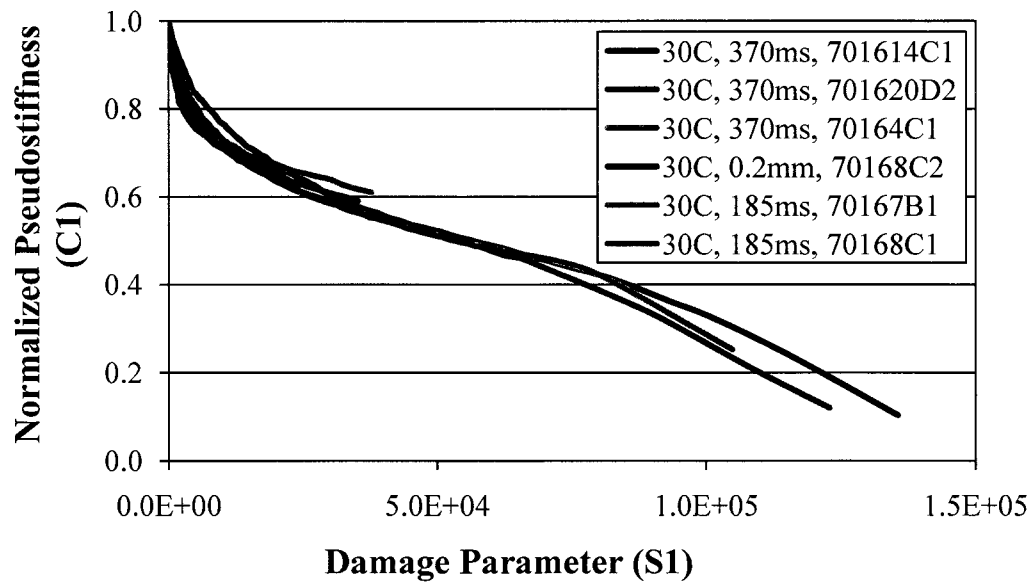**Figure B-20:** Damage characteristic curves for PG 64-16 mixture specimens using alpha = 1/n at 30 C

Figure B-21: Damage characteristic curves for PG 64-16 mixture specimens using alpha = 1 + 1/n at 20 C

Figure B-22: Damage characteristic curves for PG 64-16 mixture specimens using alpha = 1/n at 20 C

Figure B-23: Damage characteristic curves for PG 64-16 mixture specimens using alpha = 1 + 1/n at 10 C

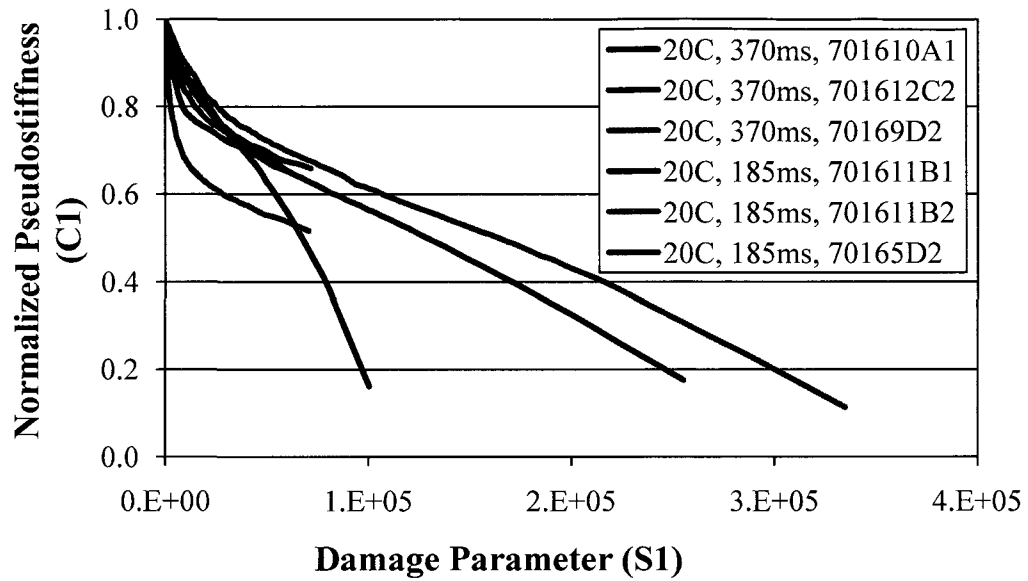**Figure B-24:** Damage characteristic curves for PG 64-16 mixture specimens using alpha = 1/n at 10 C

Figure B-25: Damage characteristic curves for PG 70-16 mixture specimens using alpha = 1 + 1/n at 30 C
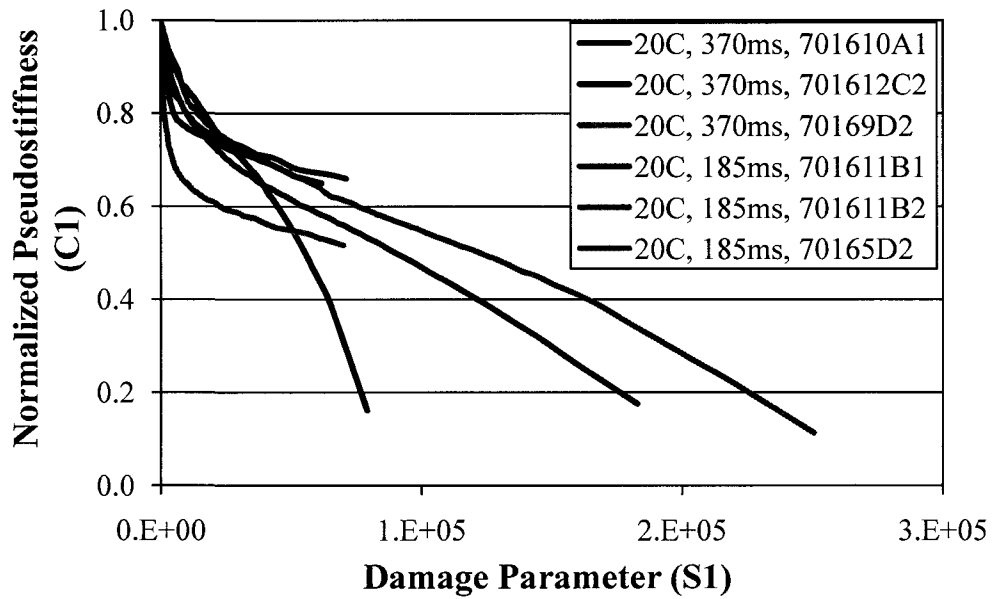

Figure B-26: Damage characteristic curves for PG 70-16 mixture specimens using alpha = 1/n at 30 C

Figure B-27: Damage characteristic curves for PG 70-16 mixture specimens using alpha = 1 + 1/n at 20 C

Figure B-28: Damage characteristic curves for PG 70-16 mixture specimens using alpha = 1/n at 20 C
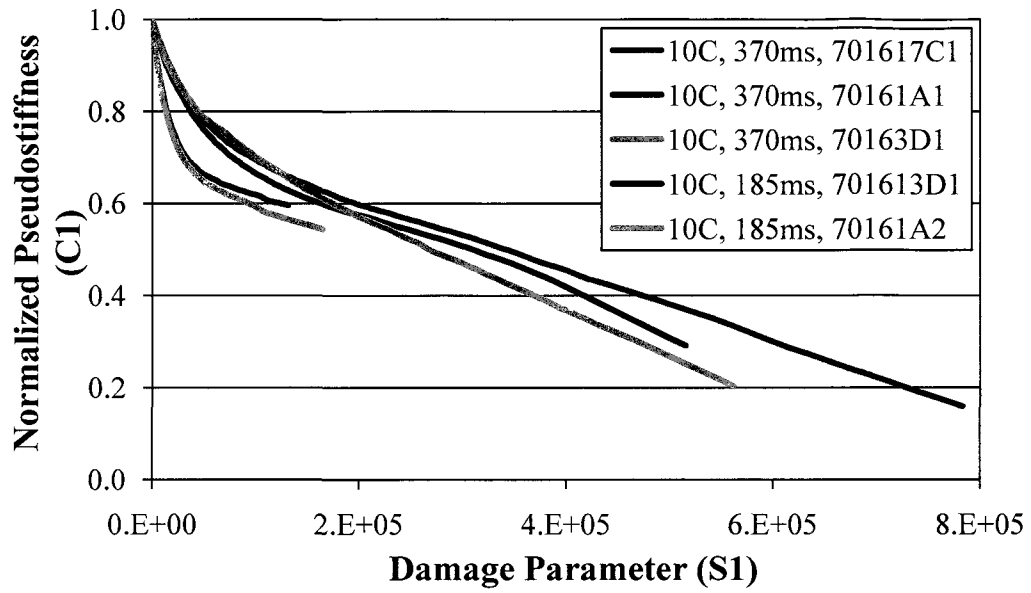
Figure B-29: Damage characteristic curves for PG 70-16 mixture specimens using alpha = 1 + 1/n at 10 C

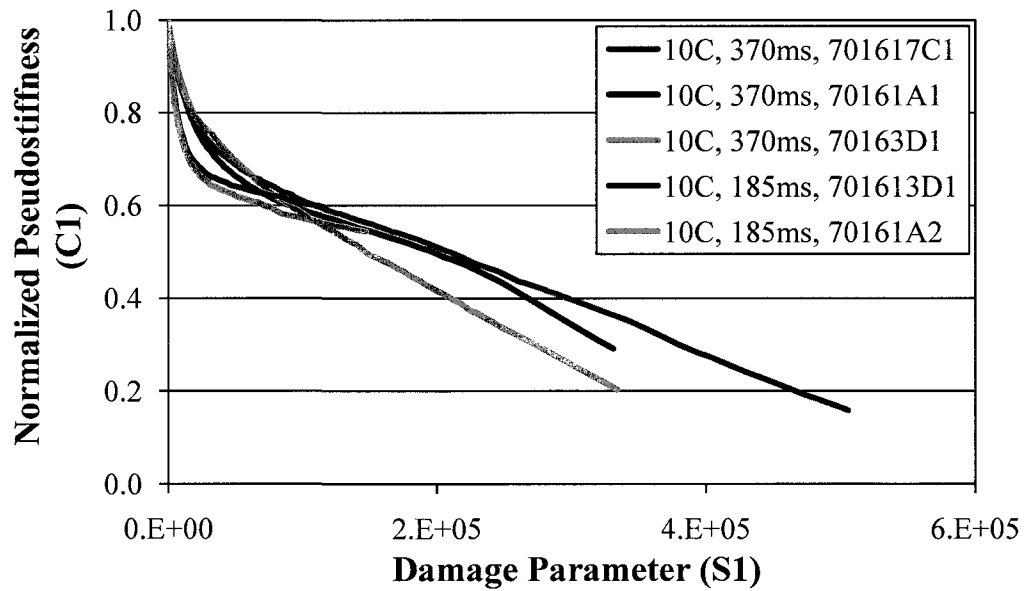Figure B-30: Damage characteristic curves for PG 70-16 mixture specimens using alpha = 1/n at 10 C

230